# REPORT DOCUMENTATION PAGE

*Form Approved*
*OMB No. 0704-0188*

| 1. AGENCY USE ONLY *(Leave blank)* | 2. REPORT DATE | 3. REPORT TYPE AND DATES COVERED |
|---|---|---|
| | 7.Jan.99 | DISSERTATION |

**4. TITLE AND SUBTITLE**
REGIONAL SCALE MODEL CLIMATOLOGY OF THE NORTH AMERICAN MONSOON SYSTEM

**5. FUNDING NUMBERS**

**6. AUTHOR(S)**
CAPT SWANSON ROBERT T

**7. PERFORMING ORGANIZATION NAME(S) AND ADDRESS(ES)**
UNIVERSITY OF UTAH

**8. PERFORMING ORGANIZATION REPORT NUMBER**

**9. SPONSORING/MONITORING AGENCY NAME(S) AND ADDRESS(ES)**
THE DEPARTMENT OF THE AIR FORCE
AFIT/CIA, BLDG 125
2950 P STREET
WPAFB OH 45433

**10. SPONSORING/MONITORING AGENCY REPORT NUMBER**

FY99-33

**11. SUPPLEMENTARY NOTES**

**12a. DISTRIBUTION AVAILABILITY STATEMENT**
Unlimited distribution
In Accordance With AFI 35-205/AFIT Sup 1

**12b. DISTRIBUTION CODE**

**13. ABSTRACT** *(Maximum 200 words)*

**14. SUBJECT TERMS**

**15. NUMBER OF PAGES**

**16. PRICE CODE**

| 17. SECURITY CLASSIFICATION OF REPORT | 18. SECURITY CLASSIFICATION OF THIS PAGE | 19. SECURITY CLASSIFICATION OF ABSTRACT | 20. LIMITATION OF ABSTRACT |
|---|---|---|---|
| | | | |

# REGIONAL-SCALE MODEL CLIMATOLOGY OF THE

# NORTH AMERICAN MONSOON SYSTEM

by

Robert Timothy Swanson, Jr.

A dissertation submitted to the faculty of
The University of Utah
in partial fulfillment of the requirements for the degree of

Doctor of Philosophy

Department of Meteorology

The University of Utah

December 1998

THE UNIVERSITY OF UTAH GRADUATE SCHOOL

# SUPERVISORY COMMITTEE APPROVAL

of a dissertation submitted by

Robert Timothy Swanson, Jr.

This dissertation has been read by each member of the following supervisory committee and by majority vote has been found to be satisfactory.
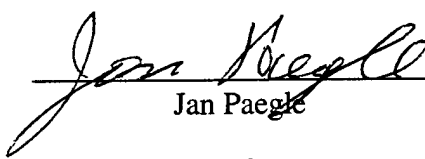
_August 24, 1998_     Chair:   John D. Horel

_August 24, 1998_     Ernesto H. Berbery

_August 24, 1998_     Jan Paegle

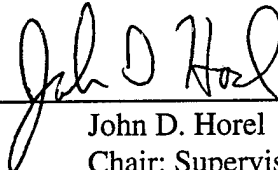_August 24, 1998_     Julia N. Paegle

_August 24, 1998_     W. James Steenburgh

# FINAL READING APPROVAL

To the Graduate Council of the University of Utah:
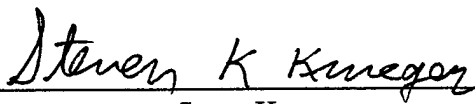
I have read the dissertation of **Robert Timothy Swanson, Jr.** in its final form and have found that (1) its format, citations, and bibliographic style are consistent and acceptable; (2) its illustrative materials including figures, tables, and charts are in place; and (3) the final manuscript is satisfactory to the supervisory committee and is ready for submission to The Graduate School.

___August 24, 1998___
Date

John D. Horel
Chair: Supervisory Committee

Approved for the Major Department

Steve Krueger
Acting Chair/Dean

Approved for the Graduate Council

David S. Chapman
Dean of The Graduate School

# ABSTRACT

The regional climate of the North American monsoon system over the eastern equatorial Pacific Ocean and adjacent land areas is simulated during June, July, and August 1990-1997. The Pennsylvania State University/National Center of Atmospheric Research Mesoscale Model 5 (MM5) is forced by the observed evolution of sea surface temperature and the National Center for Environmental Prediction (NCEP) reanalyses of the atmospheric flow on the lateral boundaries.

The MM5 reproduces many of the general features of the large-scale circulation found in the NCEP reanalyses. It does, however, develop a stronger regional meridional circulation with higher precipitation rates in the Intertropical Convergence Zone (ITCZ), stronger cross-equatorial flow in the boundary layer, and greater divergent flow aloft. The model ITCZ is displaced too far north and tends to be located over the highest sea surface temperature. Mesoscale circulation features, such as diurnal land/sea breezes and gap flows across Mexico and Central America, are captured. The observed latitudinal transition from the shallow planetary boundary layer (PBL) with stratiform clouds over the cool waters of the equatorial Pacific to a relatively deeper PBL further north is simulated by the model. More tropical cyclones develop in the MM5 than were observed and they were comparatively shorter-lived and weaker. Also, the model, as presently configured, does not realistically simulate the year-to-year variations in tropical cyclones.

The regional circulation during Summer 1997 was dominated by the planetary-scale El Niño/Southern Oscillation phenomenon. The normally cool waters along the

equator were unusually warm with enhanced convection to the south of the mean position of the ITCZ. Large-scale subsidence over Central America and the extreme eastern Pacific Ocean led to drought conditions in that region. The number and intensity of tropical cyclones observed during summer 1997 in the eastern equatorial Pacific were reduced despite the fact that the most intense hurricane of the eight seasons occurred during that year. The MM5 captures the weaker and broader ITCZ during summer 1997 over the eastern equatorial Pacific.

TABLE OF CONTENTS

## ACKNOWLEDGMENTS

# CHAPTER 1

# INTRODUCTION

## Background

General circulation models (GCMs) of the atmosphere and ocean have begun to exhibit skill for the prediction of monthly and seasonal climate anomalies in the tropics (Latif et al. 1998). For example, the evolution of equatorial Pacific sea surface temperature (SST) during the 1997-1998 El Niño/Southern Oscillation (ENSO) episode was captured to a large degree at lead times from 3 to 6 months in advance. With this increase in reliability, atmospheric GCMs (AGCMs) are frequently used as part of a coupled modeling system to understand the dynamical processes of the atmosphere-land-ocean system (Delecluse et al. 1998).

Uncoupled AGCMs are also used in climate and climate variation studies. These models are often forced by the observed SST over many years in order to study the seasonal cycle in the atmosphere and the sensitivity of the atmosphere to interannual variations in the state of the ocean (Chen and Van den Dool 1997; Vitart et al. 1997). However, AGCMs and coupled GCMs fail to simulate fundamental aspects, such as the spatial and temporal distributions of the seasonal evolution of precipitation in the tropics (Mechoso et al. 1995). Mesoscale convective systems (MCSs) and tropical cyclones play a significant role in the organization of precipitation in many areas (Mohr and Zipser 1996). As a result of the course sampling of precipitation in GCMs, direct comparison with station data is difficult along coasts and major orographic barriers.

As computing resources improve over the next decade, the length scales resolved by GCMs will decrease. This, coupled with improvements to physical parameterizations in the GCMs, increase the likelihood that global models will more accurately capture smaller scale features including aspects of the seasonal evolution of precipitation in the tropics. However, the benefits of continued improvements in model resolution on the global scale are not clear. Would it be better to expend the computing resources on ensemble simulations rather than increase the model's spatial resolution (Delecluse et al. 1998)? Should inner nests that resolve the circulation at higher resolution be embedded within the GCM (Giorgi 1990) or should numerical techniques be employed to resolve the circulation at higher resolutions in some regions at the expense others (Paegle 1989)?

Advances in observation and data analysis have kept pace with model improvements. The National Centers for Environmental Prediction (NCEP) in cooperation with the National Center for Atmospheric Research (NCAR) have reanalyzed the global circulation over the span of several decades (Kalnay et al. 1996). These reanalyses include all available data (ship and aircraft observations, satellite radiances, in situ measurements, etc.) in order to develop the best possible analysis every 6 h. The NCEP/NCAR reanalyses have been very successful at helping to define the seasonal evolution of the planetary-scale circulation. However, the primary data sets are archived at a 2.5° x 2.5° resolution. Thus, the NCEP reanalyses suffer from some of the same limitations as the GCM simulations; the coarse resolution of the reanalyses miss many significant weather features. For example, as will be shown later, tropical cyclones are not evident in the reanalysis grids. Eventually, reanalyses may be completed at finer resolution for selected components of the globe, such as the Americas. At present, however, the seasonal evolution of the three-

dimensional structure of the atmosphere on the mesoscale remains difficult to define both observationally and in model simulations. The research described here provides insight into the mesoscale evolution of the atmosphere during summer.

## The North American Monsoon System

The seasonal and interannual evolution of the coupled atmosphere-land-ocean system over the tropical Americas has received increased attention (Douglas et al. 1993; Adams and Comrie 1997; Barlow et al. 1998). The Pan American Climate Studies (PACS), initiated by the National Oceanic and Atmospheric Administration's (NOAA) Office of Global Programs, and Variability of American MOnsoon Systems (VAMOS) research programs are helping to focus empirical, numerical, and observational efforts in this region (NOAA 1998).

Following the perspective of the VAMOS program, the North American monsoon system (NAMS) is considered here to include the regions of strong convection during Northern Hemisphere summer over Central America and Mexico as well as the InterTropical Convergence Zone (ITCZ) over the eastern equatorial Pacific. The 'monsoon' of northwestern Mexico and the southwestern United States has many similarities to the Asian monsoon (Tang and Reiter 1984; Adams and Comrie 1997). For example, a significant fraction of the rainfall during the year occurs during a short period from July to September. In addition, the highest temperatures during the year tend to be recorded immediately prior to the relatively sudden onset of rainfall (Higgins et al. 1998).

As a means to examine the spatial variation of the rainfall in the region, Figure 1.1a shows the JJA long-term climatological daily mean precipitation rate as determined by Legates and Wilmott (1990). This resource is one of the few rainfall climatologies

available at roughly 50 km resolution for this region. The ITCZ extends to the north of 10° N between 110° W and 120° W. Heavy rainfall is also found along the coastal areas of southwestern Mexico.

Horel et al. (1989) and Adams and Comrie (1997) describe the seasonal evolution of the NAMS. The dominant region of convection shifts northward from Amazonia after January-February to its northernmost extent during July-August over the eastern equatorial Pacific and adjacent regions of Central America and southern Mexico. The northern extension of the NAMS in northwest Mexico and the southwestern United States has received considerable attention due to the relatively sudden onset of precipitation in those regions (Douglas et al. 1993; Douglas and Li 1996; Adams and Comrie 1997; Stensrud et al. 1997; Higgins et al. 1998). In order to focus on the mesoscale aspects of this seasonal progression, the daily precipitation rate over land is presented in Figure 1.1b. This shows that the heaviest precipitation associated with the northern extension is found along the western slopes of the Sierra Madre Occidental of Mexico and the southwest slopes of the Sierra Madre del Sur of southern Mexico.

The schematic in Figure 1.2a, adapted from NOAA (1998), shows several characteristics of the evolution of the NAMS based on satellite estimates of convective cloud frequency (Negri et al. 1993; J. Gourley 1998, personal communication). The seasonal differences (July minus June) show more convective clouds over northwestern Mexico during July, and less convective clouds over southern Mexico and Central America during the same period. Heavy rainfall originates over southern Mexico during May and spreads northward along the western slopes of the Sierra Madre Occidental into southern Arizona over the next two months (Higgins et al. 1998). The largest precipitation amounts
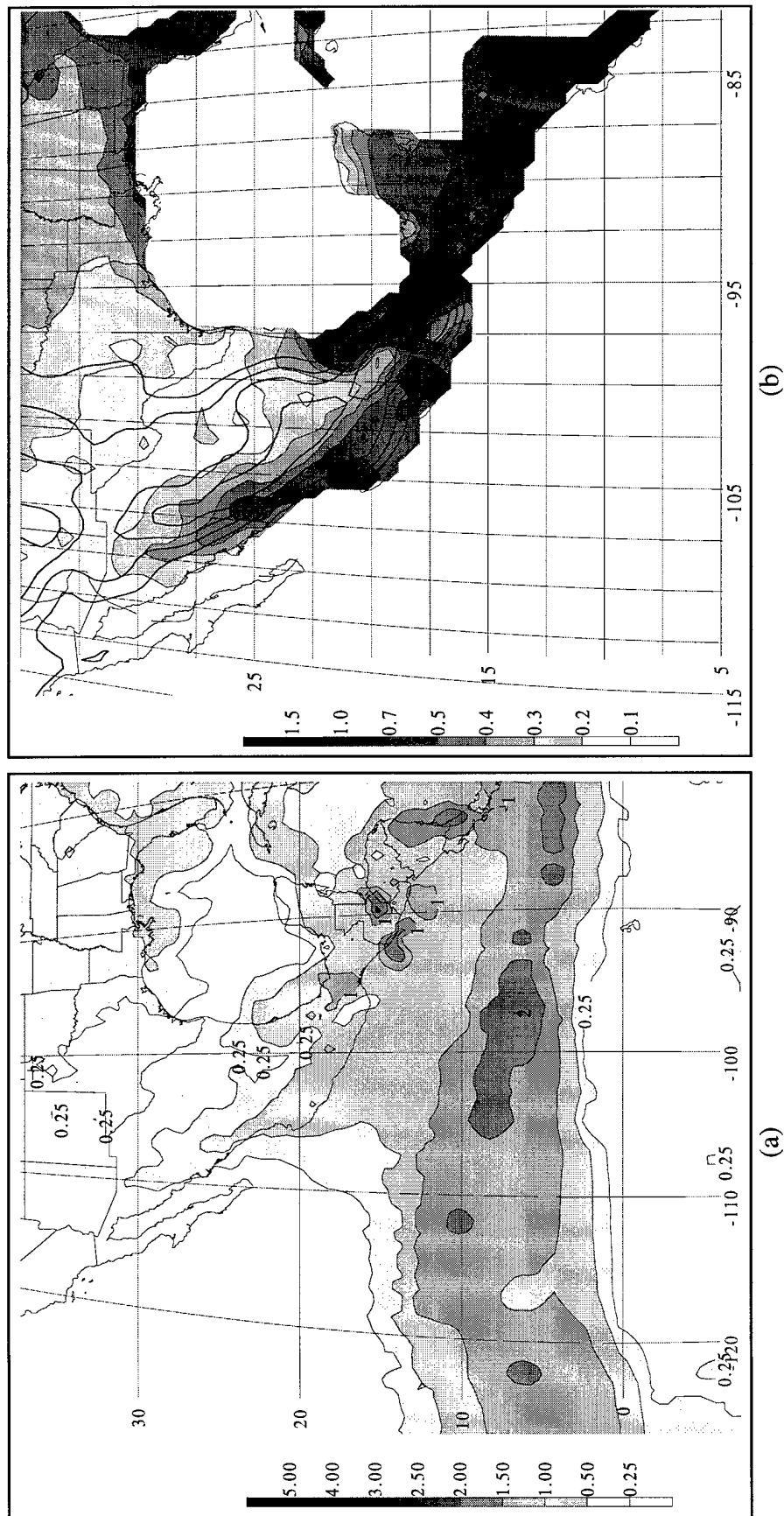
Figure 1.1.    Precipitation rate in cm day$^{-1}$ for JJA from Legates and Wilmott (1990) for (a) region of interest with values over 0.25 cm day$^{-1}$ shaded according to the scale on the left; contour intervals are 0.25, 0.5, 1, 1.5, 2, 2.5, 3, 4, and 5 cm day$^{-1}$ with every other contour labeled and (b) land only with values over 0.1 cm day$^{-1}$ shaded according to the scale on the left; contour intervals are 0.1, 0.2, 0.3, 0.4, 0.5, 0.7, 1, and 1.5 cm day$^{-1}$. Large scale terrain features are contoured at 500 m intervals in (b).

occur during June and September in southern Mexico and Central America with a midsummer "drought" during July and August in this region.

Aspects of the seasonal evolution of the ITCZ during summer are also evident in Figure 1.2a. During July, convection increases to the west of 105° W and decreases to the east. The easternmost extension of this decrease extends over southern Mexico and Central America and is associated with the aforementioned midsummer drought. The increased convection to the west of 105° W will be shown to be due in part to the effect of tropical cyclones that form along the mean position of the ITCZ and are subsequently advected westward by the large-scale flow.

As an example of mesoscale circulations embedded within the NAMS, the schematic in Figure 1.2b depicts the difference in convective frequency between evening and morning, which helps to define the cumulative effects of mountain/valley and land/sea breezes (Negri et al. 1993; Mohr and Zipser 1996). More frequent evening convection is evident over the high terrain and along the coastline while more frequent morning convection appears immediately offshore. As shown by Mohr and Zipser (1996), some of these differences arise from organized MCSs that are more frequent over land during the evenings and offshore during the mornings.

Cold Tongue/ITCZ Complex

The annual appearance of cool water extending westward from the coast of South America near the equator is a dominant feature of the equatorial Pacific Ocean (Horel 1982; Wallace et al. 1989). Figure 1.3 shows the climatological SST averaged over the 8-year period (1990-1997) during the summer season (June-August). This cold tongue along the equator is coupled strongly to the atmospheric planetary boundary layer (PBL)
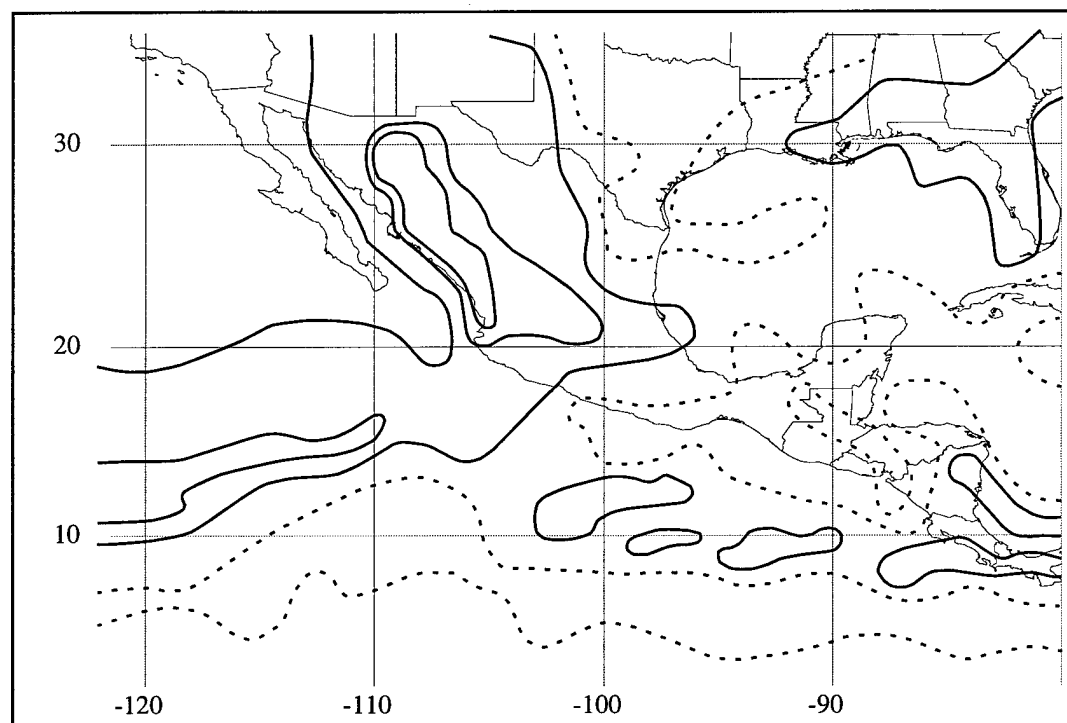
(a)
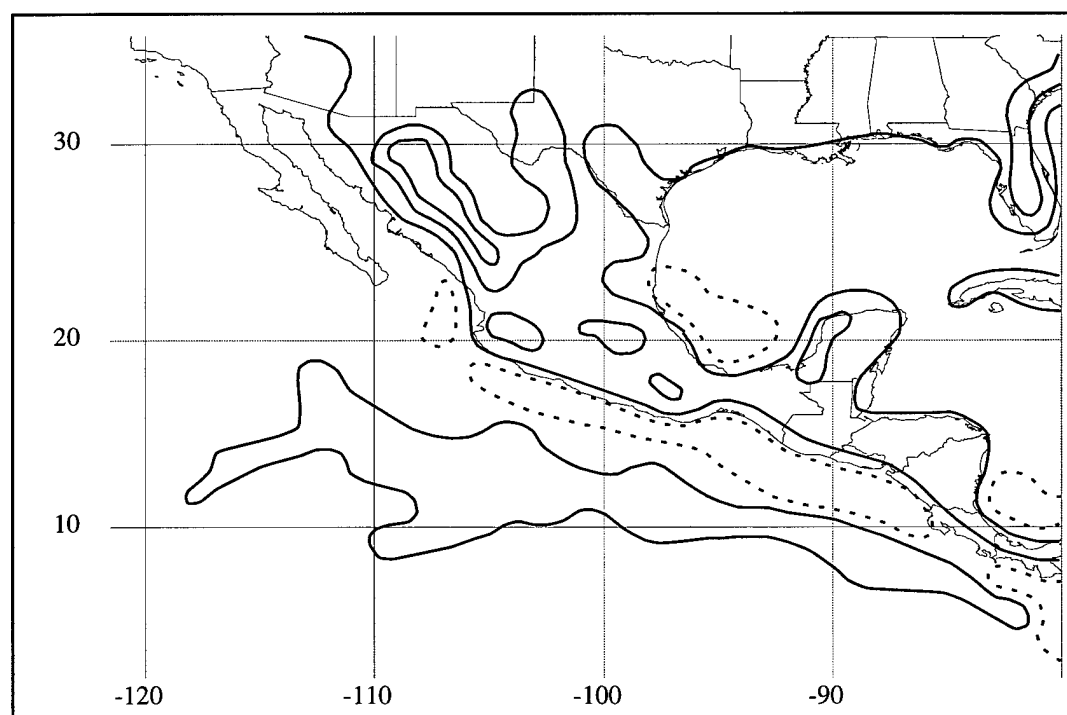
(b)

Figure 1.2.  Schematic differences in convective cloud between (a) July and June, and (b) Evening and morning. Solid (dashed) contours denote (a) greater convection during July (June), and (b) greater convection during evening (morning). Adapted from NOAA (1998).
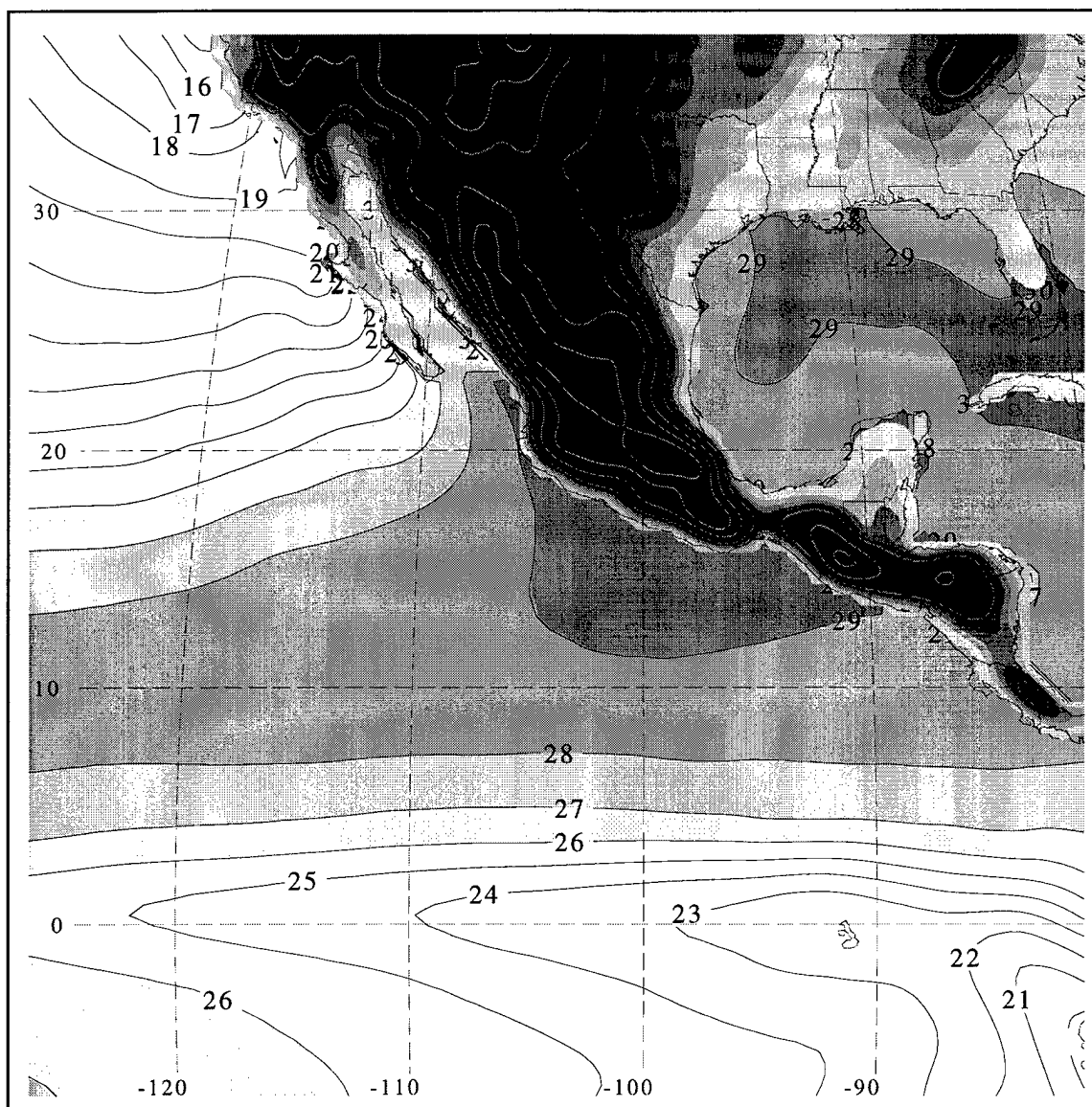
Figure 1.3.　　Terrain and mean SST in °C for JJA 1990-1997. Terrain contour intervals are 1000 m. SST contour intervals are 1 °C. SST is shaded above 26 °C.

through radiative exchange, and sensible and latent heating (Kessler et al. 1998). The ITCZ lies over the warmer ocean water, however it is not coincident with the highest SST shown in Figure 1.3.

Figure 1.4 (courtesy of S. K. Esbensen and W. S. Kessler) depicts schematically the structure of the upper ocean and PBL across the cold tongue/ITCZ complex (CTIC). The sharp SST front to the north of the equator is evident. Strong meridional winds in the PBL blow across the equator over the cold tongue towards the ITCZ (Wallace et al. 1989; Bond 1992; Xie 1998). The depth of the PBL tends to be lowest over the cold tongue with stratiform clouds prevailing in that region (Klein and Hartmann 1993). To the north of the SST front, the depth of the PBL increases until deep convection breaks out in the ITCZ.

## Goals of This Research

Some of the fundamental scientific objectives of the PACS research programs (NOAA 1998) are to promote a better understanding of, and eventual prediction with lead times of a month or season of:

- the boundary forcing of seasonal to interannual climate variations over the Americas,

- the evolution of the tropical SST anomalies in the tropical Pacific and Atlantic,

- the seasonally varying mean climate over the Americas and adjacent ocean regions,

- the time-dependent structure of the CTICs over the Atlantic and eastern Pacific, and

- the relevant land surface processes over the Americas, including the effects of mesoscale orography and coastal geometry.

Both the PACS and VAMOS programs recognize that mesoscale processes affect the distribution of precipitation over the Americas and adjacent oceans. However, the numerical resources required to predict these processes at monthly and seasonal lead times

Figure 1.4.    Idealized cross-section through the CTIC in the monsoonal regime showing the atmospheric meridional circulation and the oceanic thermal structure. E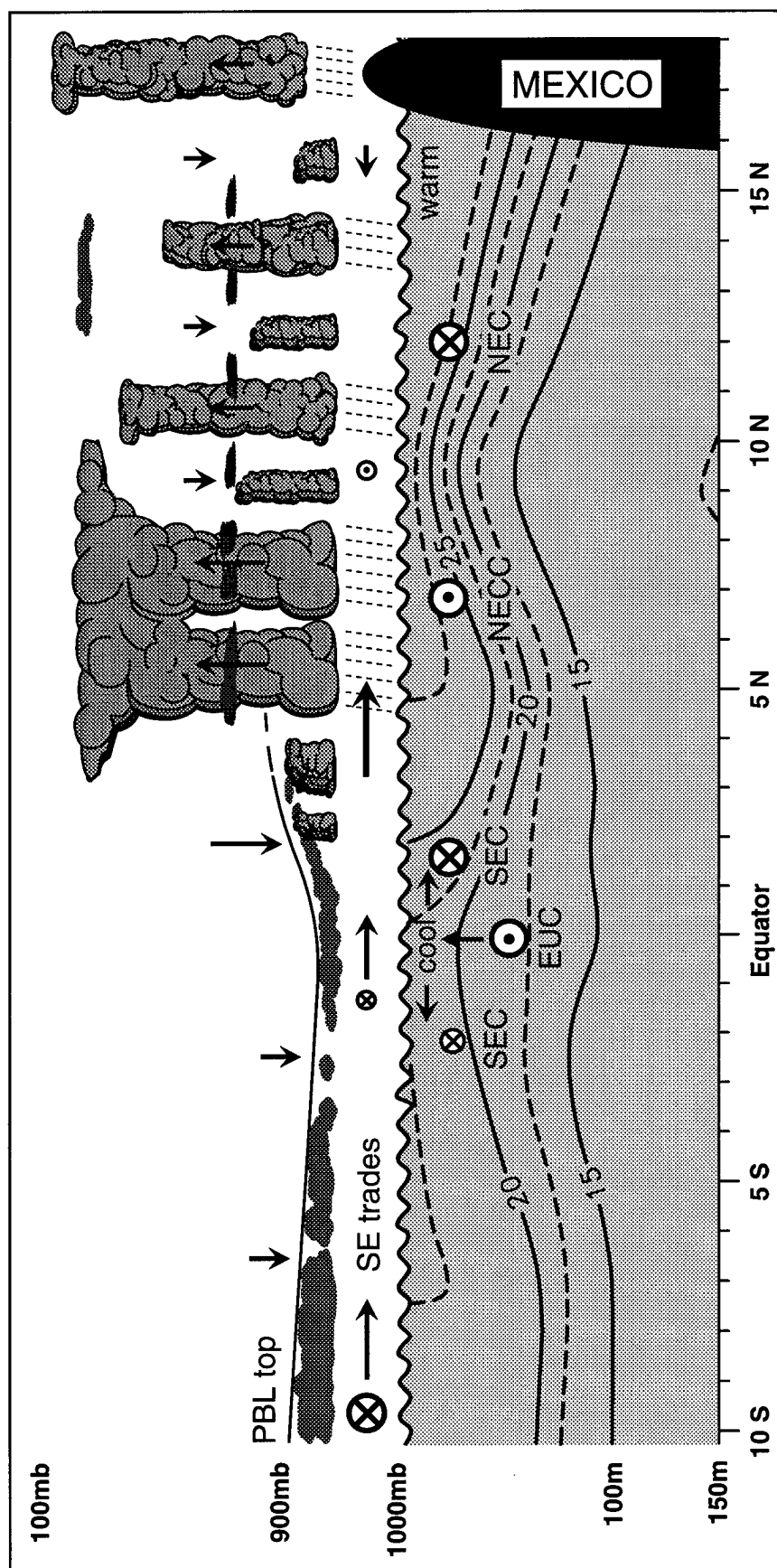ncircled X's (dots) denote westward (eastward) flowing winds or currents. (Courtesy of S. K. Esbenson and W. S. Kessler)

are not available at this time. To do so would require computational resources capable of running ensembles of GCM simulations at resolutions high enough to capture the mesoscale features of interest.

The research presented here parallels that of previous GCM diagnostic studies. The goal is to understand aspects of the diurnal, seasonal, and interannual variability of the atmospheric circulation during Northern Hemisphere summer. The domain of interest lies over the eastern Pacific Ocean and Central America, where a rich spectrum of mesoscale phenomena is observed during the summer season. A series of regional climate simulations have been completed for the months June, July, and August for the 8-year period from 1990 through 1997 using the Pennsylvania State University (PSU)/NCAR Mesoscale Model 5 (MM5). The model is forced on its lateral boundaries by the observed evolution of the large-scale circulation from the NCEP/NCAR reanalyses and at the surface by observed variations in SST from the Reynold's SST analyses (Reynolds and Smith 1994). The model develops mesoscale circulations within the region that are free to mature and decay during the 92-day simulations. Further description of this work is available on-line: **http://www.met.utah.edu/jhorel/cirp/pacs.html**.

There are several unique aspects of this study. First, the length of the regional-scale simulations is considered long for mesoscale studies (albeit relatively short compared to the climate simulations of state-of-the-art GCMs). These simulations, forced by the observed evolution on the lateral boundaries and at the ocean surface, generate model output that can be used to examine temporal (diurnal, intraseasonal, and interannual) and spatial variations in the atmospheric circulation. Another facet is the increased horizontal, vertical, and temporal resolution of the model simulations relative to the NCEP/NCAR

reanalyses (Betts et al. 1996; Higgins et al. 1996; Mo and Higgins 1996; Rasmusson and Mo 1996; Barlow et al. 1998) and the European Centre for Medium-range Weather Forecast (ECMWF) reanalyses (Schmitz and Mullen 1996; Barlow et al. 1998). Additionally, most of the NAMS is encompassed within the model domain in contrast to other regional studies that focus on specific components of the system (e.g., Hales 1974; Dunn and Horel 1994; Stensrud et al. 1995; Bowen 1996; Stensrud et al. 1997). Because the focus of this study lies on identifying mesoscale weather phenomena in a climate context, model output must be stored at high temporal resolution (3 h) for the eight seasons.

Specifically, the goals of this research are to address the following questions:

- Can the regional model develop realistic atmospheric circulations of the NAMS on a variety of temporal scales (diurnal, intraseasonal, interannual)?

- Since the model simulations are constrained by the observed state of the ocean surface and the large-scale atmospheric circulation, what value is gained by running the regional model? Does greater spatial detail both in the horizontal and vertical direction provide greater insight into the physical mechanisms associated with the NAMS?

- Are complex mesoscale phenomenon such as tropical cyclones simulated realistically by the regional model?

The research approach used here, one which constrains the regional model by observed, evolving lateral and ocean surface boundary conditions, is not without its limitations. First, the regional model does not reproduce specific observed weather features beyond a couple days into each season's simulation. Further, major weather disturbances such as tropical cyclones that develop within the model may not be consistent

with the observed flow as they approach the lateral boundaries. This inconsistency leads to unrealistic atmospheric circulations as the lateral boundary conditions and interior flow diverge (Warner et al. 1997). Also, though tropical cyclones would be expected to cool the ocean surface as a result of increased mixing in the ocean (Nelson 1998), the prescribed SST in the model prevents air-to-sea feedback in this study.

In Chapter 2, a description of the MM5 is presented. The time-averaged regional climate is examined in Chapter 3 as well as selected mesoscale features captured by these simulations. The intraseasonal variability of the NAMS is described in Chapter 4. Interannual variations are examined in Chapter 5 and the appendices. A summary and conclusions follow in Chapter 6.

CHAPTER 2

MODEL DESCRIPTION

Model Setup

The model used in this study is the MM5, version 2.0 (Grell et al. 1994). Later versions of this model are now available, but for consistency among the eight seasons of model integration, the model was fixed to this version. The model options used for this research are characterized by the following:

- nonhydrostatic dynamical treatment

- 25 vertical sigma ($\sigma$) levels extending from the surface to 10 mb; 6 levels lie below 850 mb over the ocean (the data are output on the following $\sigma$ half-levels: 0.02, 0.06, 0.11, 0.16, 0.21, 0.26, 0.31, 0.36, 0.41, 0.46, 0.51, 0.56, 0.61, 0.71, 0.76, 0.81, 0.85, 0.89, 0.93, 0.96, 0.98, 0.99, 0.999)

- 100 x 100 grid with a horizontal spacing of 50 km on the sphere (i.e. no map transformation is used)

- Kain-Fritsch cumulus parameterization (Kain and Fritsch 1990)

- explicit moisture - mixed phase (Reisner 1) (Hsie et al. 1984; Dudhia 1989)

- Blackadar boundary layer parameterization (Zhang and Anthes 1982)

- standard MM5 radiation package (Dudhia 1989)

- prescribed land use and soil moisture; with categories that range from desert to tropical forest

- two-minute time step.

The model domain extends from about 7° S to 37° N, and 76° W to 126° W as depicted in Figure 2.1. This region covers the main components of the NAMS, including the ITCZ across the eastern equatorial Pacific and regions of heavy summer precipitation over Central America and Mexico. While the domain extends into the southern United States, the lateral boundary conditions constrain the flow quite severely within approximately 2.5° of the boundary. Thus, little attention is placed on the model simulations over northern Arizona, New Mexico, or Florida.

The initial conditions are obtained from NCEP/NCAR reanalyses (Kalnay et al., 1996). The NCEP/NCAR reanalysis project is a joint effort whose goal is to produce a 40+ year (1957-present) global analysis with a fixed data assimilation system. These data are available on a 2.5° x 2.5° global grid every 6 h. We use the pressure level data sets comprised of 17 vertical levels from 1000 mb to 30 mb. These data are converted to GEMPAK format (des Jardins et al. 1990) and then interpolated to MM5 input grids. The lateral boundary conditions are updated at 6-h intervals throughout the model run from the same data set. SST is prescribed from weekly averages derived from the Reynold's SST analyses (Reynolds and Smith 1994). This optimum interpolation analysis is produced as a weekly average and output on a 1° x 1° grid. It incorporates both in situ and satellite data.

For these simulations, some modifications were made to make the model stable during the long integrations and to yield additional diagnostic fields. According to Wang and Seaman (1997), the Kain-Fritsch cumulus parameterization did well forecasting convective precipitation during the warm season at a resolution (36 km) similar to that used here. Thus that scheme was used here with one small change: the 'radius of convection' was changed to 1.0 km from the original 1.5 km in order to simulate the
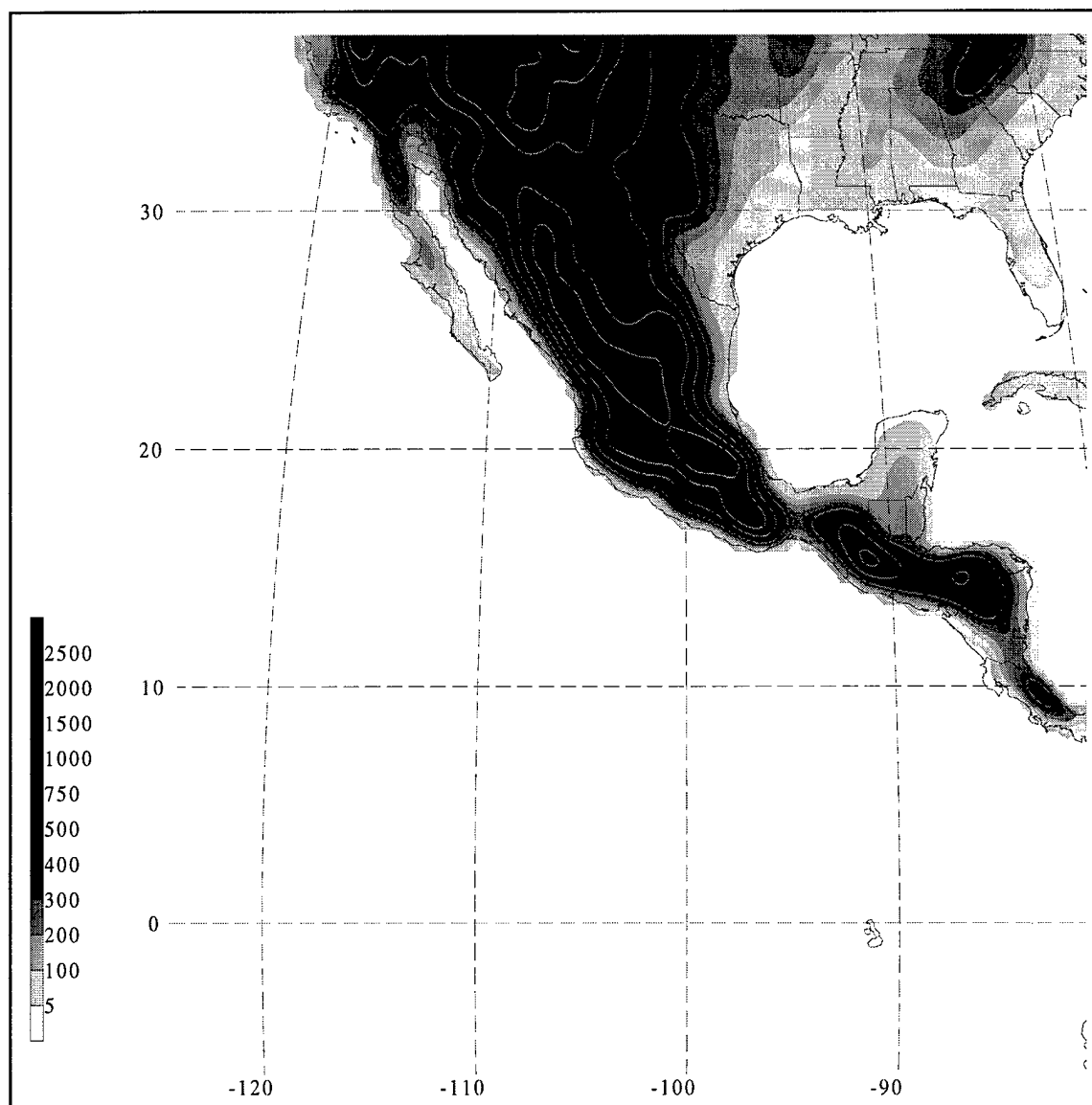
Figure 2.1.　　MM5 model domain and terrain. Terrain height values are shown in shaded scale on left. Contour intervals are 1000 m.

slower ascent rate of tropical convection and reduce the total amount of precipitation in the ITCZ. Additional code was added to output the sensible, latent, and radiative heat fluxes; evaporation; and precipitation types. Further, some manual adjustments were made to the land/sea data points to more realistically represent the coastlines. Finally, SST in the Gulf of California is poorly specified in the Reynold's SST analysis as a result of limited observations. Therefore, SST in the Gulf was fixed to climatological values 26 °C, 28 °C, and 30 °C during the months June, July, and August, respectively (Robinson 1973).

The model simulations were run using eight of twelve processors on a Silicon Graphics Power Challenge computer. Each 92-day simulation took approximately 72 wall hours to complete and produced 15 gbytes of output data. Accumulated precipitation rates are output every hour. All other fields are output at 3-h intervals. The model output was post-processed to GEMPAK grids and left in its original $\sigma$ coordinate. This was done to retain the highest realistic vertical resolution possible in the PBL and to minimize errors introduced by interpolating the non-hydrostatic output. In some instances the mean fields were interpolated to pressure coordinates to allow direct comparison to the NCEP reanalysis data. The NCEP reanalysis data were interpolated horizontally to the MM5 grid for comparison. It should be noted that the vertical resolution of the NCEP/NCAR reanalysis data in the PBL is limited to the following standard layers: 1000 mb, 925 mb, and 850 mb.

## Model Design Limitations

Computational resource limitations require trade-offs between enhancing the horizontal and vertical resolution in order to adequately describe important mesoscale features, wider geographical domain in order to capture more completely the NAMS, and

longer model integrations in order to simulate the entire seasonal evolution of the NAMS. For example, horizontal resolution higher than 50 km would have improved the treatment of tropical cyclones and coastal circulations. In retrospect, the model domain should have been extended further west in order to allow tropical cyclones to evolve more accurately to the west of 120° W.

Other potential problems with the model setup should be noted. Delworth and Manabe (1989) point out that inaccurate soil moisture content can negatively impact model simulations. They show that soil wetness anomalies can affect the PBL relative humidity and temperature by altering the fluxes of latent and sensible heat. The fixed soil moisture as a function of land-use category used in these simulations reduce the available moisture during the rainy season in normally arid regions. This may contribute to lower precipitation amounts over some land areas than observed and limit any long-term feedbacks between the land surface and atmosphere. Also the lack of atmosphere to ocean forcing prevents the mesoscale momentum and heat fluxes near the surface from affecting the SST. This lack of coupling prevents any modification of the SST by the tropical cyclones that develop within the model. As noted by Nelson (1998), SST can be reduced by up to 4 °C in areas of heavy convection such as beneath a hurricane.
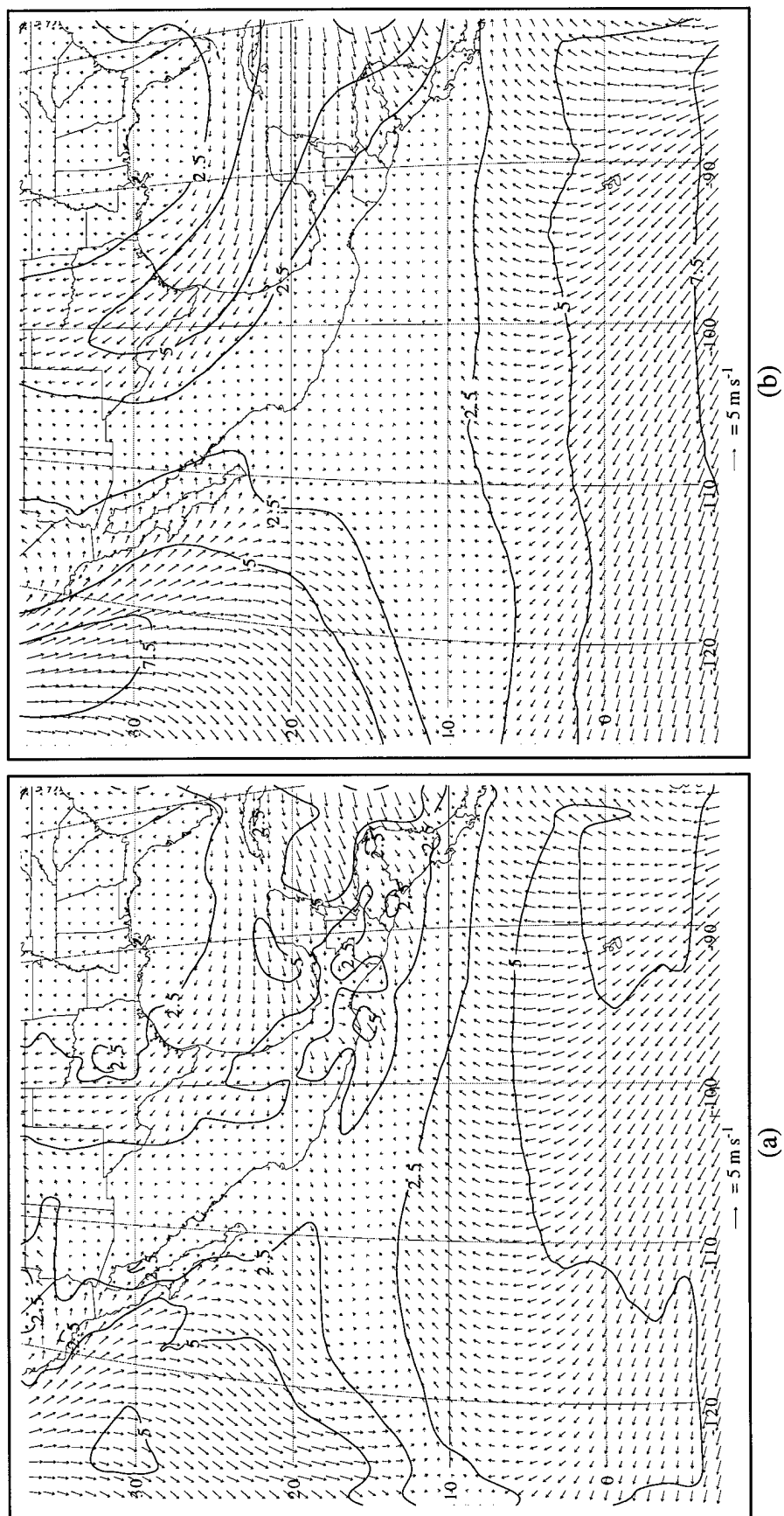
CHAPTER 3


REGIONAL CLIMATE


In order to focus initially on many of the basic characteristics of the NAMS and

CTIC, the model's atmospheric circulation averaged over all eight summer seasons (JJA

1990-1997) are examined. Where applicable, the circulation determined from the MM5 is

contrasted to that of the corresponding NCEP reanalyses and other data sources.

Next, aspects of the regional climate that emphasize phenomena on the mesoscale

are examined. These include: precipitation distribution, diurnal mountain/valley and land/

sea breezes, parcel motion, and tropical cyclones.


<u>Large-Scale Aspects of the Regional Climate</u>

<u>Surface and Upper-Tropospheric Wind</u>

The 10 m (lowest half-$\sigma$ layer) above ground level (AGL) winds from the MM5

and NCEP reanalyses are shown in Figure 3.1. The wind vectors are plotted at every other

grid point for clarity. This convention is followed in all of the figures shown in the text.

Major flow features evident in both panels are: meridional winds across the cold tongue

near the equator, strong northerly winds to the west of Baja California that are associated

with the North Pacific anticyclone and onshore flow into Texas from the Gulf of Mexico

associated with the low-level jet in this region. Channeling of the near-surface flow

through gaps in the terrain of Mexico and Central America (see Figure 2.1) are evident in

the MM5 especially in the Gulfs of Tehuantepec, Honduras, and Papagayo.

Figure 3.1. 10 m AGL winds and isotachs in m s$^{-1}$ for JJA 1990-1997 for (a) MM5 and (b) NCEP. Contour intervals are 2.5 m s$^{-1}$.

The 200 mb winds from the MM5 and NCEP reanalyses are shown in Figure 3.2. Major flow features found in both of these panels include: northeasterly flow between 10° N and the equator, an anticyclone aloft centered near 20° N, 110° W, and subtropical trough to the west of Baja California. The strength of the divergent flow from the anticyclone is noticeably stronger in the MM5 compared to the NCEP reanalyses. In addition, inconsistencies between the lateral boundaries and the interior flow are evident in the southernmost extent of the subtropical trough.

Precipitation

As noted by Barlow et al. (1998), the observed precipitation rates in the oceanic component of the NAMS are difficult to estimate. Estimates of maximum precipitation rates during summer range from 0.3 cm day$^{-1}$ to 4 cm day$^{-1}$ over the ITCZ and vary from 0.1 cm day$^{-1}$ to 5 cm day$^{-1}$ over Mexico and Central America (Legates and Wilmott 1990; Negri et al. 1993; Janowiak et al. 1995; Huffman et al. 1997; Barlow et al. 1998; Higgins et al. 1998; Xie and Arkin 1998). The daily precipitation rates from the MM5 and the NCEP reanalysis fall within those ranges and are shown in Figure 3.3. In contrast to the near-surface and upper-tropospheric wind fields, the differences in precipitation rates between the MM5 and the NCEP reanalyses are quite large. The NCEP reanalyses place the maximum precipitation over Panama, with other local maxima along the ITCZ, over western Mexico and Florida. As discussed by Higgins et al. (1996) and Barlow et al. (1998), the NCEP reanalyses tend to overestimate precipitation over land by as much as a factor of two.

In contrast to that in the NCEP reanalysis, the maximum precipitation in the MM5 is centered near 13° N, between 110° W and 100° W. The latitudinal position of the ITCZ
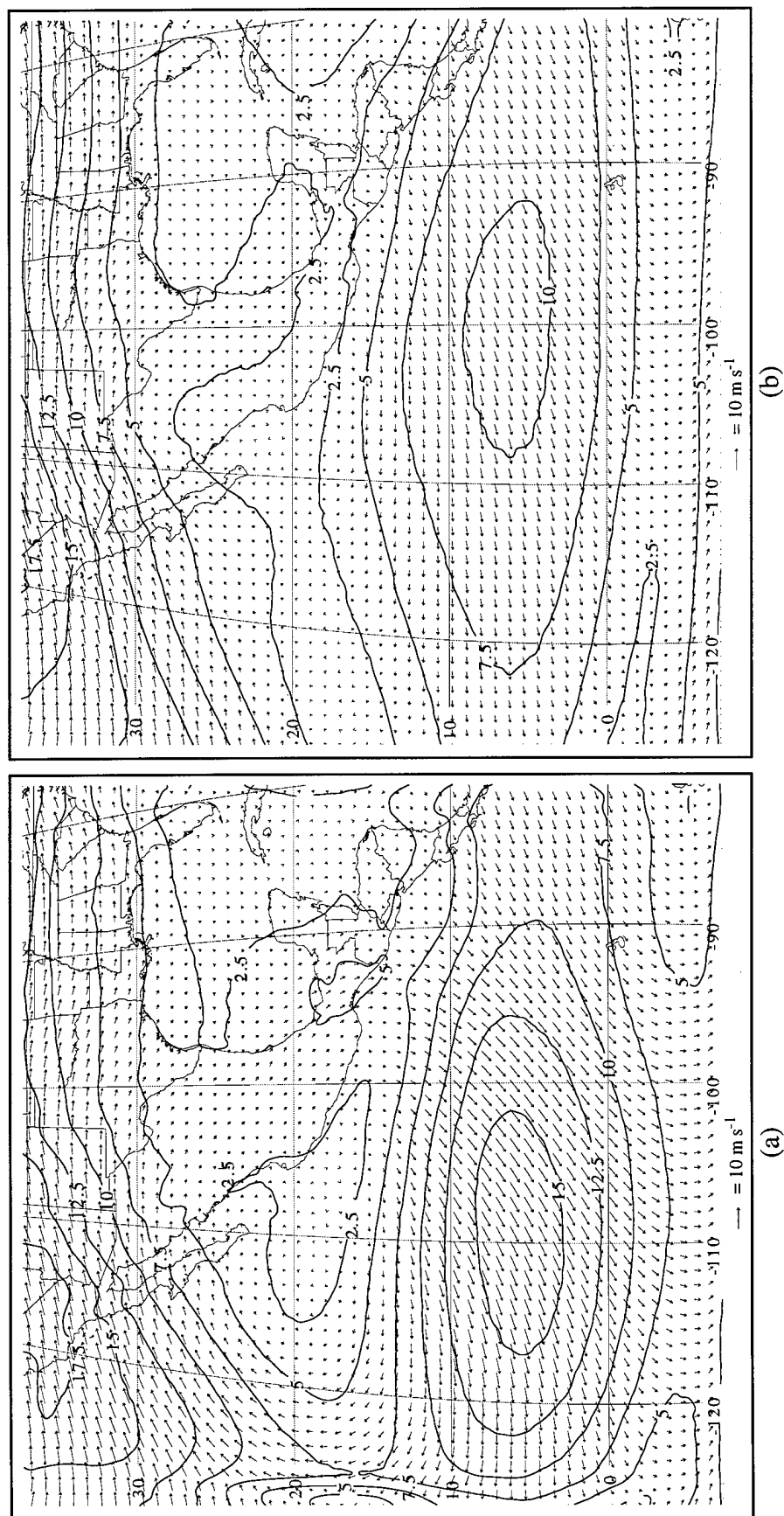
(b)

(a)

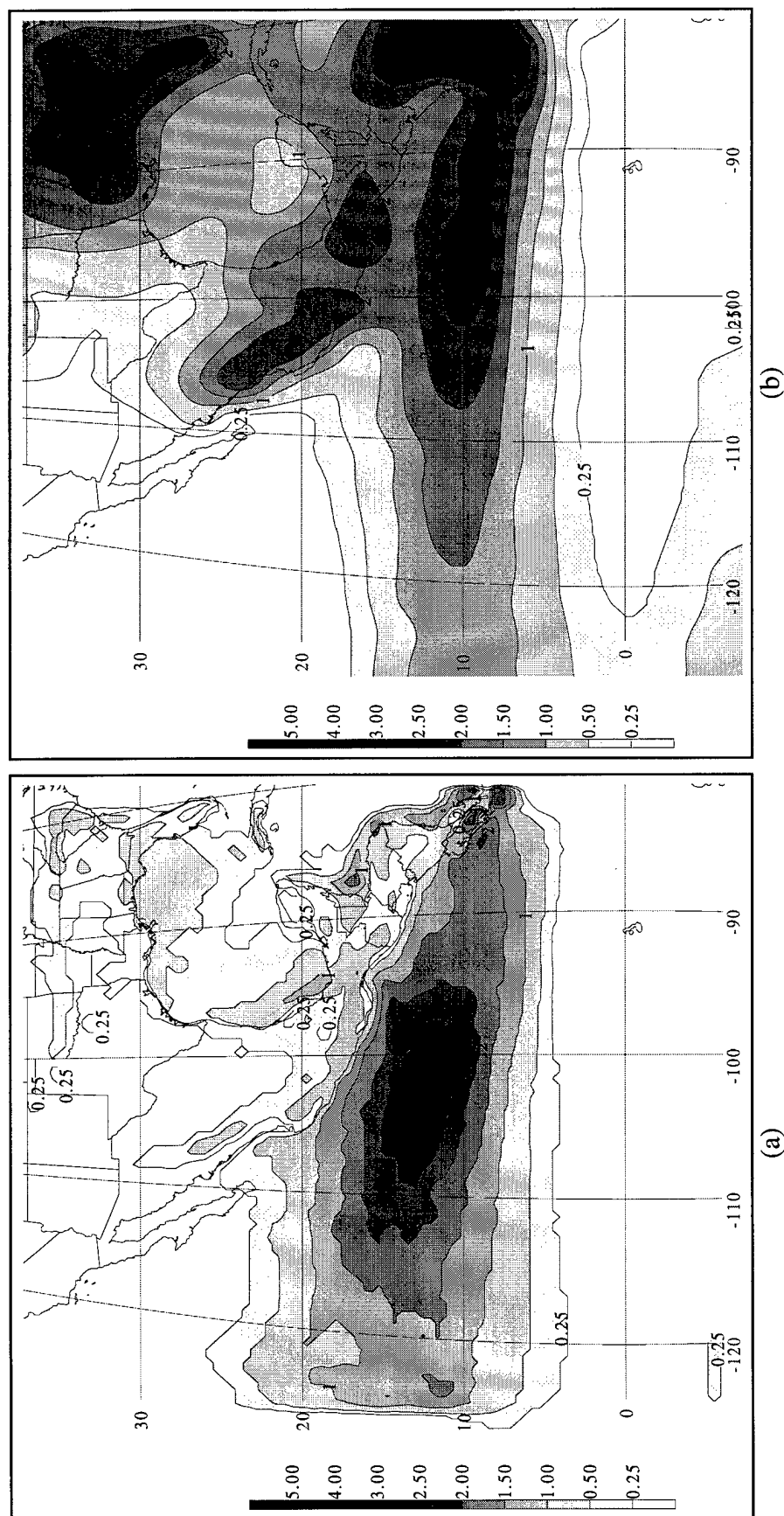Figure 3.2.    200 mb winds and isotachs in m s⁻¹ for JJA 1990-1997 for (a) MM5 and (b) NCEP. Contour intervals are 2.5 m s⁻¹.

Figure 3.3. Precipitation rate in cm day⁻¹ for JJA 1990-1997 for (a) MM5 and (b) NCEP. Values over 0.25 cm day⁻¹ are shaded according to the scale on the left. Contour intervals are 0.25, 0.5, 1, 1.5, 2, 2.5, 3, 4, and 5 cm day⁻¹ with every other contour labeled.

in the region is further north than that observed (Figure 1.1a). The heaviest precipitation tends to occur in the model where the SST is the highest. Such behavior is common in GCM simulations as well and reflects the sensitivity of model convective parameterization schemes to surface temperature in the tropics. On the other hand, there is considerable uncertainty regarding the actual distribution of precipitation in the region (Janowiak et al. 1995). Other climatologies place the precipitation maximum along 10° N, although most of these are computed on a coarse (2.5° x 2.5° latitude-longitude) grid.

Greater precipitation is evident along the northern flank of the ITCZ with less precipitation over land. Given the spread in observed precipitation estimates over the oceans, it is difficult to critique the MM5 simulations in great detail. Over land, the MM5 precipitation rates are comparable to station and satellite observations in northern Mexico (Legates and Wilmott 1990; Negri et al. 1993; Higgins et al. 1998). However, the model may not develop enough precipitation in some areas, such as the Sonora desert, due to the aforementioned lack of land surface-atmosphere feedback in this region. This may inhibit precipitation because the moisture availability in this seasonally arid region is fixed. Another possible deficiency includes excessive precipitation immediately offshore southern Mexico and Central America. Inaccurate treatment of coastal land/sea breezes as a result of the relatively coarse resolution of the MM5 (50 km) may be responsible.

Vertically Integrated Moisture Flux

Many investigators (e.g., Berbery et al. 1996; Higgins et al. 1996; Mo and Higgins 1996; Rasmusson and Mo 1996; Schmitz and Mullen 1996; Wang and Paegle 1996; Paegle and Mo 1997) have used the moisture flux as a means to evaluate components of the water budget as well as to define regional transport of moisture. Total water content in

the MM5 during the 92-day simulations is not conserved as a result of a number of small, cumulative errors. These errors include: model numerics such as diffusion, inaccuracies in the advection of cloud water and moisture within the domain (especially near the boundaries), and treatment of the vertical transport of moisture in the Kain-Fritsch cumulus parameterization scheme. Nevertheless, the model's total vertically integrated moisture flux provides a useful diagnostic of the net effects of moisture and wind.

The total vertically integrated moisture flux was initially calculated for each time step and then averaged over the eight summers. It is shown for the MM5 and the NCEP reanalyses in Figure 3.4. Both the MM5 and the NCEP reanalyses show a well defined cross-equatorial moisture flux and a comparable flow pattern into Texas from the Gulf of Mexico. A stronger moisture flux into the ITCZ from the south is present in the MM5. In addition, strong moisture fluxes are evident near the western coast of central Mexico. These will later be related to the occurrence of tropical cyclones. This tropical-cyclone influenced moisture flux breaks up the east-west moisture pipeline through the mean position of the ITCZ. Schmitz and Mullen (1996) noted similar features in the ECMWF reanalyses which were conspicuously absent from the NCEP reanalyses.

Following Schmitz and Mullen (1996) and others, the vertically integrated moisture flux is also examined as a function of height. The MM5 and NCEP lower-tropospheric contributions to the moisture flux (surface to 0.69 $\sigma$) are shown in Figure 3.5. As expected, the primary source of most of the total moisture flux (Figure 3.4) is from this layer, which is roughly equivalent to the surface to 700 mb layer over oceanic regions. Minor distortions to the mean moisture flux result from terrain effects such as near the Isthmus of Tehuantepec. The mid-to-upper tropospheric (0.69 $\sigma$ to 0.1 $\sigma$) contribution
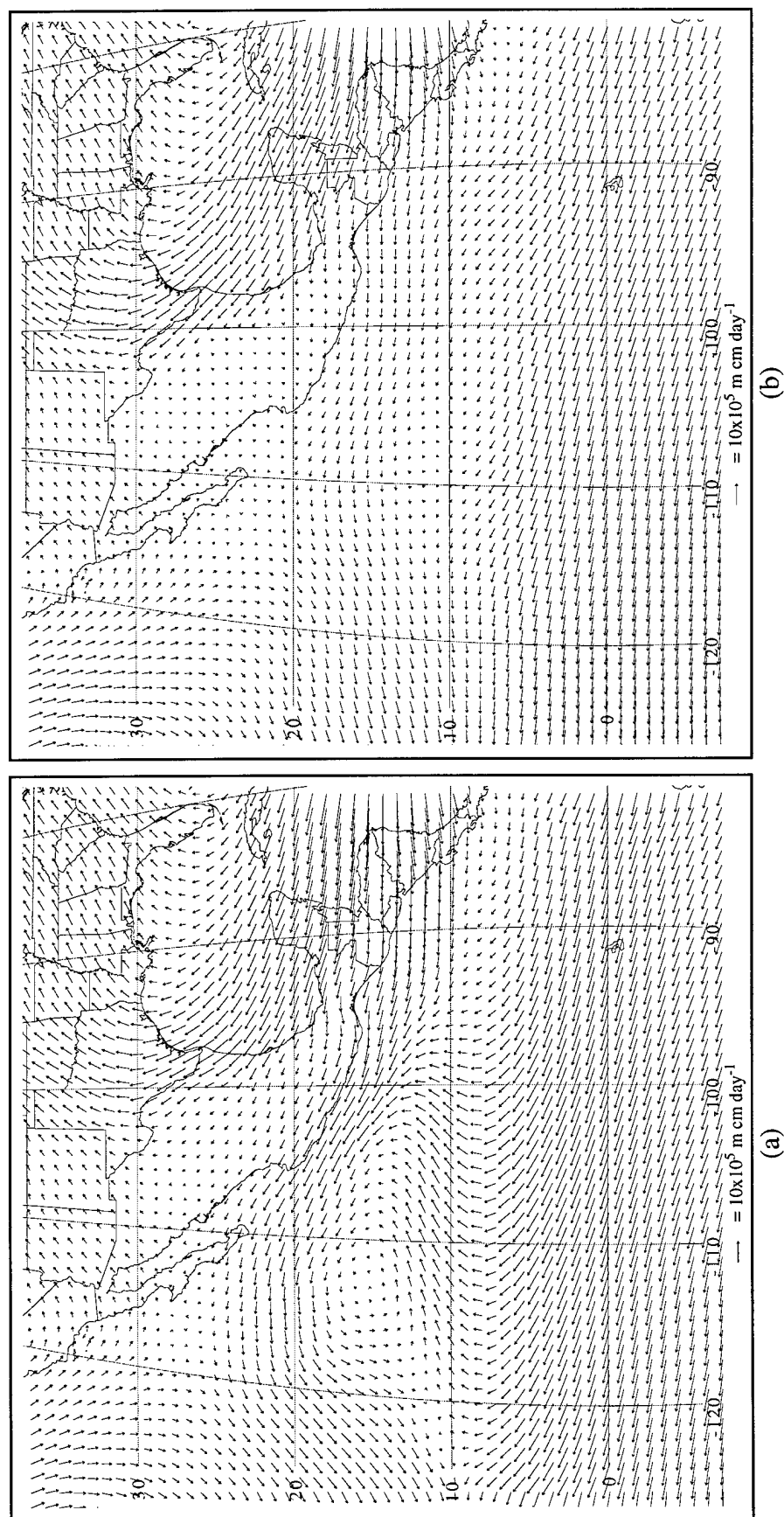
Figure 3.4. Total vertically integrated moisture flux in $10^5$ m cm day$^{-1}$ for JJA 1990-1997 for (a) MM5 and (b) NCEP.
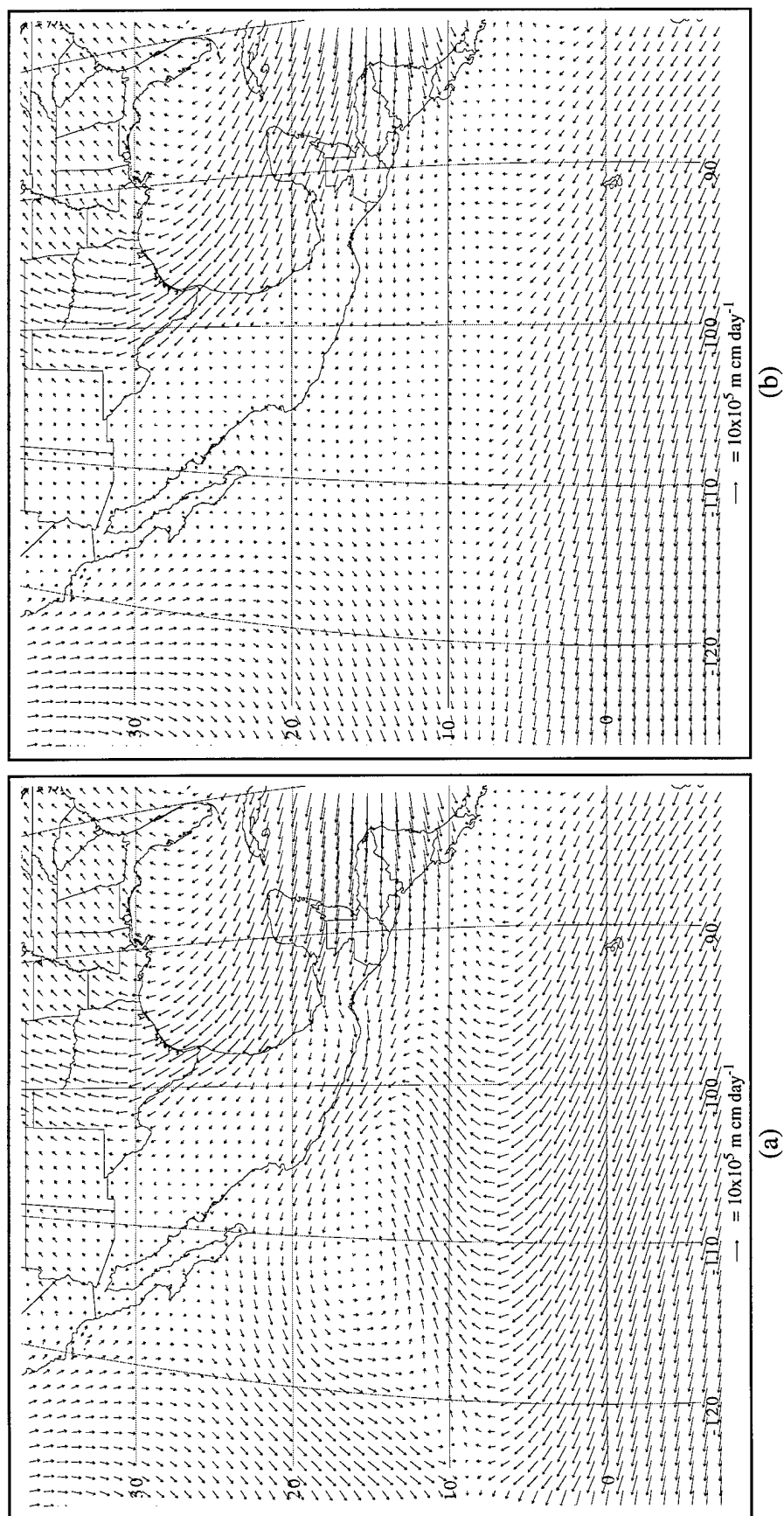
Figure 3.5.  Lower tropospheric (surface to 0.69 σ) contribution to the total vertically integrated moisture flux in $10^5$ m cm day$^{-1}$ for JJA 1990-1997 for (a) MM5 and (b) NCEP.

(not shown) to the total moisture flux is small, but indicates a general east-to-west flux of moisture.

## Vertical Cross Sections Through the CTIC

The climatological mean SST is shown in Figure 3.6. The equatorial cold tongue is evident as well as the high SST beneath the ITCZ (Figure 3.3). To further examine the physical processes in the CTIC, two vertical cross sections from the MM5 (comparable to the schematic cross section in Figure 1.4) are examined. The cross sections extend along 105° W and 95° W from 5° S to 35° N (Figure 3.6). Similar figures from the NCEP reanalyses are not shown, since the resolution of the PBL in the NCEP reanalyses is too coarse to derive any useful information.

The cross section along 105° W, shown in Figure 3.7, cuts directly across the region of maximum model precipitation in the ITCZ (Figure 3.3). Mean surface temperature (SST over water, ground temperature over land) along 105° W is shown by the dashed line in the lower graph. The equatorial cold tongue is apparent with average values lower than 25 °C; cool surface temperatures are also evident over the high terrain. Average daily precipitation rates, denoted by the solid line in the lower graph, show precipitation rates on the order of 3 cm day$^{-1}$ in the vicinity of the ITCZ with smaller peak amounts over the high terrain. As noted before, the ITCZ is simulated to lie further north than the observed position and tends to lie in the region of the highest SST.

Strong, low level southerly flow is evident across the equator within a deep layer in the PBL. The strongest low-level flow is around 950 mb near 3°-5° N, with greater meridional shear over the equator comparable to the conditions observed by Bond (1992). Return flow aloft is evident above 350 mb (see also Figure 3.2). Subsidence above the
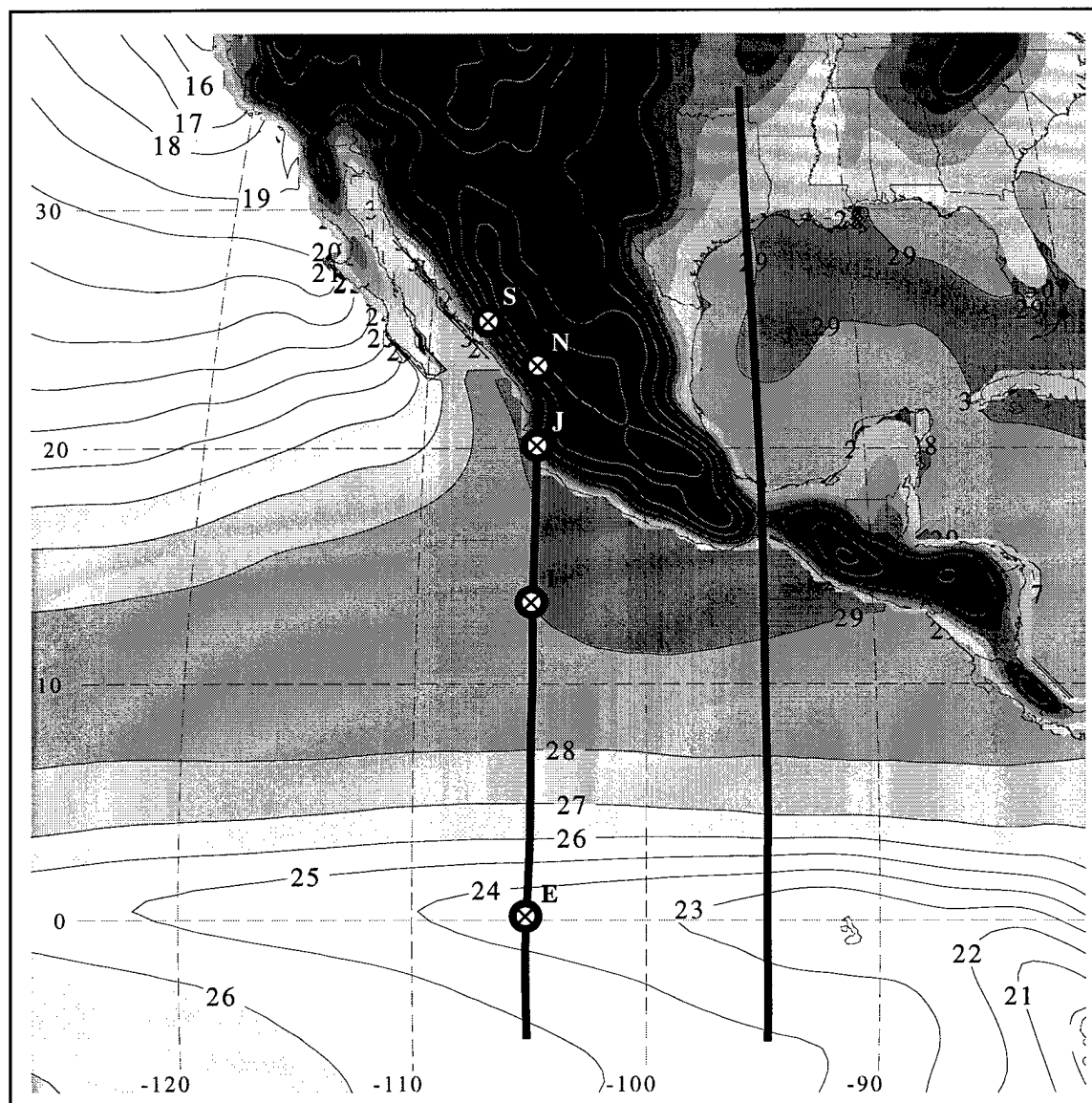
Figure 3.6.    MM5 model terrain, locations of vertical cross sections (solid lines),
locations of parcel trajectory ending locations (crosses), and mean SST in
°C for JJA 1990-1997. Terrain contour intervals are 1000 m. SST contour
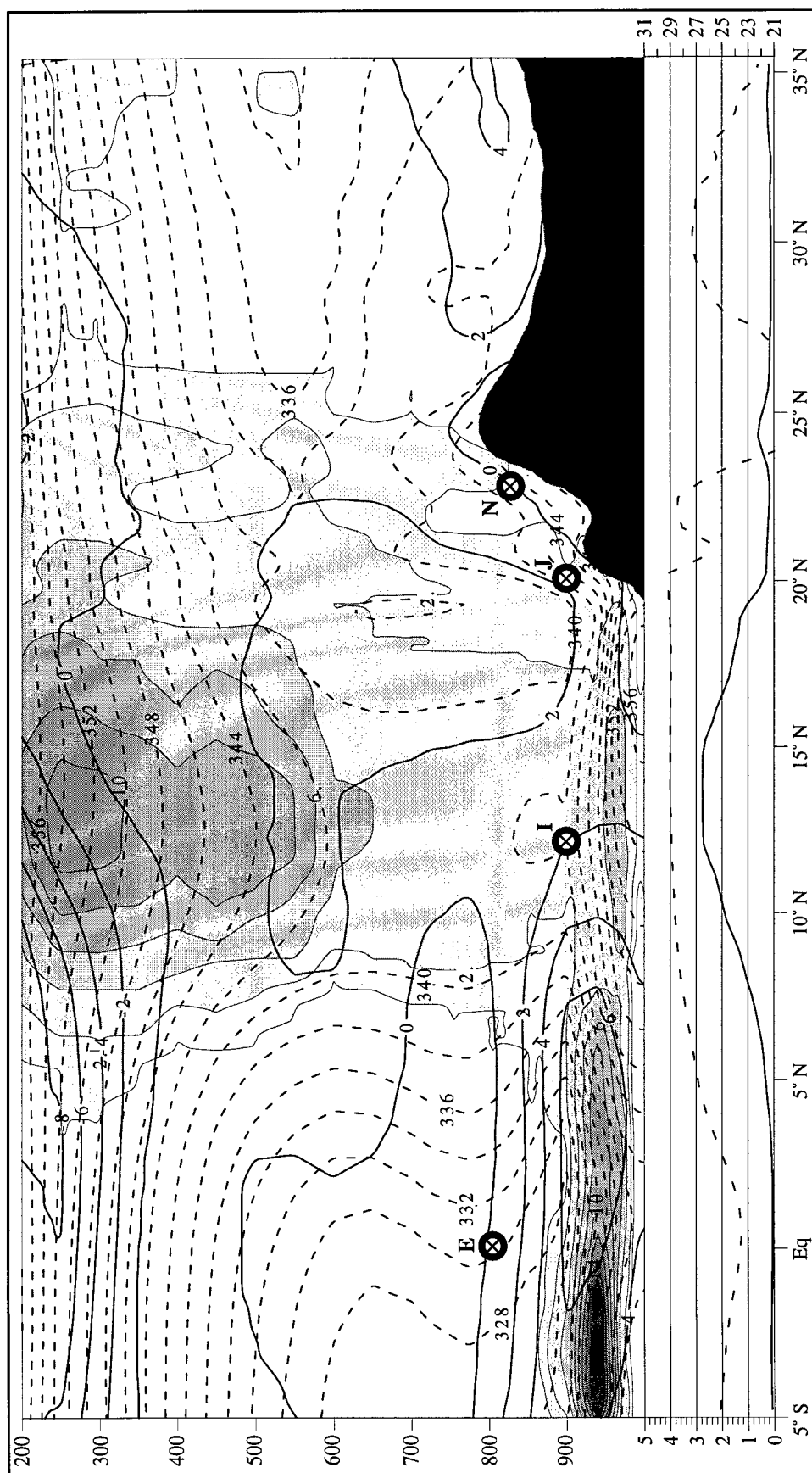intervals are 1 °C. SST is shaded above 26 °C.

Figure 3.7.    Vertical cross section for JJA 1990-97 along 105° W from 5° S to 35° N. The vertical coordinate is pressure in mb. The thin dashed lines are $\theta_e$ in K. The thicker solid lines denote the meridional wind component in m s$^{-1}$. The shaded regions and associated contours are total LWC in 10$^{-2}$ g kg$^{-1}$. The lower graph shows the corresponding average precipitation rate in cm day$^{-1}$ (solid line) and the surface temperature in °C (dashed line) along 105° W.

PBL, as shown schematically in Figure 1.4, is suggested by the low values of equivalent potential temperature ($\theta_e$) above the PBL and the higher values of $\theta_e$ between 800-700 mb. Kloesel and Albrecht (1989) attribute the latter to an increase in water vapor above the trade wind inversion. Note that the height of the PBL inversion is lowest just north of the equator and weakens near 8° N. High values of liquid water content (LWC) are evident in the PBL in the equatorial region, which reflects the model's treatment of stratus clouds over a 2500 km$^2$ region. Stratus clouds over the ocean have a typical LWC of 0.1 to 0.24 g kg$^{-1}$ (Liou 1992), which is comparable to the 0.08 to 0.14 g kg$^{-1}$ shown in the cross section below 900 mb. The circulation features evident in Figure 3.7 are consistent with the limited observations of the PBL structure over the cold tongue (Kloesel and Albrecht 1989; Bond 1992).

Further to the north near the ITCZ, high values of $\theta_e$ are evident near the surface with large total water/ice content values. The model's ice content for mid-high level clouds range from 0.04 to 0.1 g kg$^{-1}$. These values are consistent with the observed LWC in cirriform clouds which varies from 0.01 to 0.1 g kg$^{-1}$ except in cumulonimbus anvils where the values can reach as high as 0.25 g kg$^{-1}$ (Liou 1992).

The cross section along 95° W, shown in Figure 3.8, extends across the CTIC, through the Gulf of Tehuantepec and into the central plains of the United States. Most of the features in the PBL across the CTIC and in the ITCZ are similar to those found further west. However, a more distinct jet in the PBL with peak winds at 950 mb is evident. Northerly flow near the surface over the Gulf of Tehuantepec arises from outflow through the Isthmus of Tehuantepec, which is coupled with the slight increase in precipitation in
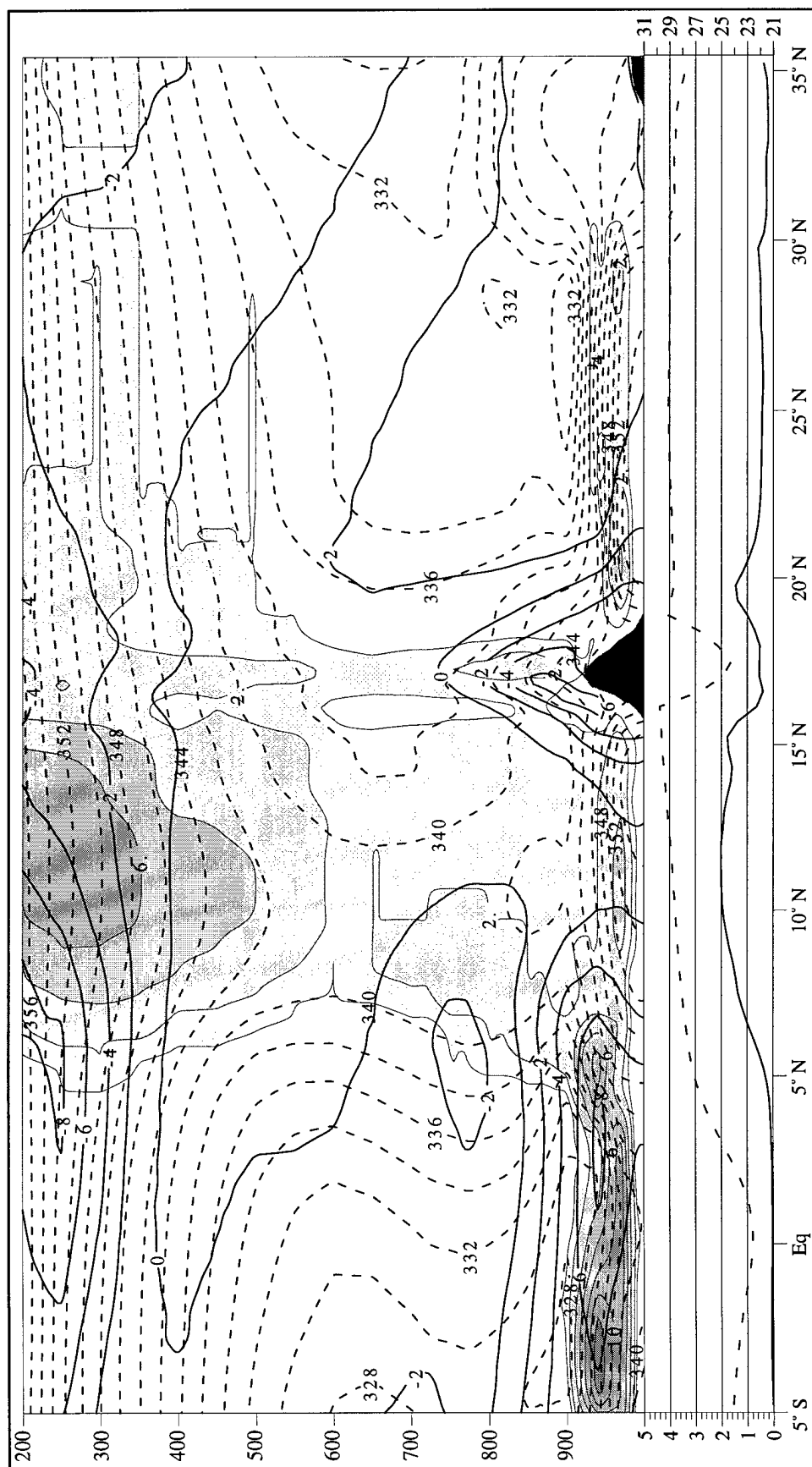
32



Figure 3.8. Vertical cross section for JJA 1990-97 along 95° W from 5° S to 35° N. The vertical coordinate is pressure in mb. The thin dashed lines are $\theta_e$ in K. The thicker solid lines denote the meridional wind component in m s$^{-1}$. The shaded regions and associated contours are total LWC in $10^{-2}$ g kg$^{-1}$. The lower graph shows the corresponding average precipitation rate in cm day$^{-1}$ (solid line) and the surface temperature in °C (dashed line) along 95° W.

this region. Steenburgh et al. (1997) simulated in more detail the circulation associated with strong outflow into the Gulf of Tehuantepec.

## Mesoscale Aspects of the Regional Climate

### Precipitation

To focus greater attention on the mesoscale distribution of precipitation over land, and to allow comparison to climatologies based on actual precipitation measurements, the precipitation over the ocean has been masked in Figure 3.9. The MM5 land only precipitation is shown in Figure 3.9a; the corresponding Legates and Wilmott (1990) observed summertime precipitation climatology appears in Figure 3.9b. As noted before, the NCEP reanalyses (Figure 3.3) tends to develop too much precipitation over most of Mexico as well as the southern United States and will not be shown here. In contrast, the precipitation in the MM5 over the eight summers (Figure 3.9a) has many similarities to the observed long-term summer climatological precipitation rates shown in Figure 3.9b (Legates and Wilmott 1990). The precipitation maximum along the western slopes of the Sierra Madre Occidental mountains is apparent as well as the precipitation maximum along the southwestern slopes of the Sierra Madre del Sur in Southern Mexico. Precipitation amounts simulated by the model tend to be lower than some estimates. As mentioned earlier, estimates of rainfall amounts over Mexico and Central America vary from 0.1 cm day$^{-1}$ to 5 cm day$^{-1}$. In addition, several large discrepancies are evident in Guatemala and Honduras where the MM5 tends to have heavy precipitation along the Caribbean coast while the heavier observed precipitation lies along the windward slopes of the mountains.
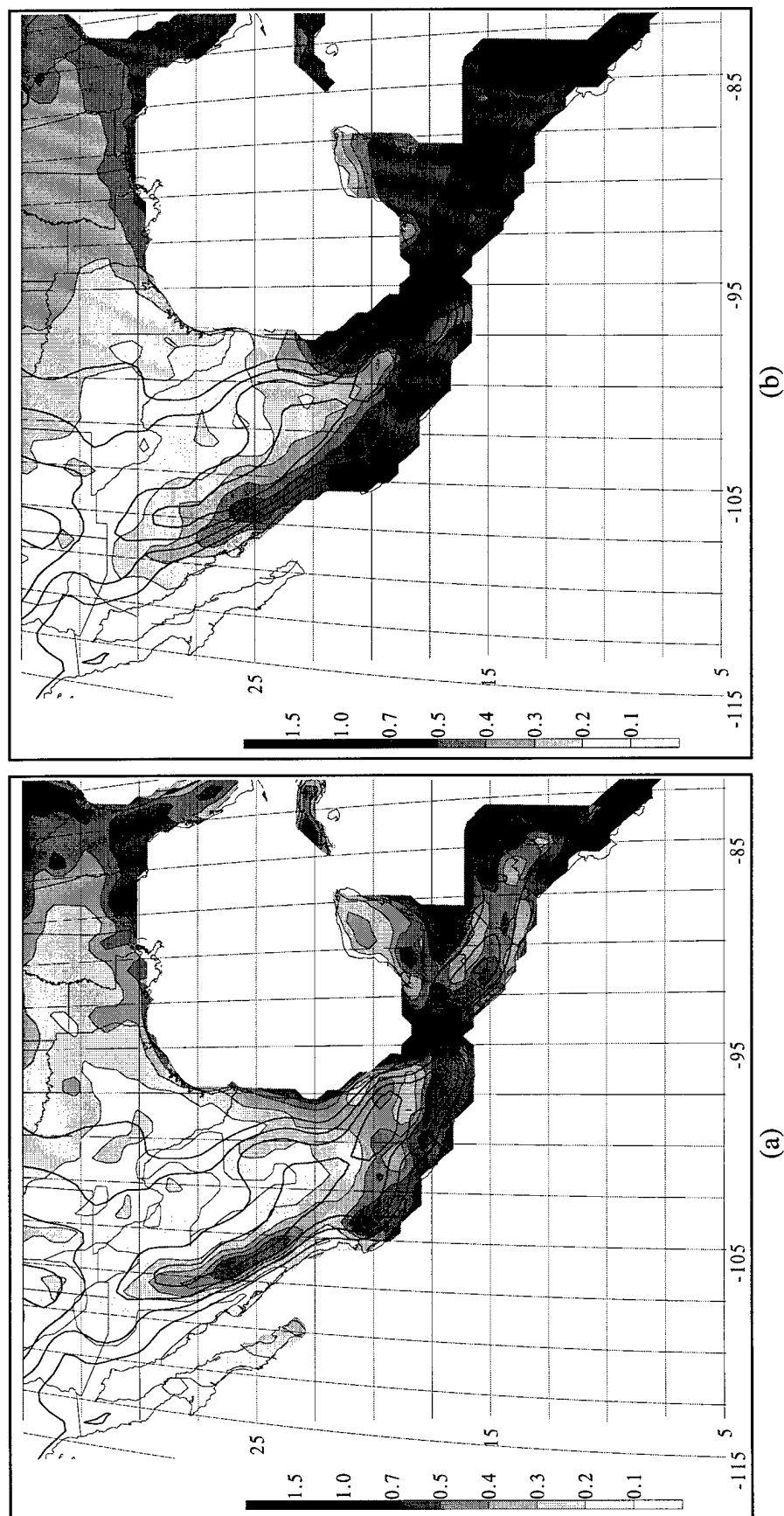
(a)

(b)

Figure 3.9. Precipitation rate in cm day$^{-1}$ and height contours in m for JJA for (a) MM5 (1990-1997) and for (b) Legates and Wilmott (1990). Precipitation masked by model's definition of oceanic areas. Values over 0.1 cm day$^{-1}$ shaded according to the scale on the left; contour intervals are 0.1, 0.2, 0.3, 0.4, 0.5, 0.7, 1, and 1.5 cm day$^{-1}$. Height contour intervals (thicker solid lines, not labeled) are 500 m.

Diurnal Circulations

As discussed briefly in Chapter 1, convective clouds tend to occur more frequently over high terrain and onshore during the late-afternoon and evening, and in the valleys and offshore during night and early morning. The schematic in Figure 1.2b was based on an analysis of infrared cloud top temperature, since hourly precipitation reports are generally unavailable over most of the NAMS region.

The differences between evening (23-00 UTC) and morning (11-12 UTC) precipitation and evening (00 UTC) and morning (12 UTC) near-surface wind during the eight-summer MM5 simulations are shown in Figure 3.10. Similar to the schematic in Figure 1.2b, greater evening convection is found near the coast in Central America and southern Mexico and along the western slopes of the Sierra Madre in northern Mexico. Greater precipitation during the early morning hours is found offshore along the coasts of southern Mexico and Central America. Other features of interest include the tendency for greater precipitation during the late afternoon in the ITCZ and the early evening maximum in precipitation over Florida.

The diurnal differences in low-level wind in are consistent with the precipitation differences: onshore/upslope flow is stronger in the afternoon while offshore/downslope flow is more prevalent during the morning.

Source Regions

The time-averaged flow shown in Figures 3.1 and 3.2 helps to define the typical low-level and upper-tropospheric air motion, respectively during this 8-year period. However, the actual motion of air parcels differs significantly from the mean at any instant. In order to assess the paths that typical air parcels might follow in the NAMS,
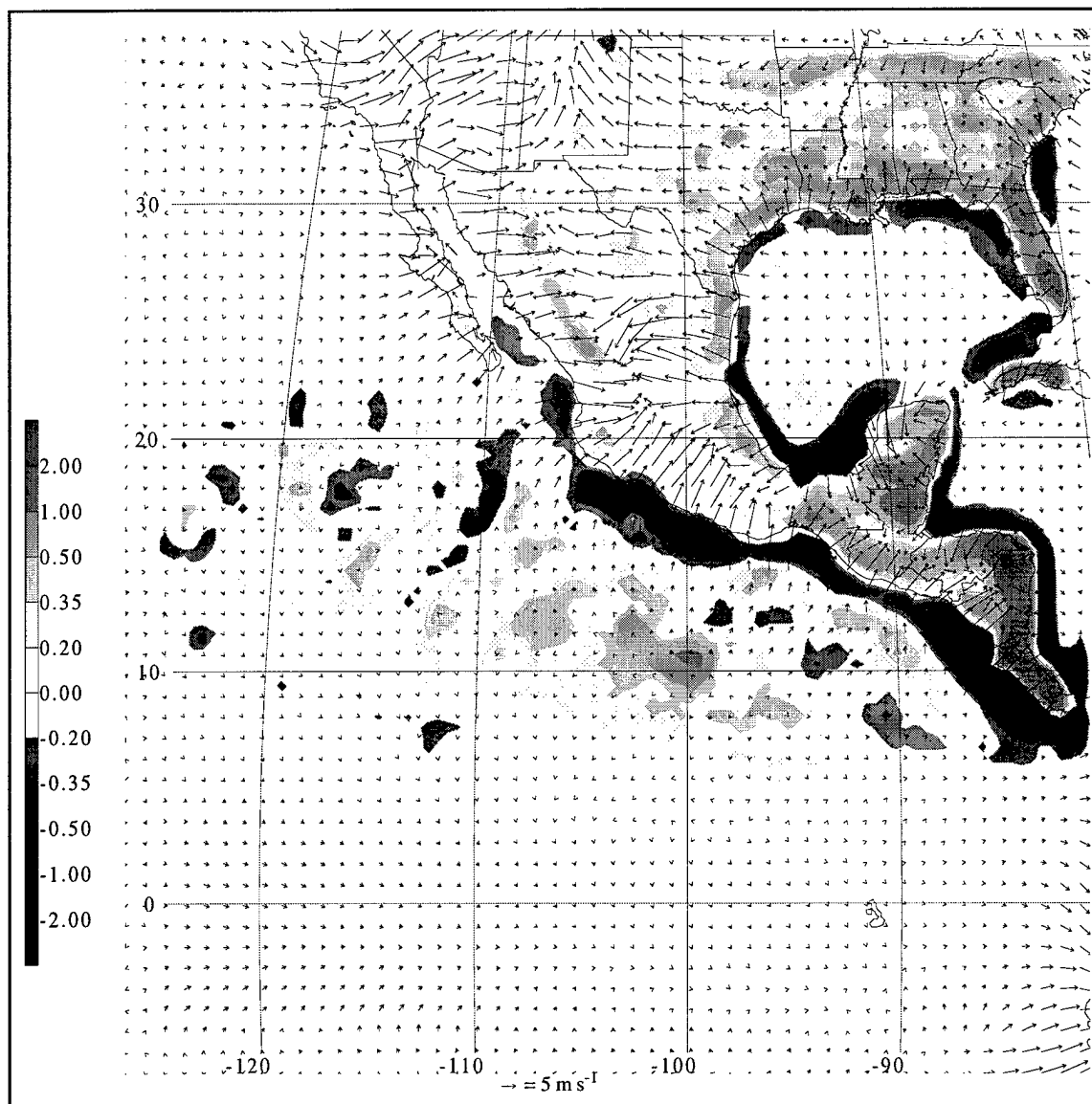
Figure 3.10.   Differences (evening minus morning) in 10 m AGL winds in m s$^{-1}$ and precipitation rate in cm day$^{-1}$ JJA 1990-1997 for MM5. Precipitation rate differences are shaded according to the scale on the left.

parcel trajectories were computed backwards in time from selected ending locations (Krishnamurti and Bounoua 1996). The positions of these ending locations are shown by the crosses in Figures 3.6 and 3.7. These ending locations are comprised of a box defined by nine adjacent grid points at three-model levels; in other words, a total of 27 parcels are launched backward at each time step. Parcel paths were computed diagnostically from the three-dimensional flow starting from every 3-h period during the eight summer seasons and tracked backwards in time for 5 days. Approximately 160,000 trajectories were calculated for each location. The parcels remain within the model domain as they are advected backward in time until they encounter one of the lateral boundaries, at which point they simply 'accumulate' along the boundary. The approach used to calculate the trajectories has a number of limitations. These include: the relatively long (3-h) time step, the inability to follow the parcels through deep updrafts since convective updrafts are parameterized in the model, and the broad spatial scale of the motion distributed over the 2500 km$^2$ grid.

Figure 3.11 summarizes the paths taken by all of the approximately 160,000 trajectories computed during the eight summers that end at the Equator, 105° W near 800 mb (denoted by the E in Figures 3.6 and 3.7). This is near the level of the profile reversal of mixing ratio discussed by Kloesel and Albrecht (1989). This ending location is representative of air parcels in the dry air above the PBL over the cold tongue. The horizontal locations of the parcels 12 h, 24 h, 48 h, 72 h, 96 h, and 120 h earlier (a-f, respectively) are summarized in each of the panels. The contours represent the percentage of time during the eight summers that the parcels are found in each grid box. Twelve hours earlier (Figure 3.11a), most of the parcels lie to the east or southeast of the initial location.
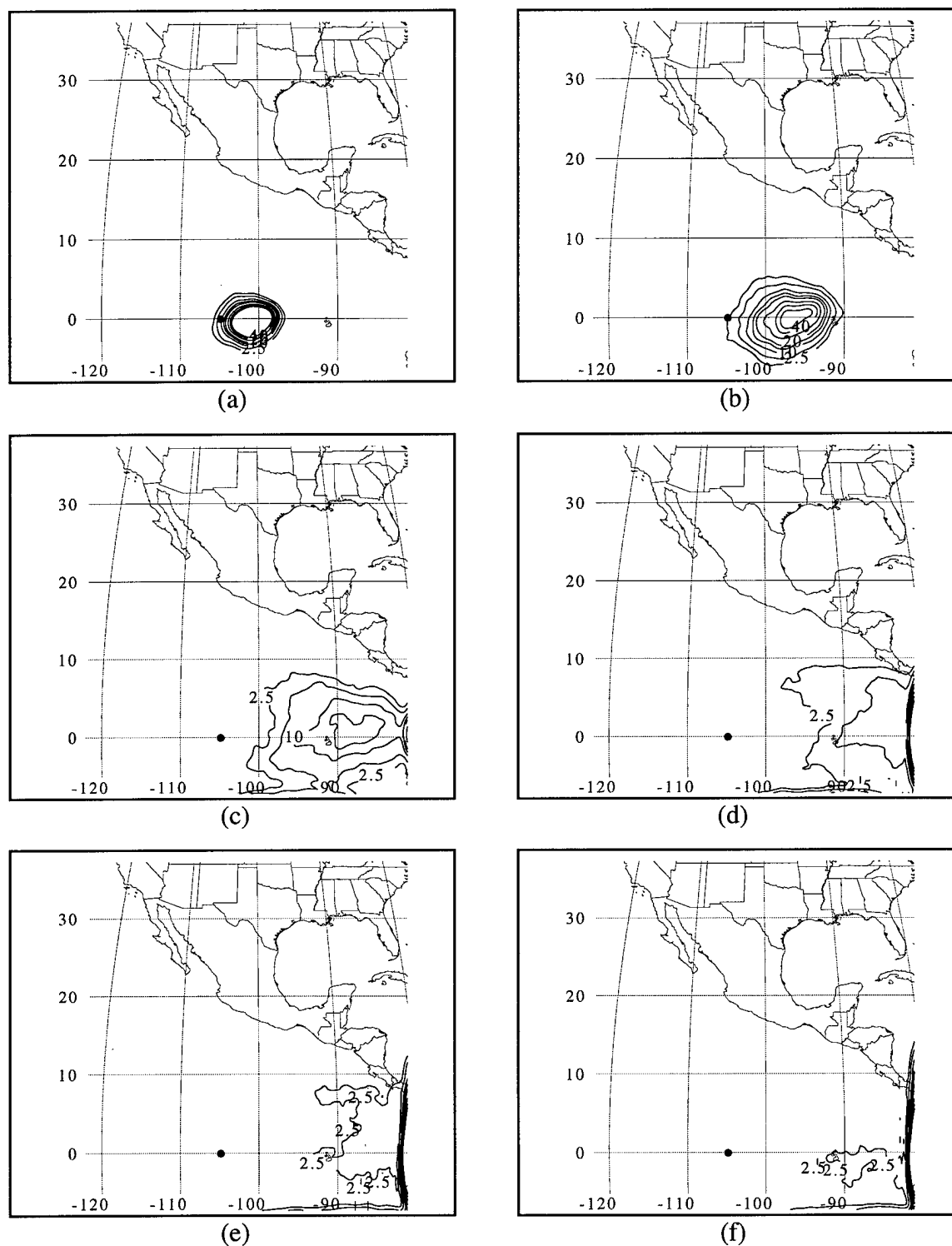
Figure 3.11.  Parcel trajectory ending locations for the point shown (Equator, 105° W, 800 mb). Panels indicate time to ending location: (a) 12 h, (b) 24 h, (c) 48 h, (d) 72 h, (e) 96 h, and (f) 120 h. Contour intervals are 0.025, 0.05, 0.1, 0.15, 0.20, 0.30, 0.40, and 0.50%; labels are scaled by 100, with every other contour labeled

At earlier times the parcels appear to travel predominantly from the east and southeast originating on the boundaries 3 to 5 days prior to reaching the ending location. Put another way, air parcels that enter the model domain along the eastern boundary near the equator tend to travel westward and some of them eventually reach the Equator, 105° W. Note that Figure 3.11 provides no information on the vertical paths of the parcels. In this instance, downward vertical motion predominates such that most of the parcels originate from 500 mb-600 mb along the eastern boundary. If the parcels at the same location (Equator, 105° W) end in the PBL, then nearly all of them originate on the southern boundary (not shown).

Figure 3.12 summarizes the parcels that end near 880 mb in the ITCZ (12° N, 105° W; denoted by the I in Figures 3.6 and 3.7). Trajectories calculated from this point show convergence of two major airstreams: one that travels nearly directly westward in the trades and one that travels northward across the cold tongue. The stronger wind speeds in the easterly trade winds lead to more parcels originating from the eastern boundary than from the southern boundary. Note at 48 h (Figure 3.12c) that there is a preference for some parcels to travel through the Tehuantepec Isthmus.

Parcels in the PBL ending in the state of Jalisco, Mexico (approximately 20° N, 105° W; denoted by the J in Figures 3.6 and 3.7) are summarized in Figure 3.13. Most of the parcels originate along the eastern boundary, travel across Central America and southern Mexico (especially through gaps in the terrain), and along the west coast of Mexico. Further north (Figure 3.14), parcels ending above the western slopes of the Sierra Madre (denoted by the N in Figures 3.6 and 3.7) primarily cross the Sierra Madre, again through gaps between mountain ranges. Still further north along the western slopes of the
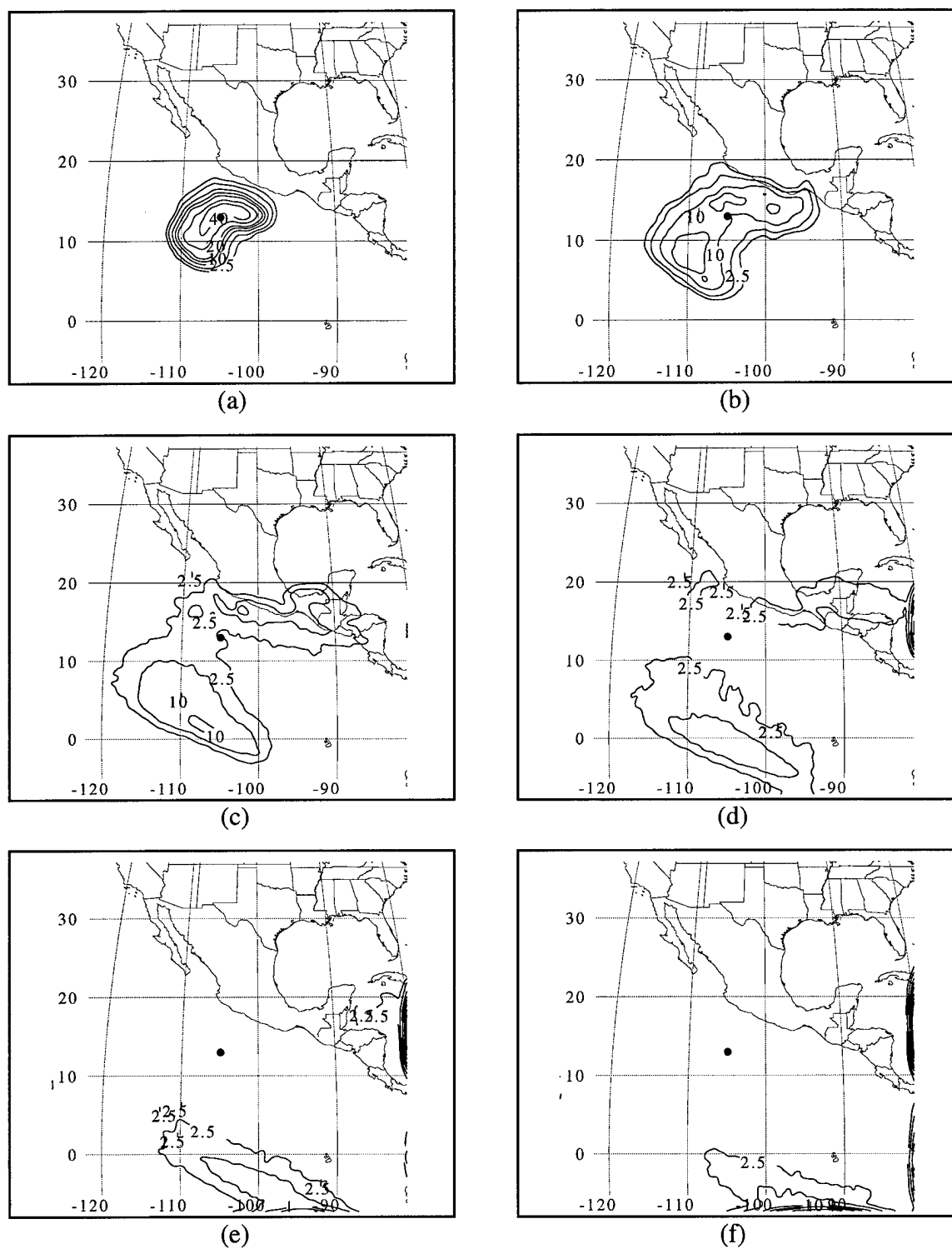
Figure 3.12. Parcel trajectory ending locations for the point shown (12° N, 105° W, 880 mb). Panels indicate time to ending location: (a) 12 h, (b) 24 h, (c) 48 h, (d) 72 h, (e) 96 h, and (f) 120 h. Contour intervals are 0.025, 0.05, 0.1, 0.15, 0.20, 0.30, 0.40, and 0.50%; labels are scaled by 100, with every other contour labeled
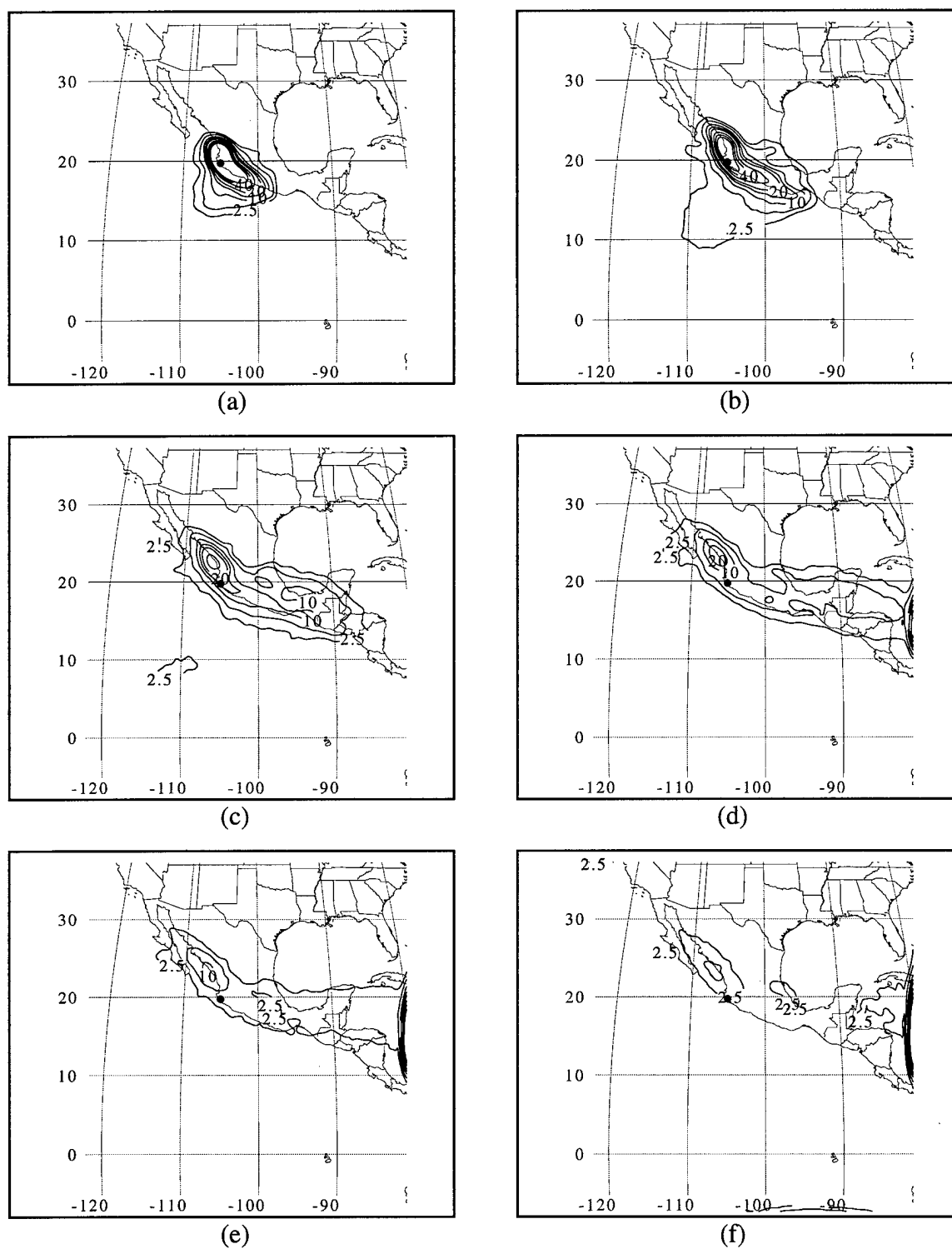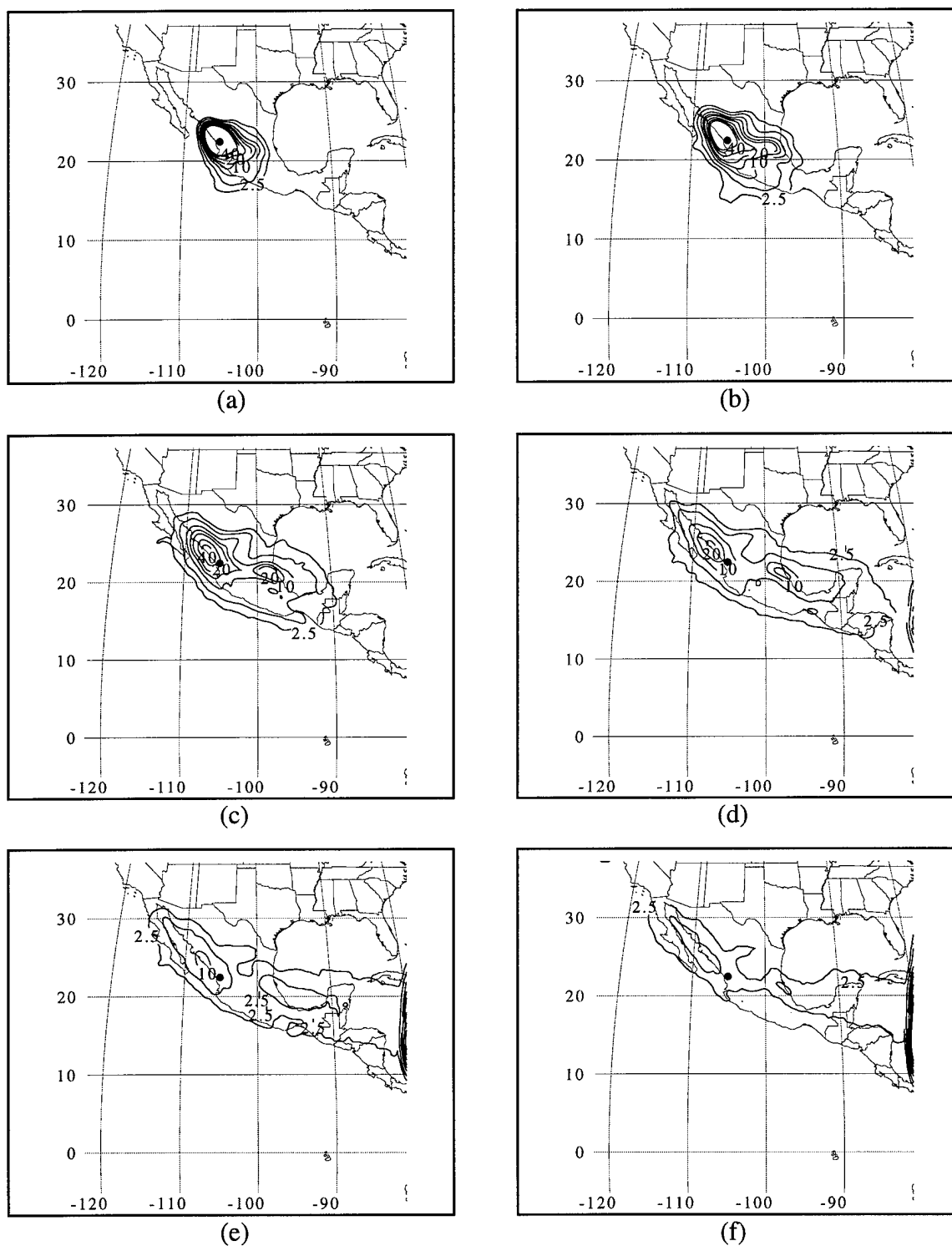
Figure 3.13.   Parcel trajectory ending locations for the point shown (20° N, 105° W, 880 mb). Panels indicate time to ending location: (a) 12 h, (b) 24 h, (c) 48 h, (d) 72 h, (e) 96 h, and (f) 120 h. Contour intervals are 0.025, 0.05, 0.1, 0.15, 0.20, 0.30, 0.40 and 0.50%; labels are scaled by 100, with every other contour labeled.

Figure 3.14.  Parcel trajectory ending locations for the point shown (23°N, 105° W, 820 mb). Panels indicate time to ending location: (a) 12 h, (b) 24 h, (c) 48 h, (d) 72 h, (e) 96 h, and (f) 120 h. Contour intervals are 0.025, 0.05, 0.1, 0.15, 0.20, 0.30, 0.40, and 0.50%; labels are scaled by 100, with every other contour labeled

Sierra Madre Occidental (denoted by the S in Figures 3.6 and 3.7; Figure 3.15), most of

the parcels originate from the eastern boundary with some traveling more slowly from the

northwest. Parcels ending in the PBL above the northern Gulf of California (not shown)

originate, for the most part, from the northwest. In other words, the model does not

capture well the occasional surge of moist air up the Gulf of California (Hales 1972;

Brenner 1974; Douglas 1995; Douglas and Li 1996; Stensrud et al. 1997) as a result of the

model's spatial resolution.

Tropical Cyclones

The NCEP reanalysis of sea-level pressure (SLP) and 10 m winds valid at 1200

UTC 23 July 1990 is shown in Figure 3.16. The distribution of SLP is relatively flat across

the domain and the winds are light, generally less than 5 m s$^{-1}$. However, at this time, an

observed hurricane (Hernan) was located at the position marked by the "H". The central

pressure of this hurricane, one of the strongest for our period, was estimated to be 928 mb

with maximum winds of 69 m s$^{-1}$ (Avila 1991). Thus, it is apparent that the NCEP

reanalyses do not resolve significant mesoscale weather features such as hurricanes.

Visual inspection of the MM5 output at 3-h intervals reveals that tropical cyclones

form frequently within this model as a result of instabilities in the trade winds which

develop in-situ or propagate into the model through the eastern boundary. The strongest

tropical cyclone simulated by the MM5 during the eight-summer seasons is shown in

Figure 3.17. This cyclone, which reached hurricane strength, lasted almost 8 days starting

at 0000 UTC 8 August and ending at 1800 UTC 15 August. It reached its maximum

intensity, (SLP roughly 953 mb and 10 m AGL winds of 35 m s$^{-1}$) at 0000 UTC 11 August

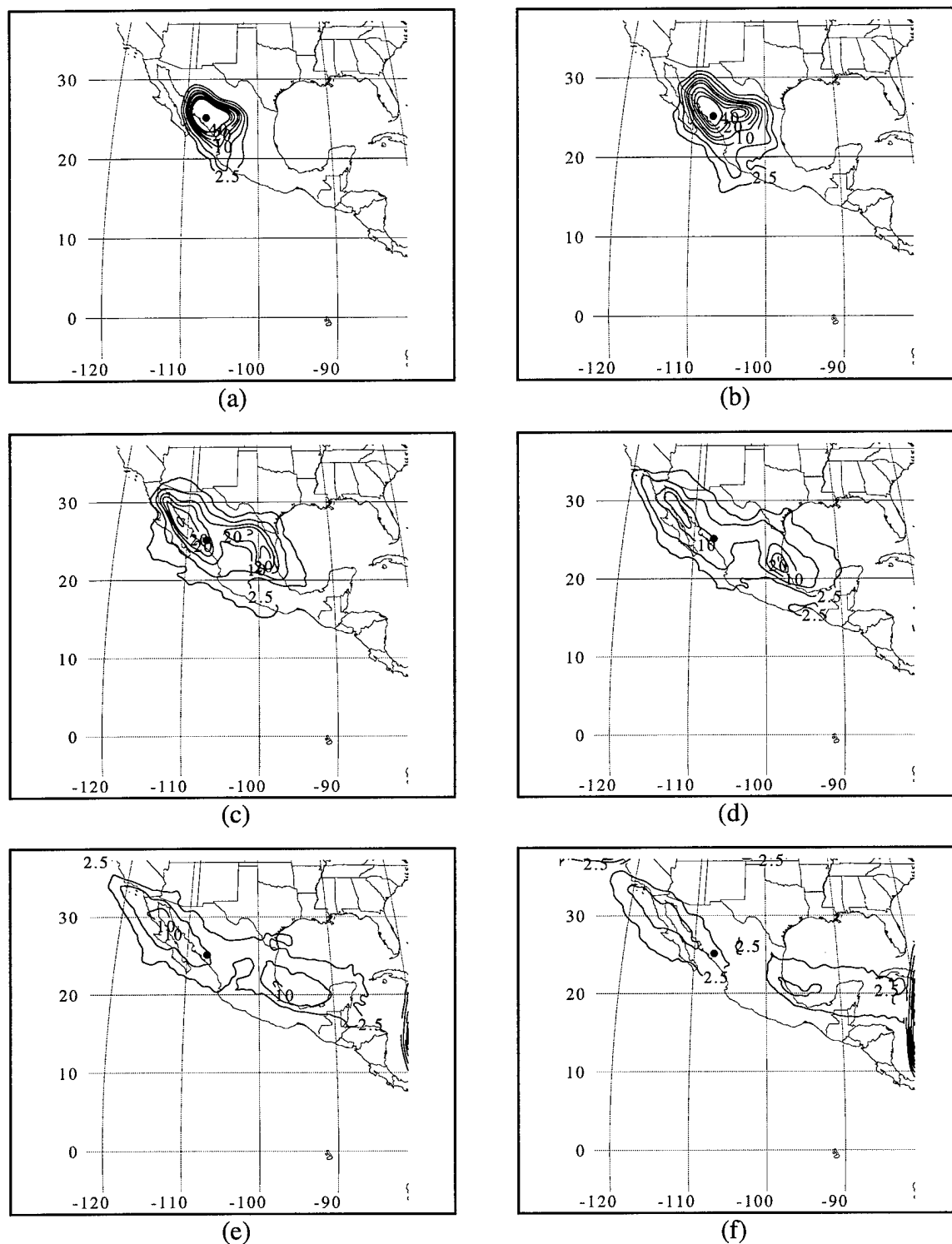1994, 1704 h into the simulation. The individual six-hourly storm locations are denoted by

Figure 3.15.  Parcel trajectory ending locations for the point shown (25° N, 108° W, 820 mb). Panels indicate time to ending location: (a) 12 h, (b) 24 h, (c) 48 h, (d) 72 h, (e) 96 h, and (f) 120 h. Contour intervals are 0.025, 0.05, 0.1, 0.15, 0.20, 0.30, 0.40, and 0.50%; labels are scaled by 100, with every other contour labeled
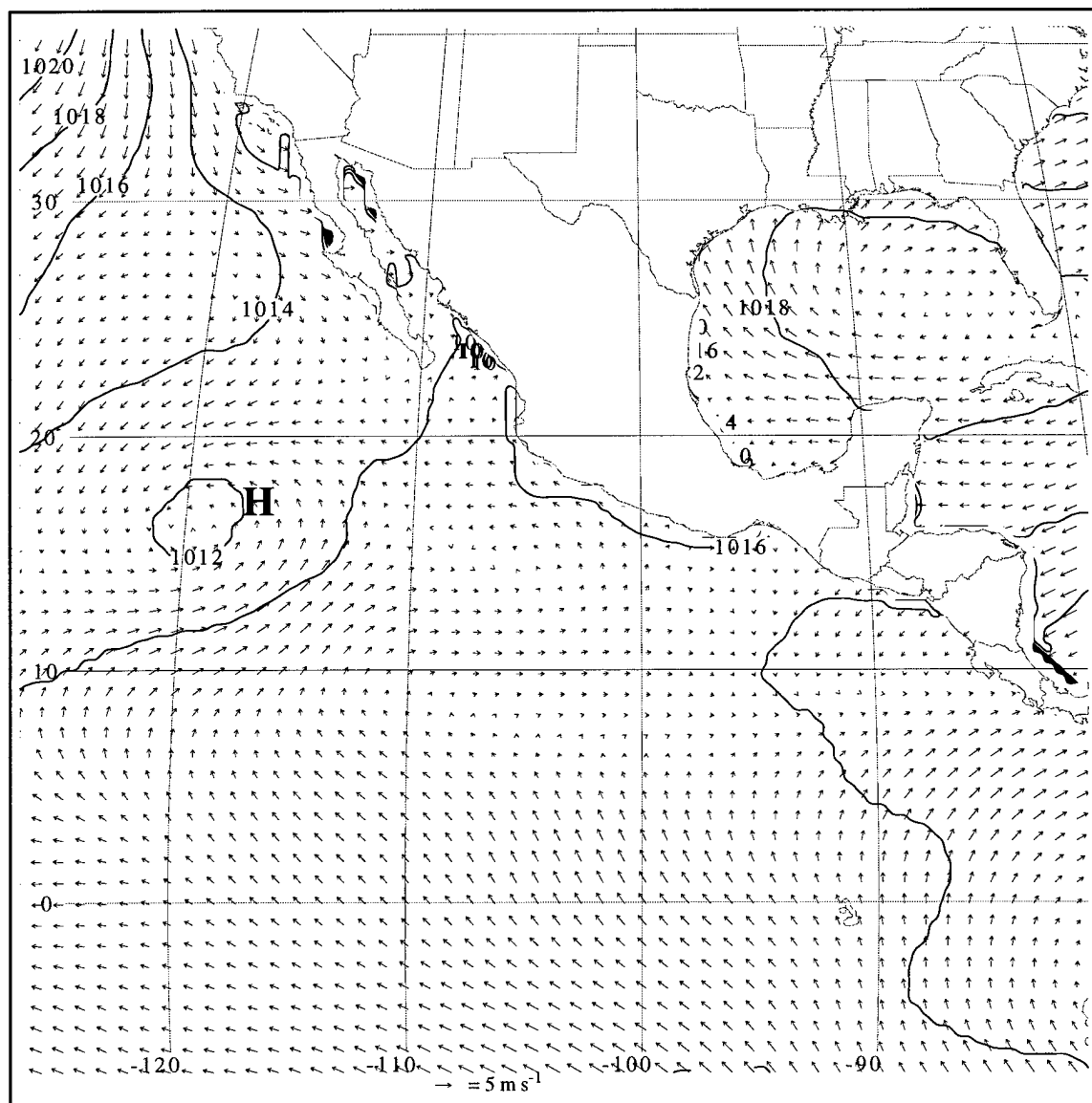
Figure 3.16.   10 m AGL wind in m s$^{-1}$ and surface pressure in mb valid at 1200 UTC 23 July 1990 for the NCEP reanalysis Contours in 2 mb intervals. The 'H' denotes the position of Hurricane Hernan at this time.
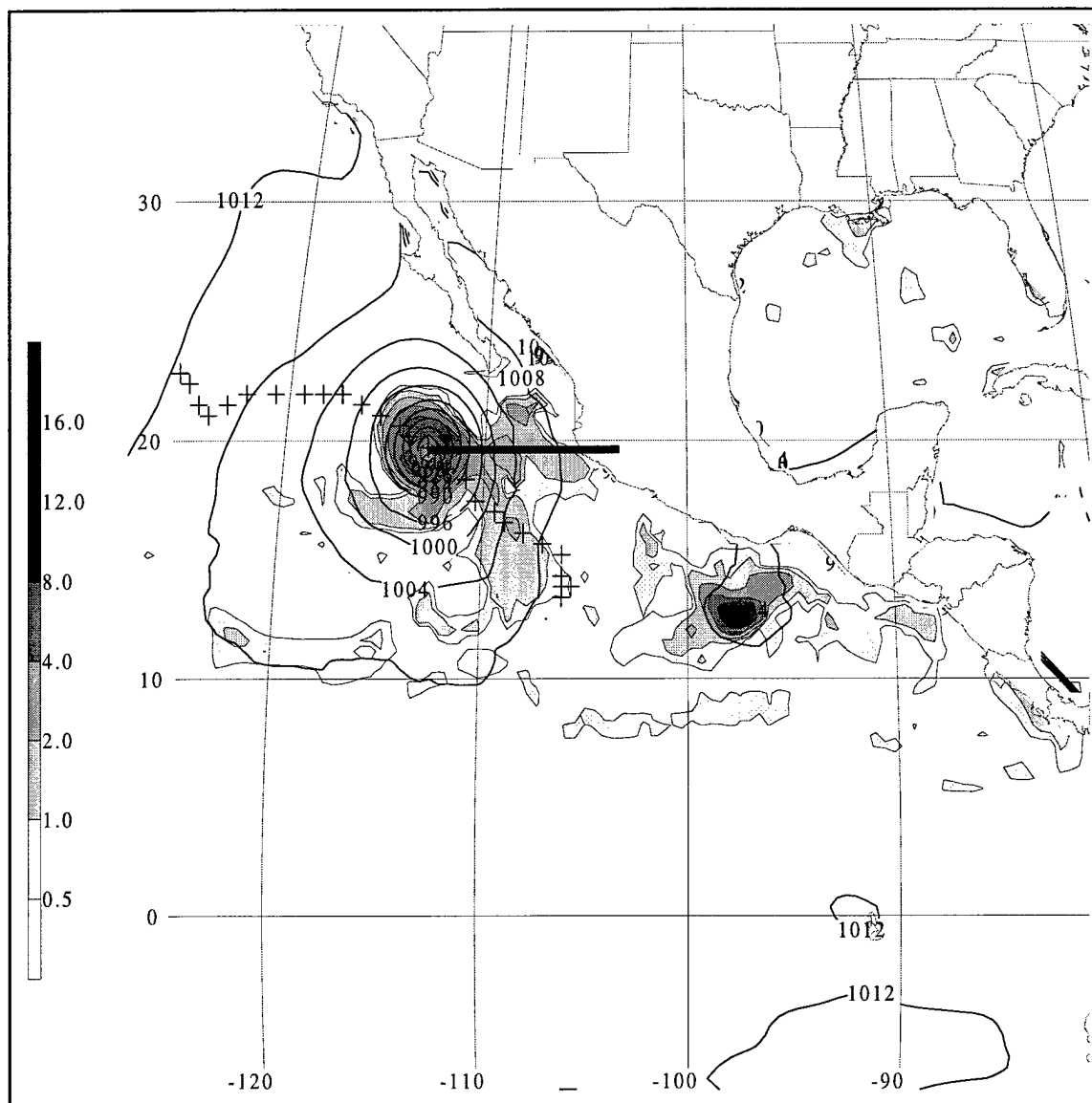
Figure 3.17. Sea-level pressure in mb and 6 h accumulated precipitation in cm valid at 0000 UTC 11 August 1994. Storm track positions (denoted by the crosses) are shown every 6 h from 0000 UTC 8 August - 1800 UTC 15 August. Precipitation amounts over 0.5 cm are shaded according to the scale on the left. The bar indicates the position of the two-dimensional vertical cross sections shown later.

the crosses that extend across the domain. Inconsistencies between the lateral boundary conditions and the cyclone winds did not allow the model cyclone to exit the domain as expected and it appears the cyclone remained within the domain approximately 18 h longer than it should (note the kink in the storm track near the western model boundary). The SLP and six-hourly accumulated precipitation are shown at the time this cyclone reached its maximum intensity. Heavy precipitation is evident near the hurricane center with rain bands spiraling outwards.

Figure 3.18 shows two-dimensional cross sections through the hurricane during its mature phase along the line shown in Figure 3.17. The tangential winds show the "eye" of the hurricane is located one grid point (50 km) to the right of the cross section's origin. The radius of maximum wind is 100 km further to the east (i.e., two grid points from the hurricane's eye). The typical observed radius of maximum wind is 10-50 km from the eye (Houze 1993). Thus, the 50 km horizontal resolution of the model is inadequate to accurately depict the tropical cyclones. Note, however, that the horizontal resolution of GCMs leads to the radius of maximum wind being more than 200 km from an ill-defined eye (Bengtsson et al. 1995; Vitart et al. 1997).

Strong convergence (divergence) is evident in the PBL (upper troposphere) according to the radial winds in Figure 3.18b. The warm core of the hurricane is clearly shown in Figure 3.18c. High $\theta_e$ values in the eye and near the surface are evident in Figure 3.18d near a rainband further to the east. Subsidence in the eye with ascent near the radius of maximum wind is apparent in Figure 3.18e. The strongest vertical velocities are associated with the rainband further to the east. High LWC in the model's eyewall and in the rainband are also apparent (Figure 3.18f).
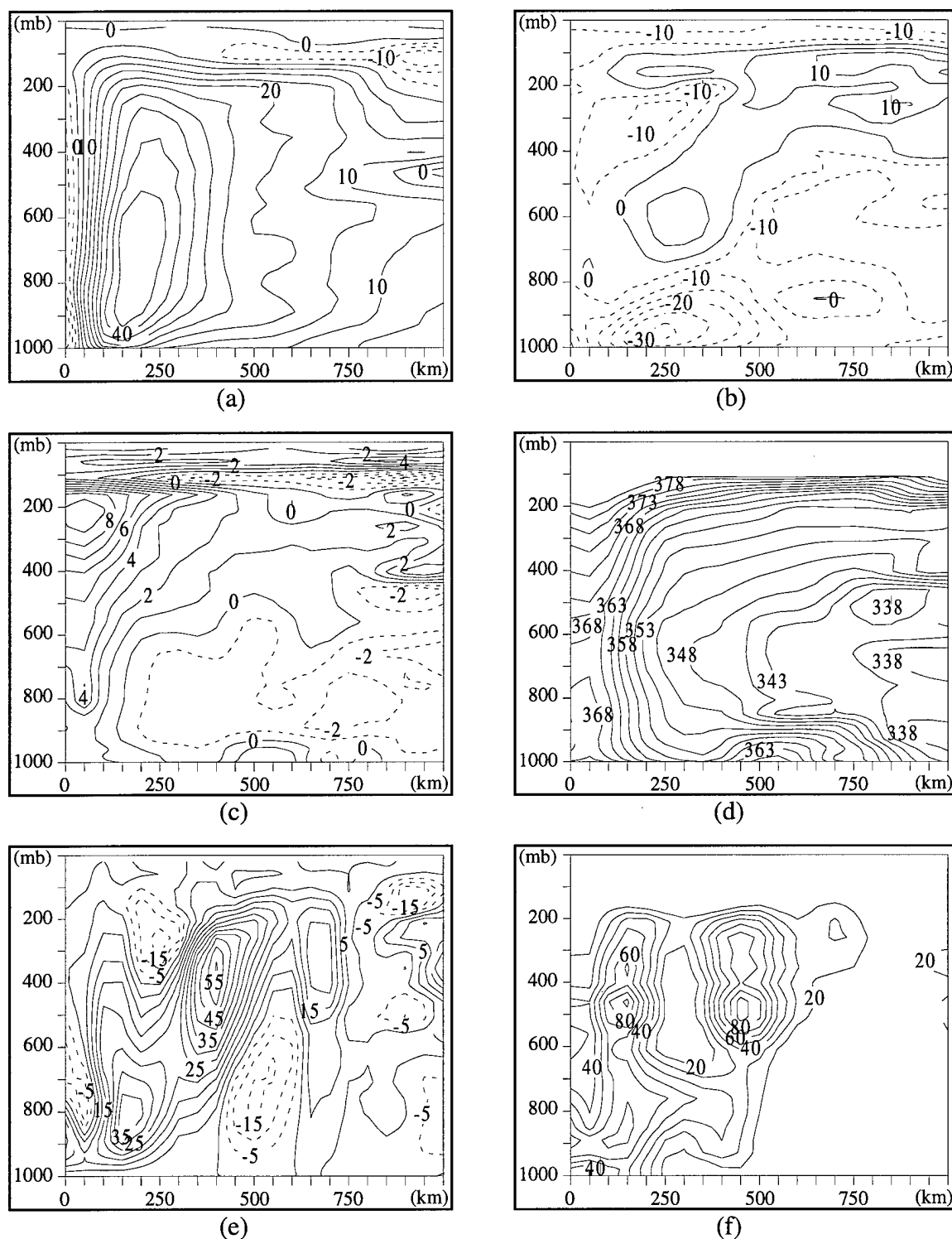
Figure 3.18.   Cross sections of (a) tangential velocity in m s$^{-1}$, (b) radial velocity in m s$^{-1}$, (c) temperature anomaly in K, (d) $\theta_e$ in K, (e) vertical velocity in cm s$^{-1}$, and (f) LWC in $10^{-2}$ g kg$^{-1}$. Vertical coordinate is pressure in mb. Bottom scale is length in km. Contour intervals are 5 for (a) and (b), 1 for (c), 2.5 for (d), 5 for (e) and 10 for (f). Every other contour is labeled.

Simulated tropical storms (T/S) and hurricanes are defined on the basis of the criteria used for observed storms and hurricanes (Houze 1993). That is, a tropical storm over the ocean occurs within the model whenever a pressure minima is accompanied by surface wind speeds greater than 17 m s$^{-1}$. Hurricane status is attained when the surface wind speeds exceed 32 m s$^{-1}$.

According to Bengtsson et al. (1995) and Vitart et al. (1997), it is important for climate models to reproduce the correct frequency of tropical cyclones, rather than the individual storms themselves. Table 3.1 summarizes the total number, type, and the average duration of observed and simulated cyclones during the eight summers (JJA only) within the MM5 domain. It also contains the total number of storm days (average duration times number of cyclones) for each of the storm types. A total of 77 cyclones were observed within the model domain. Cyclones lasted on average 3.4 days, and 46 of the 77 storms reached hurricane intensity during their lifetime. It should be noted that these'observed statistics result from a blend of objective and subjective estimates of

Table 3.1.    Total number of tropical cyclones, average duration, storm types, total storm days, minimum pressure, and maximum winds for JJA 1990-1997 for observed, model simulated based on 10 m AGL winds (MM5 1), and model simulated based on 10 m and 100 m AGL winds (MM5 2).

| | Total | Avg. Dur. (days) | T/S (#) | Hurr. (#) | Total Storm Days | T/S Storm Days | Hurr. Storm Days | Min. Pres. (mb) | Max. Wind (m s$^{-1}$) |
|---|---|---|---|---|---|---|---|---|---|
| Obs. | 77 | 3.36 | 31 | 46 | 259 | 153 | 106 | 921 | 72.0 |
| MM5 1 | | | | | | | | | |
| all cases | 668 | 0.84 | 646 | 22 | 563 | 550 | 13 | 953 | 35.4 |
| ≥ 2 days | 86 | 3.47 | 69 | 17 | 299 | 288 | 11 | 953 | 35.4 |
| MM5 2 | | | | | | | | | |
| all cases | 805 | 0.82 | 642 | 163 | 660 | 506 | 154 | 953 | 46.6 |
| ≥ 2 days | 106 | 3.38 | 31 | 75 | 358 | 236 | 122 | 953 | 46.6 |

pressure and wind derived from reconnaissance flights and satellite imagery (Avila 1991).

The lowest pressure observed during the period of study (921 mb) occurred during August

1997 associated with Hurricane Guillermo whose wind speeds were estimated at 72 m s$^{-1}$.

The number of tropical cyclones (tropical storms and hurricanes) simulated by the

MM5 is also listed in Table 3.1. The results are sensitive to the model level from which the

maximum wind is derived. Results are shown separately for storms defined from the

lowest model level (10 m AGL) or the lowest two levels (10 m and 100 m AGL). Pressure

minima coupled with strong winds occur frequently over the ocean. A total of 668 cases of

17 m s$^{-1}$ winds within 250 km of a pressure minima were identified from the 10 m AGL

winds. Many of these are short-lived and are associated with other phenomena, such as

MCSs (Mohr and Zipser 1996). The strongest systems were identified by requiring them

to last for more than 2 days. Bengtsson et al. (1995) and Vitart et al. (1997) use a 2-day

criterion to identify tropical cyclones in GCM simulations. While all of the observed

cyclones were tracked for more than 2 days, some of them remained above tropical storm

intensity for durations less than 2 days.

The total number of simulated storms that last longer than 2 days is higher than

that observed; however, the average duration is comparable. Also, if only the winds at

10 m are used, then few storms reach hurricane intensity. Many more storms would be

classified as hurricanes if the lowest two levels are used. In either case, the model tends to

generate more total storm days than those observed and the intensity of those storms tends

to be weaker (higher central pressures and lower maximum wind speeds).

To examine the spatial distribution of these cyclones, the domain is divided into

2.5° x 2.5° grid boxes and then the number of times the center of a cyclone is observed or

simulated in each box every 6 h is tabulated over the eight summers. The sum over all grid boxes yields the total storm days listed in Table 3.1. Since model cyclones cannot exist within approximately 2.5° of the western boundary, cyclones in this region are not tabulated. Observed storms are similarly restricted for consistency between the figures. Figure 3.19b shows the total number of times cyclones were observed in each grid box. Over the eastern Pacific Ocean, storms originate between 12°-14° N from 95°-105° W.

As noted by Elsberry et al. (1987), this region has the highest frequency of tropical cyclone genesis in the world. Tropical cyclones have been hypothesized to develop from MCSs that form over the mountains of Central America during the evening and then travel westward (Velasco and Fritsch 1987; Bister and Emanuel 1997). The diurnal variations in precipitation evident in Figure 3.10 may reflect in part the propagation of these MCSs. Alternatively, easterly waves that propagate across the Atlantic Ocean have been linked to the onset of Pacific tropical cyclones. As discussed by Farfán and Zehnder (1997), the orientation of the coastline of southern Mexico, low-level flow through the gaps of Central America, and southwesterly flow near 10° N may help to establish the cyclonic absolute vorticity of the basic state favorable for tropical cyclone genesis from these easterly waves.

The distribution of observed storms appears to split further west, with many storms found parallel to the Mexican coast while others remain between 12°-14° N. The frequency of occurrence of storms is, of course, much higher in the eastern Pacific compared to that in the Gulf of Mexico, especially during JJA. As also should be expected, cyclones reach hurricane intensity (Figure 3.19f) further to the west than where tropical storms originate (Figure 3.19d).
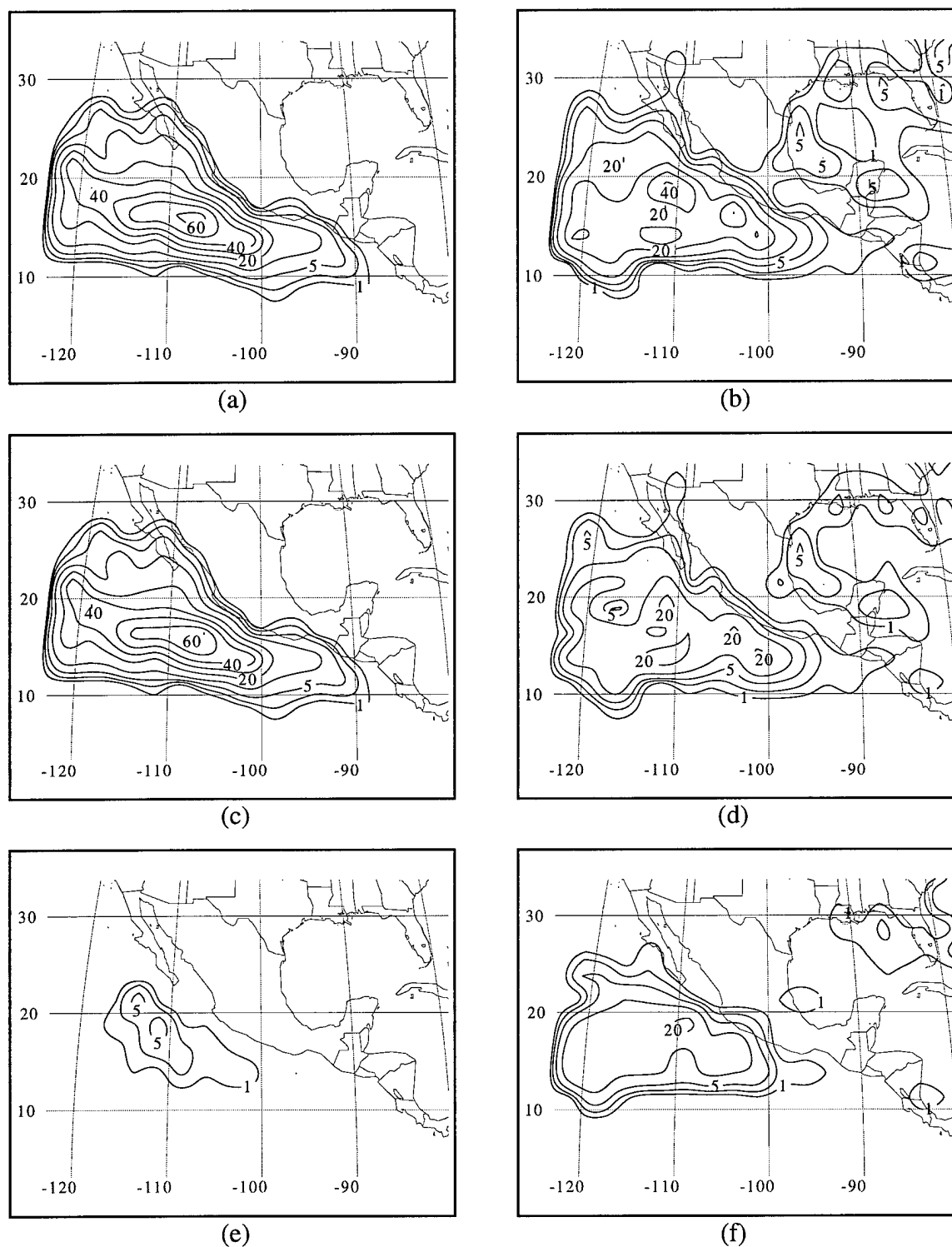
Figure 3.19. Occurrence of: all tropical cyclones in 2.5° x 2.5° grid boxes, based on 10 M AGL wind for (a) MM5 and (b) observed; tropical storms (17 m s⁻¹ ≤ wind speed < 32 m s⁻¹) for (c) MM5 and (d) observed; and hurricanes (wind speed ≥ 32 m s⁻¹) for (e) MM5 and (f) observed. Contour intervals are 1, 2.5, 5, and every 10 thereafter with every other contour labeled.

The spatial distribution of the locations of all model tropical cyclones is shown in Figure 3.19a based on the model winds at 10 m AGL only. As expected from Table 3.1, the occurrence of cyclones is higher than that observed. In addition, more of the model storms tend to be consolidated into a single preferred track in contrast to the split track observed. Storms in the Gulf of Mexico are conspicuously absent as a result of the nearby eastern boundary of the model. Hurricane-force winds are simulated at 10 m AGL only for a few major storms (Figure 3.19e), nearly all of the cyclones remain at tropical storm intensity (Figure 3.19c).

The analysis was repeated to include winds at the lowest two model levels and the results are summarized in Figure 3.20. The observed distributions are repeated in the right column. Greater occurrence of hurricane-force winds over the eastern equatorial Pacific is evident in Figure 3.20e. A couple of cyclones reach tropical storm intensity in the Gulf of Mexico (Figure 3.20c).

## Summary

Mean atmospheric flow patterns are well simulated in this experiment. The spatial distribution of precipitation is mostly consistent with satellite observations, although the ITCZ in the model may be placed too far north. Climatological precipitation amounts over land match observed values closer than those available from the NCEP reanalyses. The vertical structure of the atmospheric circulation across the CTIC is consistent with conceptual models for the region and provide useful information that cannot be gained from lower resolution data sets. The model tropical cyclone distribution shows some deficiencies in the way the MM5 simulates these complex, mesoscale systems; the model tends to generate more, and weaker, cyclones than are observed.
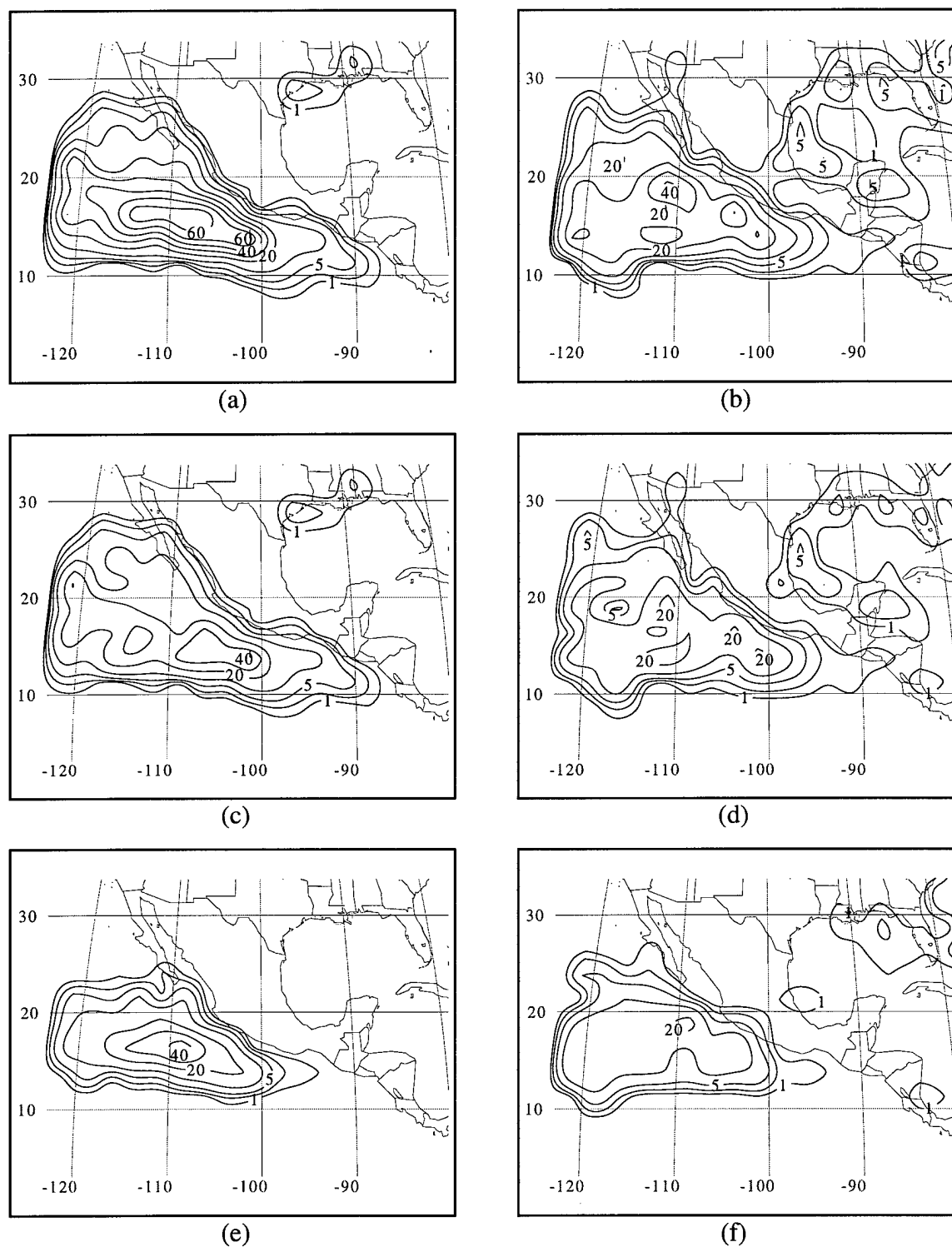
Figure 3.20.   Occurrence of: all tropical cyclones in 2.5° x 2.5° grid boxes, based on
10 m and 100 m AGL wind for (a) MM5 and (b) observed; tropical storms
(17 m s⁻¹ ≤ wind speed < 32 m s⁻¹) for (c) MM5 and (d) observed; and
hurricanes (wind speed ≥ 32 m s⁻¹) for (e) MM5 and (f) observed. Contour
intervals are 1, 2.5, 5, and every 10 thereafter with every other contour
labeled.

CHAPTER 4

SEASONAL EVOLUTION OF THE NAMS

The seasonal evolution of precipitation and atmospheric circulation in the NAMS

is quite pronounced (Higgins et al. 1998). The onset of precipitation along the western

slopes of the Sierra Madre during late June-early July was shown schematically in Figure

1.2a. At roughly the same time, precipitation shifts northwestward along the ITCZ while it

diminishes further east along the ITCZ and over Central America.

Month-to-month changes in the regional circulation have been averaged over the

eight summers. Differences in the mean circulation between July and June help to define

the onset of the northernmost extent of the NAMS while those between August and July

reflect the further evolution of the NAMS during the peak of the summer season.

<u>Large-Scale Aspects of the Seasonal Evolution</u>

<u>Surface Wind and Precipitation</u>

Differences in surface wind and precipitation between July and June for the MM5

and the NCEP reanalyses are shown in Figure 4.1. Differences here are defined as the

former minus the latter, or July minus June in this case. The precipitation differences

simulated by the MM5 show the mid-summer drought observed over Central America and

southern Mexico as well as greater precipitation along the western slopes of the Sierra

Madre of northern Mexico. In contrast to the greatly enhanced frequency of convective

clouds in the latter region during July compared to June (Figure 1.2a), the model's
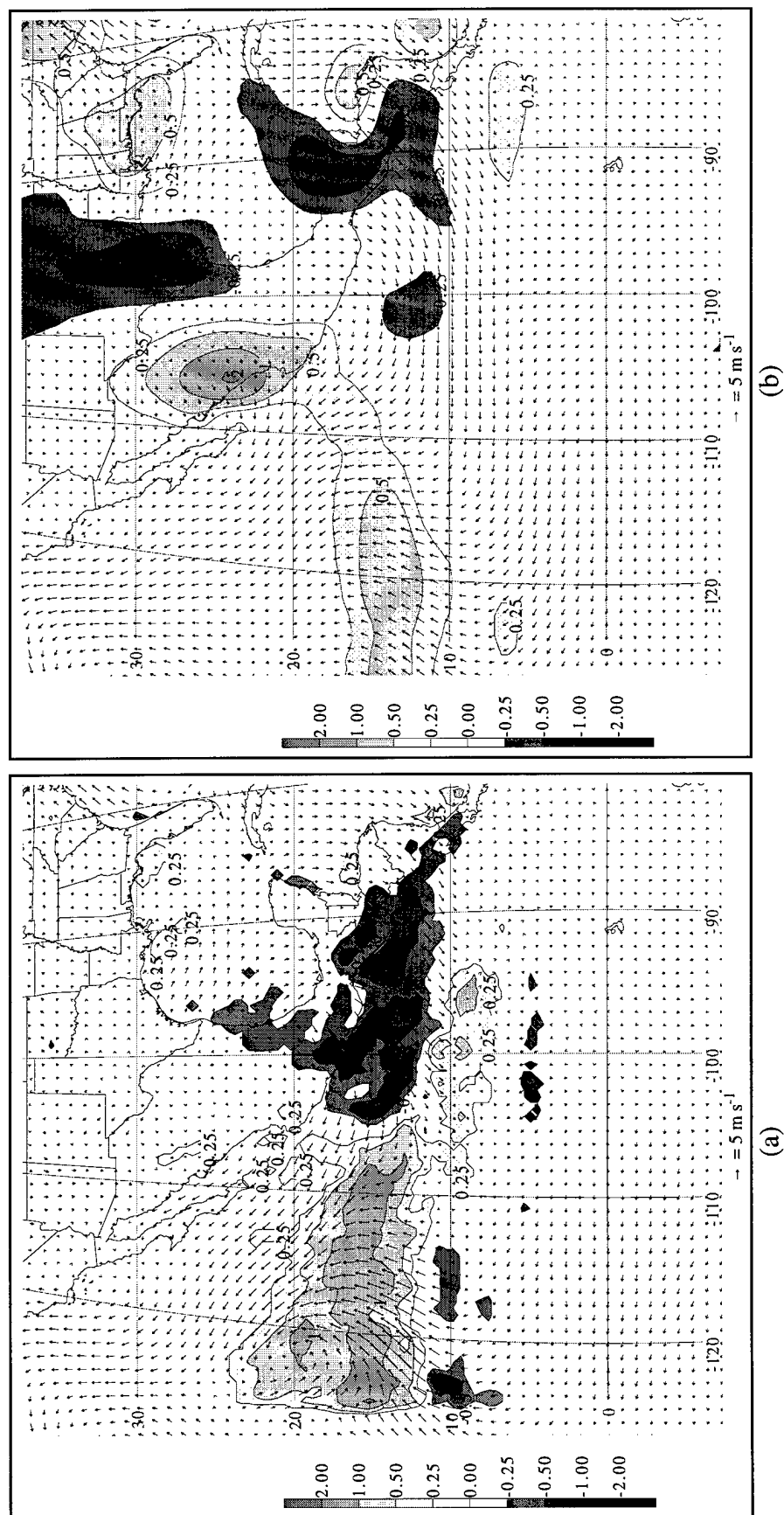
Figure 4.1.    Differences in 10 m AGL wind in m s$^{-1}$ and precipitation rate in cm day$^{-1}$ between July and June for (a) MM5 and (b) NCEP. Light (dark) shading denotes higher (lower) precipitation rates in July vs. June. Precipitation rate differences are shaded according to the scale on the left.

precipitation differences are relatively small. Higgins et al. (1998) estimate the areally averaged precipitation difference in this region to be on the order of 0.3 cm day$^{-1}$, which is comparable to the local maxima in the MM5 in the region. Stronger northeasterly tradewind flow away from Central America is evident in July compared to June and a stronger southerly meridional wind appears further west.

The NCEP reanalyses has many features in common with the MM5. A notable difference, however, is the much stronger monsoon evidenced in the precipitation rate differences over northwestern Mexico in the NCEP reanalysis. Similarities between the NCEP and MM5 10 m AGL wind suggest that the changes in circulation are driven by planetary-scale processes.

The differences in 10 m AGL wind and precipitation between August and July are shown in Figure 4.2. Both the MM5 and NCEP reanalyses indicate that the ITCZ reaches its northernmost extent during August. The NCEP reanalyses suggest continued amplification of the monsoon over northwestern Mexico while the precipitation rates produced by the MM5 in this region are much lower. Differences in near-surface wind between August and July tend to be small, yet still reflect a general weakening of the trade wind flow.

Upper-Tropospheric Wind

Differences in 200 mb wind between July and June are shown in Figure 4.3. Both the NCEP reanalyses and the MM5 are dominated by the spin-up of the North American anticyclone along the northern boundary of the MM5 model domain with stronger easterly flow aloft between 20°-30° N. The northward progression of the anticyclone during July leads to the cyclonic wind differences centered over southern Mexico in the MM5 and
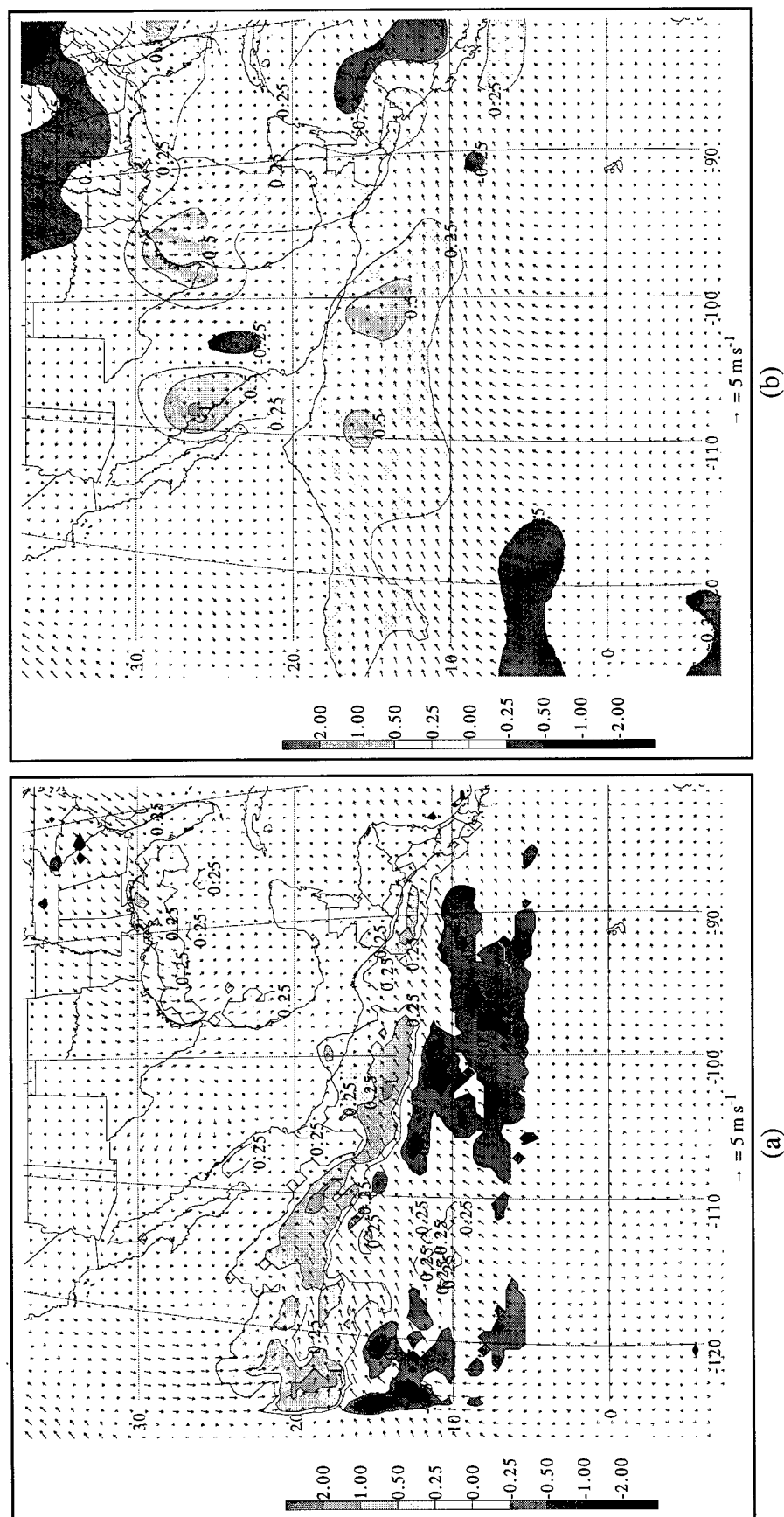
Figure 4.2.    Differences in 10 m AGL wind in m s⁻¹ and precipitation rate in cm day⁻¹ between August and July for (a) MM5 and (b) NCEP. Light (dark) shading denotes higher (lower) precipitation rates in August vs. July. Precipitation rate differences are shaded according to the scale on the left.
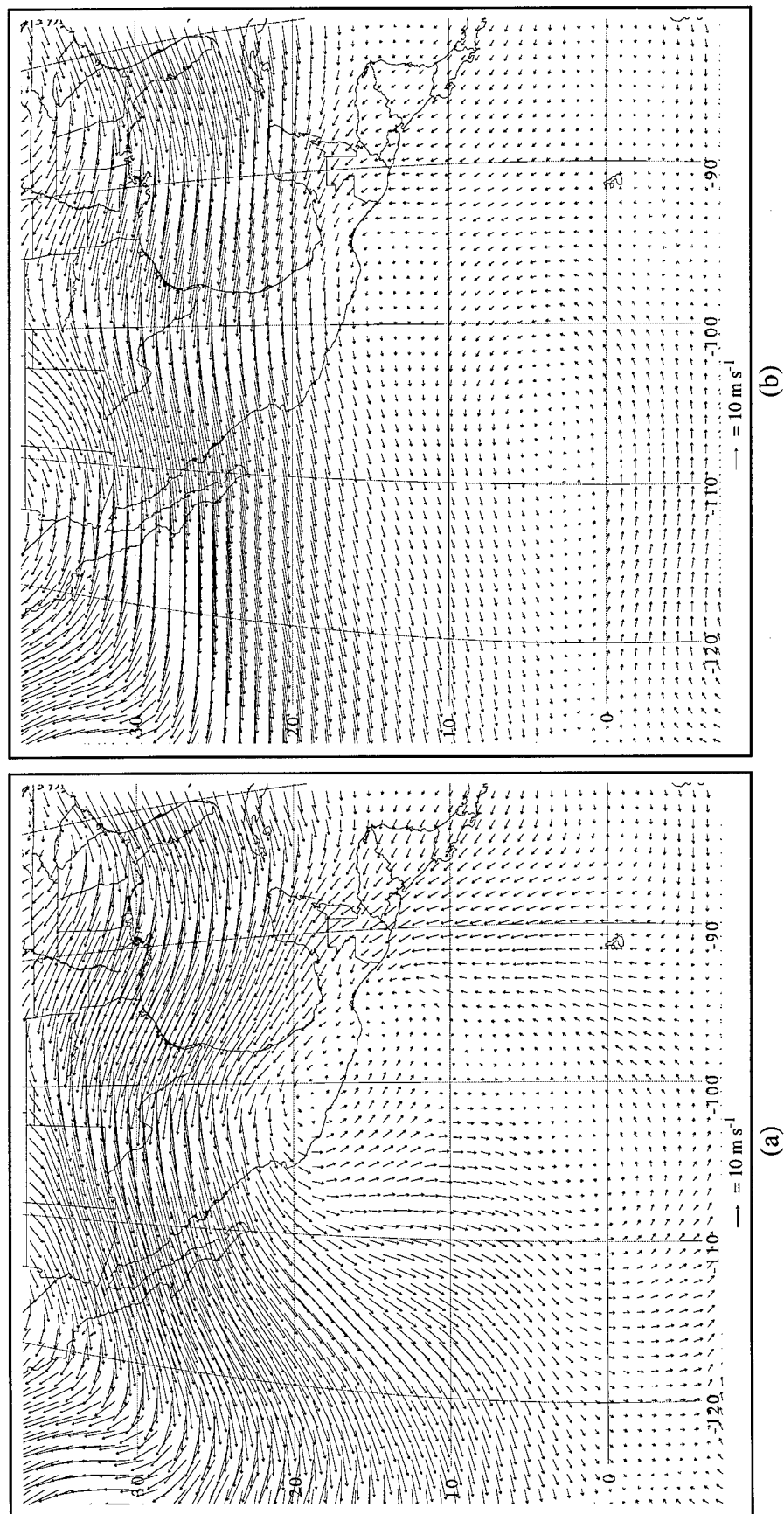
Figure 4.3.    Differences in 200 mb wind between July and June in m s⁻¹ for (a) MM5 and (b) NCEP.

greater divergent flow aloft over the region of enhanced convection during July over the western portions of the ITCZ. The differences in upper-level flow between August and July (Figure 4.4) are relatively weak compared to those in Figure 4.3. Most noticeable is the enhanced easterly flow along the equator during August compared to that during July.

Vertically Integrated Moisture Flux

The July minus June moisture flux differences presented in Figure 4.5 show that both the MM5 and NCEP reanalyses exhibit enhanced moisture flux through Central America and along the ITCZ during July. Thus, the mid-summer drought in Central America and southern Mexico (Figure 4.1) does not result from a lack of moisture. The moisture flux differences are noticeably stronger in the MM5 to the west of Mexico as a result of tropical cyclones. In addition, the inability of the tropical cyclones to exit easily the western boundary leads to the strong, cyclonic-appearing circulation near the western boundary.

Weaker moisture fluxes into the central United States from the Gulf of Mexico are evident in the differences between August and July shown in Figure 4.6. Generally weaker moisture flux along 15° N is evident in the MM5 with greater flux near Baja California as a result of tropical storms penetrating further northward.

Vertical Cross Sections Through the CTIC

Changes in the vertical structure of the atmospheric circulation across the CTIC between July and June are shown in Figure 4.7 in the cross section along 105° W similar to that presented in Chapter 3. The greatest increase in SST is near the coast with lower SST to the south of 16° N. Higher temperatures are also evident over the southern United
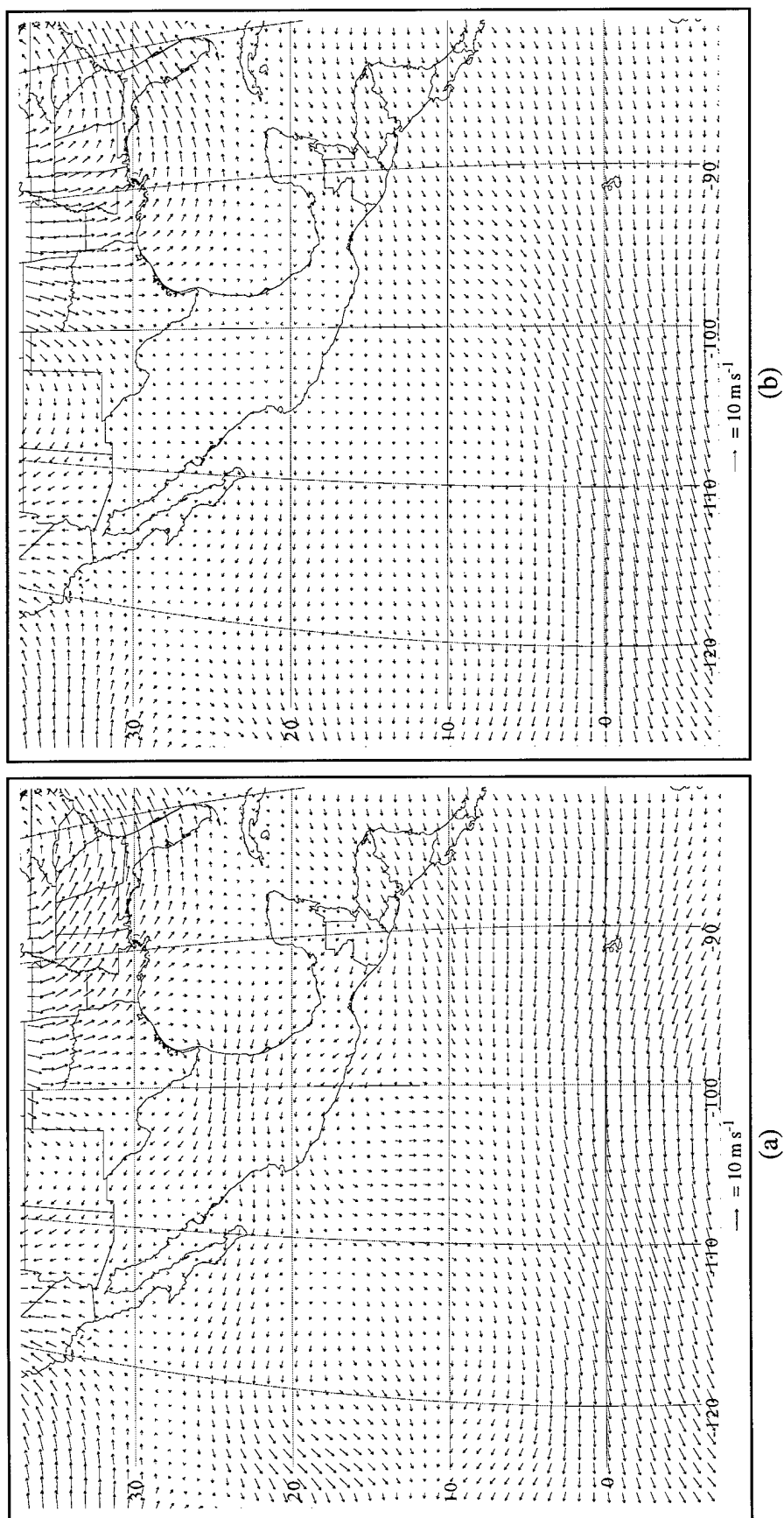
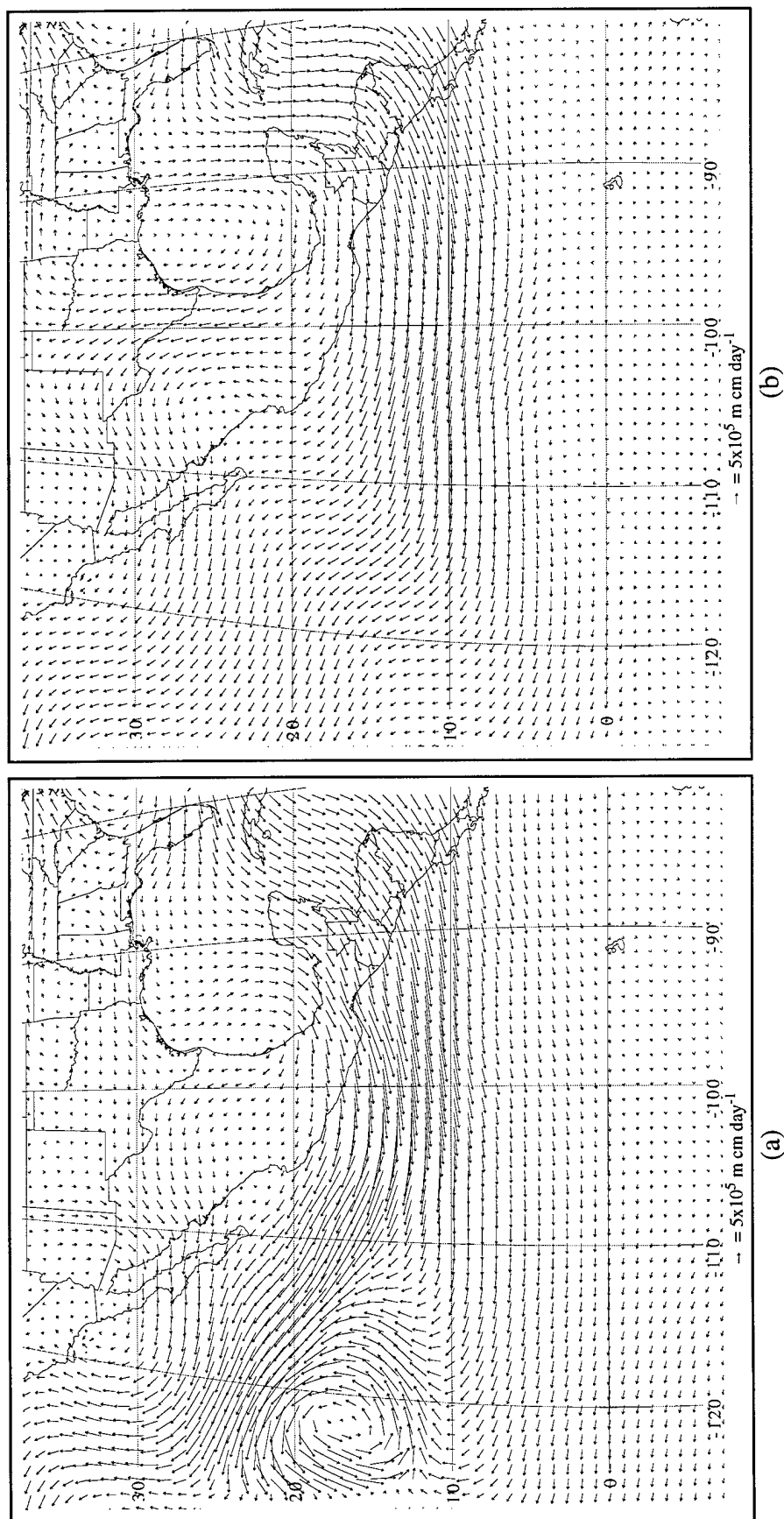Figure 4.4.    Differences in 200 mb wind between July and August in m s⁻¹ for (a) MM5 and (b) NCEP.

62



Figure 4.5.    Differences in total vertically integrated moisture flux between July and June in $10^5$ m cm day$^{-1}$ for (a) MM5 and (b) NCEP.
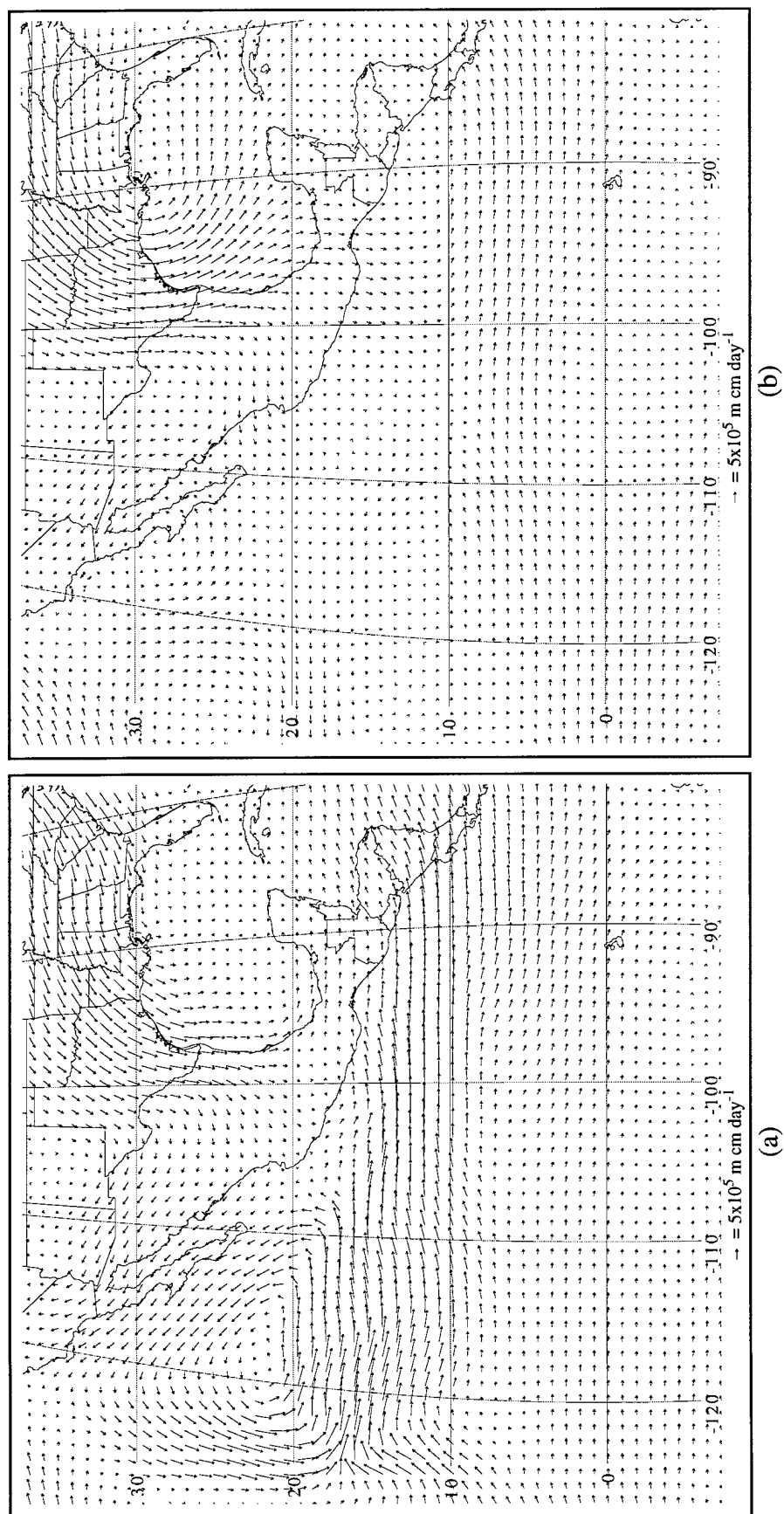
Figure 4.6.  Differences in total vertically integrated moisture flux between August and July in $10^5$ m cm day$^{-1}$ for (a) MM5 and (b) NCEP.

Figure 4.7. Vertical cross section of differences between July and June along 105° W from 5° S to 35° N. The vertical coordinate is pressure in mb. The thin dashed lines are $\theta_e$ K. The thicker solid lines are the meridional wind in m s$^{-1}$. Shaded regions and contours are total LWC in 10$^{-2}$ g kg$^{-1}$. The lower graph shows the precipitation rate (solid line, scale to left) in cm day$^{-1}$ and surface temperature differences (dashed line, scale to right) in °C. Contour intervals are ±0.5, ± 1 thereafter.

States. Values of $\theta_e$ throughout the troposphere increase in July to the north of 22° N and decrease to the south. Additionally, higher precipitation rates in July are evident from 8°-12° N and north of 17° N. While the latter conforms to the conventional view that greater precipitation rates move northward as the troposphere becomes warmer and more moist, the higher precipitation rates between 8°-12° N occur where SST has decreased and $\theta_e$ is lower. Slightly stronger meridional wind convergence in the PBL between 7°-10° N may help to explain this result. Greater liquid/ice water content during July, which is associated with increased precipitation, is evident between 8°-12° N and 20°-25° N. Higher LWC is also evident in the PBL over the cold tongue.

Differences in the tropospheric circulation between August and July along 105° W are shown in Figure 4.8. Generally surface temperatures are lower in August compared to July, however, temperatures are slightly higher between 15°-20° N. A sharp increase in precipitation is evident near 15° N. This is coupled with a well-defined vertical column of liquid/ice water. Less precipitation and lower liquid/ice water content are found to the north and south. Differences in $\theta_e$ are small between August and July. Stronger meridional wind convergence in the PBL is evident near 15° N with stronger divergence aloft. The depth of the PBL diminishes during August over the cold tongue as SST decreases. In addition, the LWC contained in the model's stratiform clouds in the PBL increases.

## Mesoscale Aspects of the Seasonal Evolution

### The Mexican Monsoon

Features over land of the simulated month-to-month variation of rainfall are contrasted in Figure 4.9 to the observed variation estimated by Legates and Wilmott (1990). The rainfall from the NCEP reanalyses are not shown here since they exhibit no
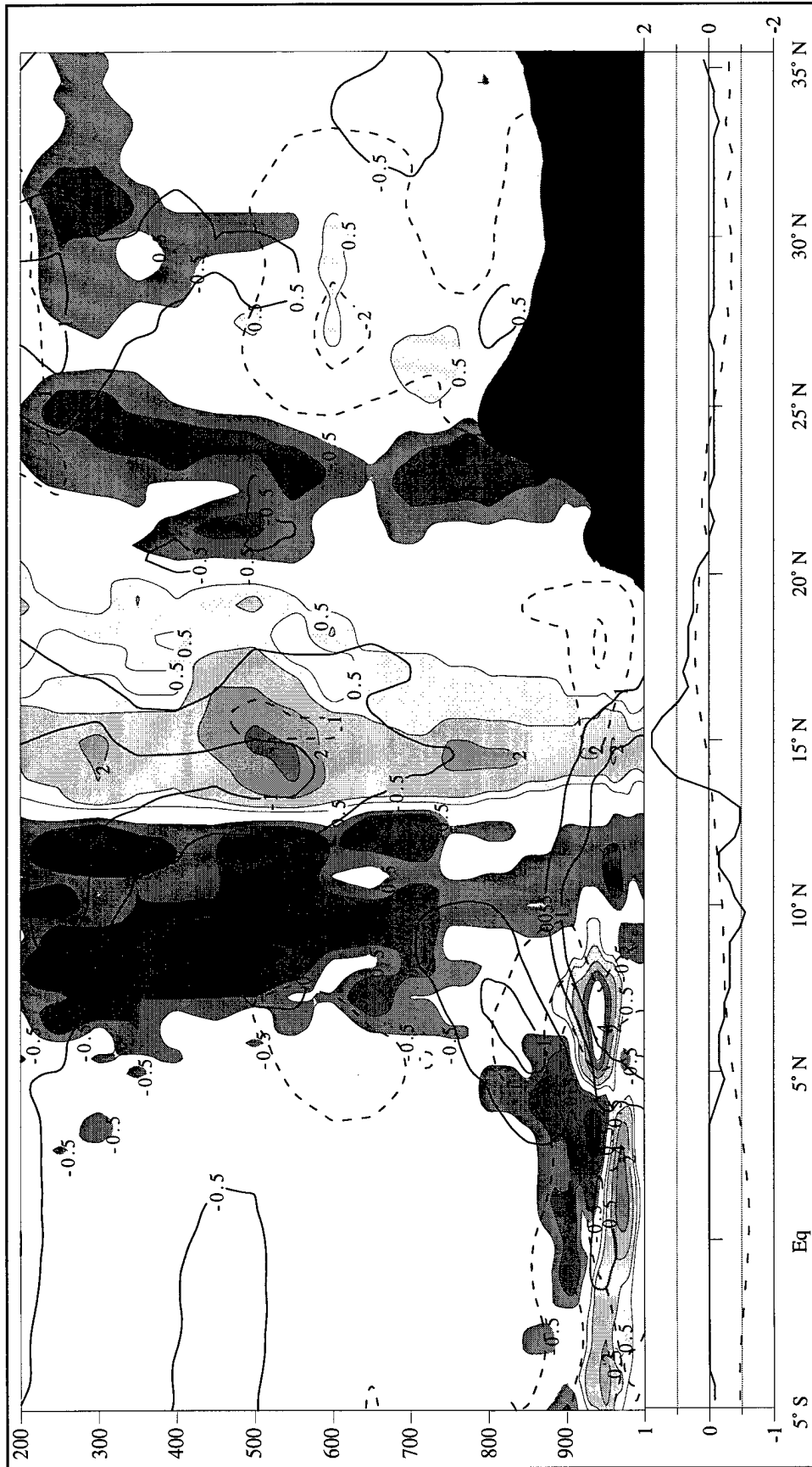
Figure 4.8. Vertical cross section of differences between August and July along 105° W from 5° S to 35° N. The vertical coordinate is pressure in mb. The thin dashed lines are $\theta_e$ K. The thicker solid lines are the meridional wind in m s⁻¹. Shaded regions and contours are total LWC in $10^{-2}$ g kg⁻¹. The lower graph shows the precipitation rate (solid line, scale to left) in cm day⁻¹ and surface temperature differences (dashed line, scale to right) in °C. Contour intervals are ±0.5,± 1 thereafter.
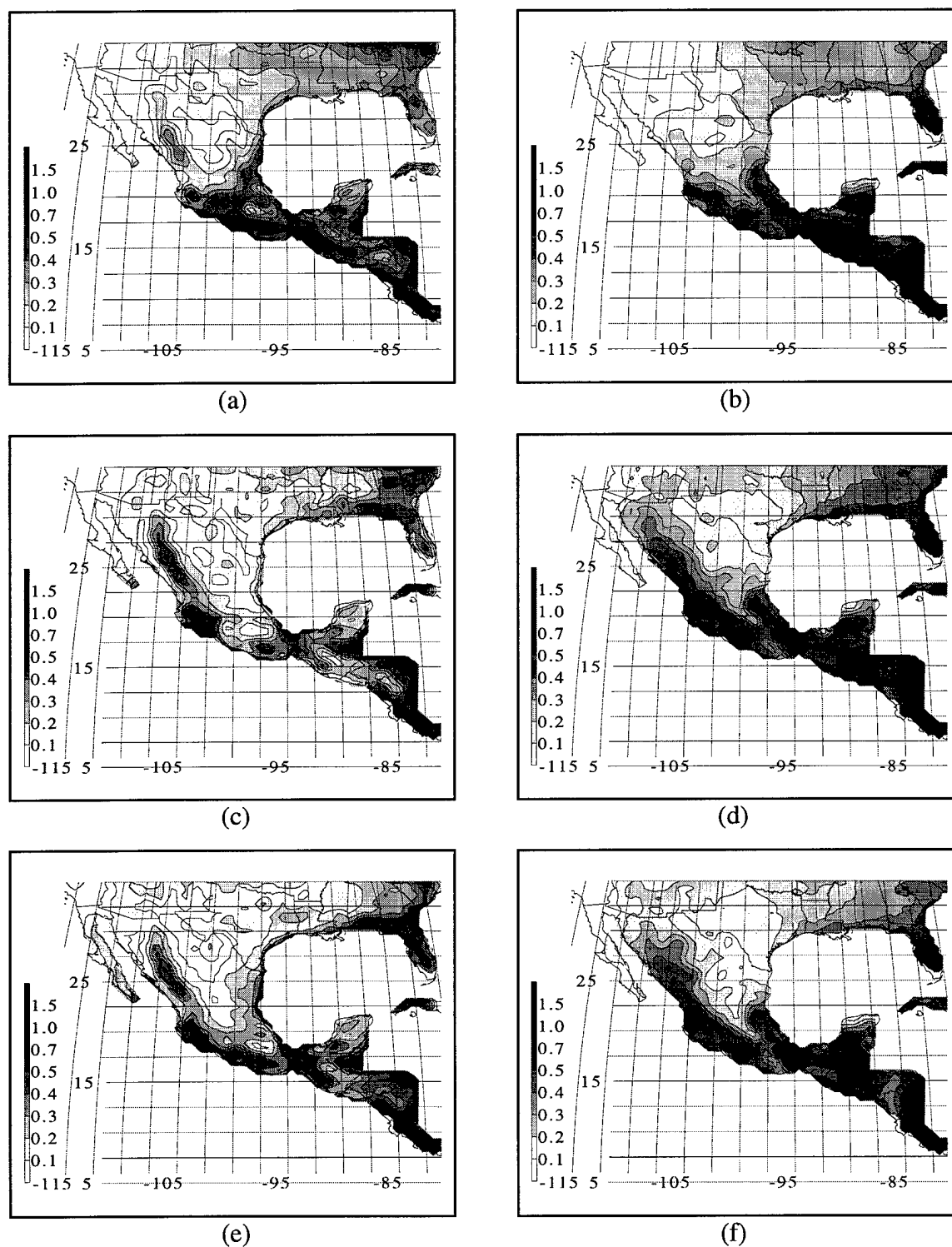
Figure 4.9.    Precipitation rate in cm day⁻¹ for (a) June (MM5), (b) June (observed), (c) July (MM5), (d) July (observed), (e) August (MM5), and (f) August (observed). MM5 rates are for 1990-1997, observed are Legates and Wilmott (1990). Values over 0.1 cm day⁻¹ shaded according to the scale on the left; contour intervals are 0.1, 0.2, 0.3, 0.4, 0.5, 0.7, 1, and 1.5 cm day⁻¹.

mesoscale structure. The heaviest rainfall during June is observed in Guatemala and Nicaragua (Figure 4.9b) with maximum rainfall rates in excess of 1.5 cm day$^{-1}$. Rainfall less than 0.5 cm day$^{-1}$ is seen over Mexico to the north of 20° N. While the MM5 captures many of the mesoscale features in rainfall (Figure 4.9a), the onset of the monsoon over northwestern Mexico to the north of 20° N is earlier than typically observed.

The northward extension of the Mexican monsoon into Arizona and New Mexico during July is evident in Figure 4.9d. The MM5 tends to focus the rainfall more along the western slopes of the Sierra Madre Occidental mountains (Figure 4.9c), than the Legates and Wilmott (1990) analysis (Figure 4.9d). However, the MM5 climatology is consistent with unpublished atlases of monthly rainfall developed in Mexico (A. Douglas 1998, personal communication). The model also tends to have less rainfall to the east of the mountains, most notably near Veracruz, Mexico, and to the east of the mountains from Guatemala to Nicaragua. High rainfall rates along the western and southwestern coasts of Mexico are evident during August in Figure 4.9f. Rainfall rates in the MM5 tend to be lower along the coastal regions of Western Mexico (Figure 4.9e).

The similarities and differences between the observed rainfall over land areas demonstrates the sensitivity to the specification of the underlying terrain. Since the model's terrain is relatively smooth compared to the actual terrain, local features are often missed or misplaced. Nonetheless, considerable regional detail is captured that is not available in the NCEP reanalyses.

## Tropical Cyclones

The month-to-month changes in the observed and simulated distribution of all cyclones (tropical storms and hurricanes) are shown in Figure 4.10. Cyclones are observed
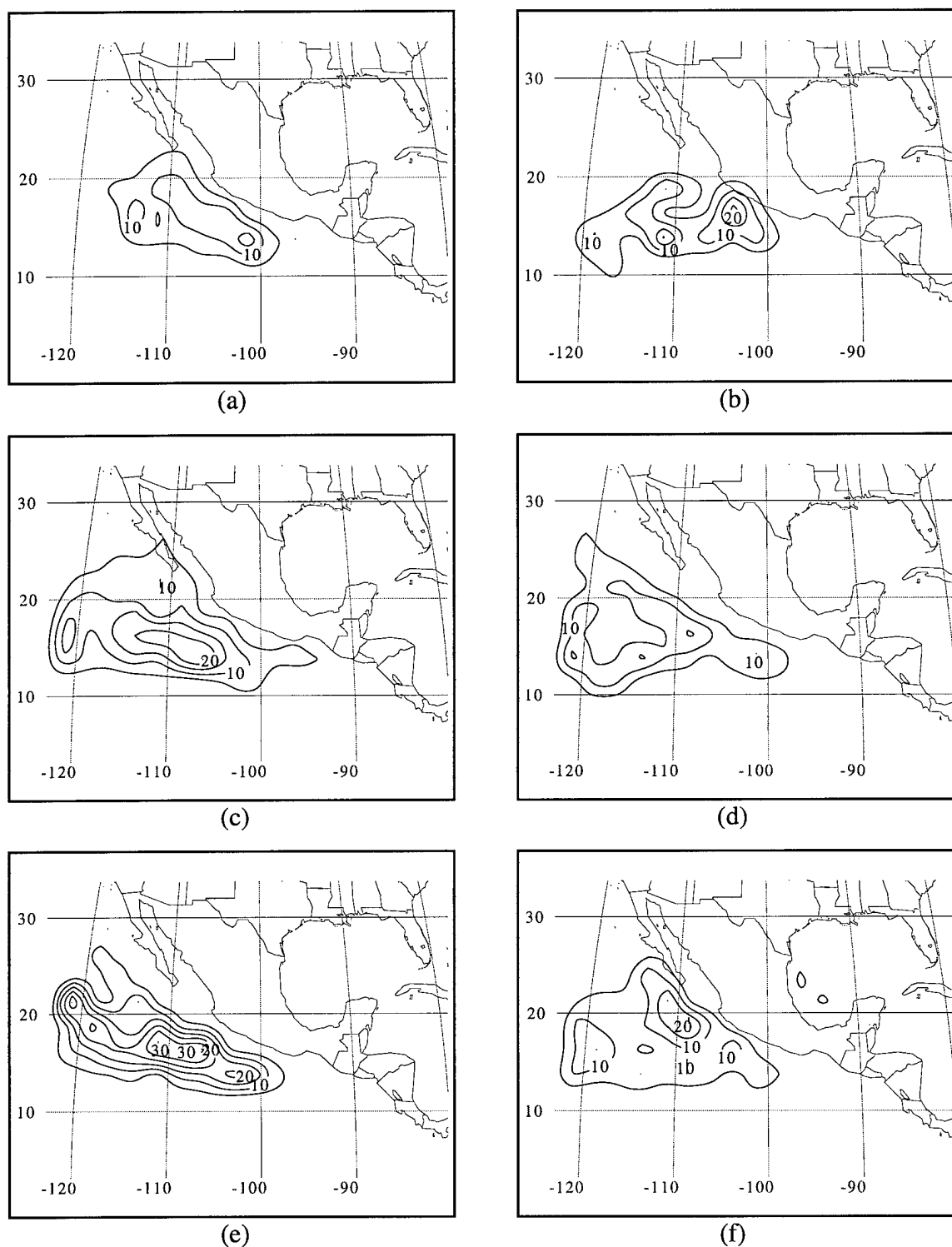
Figure 4.10.   Occurrence of all tropical storms and hurricanes in 2.5° x 2.5° grid boxes, based on 10 m AGL winds for (a) June (MM5), (b) June (observed), (c) July (MM5), (d) July (observed), (e) August (MM5), and (f) August (observed). Contour intervals are 1, 2.5, 5, and every 10 thereafter with every other contour labeled.

frequently during June near the southwestern coast of Mexico and along the ITCZ (Figure 4.10b). A well-defined common track oriented from the southwest to the northwest is evident during July as well as further west near 120° W (Figure 4.10d). Tropical storms and hurricanes become more common near Baja California during August (Figure 4.10f).

The distribution of simulated cyclones defined by the 10 m AGL wind only during June are shown in Figure 4.10a. The distribution defined from the two-lowest model levels (not shown) is nearly identical during all months. The model storms tend to follow a course parallel to the coast during June while a greater number of the observed storms tend to track westward along 15° N. During July (Figure 4.10c), the model storms tend to move along a preferred path rather than exhibit the broader variation observed. The MM5 develops too many tropical storms and hurricanes during August (Figure 4.10e) compared to that observed (Figure 4.10f). The model storms tend to track further westward than observed.

CHAPTER 5

INTERANNUAL VARIABILITY

The eight simulations from 1990-1997 provide a basis from which to evaluate year-to-year variations in the regional circulation. The 1997 summer was the most anomalous of the eight due to the global atmosphere and Pacific Ocean changes associated with the ENSO phenomenon (Wallace et al. 1998). However, the entire 8-year period is unprecedented relative to the record of the tropical Pacific Ocean during the past 50 years. Above normal SST was observed across the equatorial Pacific Ocean during each of the summers from 1990 to 1995; 1996 was the only year that had lower than normal SST.

Interannual variations in the regional circulation are summarized in the Appendices. Figures are presented for: seasonal averages of precipitation; SST, surface wind, upper-tropospheric wind and moisture flux anomalies relative to the 8-year mean; and selected cross sections across the CTIC. The intensity of the 1997 anomalies relative to the 8-year climatology discussed in Chapter 3 are quite remarkable and will be shown next. The interannual variations in tropical cyclones will then be summarized as a means to assess variations in the regional circulation that arise from mesoscale processes.

JJA 1997: Strong ENSO Event

Monitoring of the 1997-1998 ENSO event has occurred on an unprecedented scale. Considerable information is available via the Internet (**http://www.ogp.noaa.gov**, **http://www.cdc.noaa.gov, http://www.pmel.noaa.gov/toga-tao/el-nino**). The 1997-1998

ENSO developed rapidly during spring 1997. By summer 1997, positive SST anomalies in the equatorial Pacific were larger than those observed during any of the ENSO events for which adequate records are available. Above normal SST in the eastern equatorial Pacific began to subside during spring 1998 with SST falling below normal by late summer in the central equatorial Pacific.

Major shifts in equatorial convection were observed during 1997-1998. Droughts developed over Indonesia and the Maritime Continent by summer 1997 while heavy precipitation developed in the central equatorial Pacific Ocean. During summer 1997, anomalously strong convection was observed over the cold tongue in the eastern equatorial Pacific with drought over Central America and the Caribbean region. These anomalous conditions persisted through spring 1998.

The average daily precipitation rates for JJA 1997 from the MM5 and NCEP reanalyses are shown in Figure 5.1. Both the NCEP reanalyses and MM5 simulation exhibit widespread precipitation across the eastern equatorial Pacific Ocean. Overall the MM5 simulates a weaker and more dispersed ITCZ during 1997 compared to that in the other years (see Figure 3.3 and Appendix A). Disparities in precipitation amount between the NCEP reanalyses and MM5 simulation over Mexico are quite apparent. The influence of a fairly strong Gulf of Mexico cyclone (Hurricane Douglas) can be seen in both panels near Florida and Georgia.

The departures from the 8-year climatology of the low-level winds and daily precipitation rate are shown in Figure 5.2. Both the NCEP reanalyses and MM5 simulation show the weakening of the ITCZ to the south of Mexico and strengthening along the southern edge of the ITCZ. Anomalous northerly meridional surface winds

73
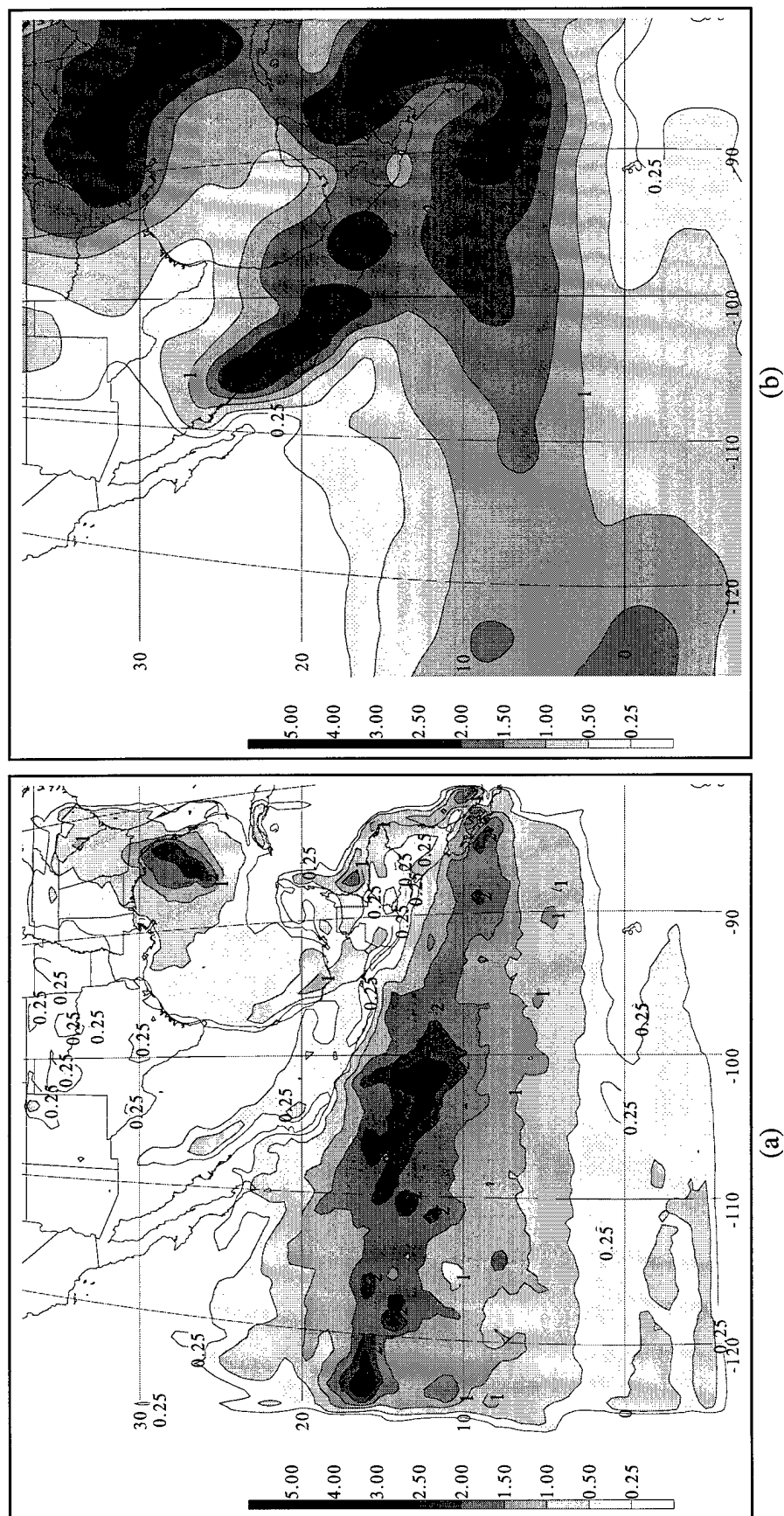


Figure 5.1. Precipitation rate in cm day⁻¹ for JJA 1997 for (a) MM5 and (b) NCEP. Values over 0.25 cm day⁻¹ are shaded according to the scale on the left. Contour intervals are 0.25, 0.5, 1, 1.5, 2, 2.5, 3, 4 and 5 cm day⁻¹ with every other contour labeled.
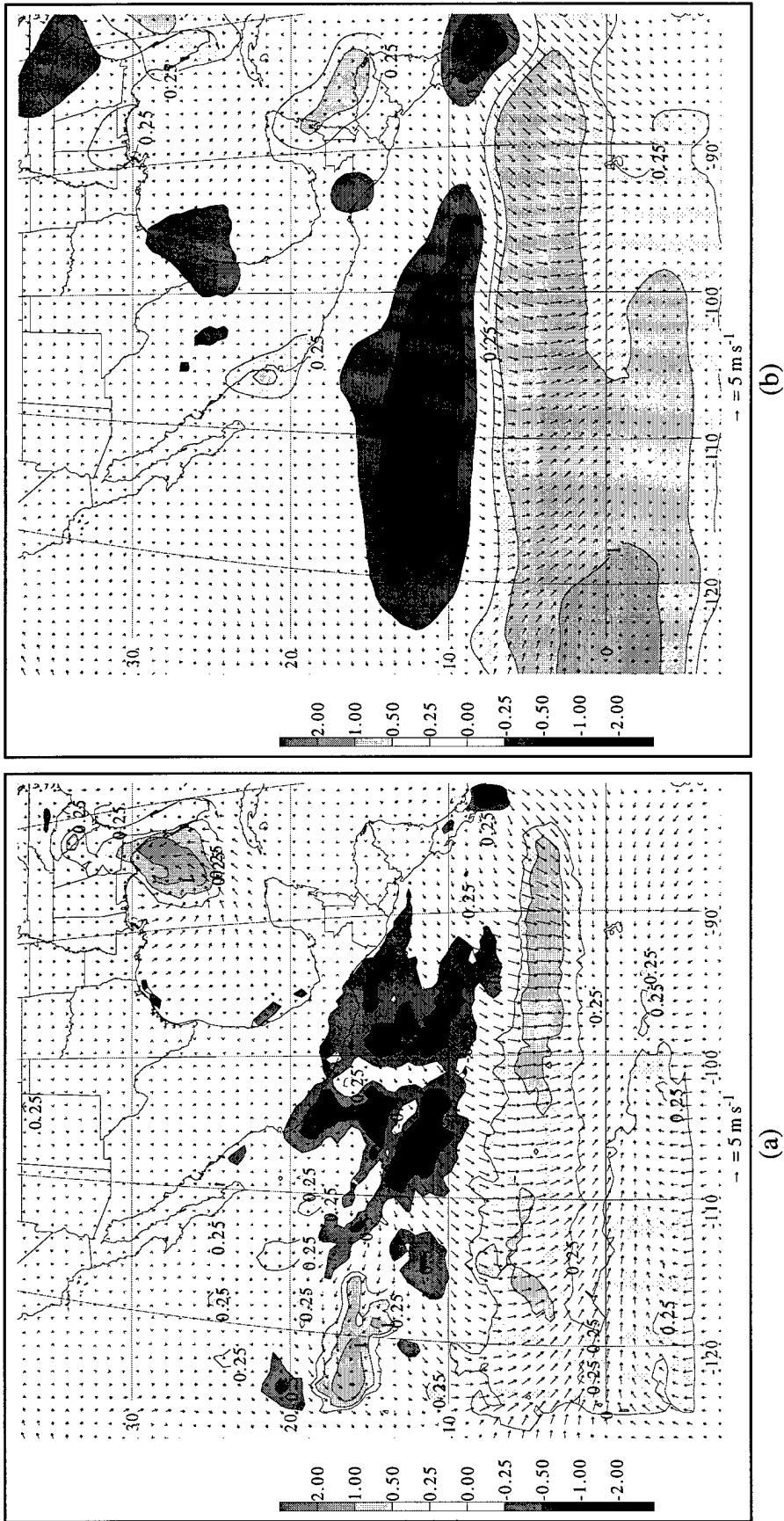
Figure 5.2.    10 m wind anomalies in m s⁻¹ and precipitation rate anomalies in cm day⁻¹ for JJA 1997 for (a) MM5 and (b) NCEP. Values ≥ 0.25 and ≤ -0.25 cm day⁻¹ are shaded according to the scale on the left. Contour intervals are ±0.25 and ±0.5 cm day⁻¹ thereafter.

(weaker southerly meridional wind) are found to the south of 12° N. Anomalous surface convergence over the anomalously warm waters of the cold tongue is also evident. Again, the influence of Hurricane Douglas and the analogous storm in the MM5 is reflected in the positive precipitation anomalies near Florida.

Upper-tropospheric wind anomalies during 1997 are shown in Figure 5.3. Stronger westerly flow over the CTIC appears in the NCEP reanalyses and the MM5. The upper-level anticyclone along the northern boundary tends to be weaker, except over Texas.

The observed SST anomalies during 1997 are shown in Figure 5.4. Temperatures 4 °C higher than the 8-year climatology are evident near the Galapagos Islands. SST was also higher than normal near Baja California. SST differences in the Gulf of California between the panels are present due to the use unmodified SST in the NCEP processing. The total vertically integrated moisture flux anomalies are superimposed on the SST anomalies in Figure 5.4. These show a weaker than normal moisture flux across the cold tongue. Thus, the anomalous convection over the cold tongue did not result from extra moisture being advected over the unusually high SST; rather, it came from relaxation of the normally strong dynamical constraints to convection described by Kloesel and Albrecht (1989). Cyclonic moisture flux anomalies near the western boundary over the ITCZ result in part from simulated tropical storms that tended to be trapped within the model domain as a result of inconsistent lateral boundary conditions.

The vertical cross section along 105° W for summer 1997 is shown in Figure 5.5. In order to focus on the dynamical processes involved, the seasonal mean values are shown rather than departures from the 8-year climatology (Figure 3.7). The weak gradient in SST across the cold tongue is quite apparent in the lower panel. Less rainfall in the
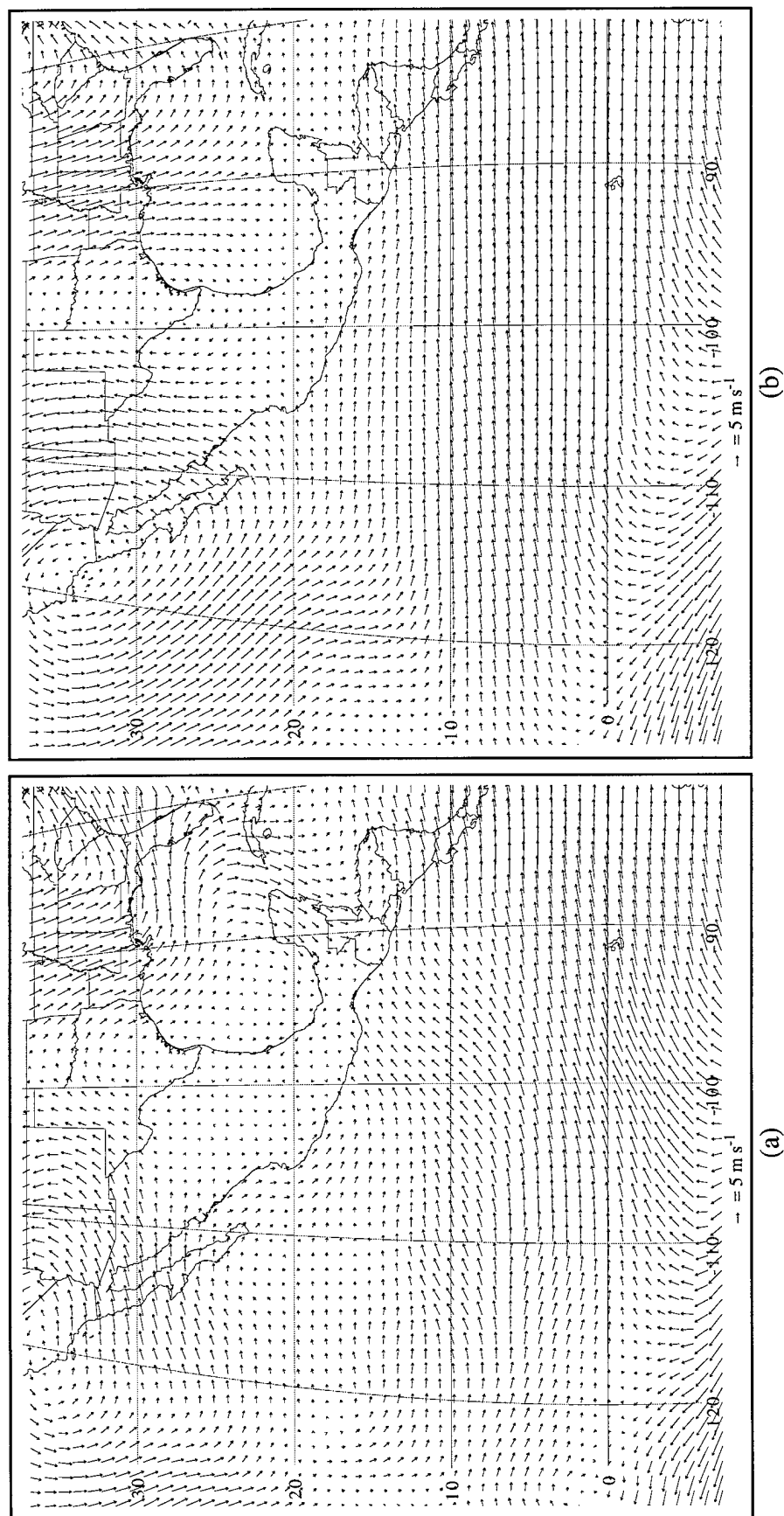
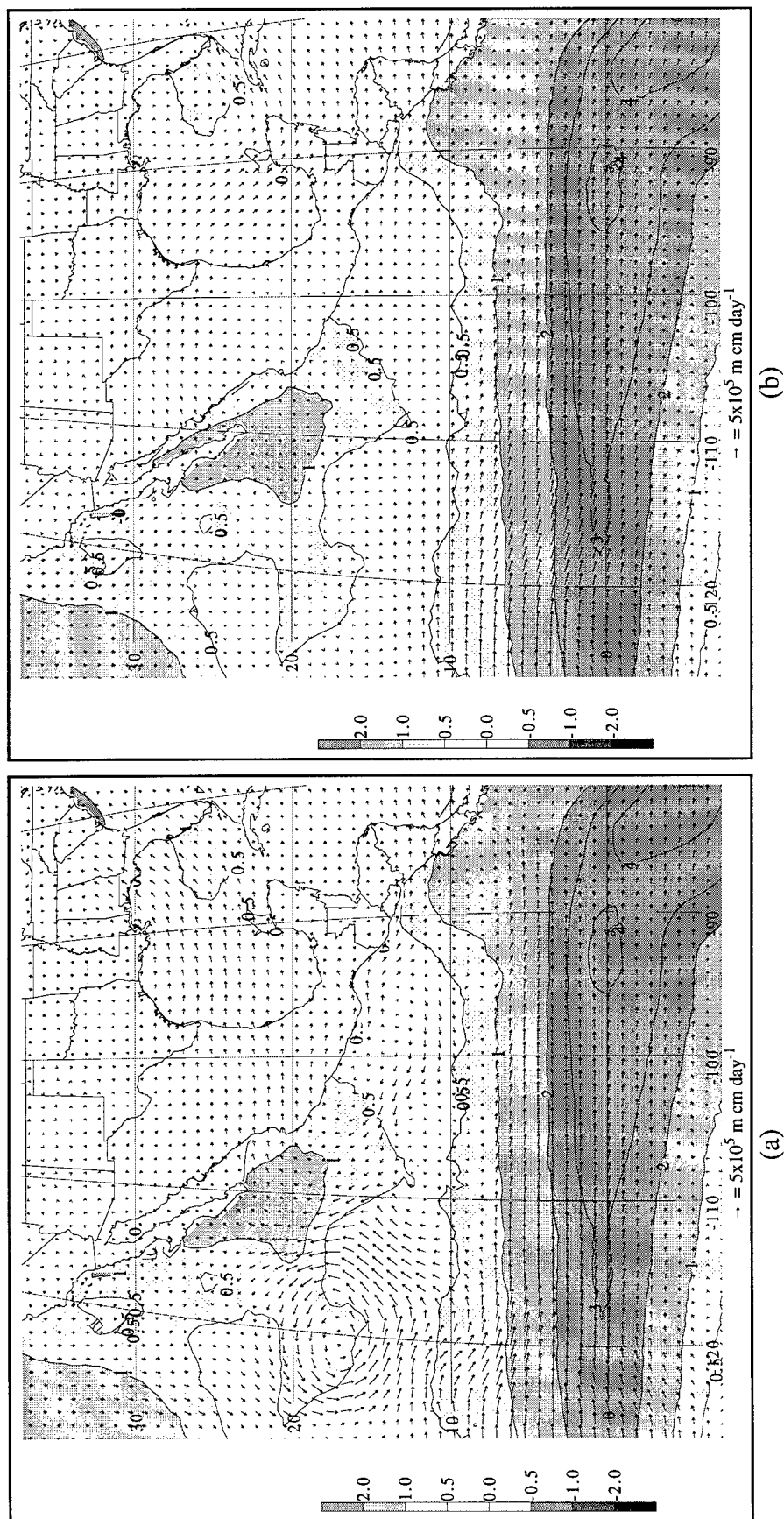Figure 5.3.    200 mb wind anomalies in m s⁻¹ for JJA 1997 for (a) MM5 and (b) NCEP.

(b)

(a)

Figure 5.4.  Total vertically integrated moisture flux anomalies in $10^5$ m cm day$^{-1}$ and SST anomalies in °C for JJA 1997 for (a) MM5 and (b) NCEP. Moisture flux anomalies in units of $10^5$ m cm day$^{-1}$. Contour intervals for SST anomalies are ±0.5 °C and ±1 °C thereafter. Values ≥ 0.5 °C and ≤ -0.5 °C are shaded.
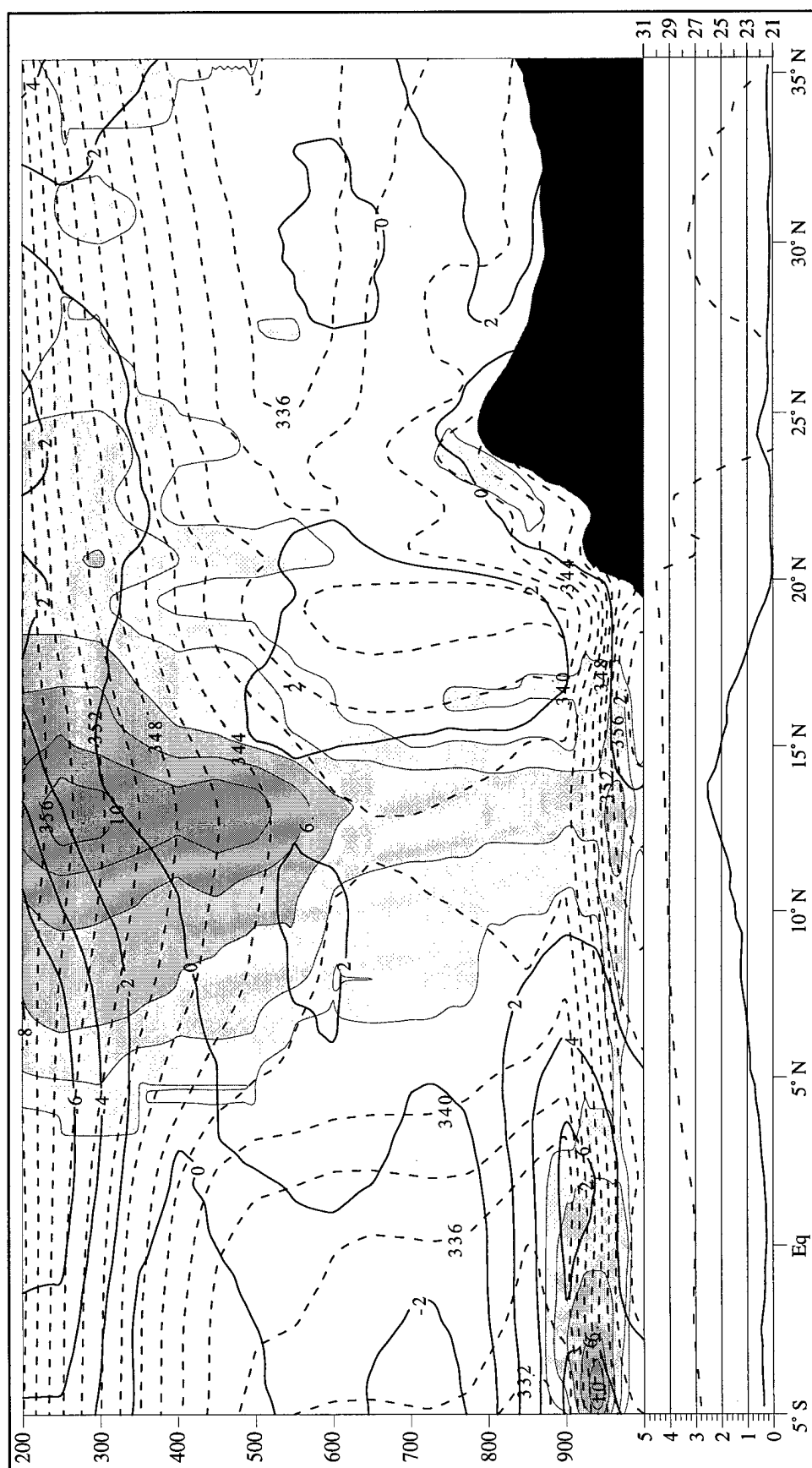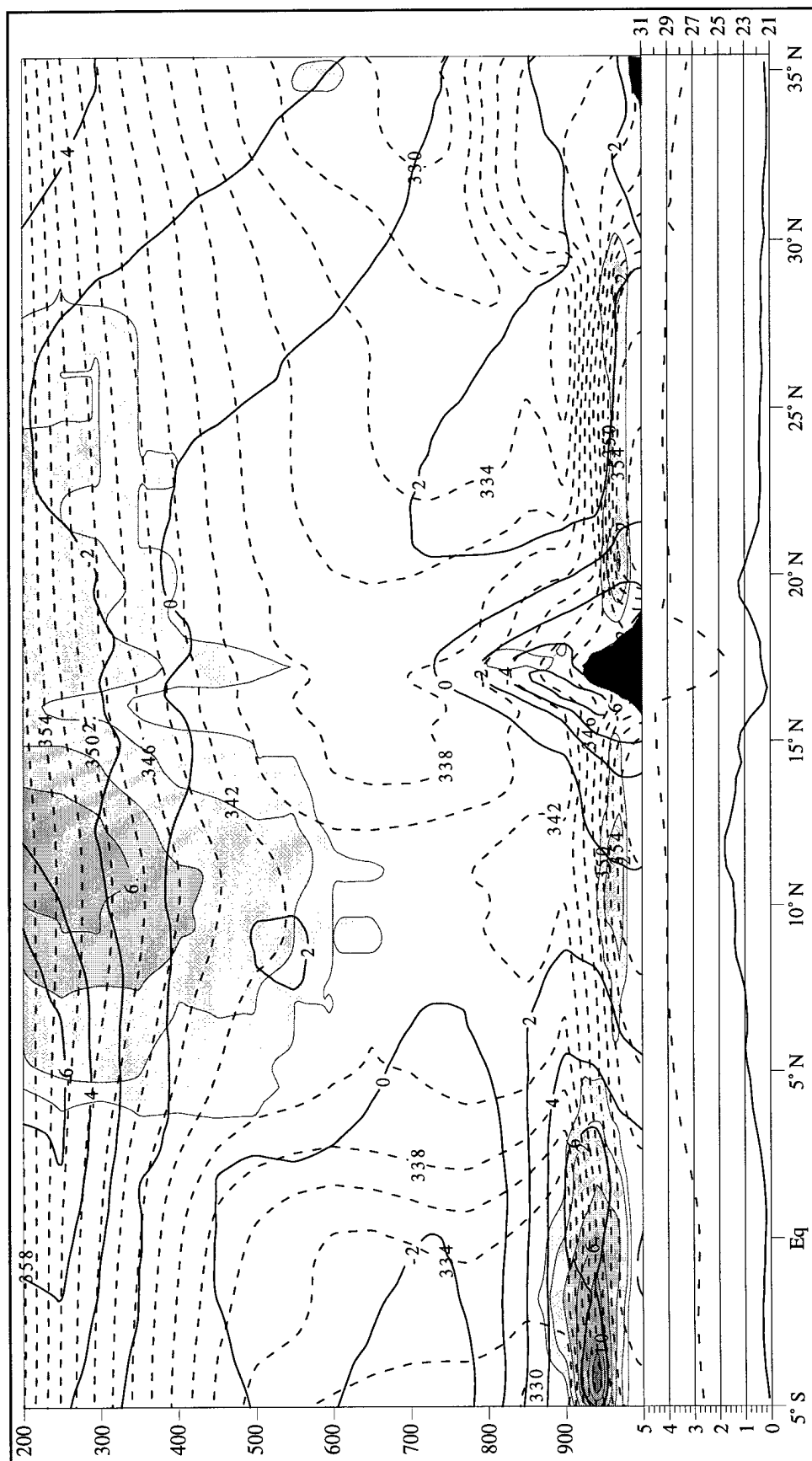
Figure 5.5. Vertical cross section for JJA 1997 along 105° W from 5° S to 35° N. The vertical coordinate is pressure in mb. The thin dashed lines are θ_e in K. The thicker solid lines denote the meridional wind component in m s⁻¹. The shaded regions and associated contours are total LWC in 10⁻² g kg⁻¹. The lower graph contains the average precipitation rate in cm day⁻¹ (solid line) and the average SST in °C (dashed line) along 105° W.

78

ITCZ and greater rainfall south of 6° N is also evident. A narrower ITCZ during 1997 is evident in the liquid/ice water content field in the troposphere.

The characteristics of the PBL during 1997 (Figure 5.5) differ significantly from the 8-year average (Figure 3.7). Lower LWC (fewer stratus clouds in the PBL), weaker inversion with a higher inversion height, higher $\theta_e$ and weaker cross-equatorial meridional flow are evident during 1997.

Figure 5.6 shows the cross section along 95° W during 1997. This figure should be compared to the 8-year climatology previously shown in Figure 3.8. The flat gradient in SST and the high temperatures during 1997 in the equatorial region are quite apparent in the lower panel. Similar to the conditions found along 105° W, the cross-equatorial meridional flow is weaker and less LWC in stratiform clouds is found during 1997. Most conspicuous in 1997 is the decrease in liquid/ice water content in the mid-troposphere over the ITCZ that reflects increased large-scale subsidence in the region. The strength of the gap flow across Mexico shows little change.

The other seven summers besides 1997 exhibit many other interesting variations from one another. Comparable figures to those presented here are shown in the appendices.

## Tropical Cyclones

As a means to summarize the complex large-scale and mesoscale interactions that take place in this region, the year-to-year variations in tropical storms and hurricanes are examined in the MM5 simulations and contrasted to those observed. Table 5.1 summarizes some of the characteristics of the observed tropical cyclones (tropical storms and hurricanes) and those simulated by the MM5. The cumulative statistics were already

Figure 5.6.    Vertical cross section for JJA 1997 along 95° W from 5° S to 35° N. The vertical coordinate is pressure in mb. The thin dashed lines are $\theta_e$ in K. The thicker solid lines denote the meridional wind component in m s$^{-1}$. The shaded regions and associated contours are total LWC in $10^{-2}$ g kg$^{-1}$. The lower graph contains the average precipitation rate in cm day$^{-1}$ (solid line) and the average surface temperature in °C (dashed line) along 95° W.

Table 5.1.  Total yearly number of tropical cyclones, average duration, storm types, total storm days, minimum pressure and maximum winds for JJA 1990-1997 for observed, model simulated based 10 m AGL winds (MM5 1) and model simulated based on 10 m and 100 m AGL winds (MM5 2).

| | Total | Avg. Dur. (days) | T/S (#) | Hurr. (#) | Total Storm Days | T/S Storm Days | Hurr. Storm Days | Min. Pres. (mb) | Max. Wind (m s$^{-1}$) |
|---|---|---|---|---|---|---|---|---|---|
| **Obs.** | | | | | | | | | |
| 1990 | 12 | 4.40 | 4 | 8 | 53 | 29 | 24 | 928 | 69.5 |
| 1991 | 7 | 3.82 | 2 | 5 | 27 | 17 | 10 | 960 | 51.5 |
| 1992 | 13 | 3.63 | 6 | 7 | 47 | 23 | 24 | 935 | 64.3 |
| 1993 | 12 | 3.02 | 5 | 7 | 36 | 20 | 16 | 942 | 61.7 |
| 1994 | 7 | 2.50 | 5 | 2 | 18 | 14 | 4 | 967 | 46.3 |
| 1995 | 10 | 3.92 | 4 | 6 | 39 | 28 | 11 | 945 | 59.2 |
| 1996 | 7 | 3.32 | 2 | 5 | 23 | 13 | 10 | 946 | 59.2 |
| 1997 | 9 | 1.75 | 6 | 3 | 16 | 9 | 7 | 921 | 72.0 |
| **MM5 1** | | | | | | | | | |
| 1990 | 20 | 3.54 | 18 | 2 | 71 | 68 | 3 | 957 | 33.9 |
| 1991 | 12 | 2.94 | 9 | 3 | 35 | 34 | 1 | 969 | 32.2 |
| 1992 | 6 | 3.38 | 5 | 1 | 20 | 19 | 1 | 957 | 35.4 |
| 1993 | 15 | 3.43 | 12 | 3 | 52 | 50 | 2 | 969 | 29.5 |
| 1994 | 11 | 3.34 | 8 | 3 | 37 | 34 | 3 | 953 | 34.9 |
| 1995 | 4 | 4.12 | 3 | 1 | 17 | 16 | 1 | 970 | 33.3 |
| 1996 | 11 | 3.95 | 9 | 2 | 44 | 43 | 1 | 964 | 30.3 |
| 1997 | 7 | 3.43 | 5 | 2 | 24 | 23 | 1 | 971 | 32.4 |
| **MM5 2** | | | | | | | | | |
| 1990 | 21 | 3.67 | 1 | 20 | 77 | 48 | 29 | 957 | 44.4 |
| 1991 | 16 | 2.88 | 6 | 10 | 46 | 34 | 12 | 969 | 40.8 |
| 1992 | 8 | 3.22 | 3 | 5 | 26 | 15 | 11 | 957 | 46.6 |
| 1993 | 17 | 3.47 | 5 | 12 | 59 | 39 | 20 | 969 | 36.7 |
| 1994 | 14 | 3.11 | 3 | 11 | 44 | 25 | 19 | 953 | 46.3 |
| 1995 | 5 | 4.00 | 1 | 4 | 20 | 13 | 7 | 970 | 42.7 |
| 1996 | 14 | 3.66 | 6 | 8 | 51 | 34 | 17 | 964 | 38.5 |
| 1997 | 10 | 3.28 | 5 | 5 | 33 | 26 | 7 | 971 | 41.3 |

presented in Table 3.1. The highest total number of observed storms occurred during JJA 1992, with nearly similar totals during 1990 and 1993. The greatest number of hurricanes was observed during 1990. Category 4 or stronger hurricanes (central pressures below 945 mb) were observed during 1990, 1992, 1993 and 1997.

While on average the MM5 develops too many tropical cyclones (Table 3.1), during some years (e.g., 1992 and 1995), the model develops many fewer than that observed, even if the two-lowest model levels are used to define the maximum wind speed. The minimum central pressure and maximum wind speed simulated by the MM5 indicate that the storms are too weak compared to those observed.

To assess more easily the year-to-year variations in storms, the total cyclone days (total number of storms times average duration) are presented in Figure 5.7 as a function
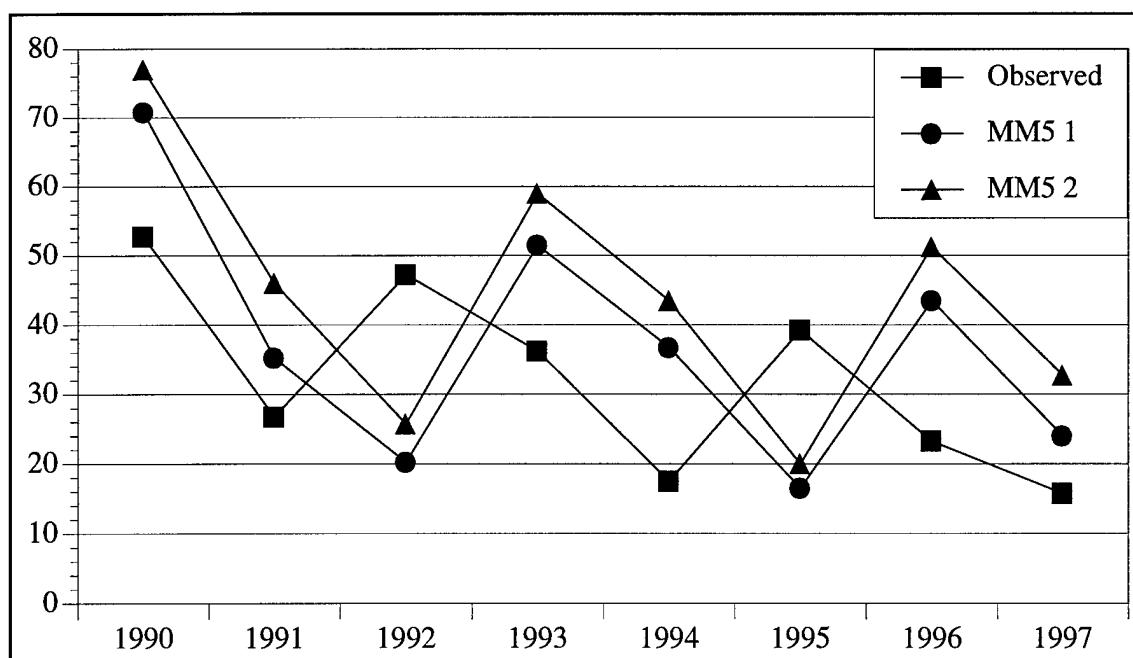


Figure 5.7.    Time series showing the total number of tropical cyclone days (total number of storms times average duration) for each year.

of year. JJA 1990 was the most active observed while 1997 was the least active (however,

Hurricane Guillermo during August 1997 was the strongest category 5 hurricane during

the 8-year period).

The year-to-year variations in the number of storm days simulated by the MM5

show little relationship to those observed. Few model cyclones were generated during

1992 and 1995, yet, a large number of cyclones were observed during these years, which

were relative maxima in storm days. In fact, the low number of degrees of freedom in

Figure 5.7 might suggest that the model storm days should be shifted forward by one year,

which has no possible physical interpretation. Thus, single realizations of the regional

climate from the MM5 forced by observed SST and lateral boundary conditions are unable

to reproduce correctly the regional conditions necessary to develop appropriate numbers

of storms with the appropriate duration. It should be noted that neither the observed or

model's year-to-year variation in cyclones are related to the year-to-year variations in local

SST. The highest SST in the cyclone genesis region was observed in 1997 and the lowest

in 1992.

Bengtsson et al. (1995) and Vitart et al. (1997) found less predictability for tropical

cyclones in the eastern Pacific Ocean than in other regions. Both studies used ensembles

of GCM experiments and produced fewer tropical cyclones in the eastern Pacific than

observed.

The observed spatial distributions of total cyclones (tropical storms and

hurricanes) are contrasted to those observed in order to evaluate variations in cyclone

genesis regions and storm tracks from year to year. Figure 5.8 shows the observed and

simulated distribution of cyclones during 1990 superimposed on the seasonally averaged
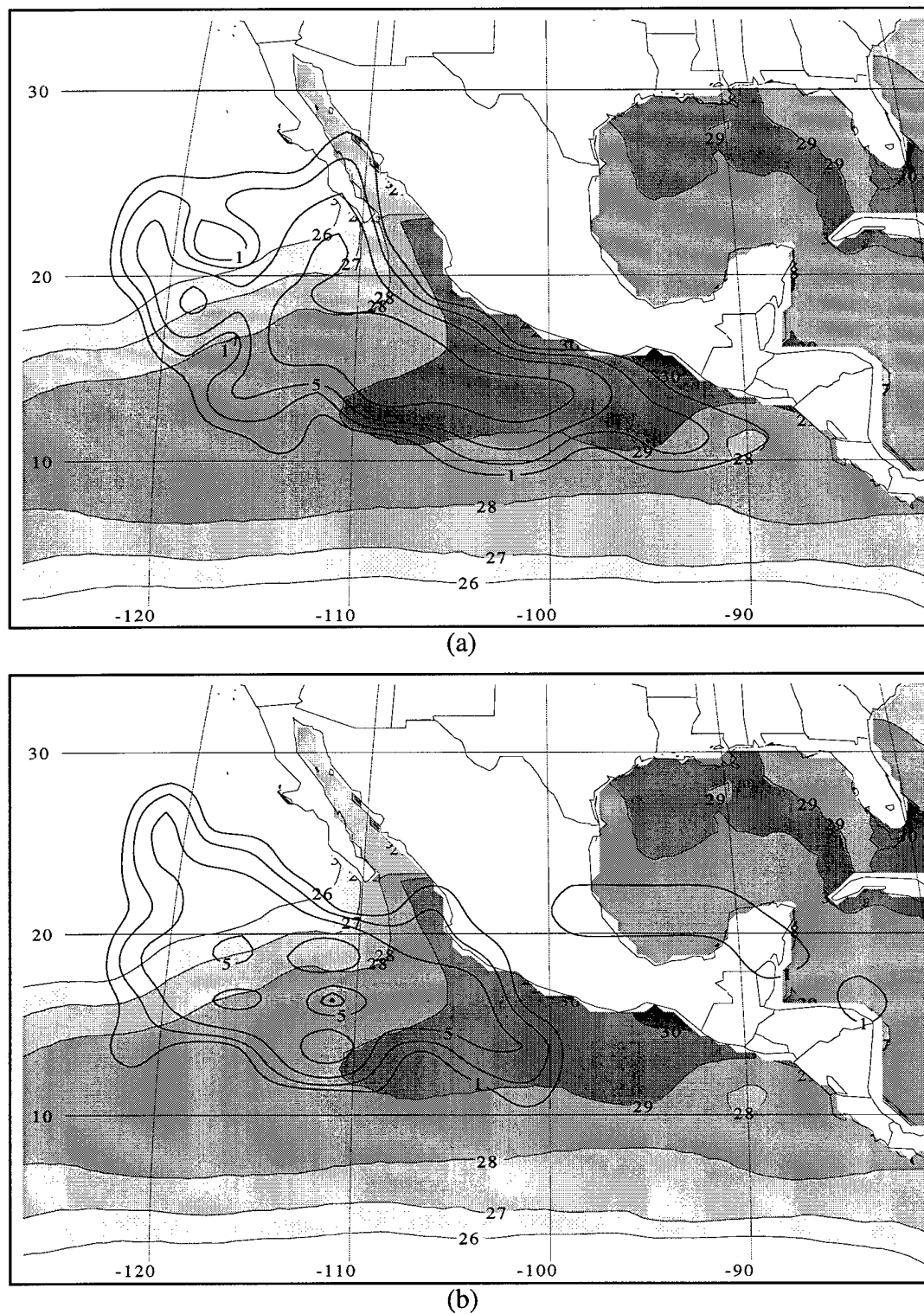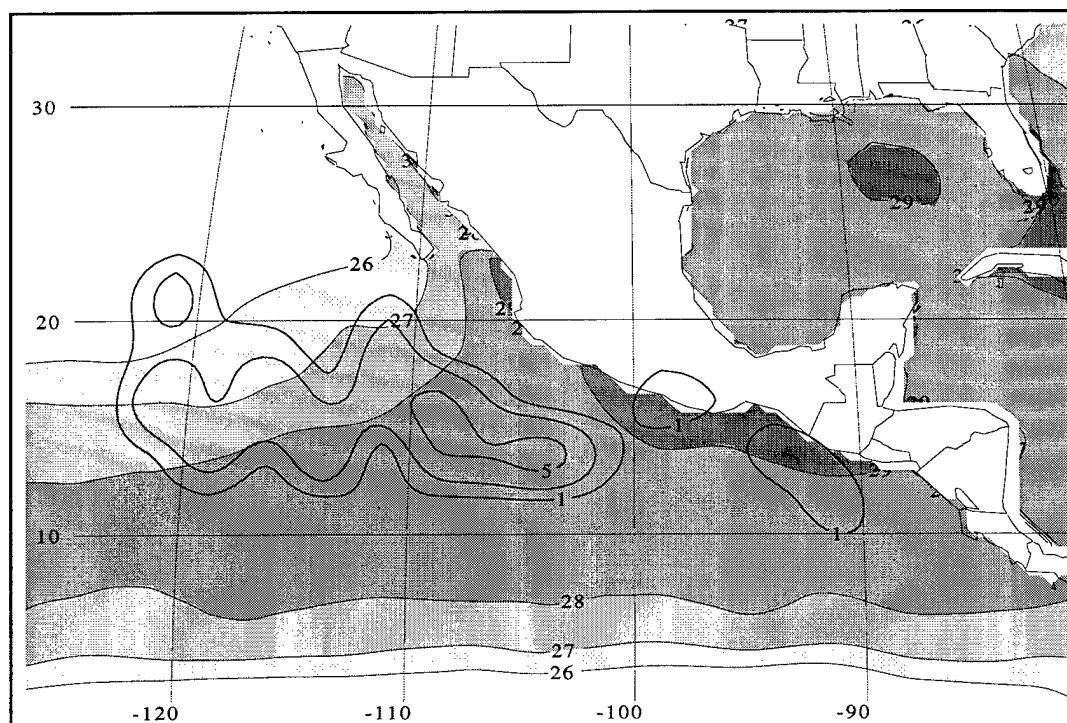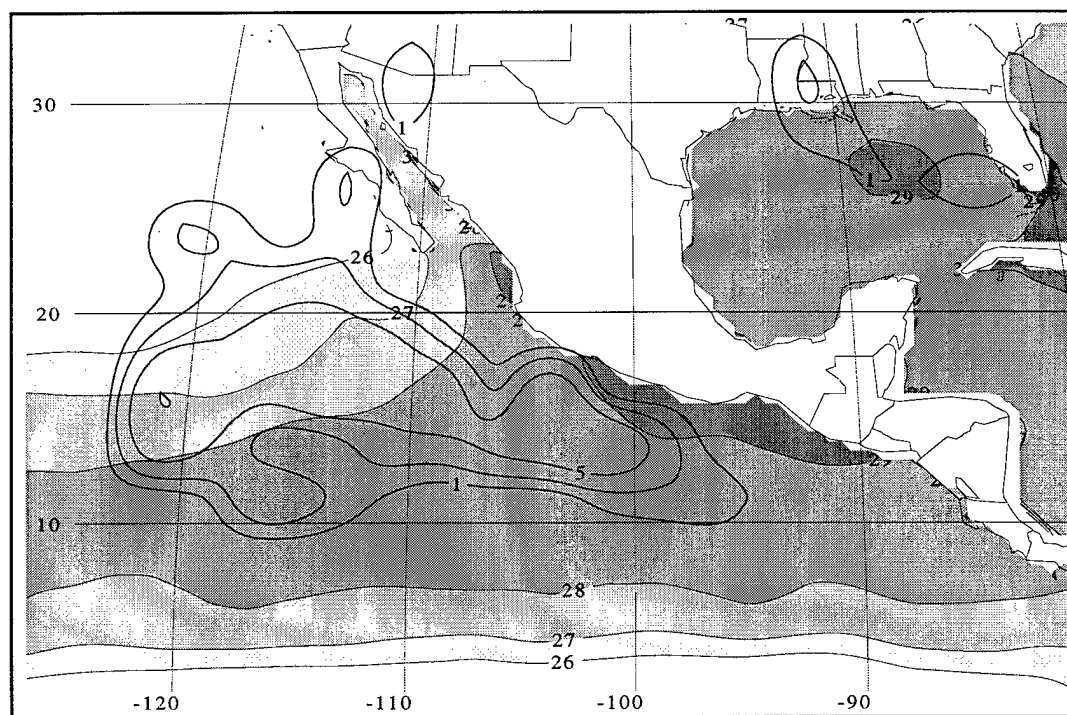
Figure 5.8.     Occurrence of all tropical storms and hurricanes in 2.5° x 2.5° grid boxes, based on 10 m AGL winds and mean SST for JJA 1990 for (a) MM5 and (b) observed. Cyclone contour intervals are 1, 2.5, 5, and every 10 thereafter with every other contour labeled. SST is contoured in 1 °C intervals and shaded for values of 26 °C and higher.

SST for that year. The model cyclones in these figures are defined from the 10 m AGL winds only. As described by Avila (1991), the eastern Pacific storm season of 1990 was characterized by a rather large number of cyclones with over 16 named for the season (4 of these occurred during September or October). This was double the average and four more than the previous record. A couple of preferred tracks are evident: one to the northwest and the other more westerly. In contrast, the MM5 produced 20 disturbances that travelled to the west-northwest.

The 1991 observed Eastern Pacific hurricane season was characterized by a low level of activity, particularly during July. This was attributed by Rappaport and Mayfield (1992) to upper-level westerly flow (Figure C.2) associated with a series of transitory large-scale disturbances. The model and observed cyclone distribution for 1991 are shown in Figure 5.9. In this year, only seven hurricanes/tropical storms fell within the JJA time period and most tended to travel in a westerly direction. The model had 12 storms of shorter duration that again tended to travel more west-northwest.

In contrast to the previous year, the observed 1992 season had a record breaking 27 tropical cyclones, 13 during JJA (Lawrence and Rappaport 1994). Their cumulative positions are shown along with the model generated cyclones in Figure 5.10. The six model storms in the eastern Pacific Ocean tended to track in a manner consistent with those observed, although a couple of the observed cyclones were able to track further northward across the lower SST. Note that Hurricane Andrew in the Gulf of Mexico was not simulated by the MM5. The eastern boundary condition from the NCEP reanalyses did not pick up this feature.
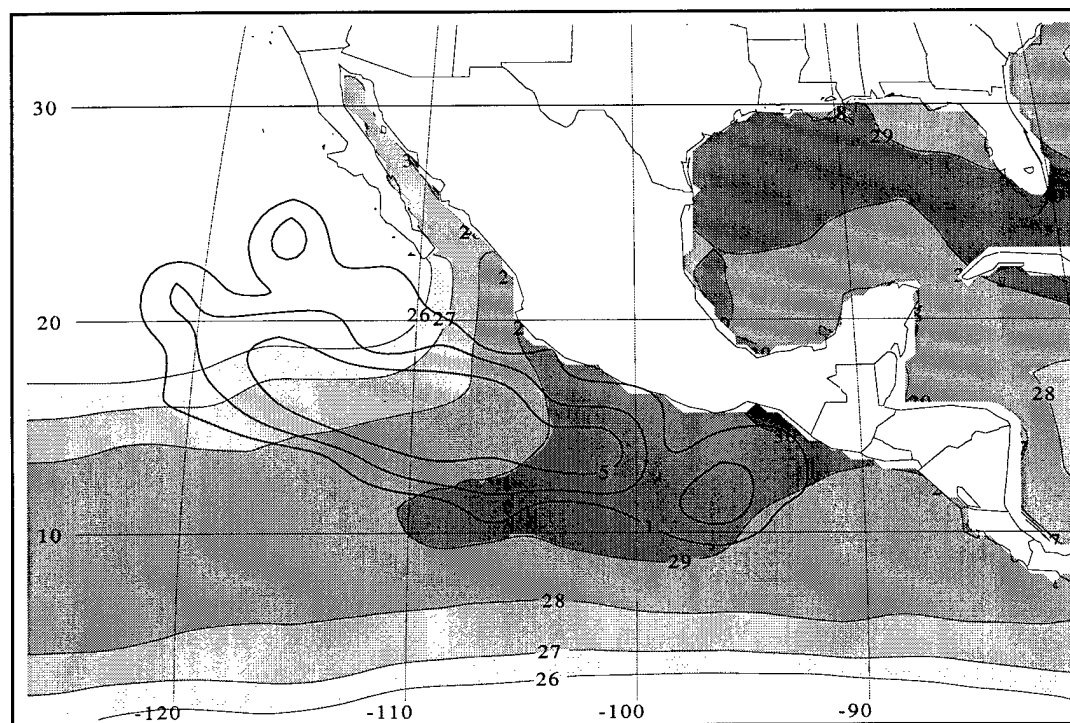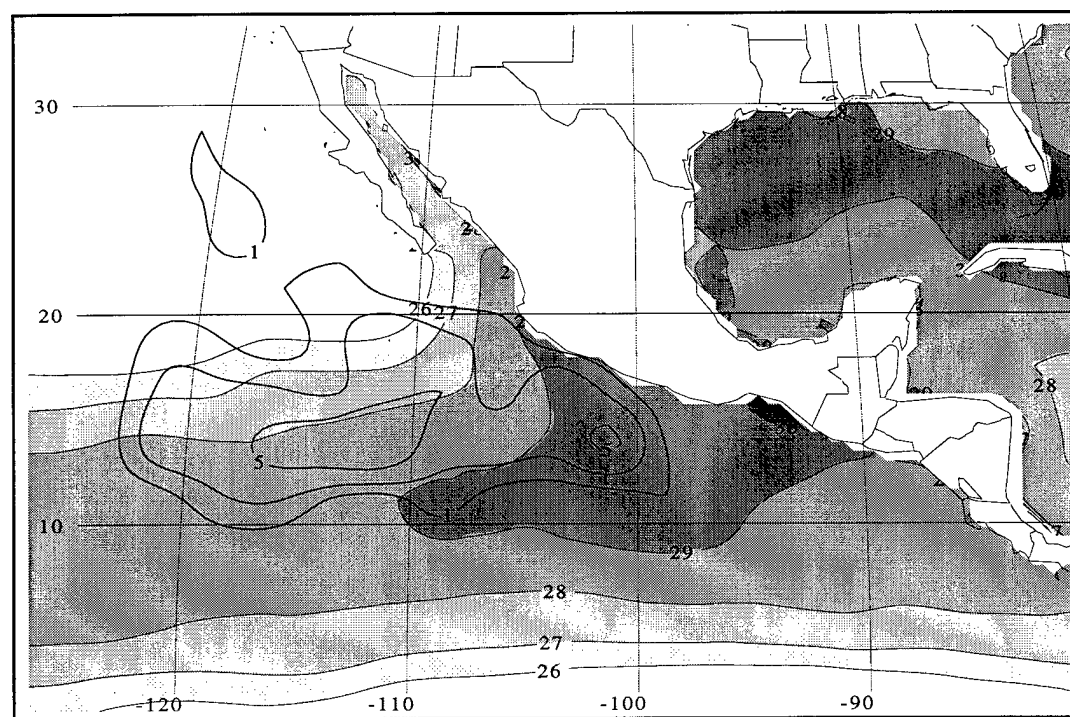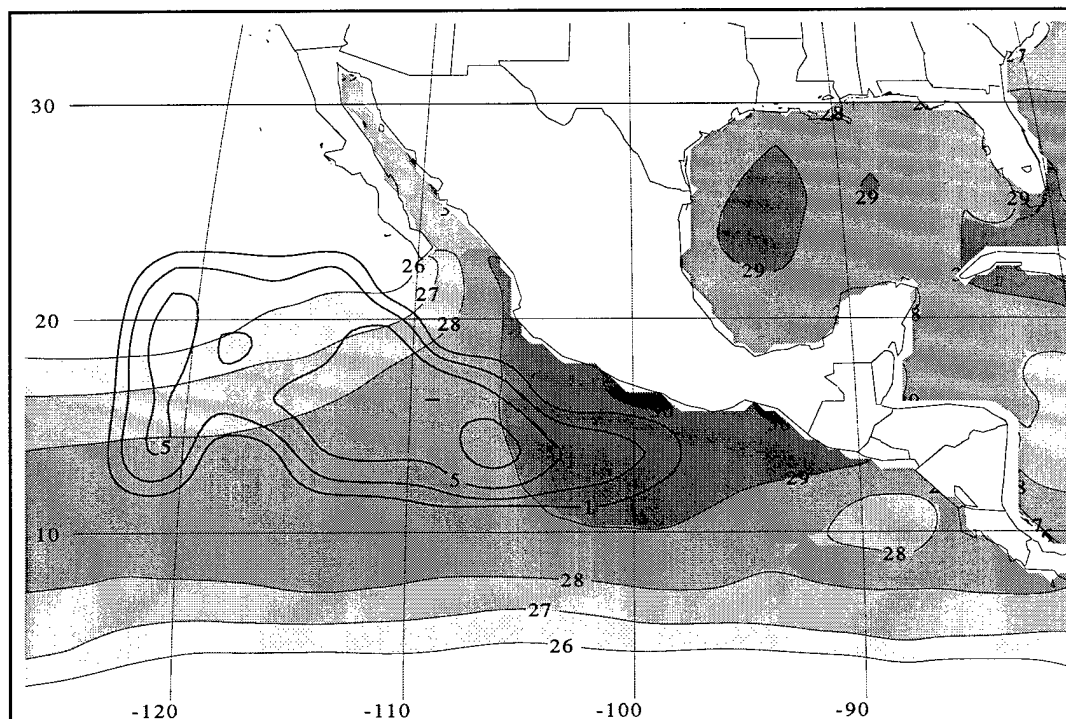
Figure 5.9.    Occurrence of all tropical storms and hurricanes in 2.5° x 2.5° grid boxes, based on 10 m AGL winds and mean SST for JJA 1991 for (a) MM5 and (b) observed. Cyclone contour intervals are 1, 2.5, 5, and every 10 thereafter with every other contour labeled. SST is contoured in 1 °C intervals and shaded for values of 26 °C and higher.
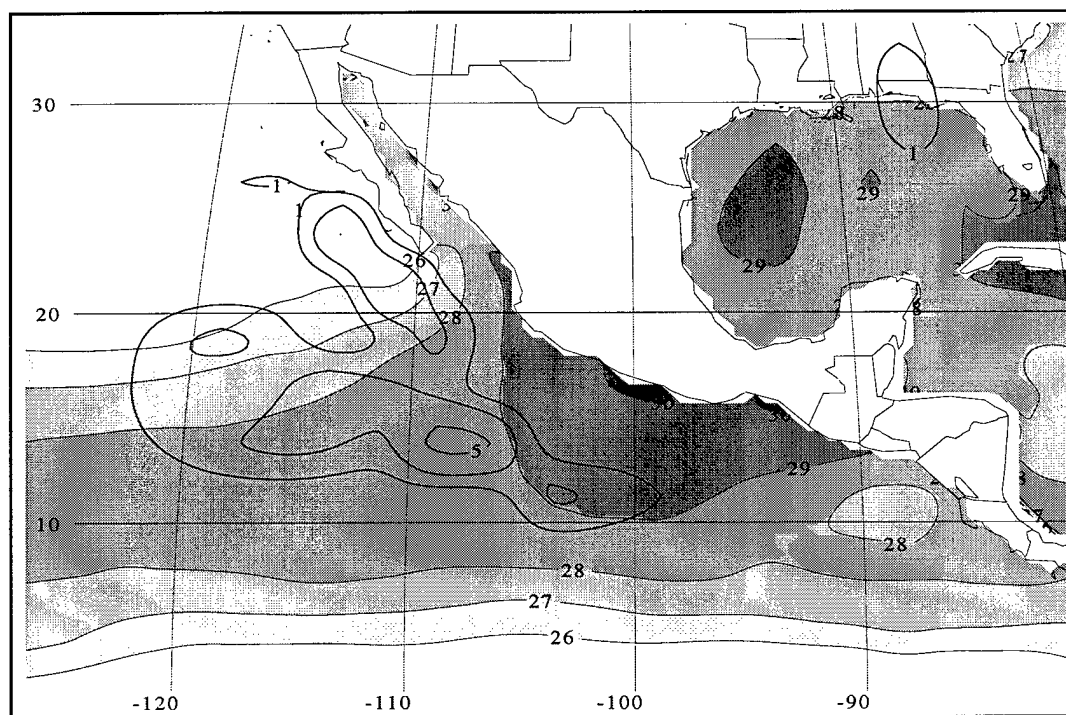
Figure 5.10.    Occurrence of all tropical storms and hurricanes in 2.5° x 2.5° grid boxes, based on 10 m AGL winds and mean SST for JJA 1992 for (a) MM5 and (b) observed. Cyclone contour intervals are 1, 2.5, 5, and every 10 thereafter with every other contour labeled. SST is contoured in 1 °C intervals and shaded for values of 26 °C and higher.

The MM5 and observed cyclone distributions for 1993 are shown in Figure 5.11. This year was quite mild compared to the previous, record breaking year. However, the observed hurricane distribution tended to exhibit some unique variability as well. An anomalous upper tropospheric trough (Figure C.4) over the western United States and Mexico set up a flow pattern favorable for a more northerly track for the observed storms (Avila and Mayfield 1995). This resulted in more storms than normal making landfall. The MM5 picked up the tendency for storms to be near the coast of Mexico and to the west of 110° W along the ITCZ. The latter feature in the model appears to emulate the development of Hurricane Adrian, which remained nearly stationary in this region (Avila and Mayfield 1995).

Figure 5.12 summarizes the tropical cyclones during 1994. One of the more unusual aspects of this year lies in the preferred region of cyclone genesis. The storms (both observed and modeled) tend to form around 105° W which is 10° to 15° further west than normal (Pasch and Mayfield 1996).

Summer 1995 was quite anomalous as well (refer to the figures in the appendices). The modeled and observed cyclones for 1995 are shown in Figure 5.13. As noted by Rappaport et al. (1998), the observed eastern Pacific season displayed the following anomalous behaviors: fewer storms in the Eastern Pacific than in the Atlantic for the first time in 26 years, second fewest storms in 30 years of tracking, and a relatively late start and early finish to the 1995 season. They note that anomalously strong easterly flow aloft (Figure C.6), coupled with anomalous westerly wind at low levels (Figure B.6) hindered cyclone development and produced an eastward shift of the genesis region. The cyclones tended to be further north than usual and JJA 1995 is the only summer during which the
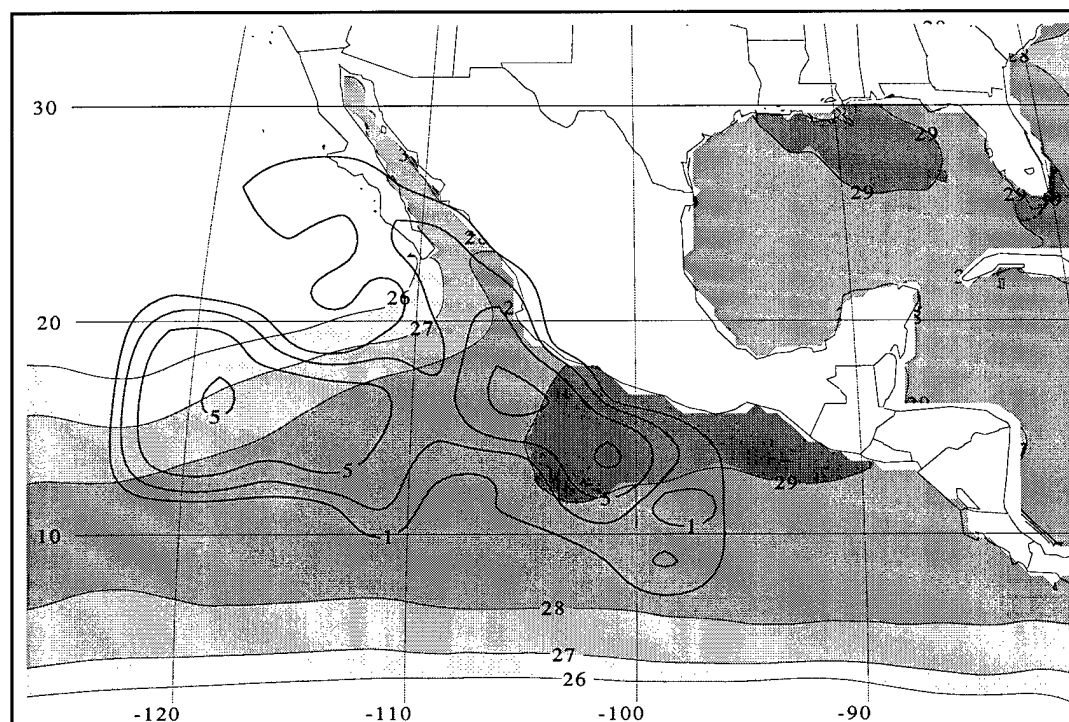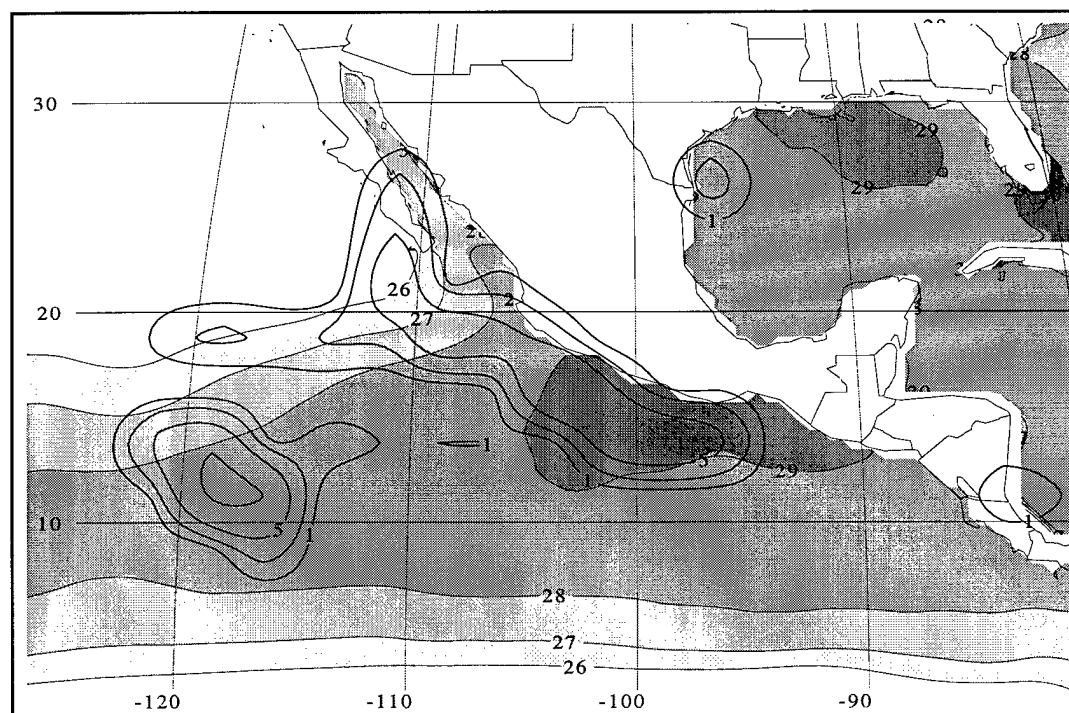
Figure 5.11.   Occurrence of all tropical storms and hurricanes in 2.5° x 2.5° grid boxes, based on 10 m AGL winds and mean SST for JJA 1993 for (a) MM5 and (b) observed. Cyclone contour intervals are 1, 2.5, 5, and every 10 thereafter with every other contour labeled. SST is contoured in 1 °C intervals and shaded for values of 26 °C and higher.
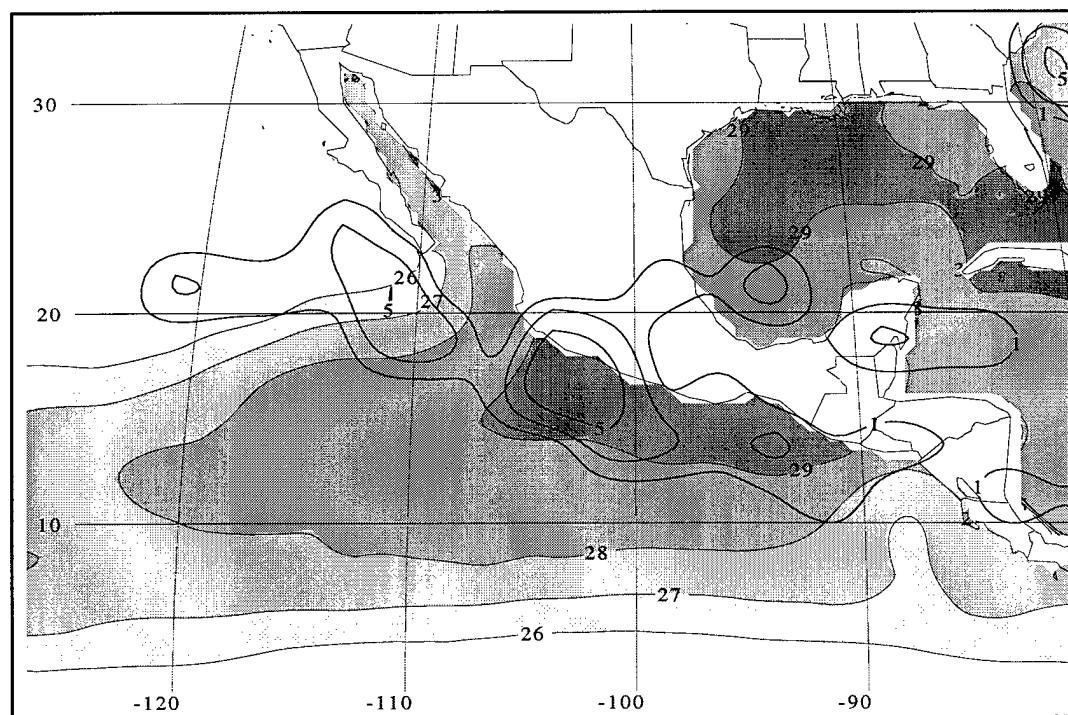
Figure 5.12.  Occurrence of all tropical storms and hurricanes in 2.5° x 2.5° grid boxes, based on 10 m AGL winds and mean SST for JJA 1994 for (a) MM5 and (b) observed. Cyclone contour intervals are 1, 2.5, 5, and every 10 thereafter with every other contour labeled. SST is contoured in 1 °C intervals and shaded for values of 26 °C and higher.
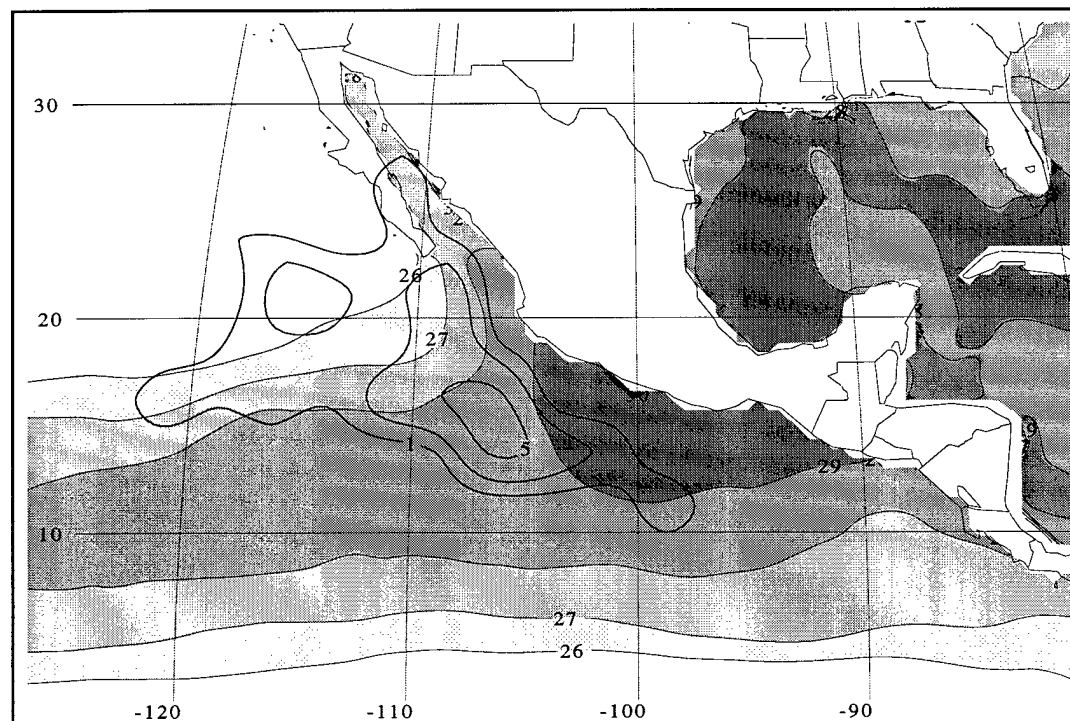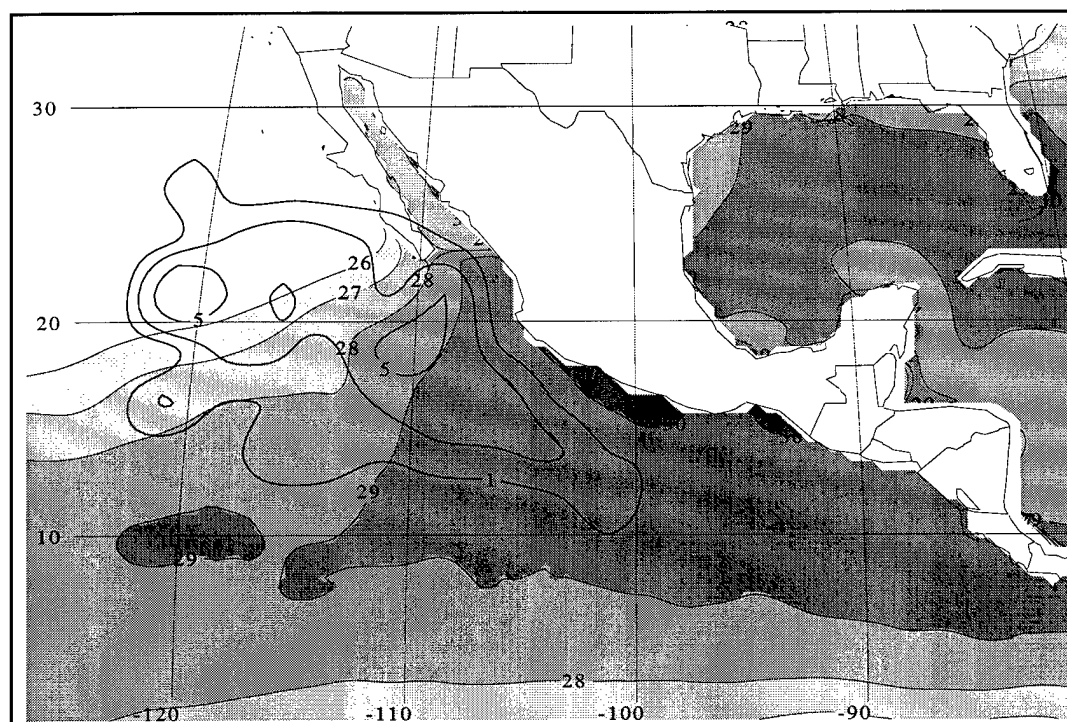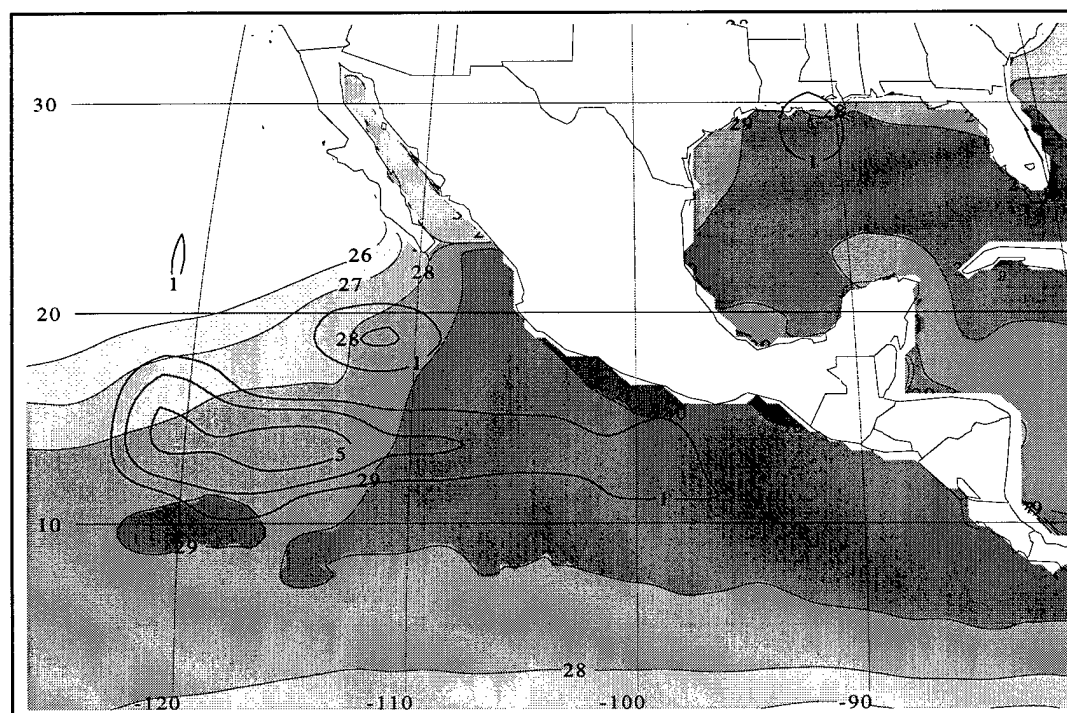
(a)
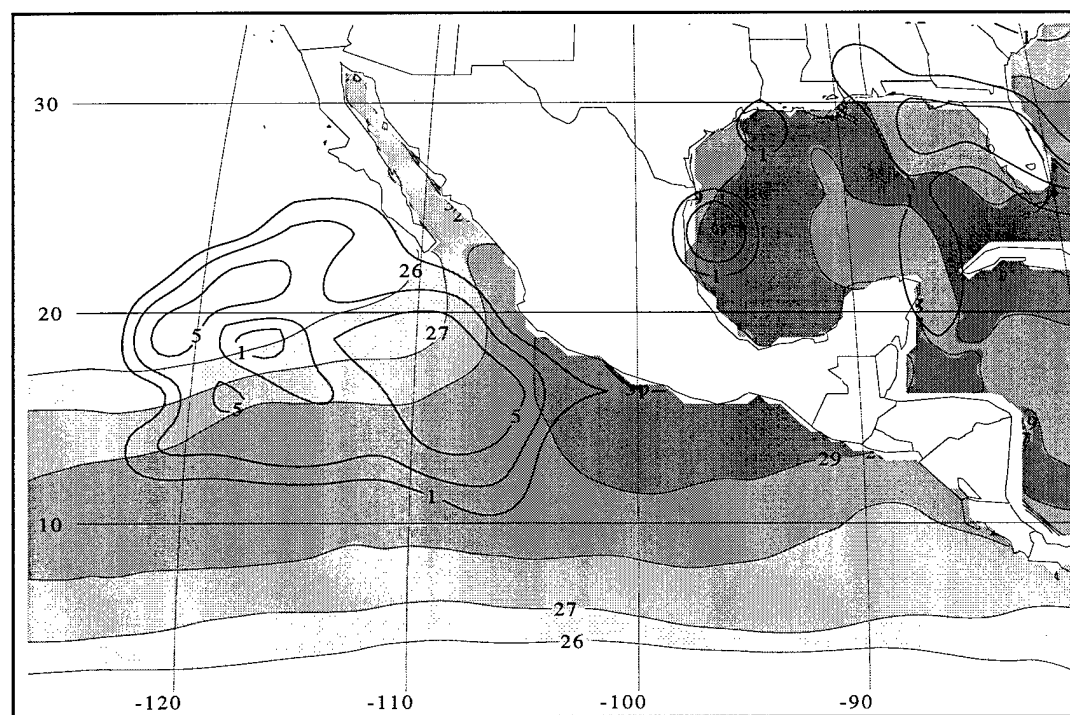


(b)

Figure 5.13.   Occurrence of all tropical storms and hurricanes in 2.5° x 2.5° grid boxes, based on 10 m AGL winds and mean SST for JJA 1995 for (a) MM5 and (b) observed. Cyclone contour intervals are 1, 2.5, 5, and every 10 thereafter with every other contour labeled. SST is contoured in 1 °C intervals and shaded for values of 26 °C and higher.

western boundary did not appear to play a role in the mature and decay stages of the simulated cyclones.

The 1996 modeled and observed cyclone distributions are shown in Figure 5.14. These storms had a tendency to form much closer to land than in previous years and to move to the northwest. This year is marked by below normal SST in the extreme Eastern Pacific (Figure D.7). There were double the amount of storms in the MM5 (14 vs. 7) than observed, but the duration was quite similar (3.6 days in the MM5 output vs. 3.3 in the observed). The number of actual storms in 1996 was the lowest for all of the years studied.

The simulated storm tracks deviate from those observed most significantly during 1997 (Figure 5.15) The observed storms, such as Hurricane Guillermo, tended to track westward while the simulated storms travelled more to the northwest where the SST was anomalously high. With the exception of Hurricane Guillermo, the storms during 1997 (both observed and modeled) tended to be less intense than during the other summers.
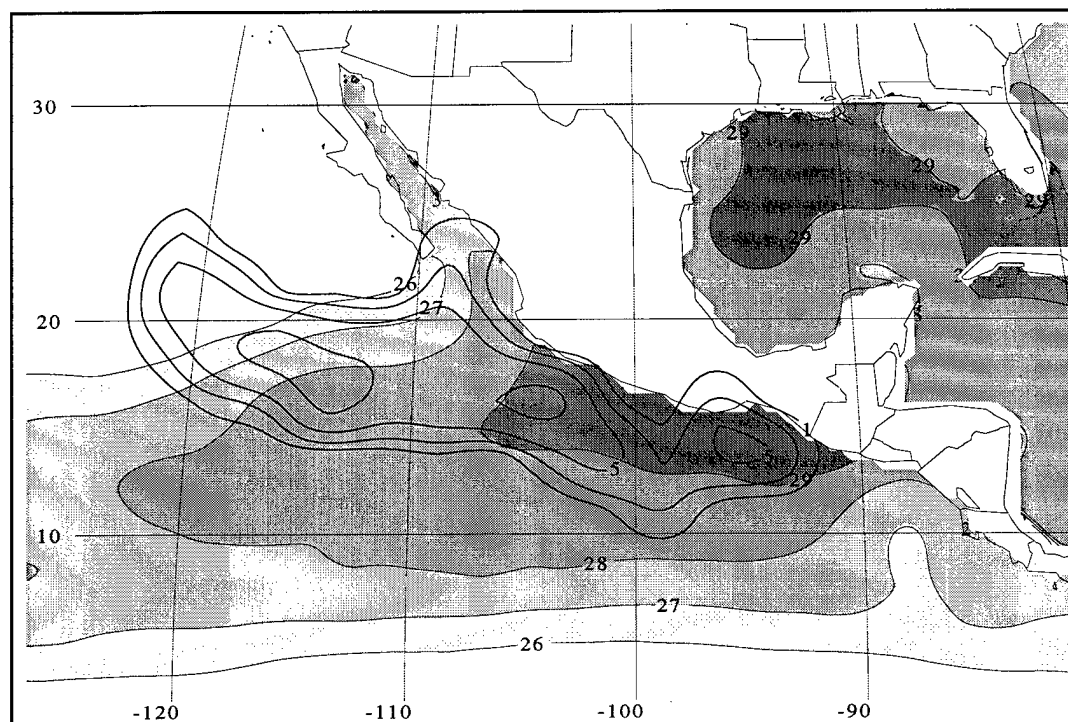
Figure 5.14.   Occurrence of all tropical storms and hurricanes in 2.5° x 2.5° grid boxes, based on 10 m AGL winds and mean SST for JJA 1996 for (a) MM5 and (b) observed. Cyclone contour intervals are 1, 2.5, 5, and every 10 thereafter with every other contour labeled. SST is contoured in 1 °C intervals and shaded for values of 26 °C and higher.

Figure 5.15.    Occurrence of all tropical storms and hurricanes in 2.5° x 2.5° grid boxes, based on 10 m AGL winds and mean SST for JJA 1997 for (a) MM5 and (b) observed. Cyclone contour intervals are 1, 2.5, 5, and every 10 thereafter with every other contour labeled. SST is contoured in 1 °C intervals and shaded for values of 26 °C and higher.

CHAPTER 6

SUMMARY AND CONCLUSIONS

GCMs have yielded a significant amount of information about the climate of the Eastern Pacific and adjacent regions, but they are unable to capture some important processes needed to understand the NAMS and eventually improve its predictability (Latif et al. 1998). A regional model was run for eight consecutive summer seasons (JJA) from 1990 to 1997. A distinguishing feature of these climate simulations is the high spatial resolution (50 km) and the relatively fine temporal resolution at which the model output is analyzed (3 h). The simulations are constrained by the observed evolution of SST and lateral boundary conditions imposed by the NCEP reanalyses.

The time-averaged circulation developed by the MM5 during the eight-year period was contrasted to that of the NCEP reanalyses during the same period. A stronger regional meridional circulation in the MM5 simulations was evident relative to that in the NCEP reanalyses as demonstrated by: heavier convection along the ITCZ; stronger southerly meridional flow across the cold tongue along the equator in the PBL; stronger northerly meridional flow in the upper troposphere; and stronger vertically integrated moisture flux into the ITCZ along its southern flank and stronger flux along the northern flank of the ITCZ.

The degree to which this more intense diabatically-forced circulation in the MM5 is realistic remains to be determined. The divergent component of the wind in the NCEP reanalyses are generally viewed to be too weak. However, the range of precipitation

estimates available for this region suggests that the precipitation rate developed by the MM5 in the ITCZ is well above the median estimate (Janowiak et al. 1995; Huffman et al. 1997; Xie and Arkin 1998).

Field programs during the next several years will provide observational data sets that can be used to validate numerical models of the PBL over the CTIC (Godfrey et al. 1998; McPhaden et al. 1998). The time-averaged boundary-layer circulation in the MM5 is consistent with the current conceptual model (Figure 1.4):

- low-level jet with peak winds near 950 mb,

- strong subsidence inversion over the cold tongue with the lowest inversion height slightly to the north of the equator; the breakdown of the strong inversion near 7° N during summer, and

- high LWC in the PBL associated with stratiform clouds.

An important question to be answered by this study was: "What additional information is provided by the regional climate simulations and what deficiencies require correction?". Care was taken to process the model output so that all temporal scales could be studied from diurnal to interannual variations. Trajectories computed every 3 h during the entire 8 years provide a means to assess actual air paths, even given the constraints of parameterized convective updrafts and the relatively large grid squares. These trajectories help to quantify, for example, what fraction of the air parcels in the ITCZ cross the cold tongue versus those that are advected by the trade winds in the Northern Hemisphere.

The diurnal variations in precipitation in the MM5 are consistent with those analyzed from convective cloud frequencies. These variations are tied to diurnal land/sea

and mountain/valley circulations in the near-surface wind field that are handled relatively crudely at 50 km, but are also consistent with observations.

The MM5 simulations provide considerable spatial detail over land compared to the NCEP reanalyses or GCM simulations. Many of the features of the Mexican monsoon are captured, including the northward progression of rainfall into Arizona and New Mexico and the inland precipitation maxima on the western slopes of the Sierra Madre Occidental of Mexico.

The time-averaged changes from month to month provide further information on the onset and evolution of the NAMS during the peak of the summer season. The westward shift of convection along the ITCZ provides a large-scale context for the mid-summer drought observed over southern Mexico and Central America during July. Greater moisture flux through the ITCZ is evident in July that weakens by August. Periods of increased precipitation are related to enhanced moisture flux convergence, reduced stability, and other dynamical processes rather than being related to increases in local SST.

Each of the eight years differed significantly from one another. However, the planetary-scale changes associated with the 1997 ENSO, such as the collapse of the equatorial cold tongue with little gradient in SST from the equator to 20° N, led to the most unusual conditions during this period. Aspects of the differences simulated during summer 1997 compared to the other years include:

- a deeper boundary layer over the cold tongue with less stratiform clouds and greater convection and

- a southward displacement of the ITCZ with weaker southerly cross-equatorial flow.

Simulation of tropical cyclones is a challenge for any climate model. The structure of the simulated cyclones is adequate in the MM5, given the limitation of the 50 km grid resolution. The statistics on the occurrence of simulated tropical cyclones depend somewhat on the criteria used. Note, however, GCMs have been even less successful at simulating cyclones realistically in this region, and have been shown to underforecast the number of cyclones in this region by as much as a factor of three (Bengtsson et al. 1995; Vitart et al. 1997). The MM5 tends to generate weaker and more frequent cyclones than those observed, but the numbers of cyclones are on the same order as those observed.

The genesis region of the tropical cyclones in the eastern Pacific Ocean between 90° W and 105° W corresponds to that observed and reflects, in some cases, amplification of easterly waves that propagate into the model domain through the eastern boundary. In situ development is favored by the cyclonic absolute vorticity in the basic state resulting from the low-level southwesterly flow to the south of 12° N and low-level easterly flow to the north of 14° N that is further enhanced by the orientation of the coastlines and gaps in the mountains of southern Mexico and Central America. The northward shift of the model's ITCZ may help generate more tropical cyclones than observed by amplifying the cyclonic shear of the mean flow. The simulated cyclones tend to follow a preferred west-northwest track while the observed cyclones tend to prefer either northwesterly or westerly paths.

The lack of feedback from the atmosphere to the ocean as the cyclones travel may also help to explain the excessive number of tropical cyclones generated by the model. The lack of expected cooling in SST (Nelson 1998) implies that conditions remain favorable for cyclone genesis even after a cyclone passage. The western lateral boundary

condition near 125° W clearly affects the mature and decaying phase of many cyclones. Inconsistencies between the lateral boundary and interior flow cause cyclones to spin near the boundary until they eventually weaken. The close proximity of the eastern boundary and the lack of strong instabilities or hurricanes (such as Hurricane Andrew during 1992) entering the domain through the boundary lead to limited development of cyclones in the Gulf of Mexico.

The most serious deficiency of the model related to tropical cyclones may be the inability to simulate the correct year-to-year variations in tropical cyclone frequency and duration. Eventually, it may become practical to embed regional models within coupled atmosphere-ocean GCMs that provide monthly or seasonal forecasts. The regional model would be expected to provide more accurate forecasts of the frequency of occurrence of mesoscale phenomena such as tropical cyclones. The coupled GCM will not be perfect and deficiencies in many aspects of the regional climate would be input to the regional model on the lower and lateral boundaries. The simulations performed here can be viewed as an idealized experiment in which perfect SST and perfect lateral boundary conditions are available. However, the variations in the total number of simulated cyclones from year-to-year do not match those observed. Further work is required to assess which techniques may be required to resolve this problem. Options include using an ensemble of regional simulations, higher horizontal resolution, or a nested atmosphere-ocean model on the mesoscale.

APPENDIX A

PRECIPITATION
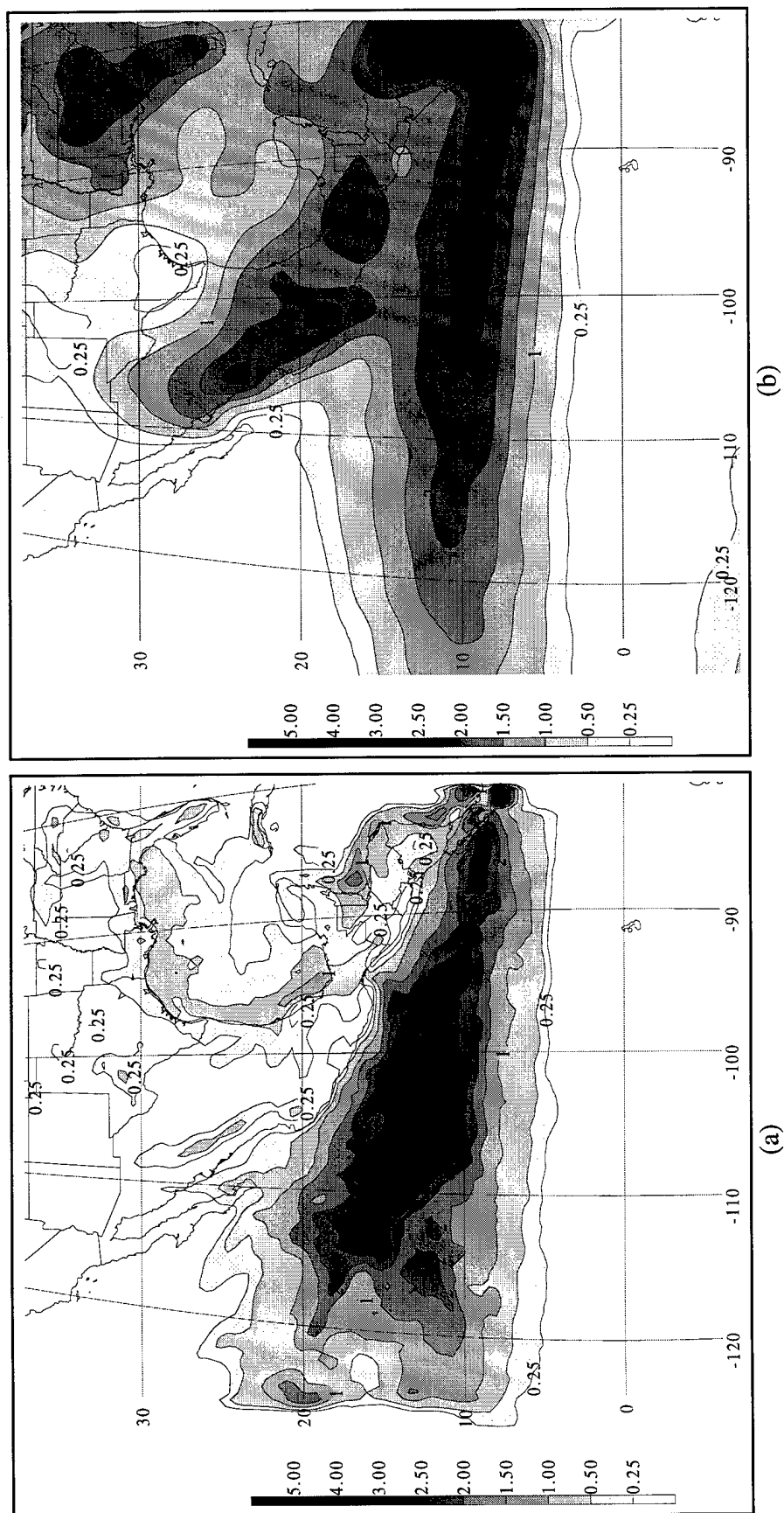
Figure A.1. Precipitation rate in cm day⁻¹ for JJA 1990 for (a) MM5 and (b) NCEP. Values over 0.25 cm day⁻¹ are shaded according to the scale on the left. Contour intervals are 0.25, 0.5, 1, 1.5, 2, 2.5, 3, 4, and 5 cm day⁻¹ with every other contour labeled.
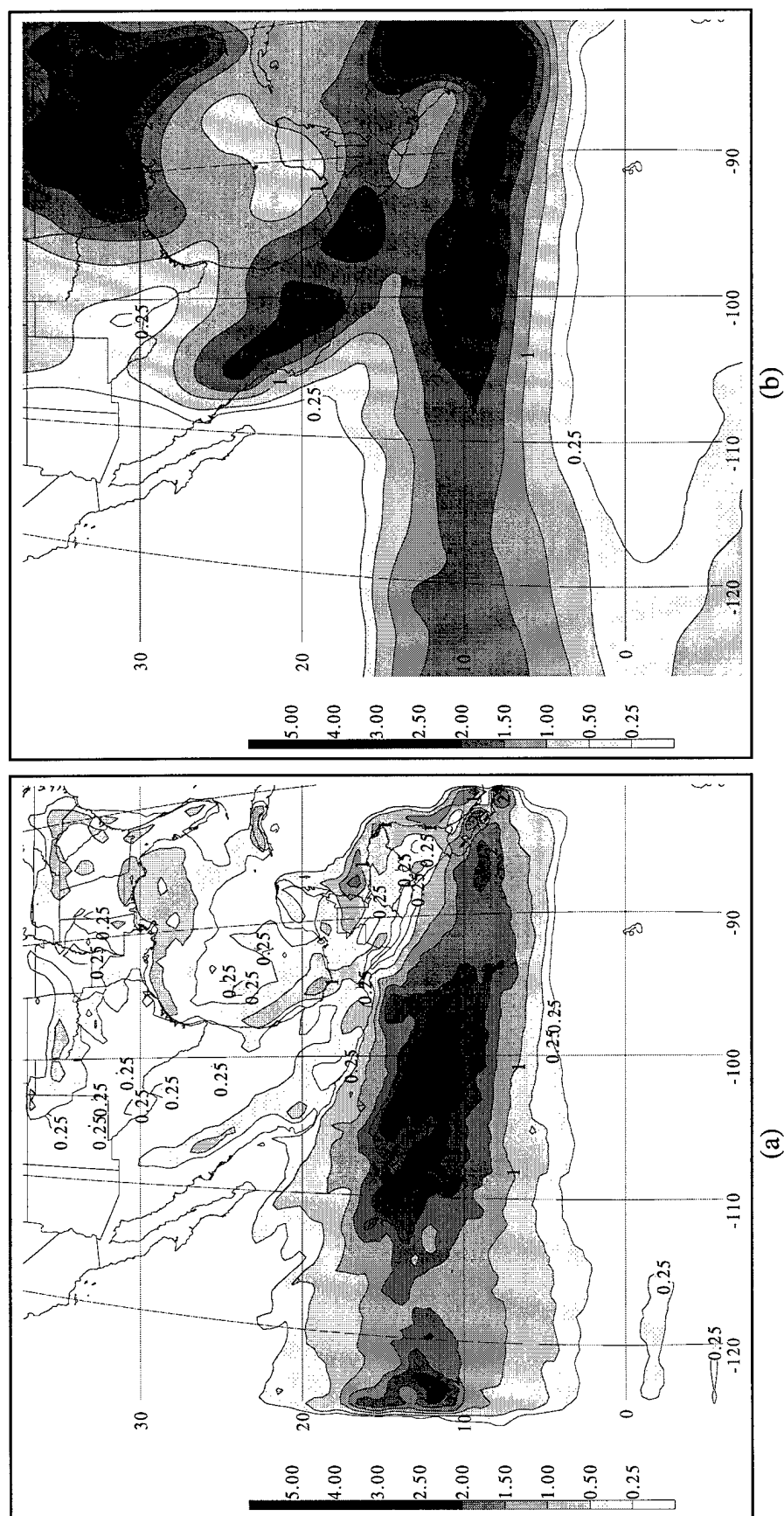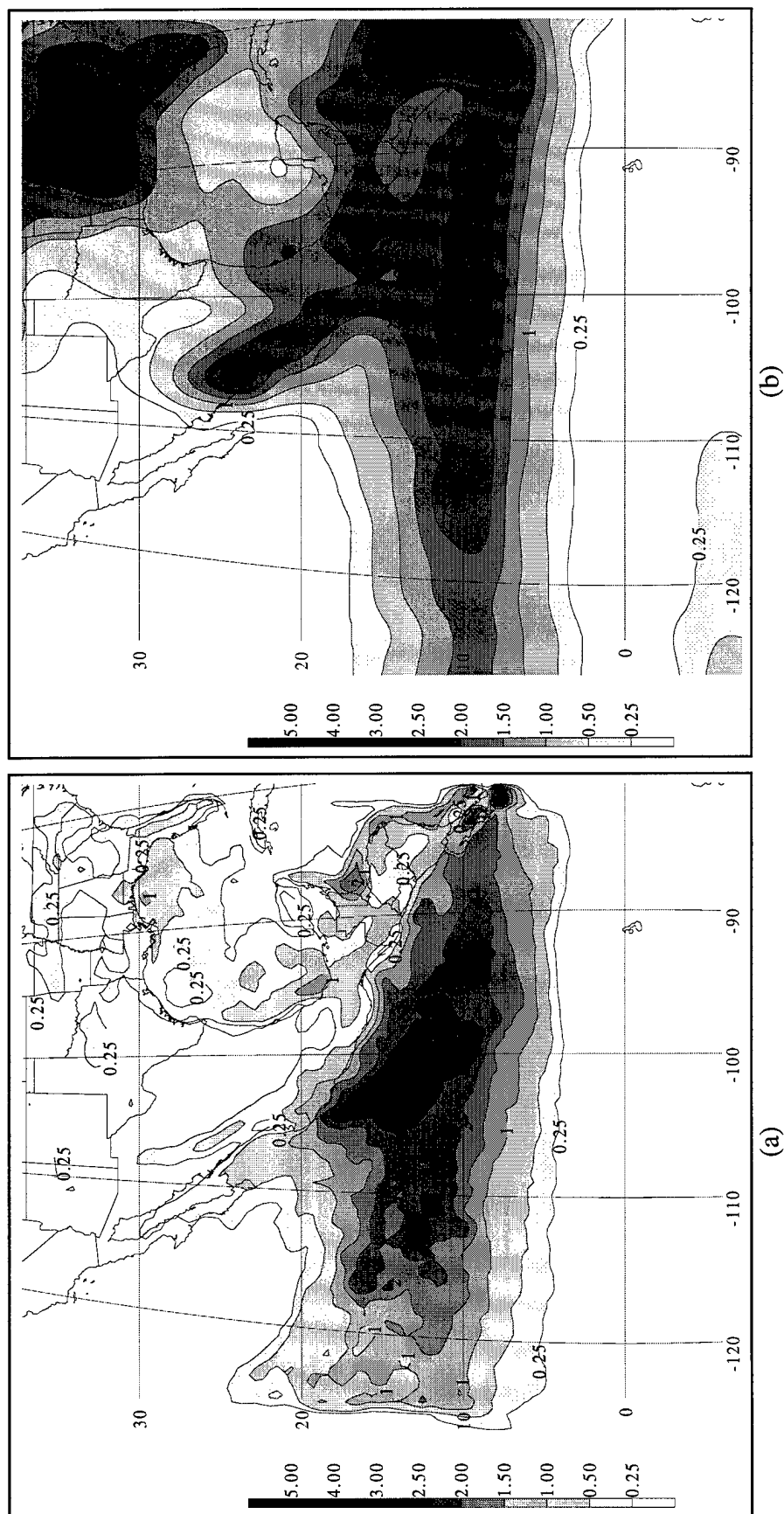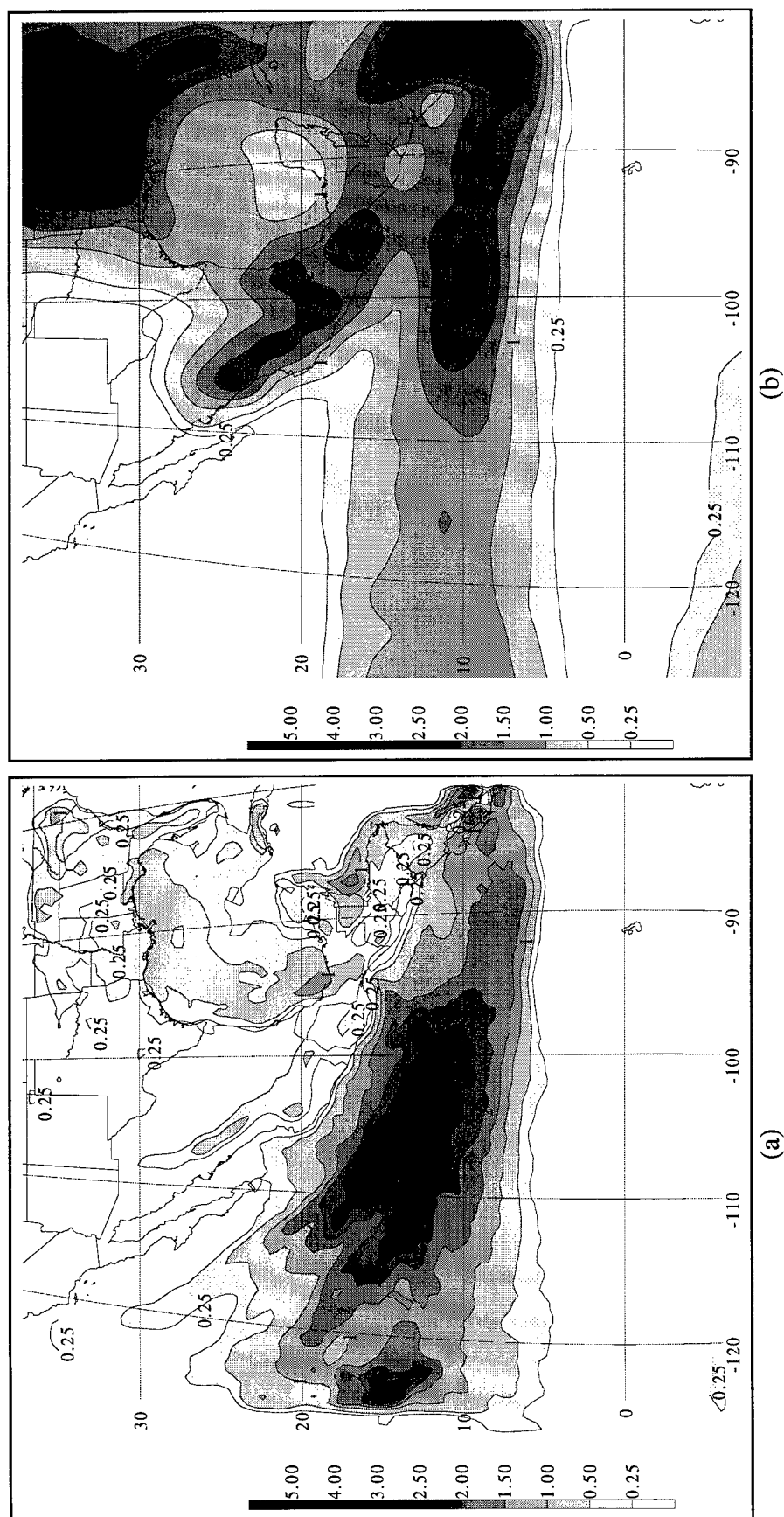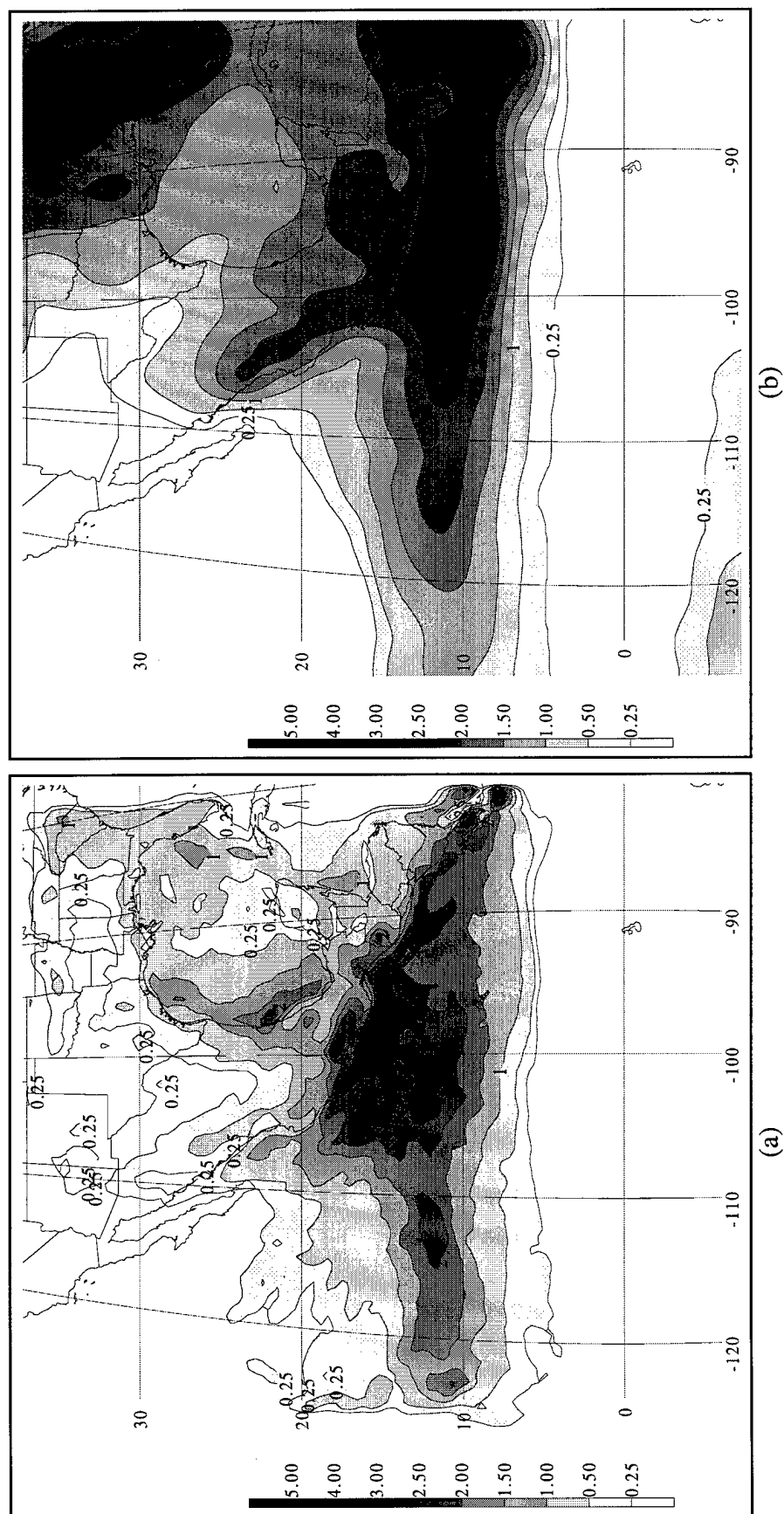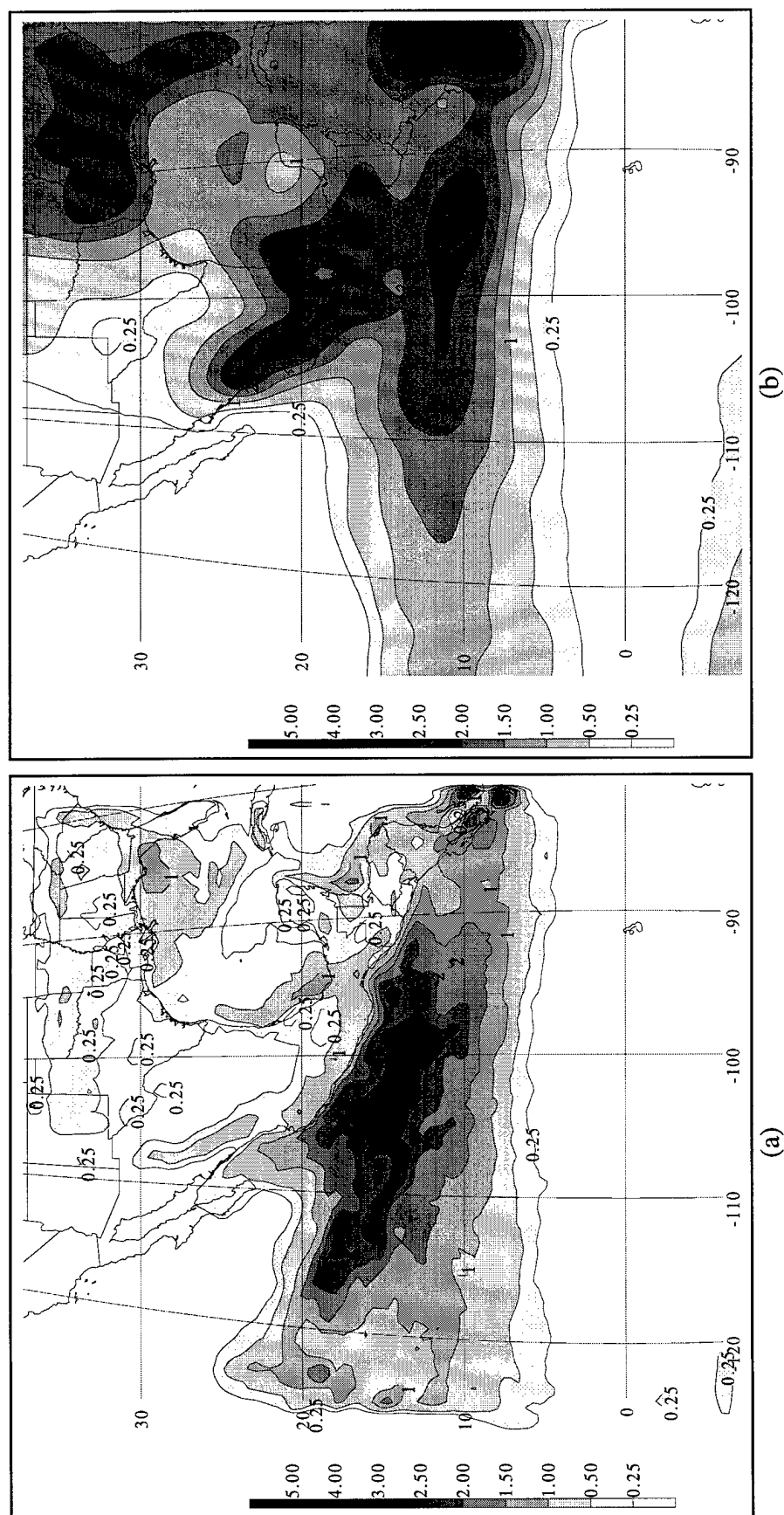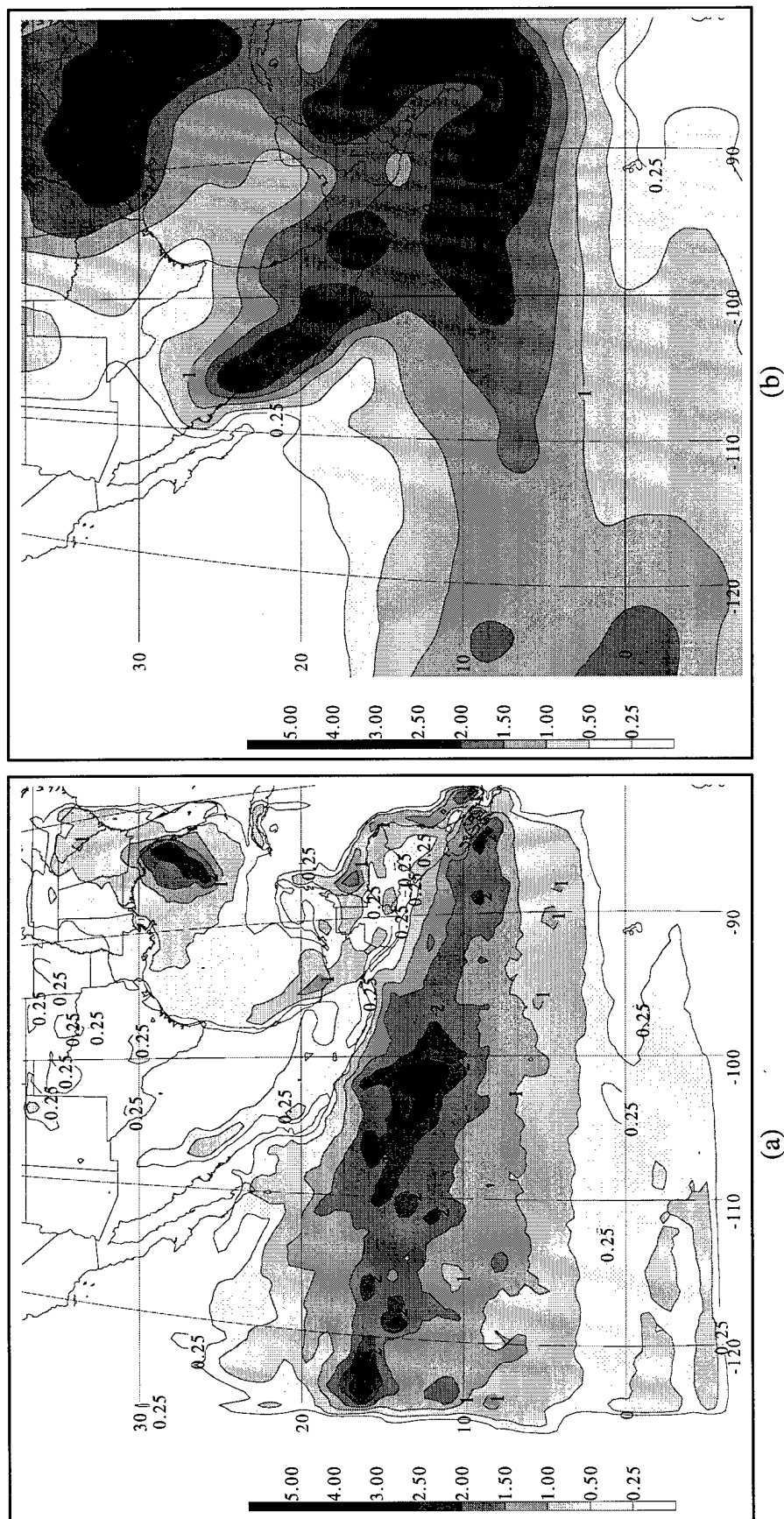
Figure A.2.  Precipitation rate in cm day⁻¹ for JJA 1991 for (a) MM5 and (b) NCEP. Values over 0.25 cm day⁻¹ are shaded according to the scale on the left. Contour intervals are 0.25, 0.5, 1, 1.5, 2, 2.5, 3, 4, and 5 cm day⁻¹ with every other contour labeled.
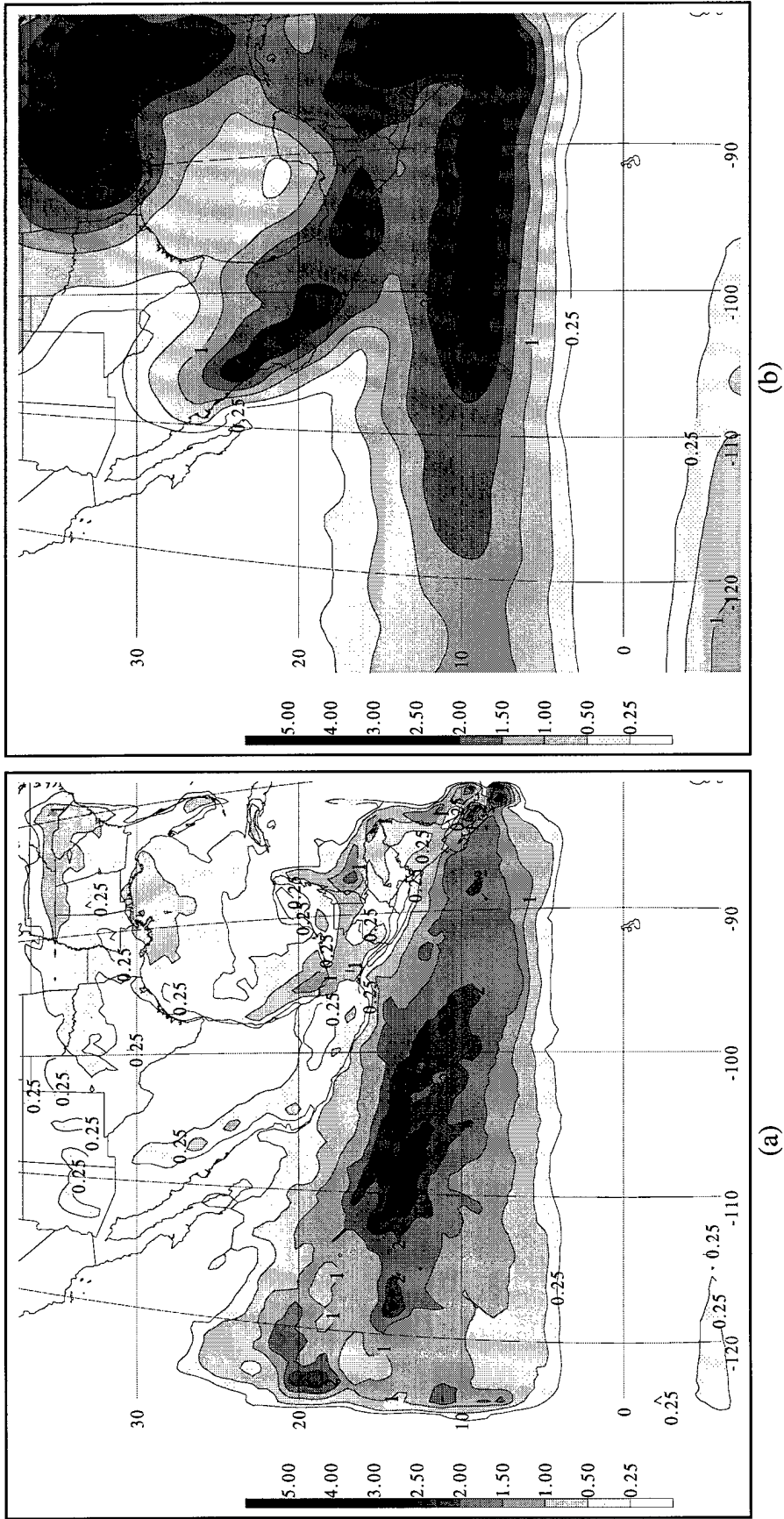
Figure A.3.    Precipitation rate in cm day$^{-1}$ for JJA 1992 for (a) MM5 and (b) NCEP. Values over 0.25 cm day$^{-1}$ are shaded according to the scale on the left. Contour intervals are 0.25, 0.5, 1, 1.5, 2, 2.5, 3, 4, and 5 cm day$^{-1}$ with every other contour labeled.

(a)                                    (b)

Figure A.4.    Precipitation rate in cm day⁻¹ for JJA 1993 for (a) MM5 and (b) NCEP. Values over 0.25 cm day⁻¹ are shaded according to the scale on the left. Contour intervals are 0.25, 0.5, 1, 1.5, 2, 2.5, 3, 4, and 5 cm day⁻¹ with every other contour labeled.

Figure A.5.  Precipitation rate in cm day⁻¹ for JJA 1994 for (a) MM5 and (b) NCEP. Values over 0.25 cm day⁻¹ are shaded according to the scale on the left. Contour intervals are 0.25, 0.5, 1, 1.5, 2, 2.5, 3, 4, and 5 cm day⁻¹ with every other contour labeled.

Figure A.6.    Precipitation rate in cm day⁻¹ for JJA 1995 for (a) MM5 and (b) NCEP. Values over 0.25 cm day⁻¹ are shaded according to the scale on the left. Contour intervals are 0.25, 0.5, 1, 1.5, 2, 2.5, 3, 4, and 5 cm day⁻¹ with every other contour labeled.

Figure A.7.   Precipitation rate in cm day$^{-1}$ for JJA 1996 for (a) MM5 and (b) NCEP. Values over 0.25 cm day$^{-1}$ are shaded according to the scale on the left. Contour intervals are 0.25, 0.5, 1, 1.5, 2, 2.5, 3, 4, and 5 cm day$^{-1}$ with every other contour labeled.

(b)

(a)

Figure A.8.    Precipitation rate in cm day⁻¹ for JJA 1997 for (a) MM5 and (b) NCEP. Values over 0.25 cm day⁻¹ are shaded according to the scale on the left. Contour intervals are 0.25, 0.5, 1, 1.5, 2, 2.5, 3, 4, and 5 cm day⁻¹ with every other contour labeled.

APPENDIX B


SURFACE WIND AND PRECIPITATION ANOMALIES

(a)

(b)
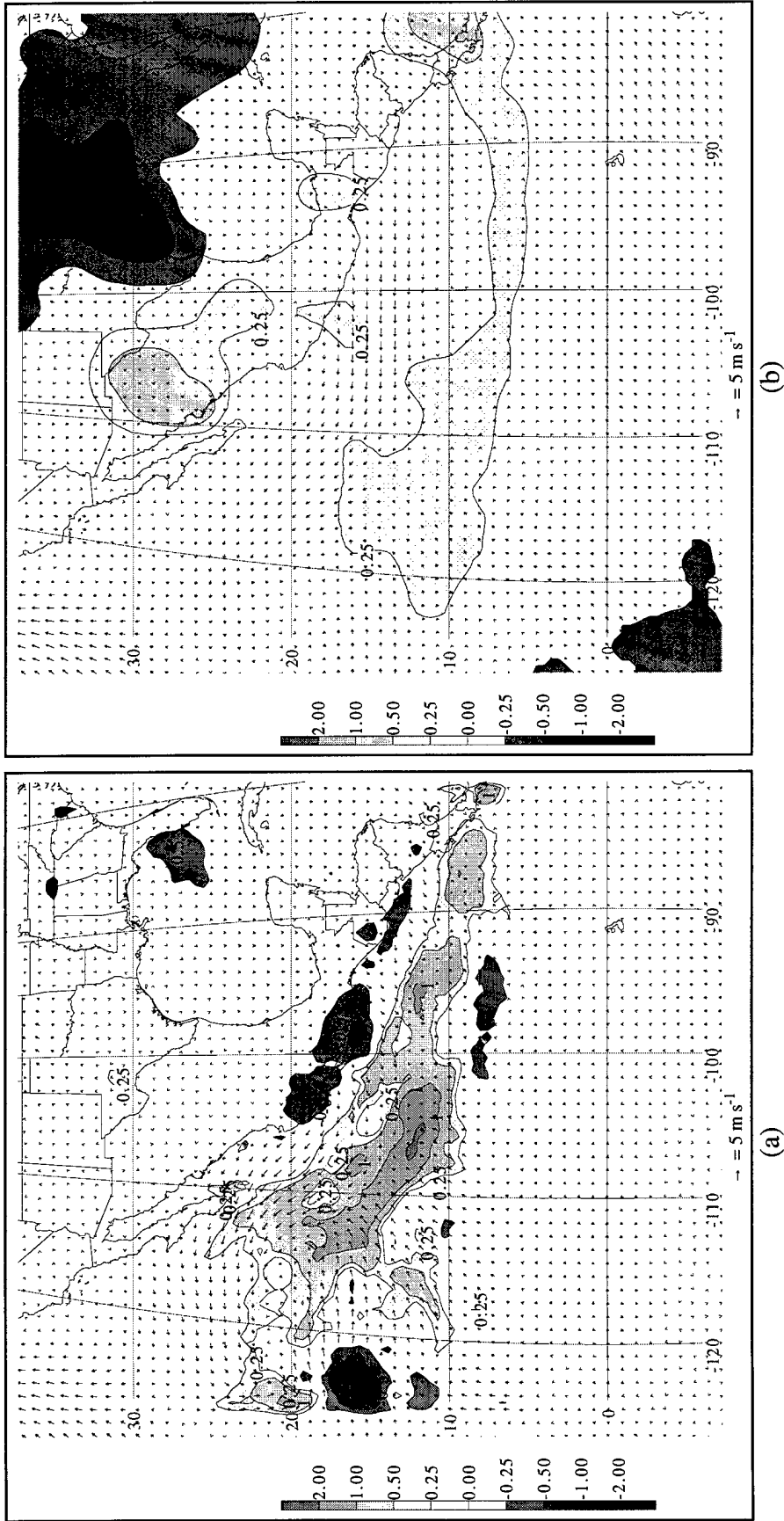
Figure B.1.   10 m wind anomalies in m s^{-1} and precipitation rate anomalies in cm day^{-1} for JJA 1990 for (a) MM5 and (b) NCEP. Values ≥ 0.25 and ≤ -0.25 cm day^{-1} are shaded according to the scale on the left. Contour intervals are ±0.25 and ±0.5 cm day^{-1} thereafter.
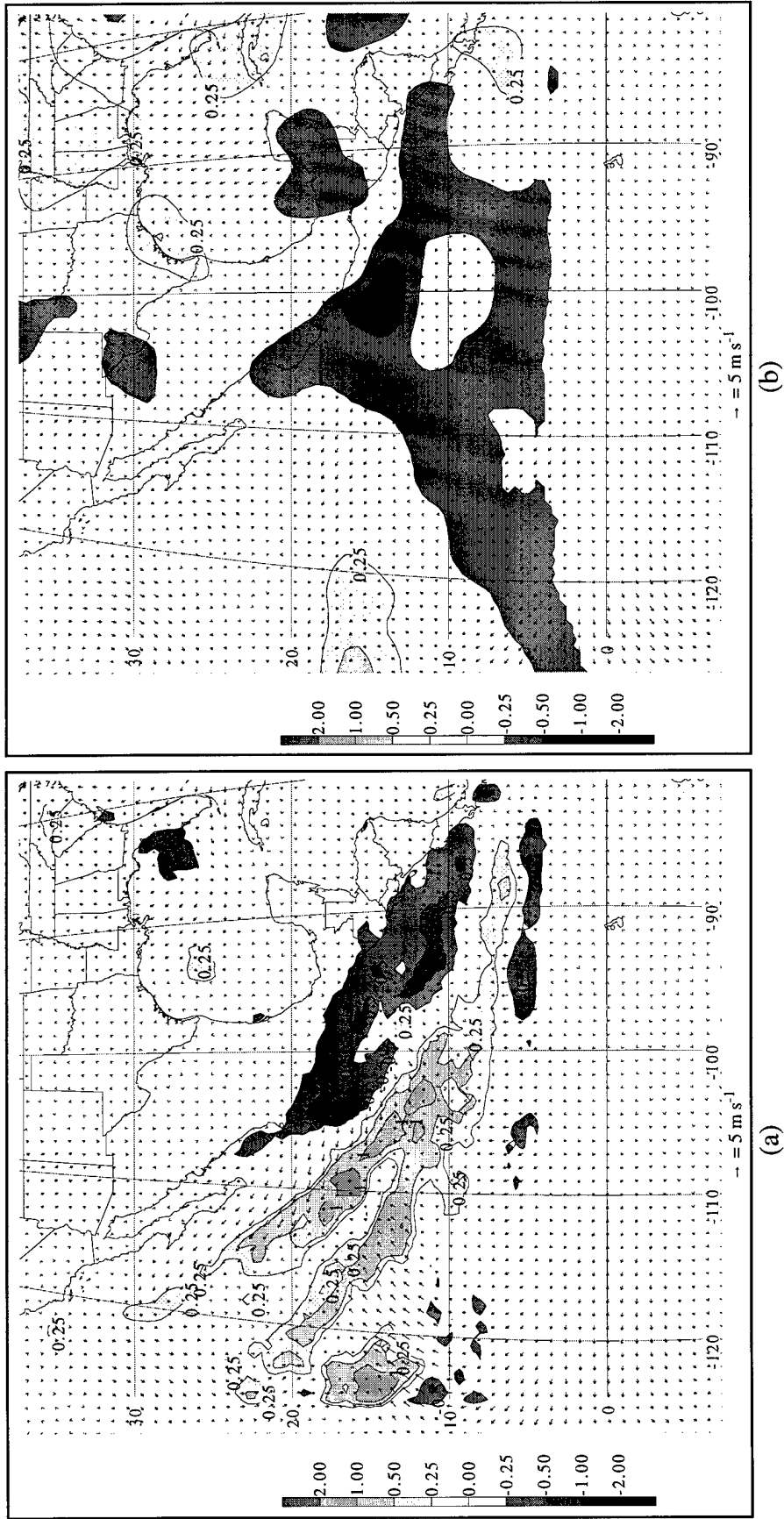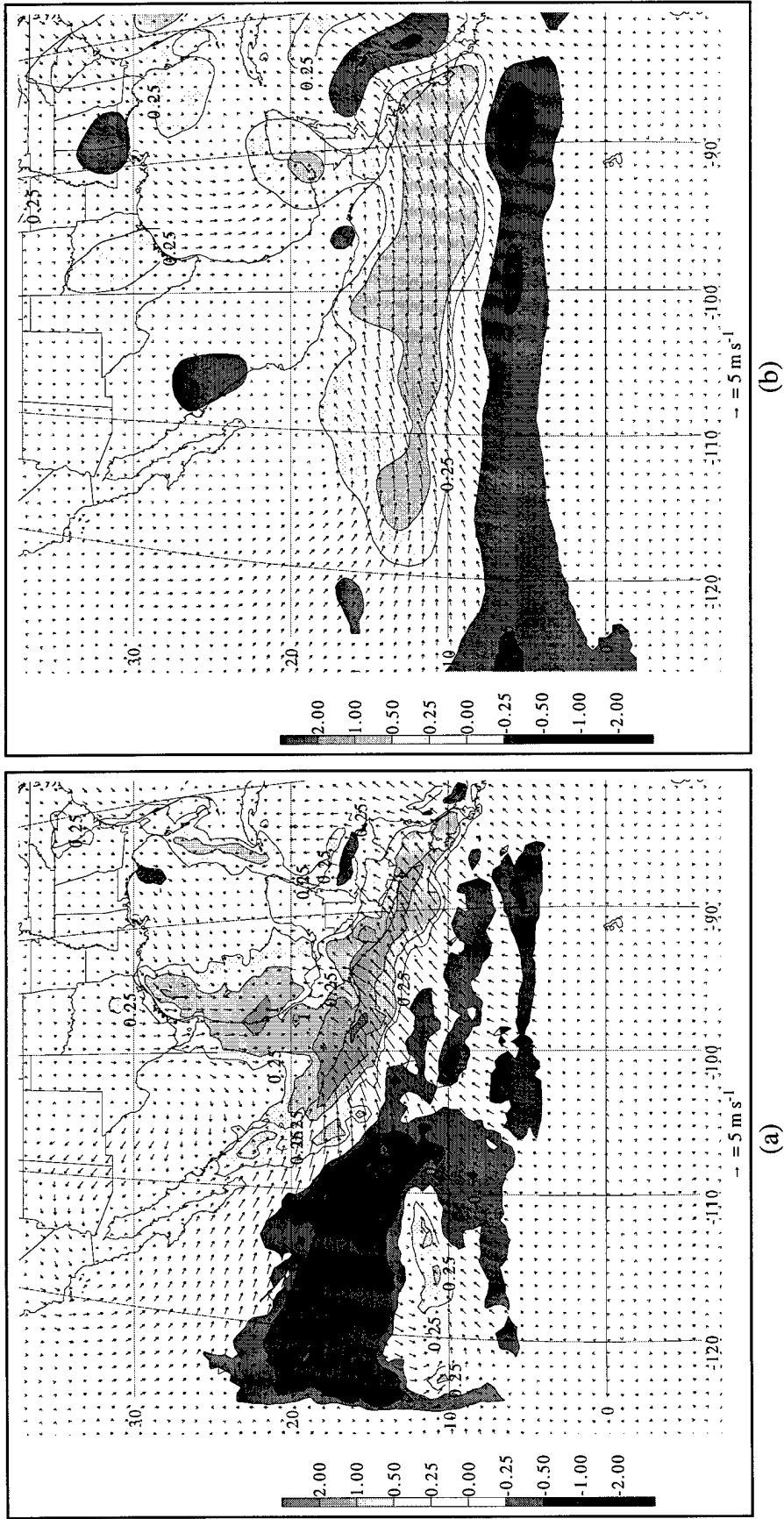
(a)

(b)
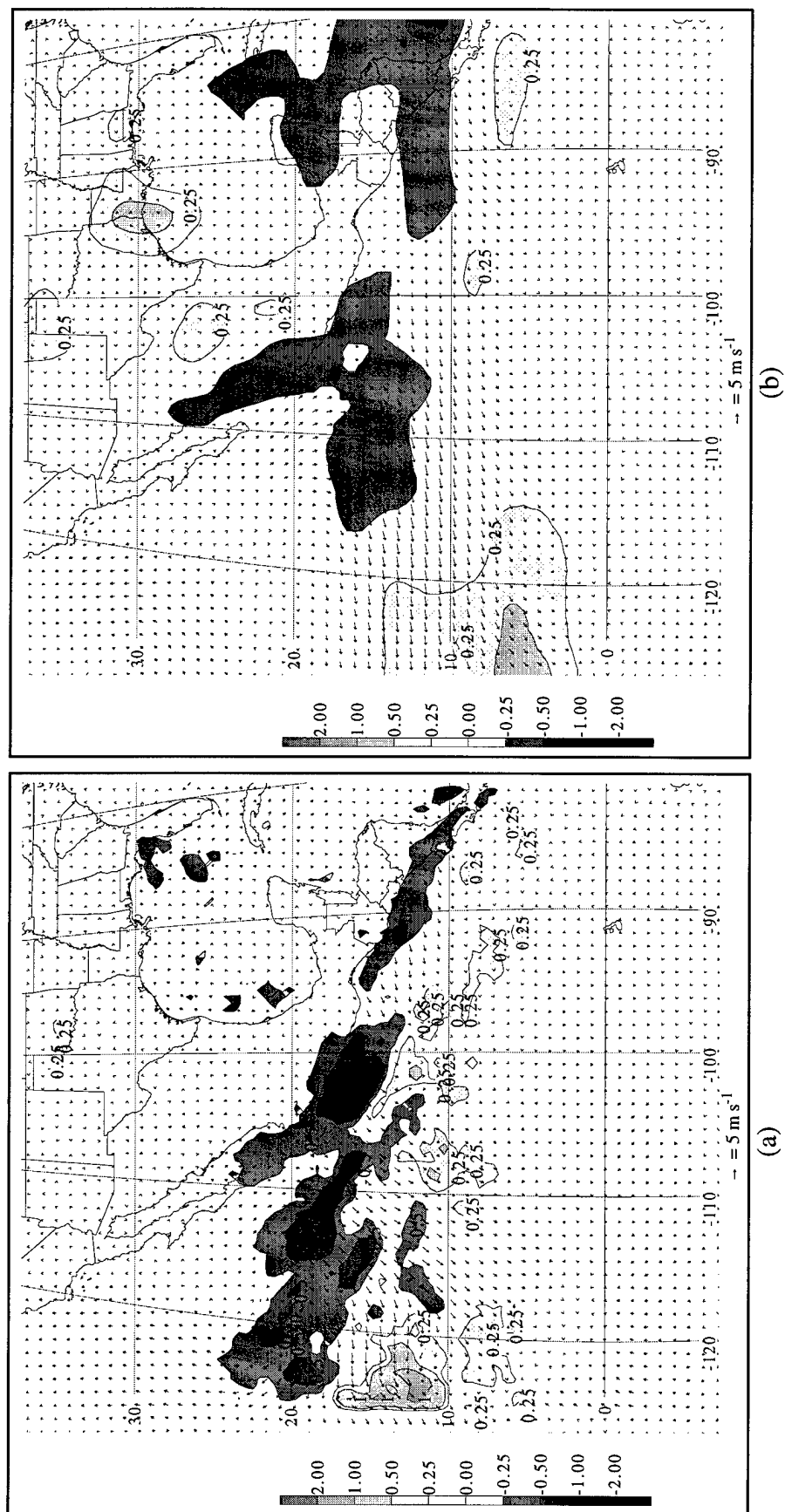
Figure B.2.    10 m wind anomalies in m s⁻¹ and precipitation rate anomalies in cm day⁻¹ for JJA 1991 for (a) MM5 and (b) NCEP. Values ≥ 0.25 and ≤ -0.25 cm day⁻¹ are shaded according to the scale on the left. Contour intervals are ±0.25 and ±0.5 cm day⁻¹ thereafter.
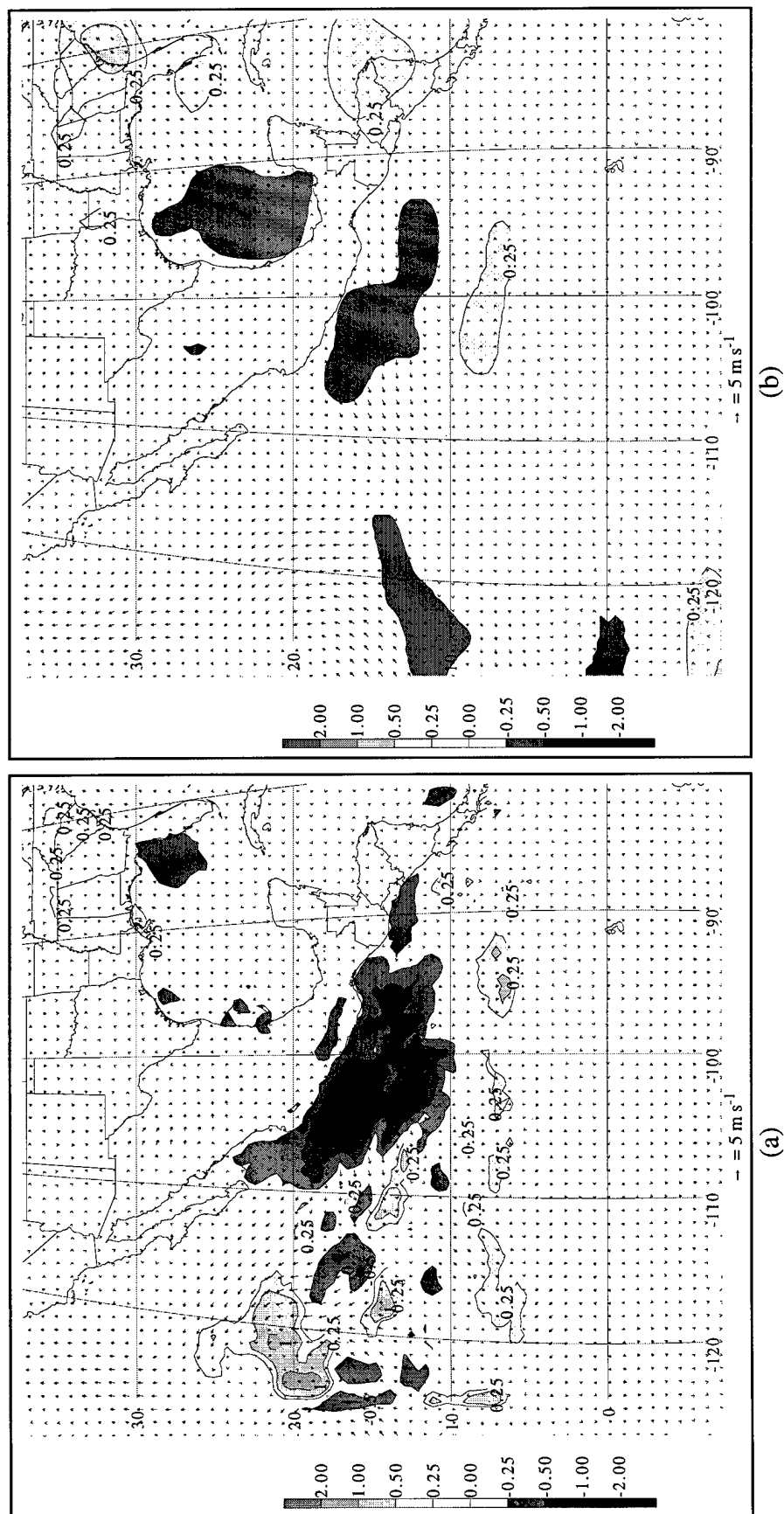
Figure B.3.    10 m wind anomalies in m s⁻¹ and precipitation rate anomalies in cm day⁻¹ for JJA 1992 for (a) MM5 and (b) NCEP. Values ≥ 0.25 and ≤ -0.25 cm day⁻¹ are shaded according to the scale on the left. Contour intervals are ±0.25 and ±0.5 cm day⁻¹ thereafter.
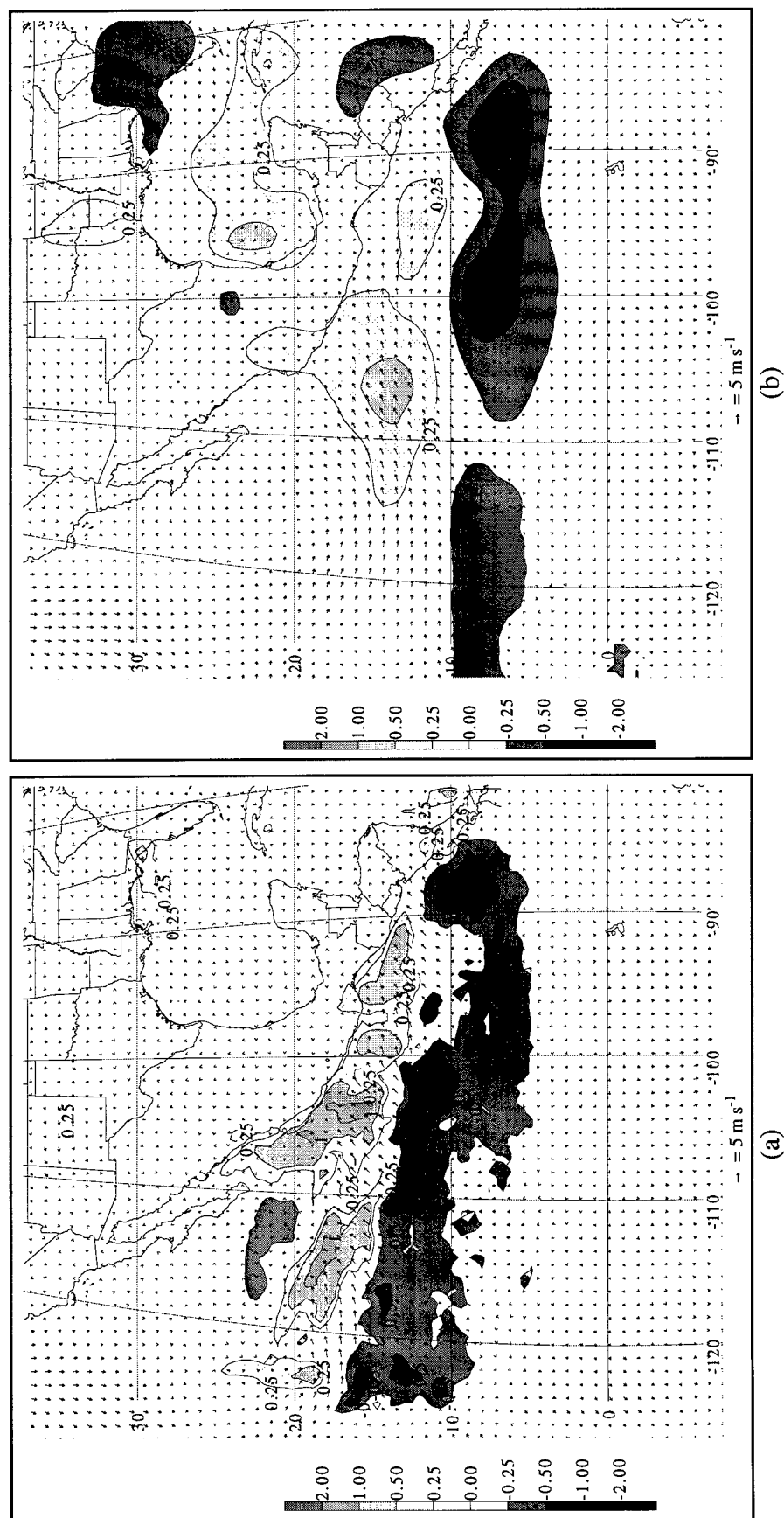
(b)

(a)
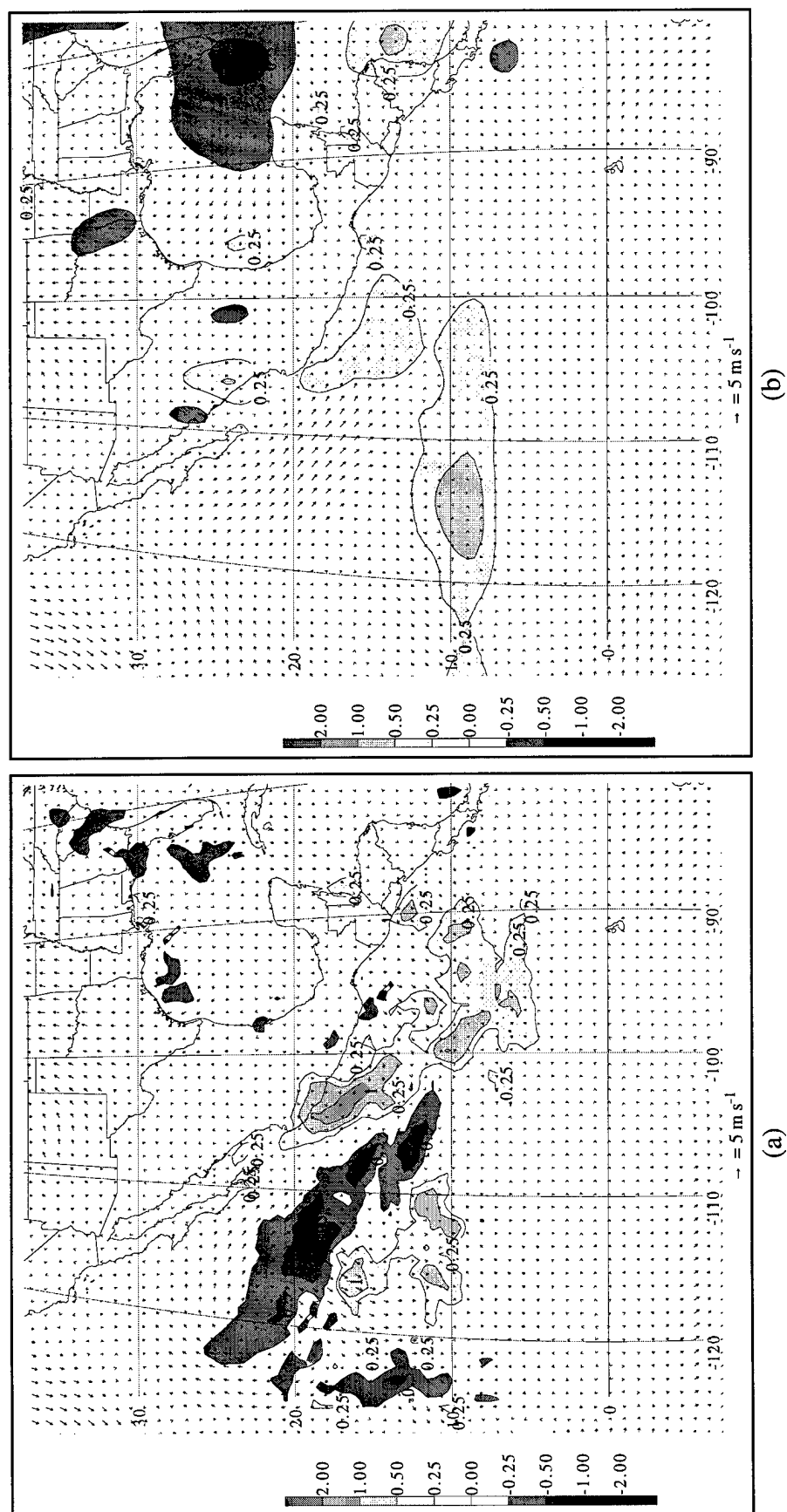
Figure B.4. 10 m wind anomalies in m s⁻¹ and precipitation rate anomalies in cm day⁻¹ for JJA 1993 for (a) MM5 and (b) NCEP. Values ≥ 0.25 and ≤ -0.25 cm day⁻¹ are shaded according to the scale on the left. Contour intervals are ±0.25 and ±0.5 cm day⁻¹ thereafter.
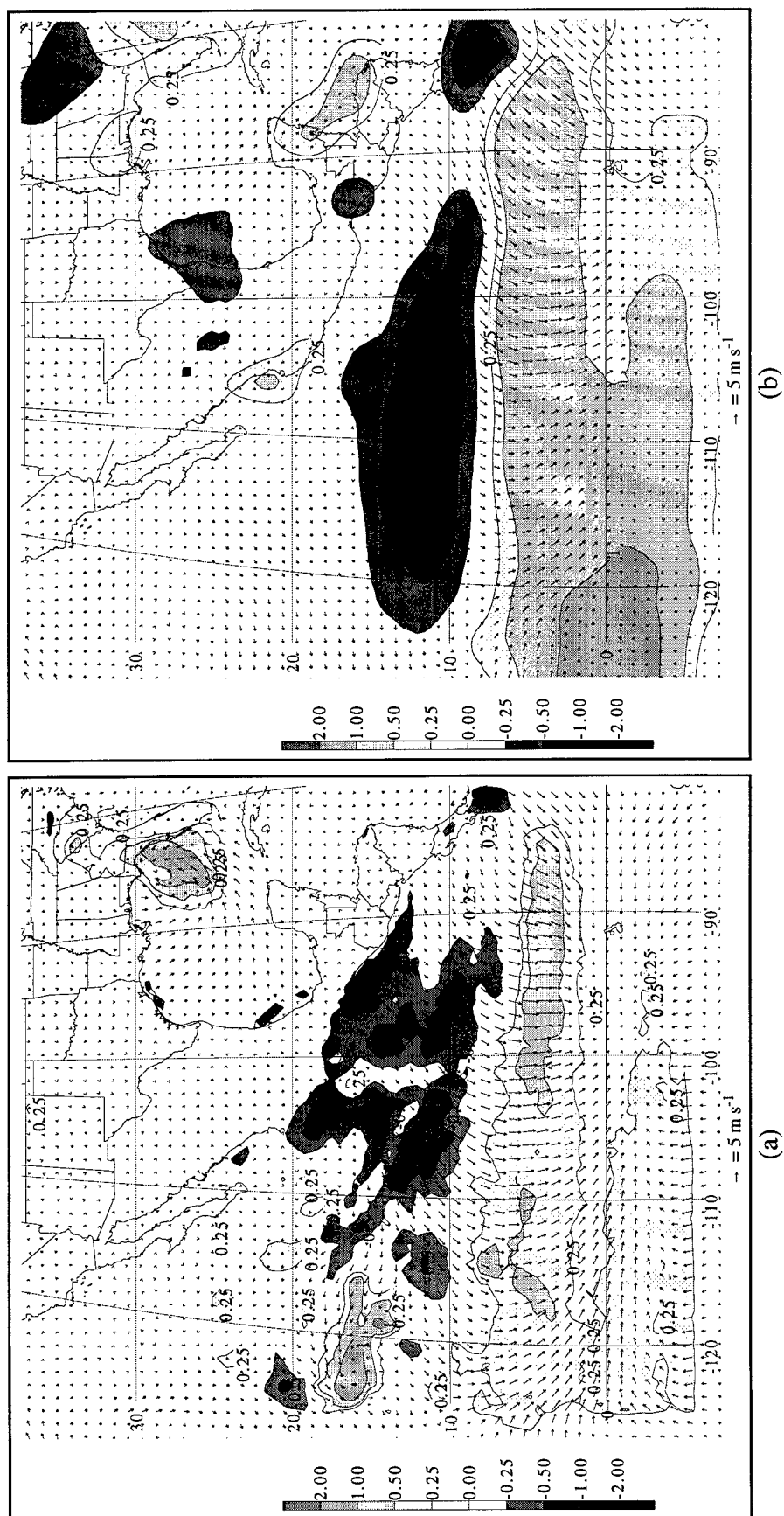
Figure B.5. 10 m wind anomalies in m s⁻¹ and precipitation rate anomalies in cm day⁻¹ for JJA 1994 for (a) MM5 and (b) NCEP. Values ≥ 0.25 and ≤ -0.25 cm day⁻¹ are shaded according to the scale on the left. Contour intervals are ±0.25 and ±0.5 cm day⁻¹ thereafter.

(b)

(a)

Figure B.6.    10 m wind anomalies in m s⁻¹ and precipitation rate anomalies in cm day⁻¹ for JJA 1995 for (a) MM5 and (b) NCEP. Values ≥ 0.25 and ≤ -0.25 cm day⁻¹ are shaded according to the scale on the left. Contour intervals are ±0.25 and ±0.5 cm day⁻¹ thereafter.

Figure B.7. 10 m wind anomalies in m s$^{-1}$ and precipitation rate anomalies in cm day$^{-1}$ for JJA 1996 for (a) MM5 and (b) NCEP. Values ≥ 0.25 and ≤ -0.25 cm day$^{-1}$ are shaded according to the scale on the left. Contour intervals are ±0.25 and ±0.5 cm day$^{-1}$ thereafter.

(b)

(a)

Figure B.8.   10 m wind anomalies in m s⁻¹ and precipitation rate anomalies in cm day⁻¹ for JJA 1997 for (a) MM5 and (b) NCEP. Values ≥ 0.25 and ≤ -0.25 cm day⁻¹ are shaded according to the scale on the left. Contour intervals are ±0.25 and ±0.5 cm day⁻¹ thereafter.

APPENDIX C


UPPER-TROPOSPHERIC WIND ANOMALIES
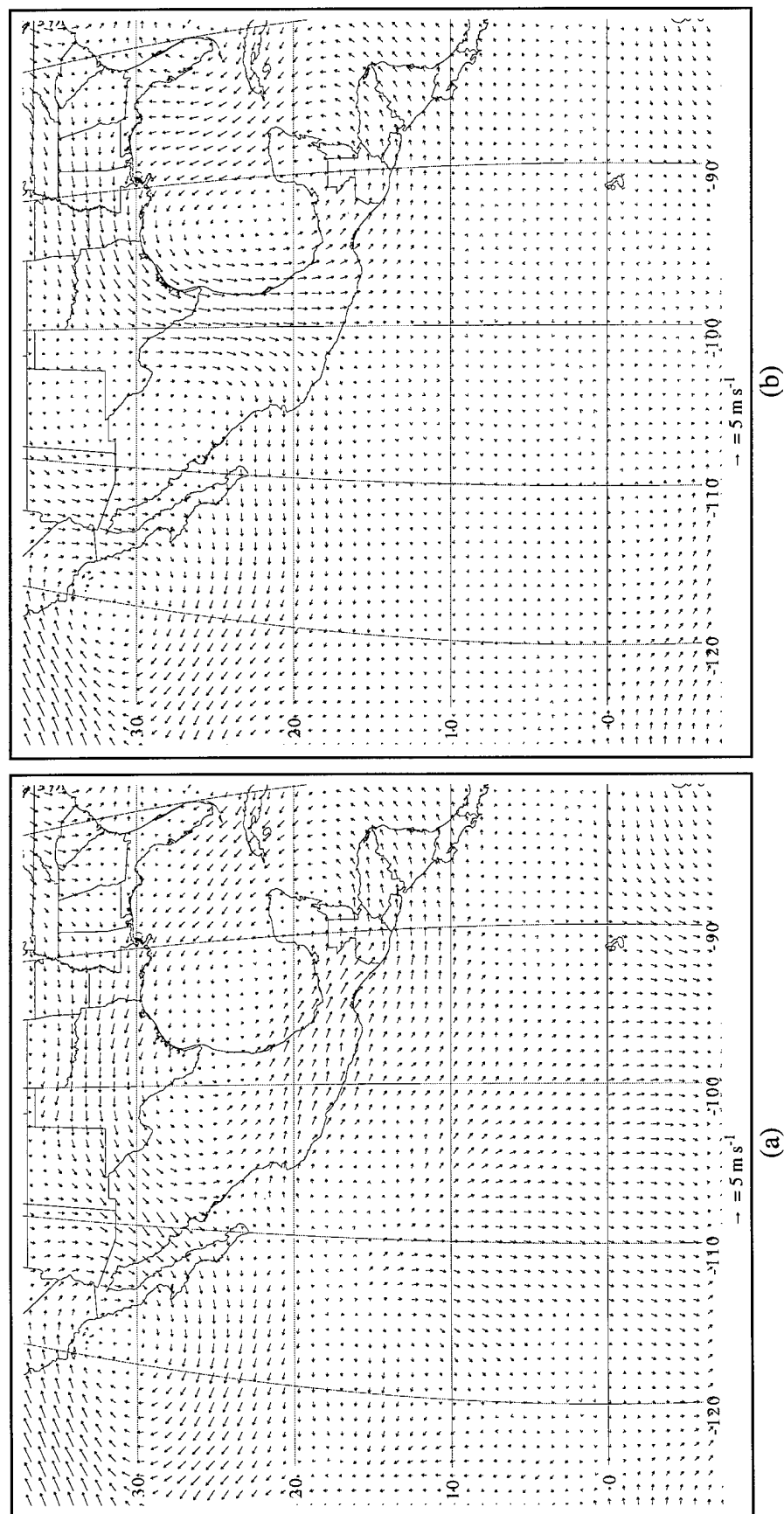
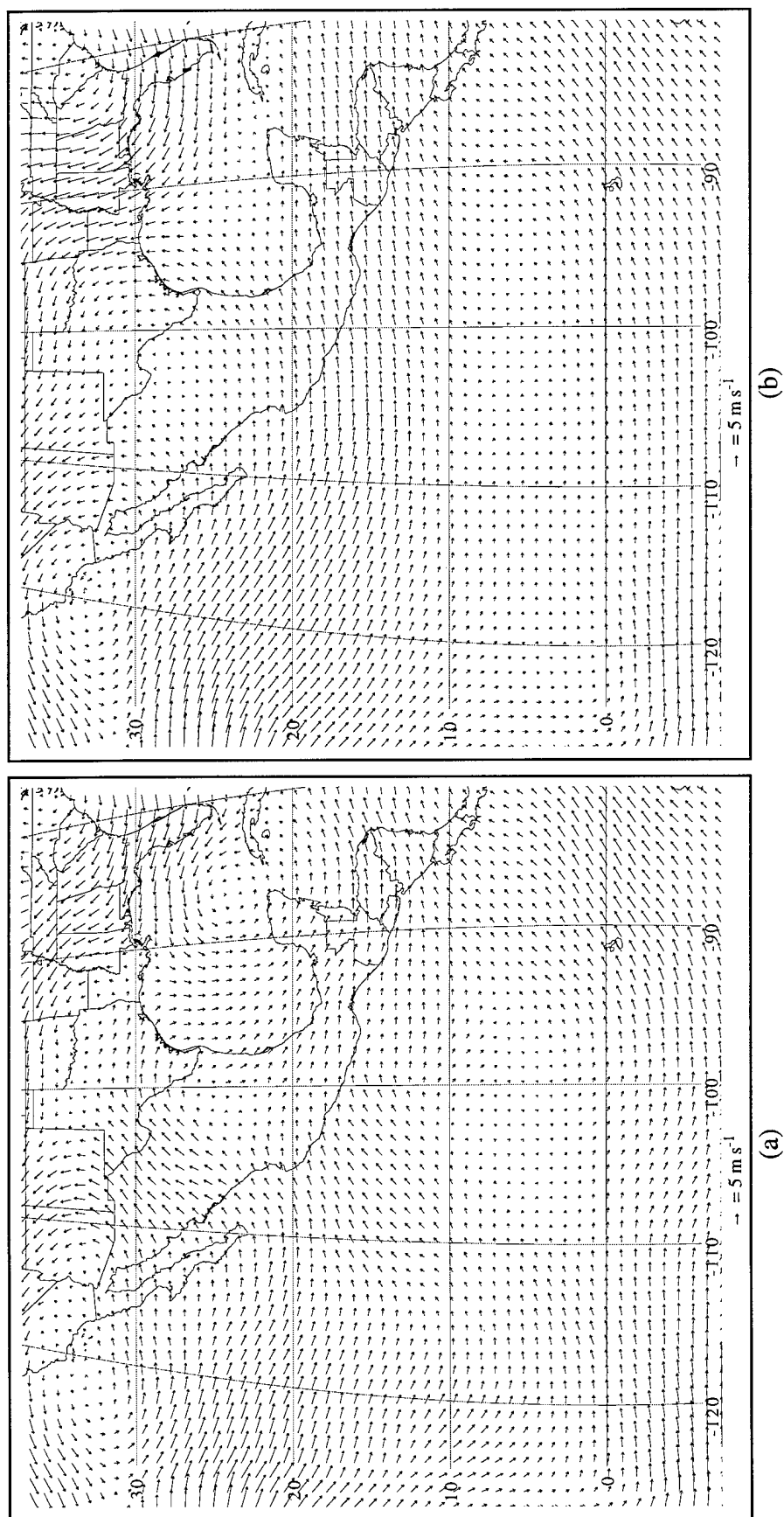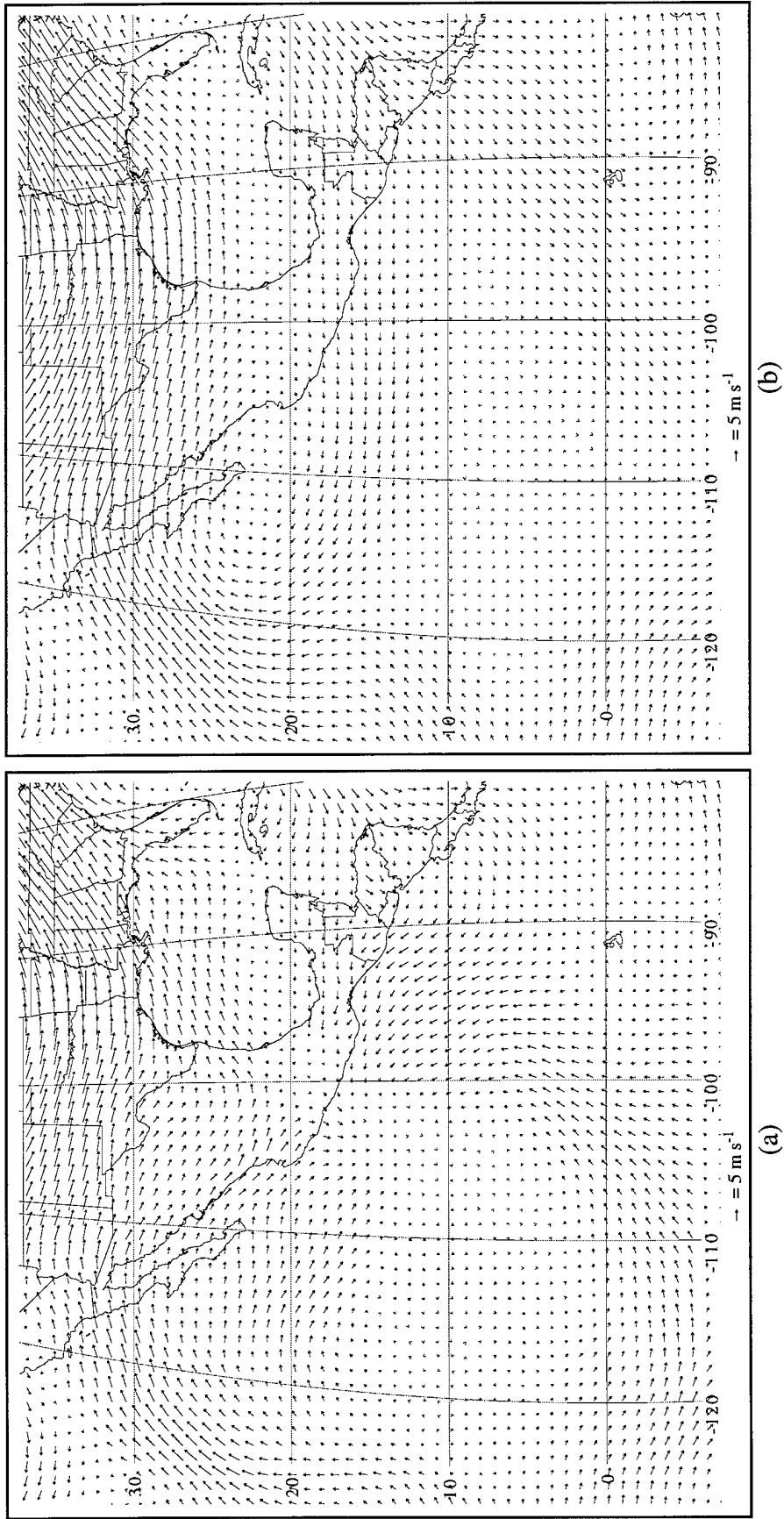Figure C.1.    200 mb wind anomalies in m s⁻¹ for JJA 1990 for (a) MM5 and (b) NCEP.

Figure C.2.    200 mb wind anomalies in m s$^{-1}$ for JJA 1991 for (a) MM5 and (b) NCEP.

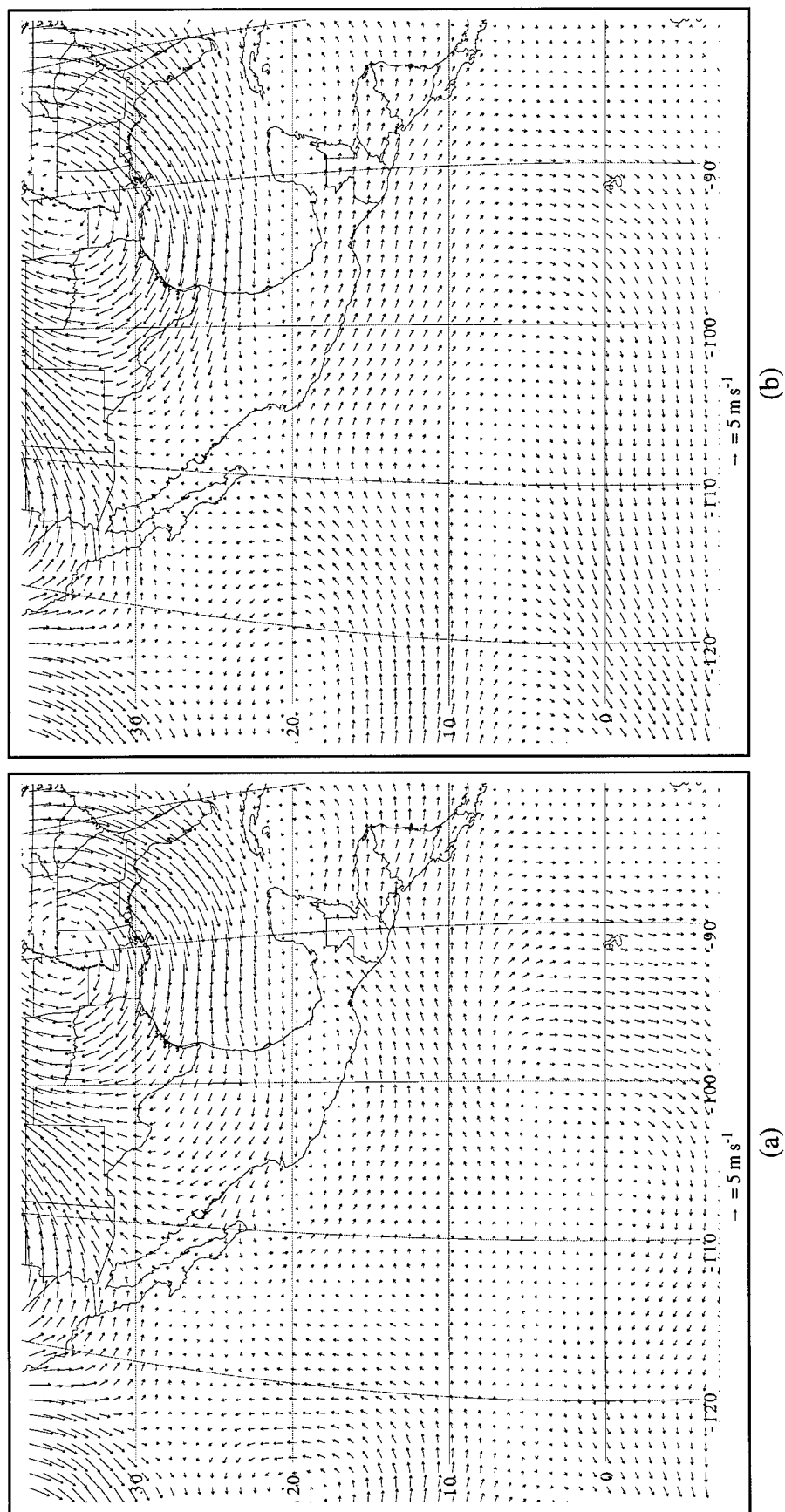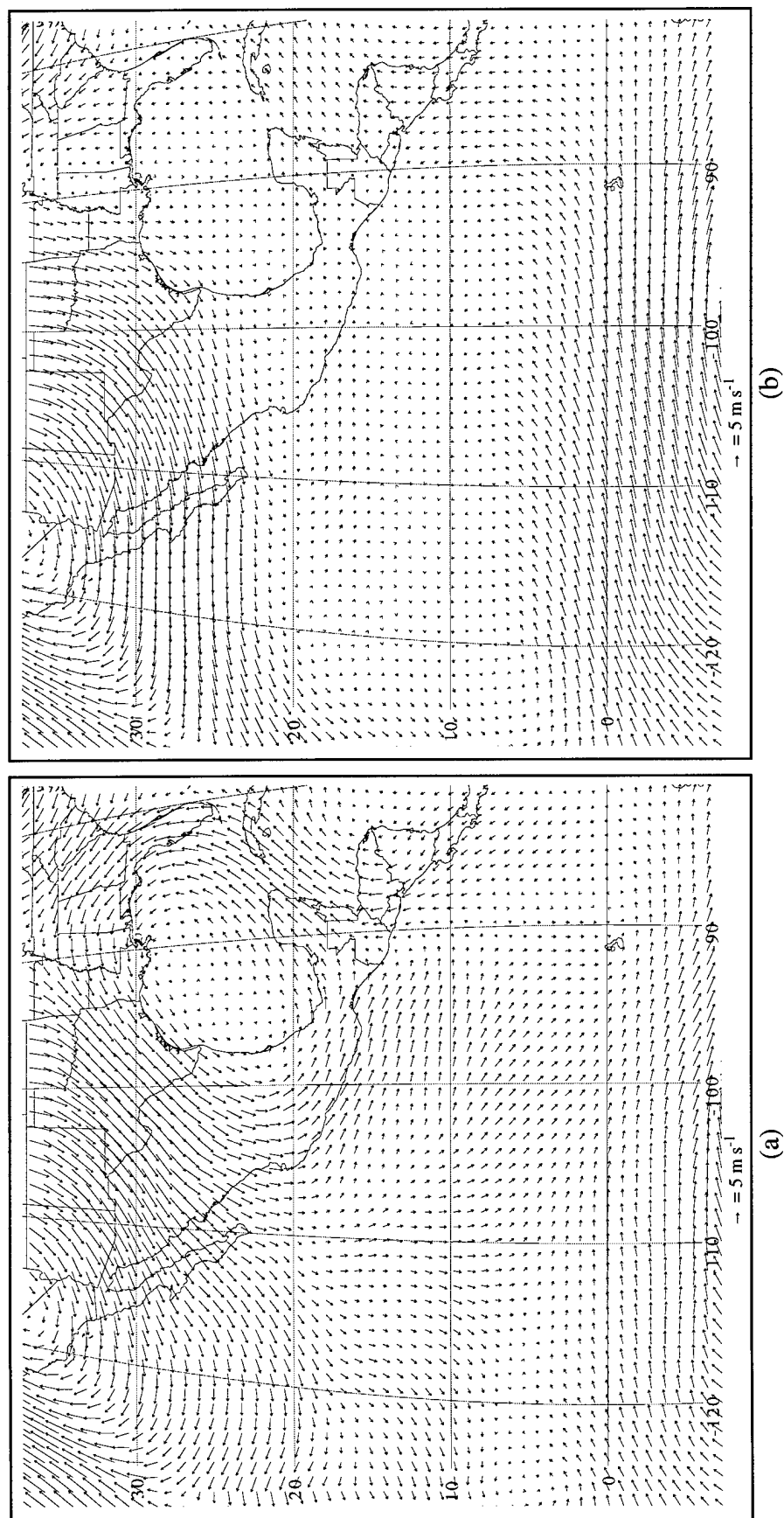Figure C.3.    200 mb wind anomalies in m s⁻¹ for JJA 1992 for (a) MM5 and (b) NCEP.

Figure C.4.    200 mb wind anomalies in m s⁻¹ for JJA 1993 for (a) MM5 and (b) NCEP.

Figure C.5. 200 mb wind anomalies in m s⁻¹ for JJA 1994 for (a) MM5 and (b) NCEP.
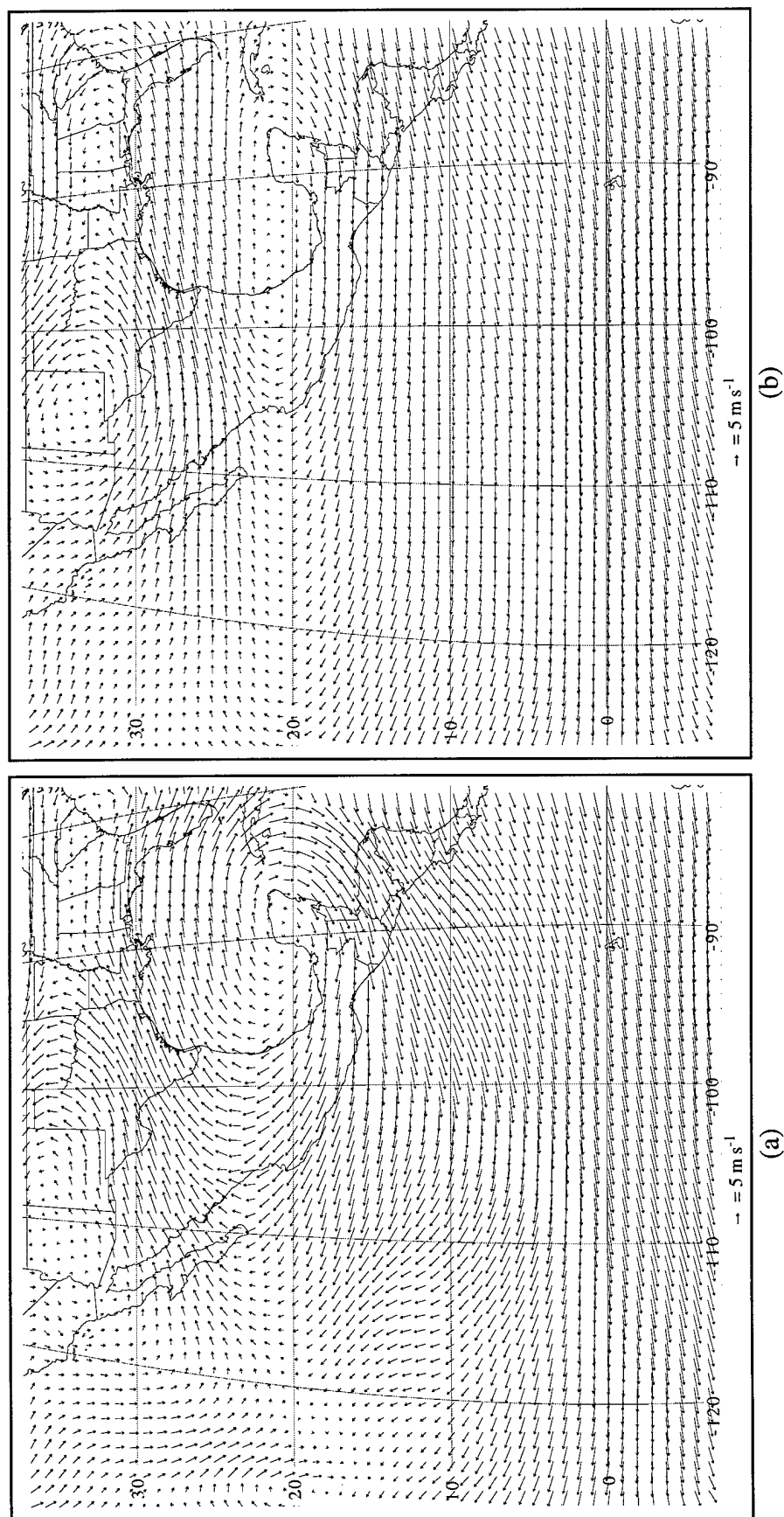
(b)

(a)

Figure C.6.    200 mb wind anomalies in m s$^{-1}$ for JJA 1995 for (a) MM5 and (b) NCEP.

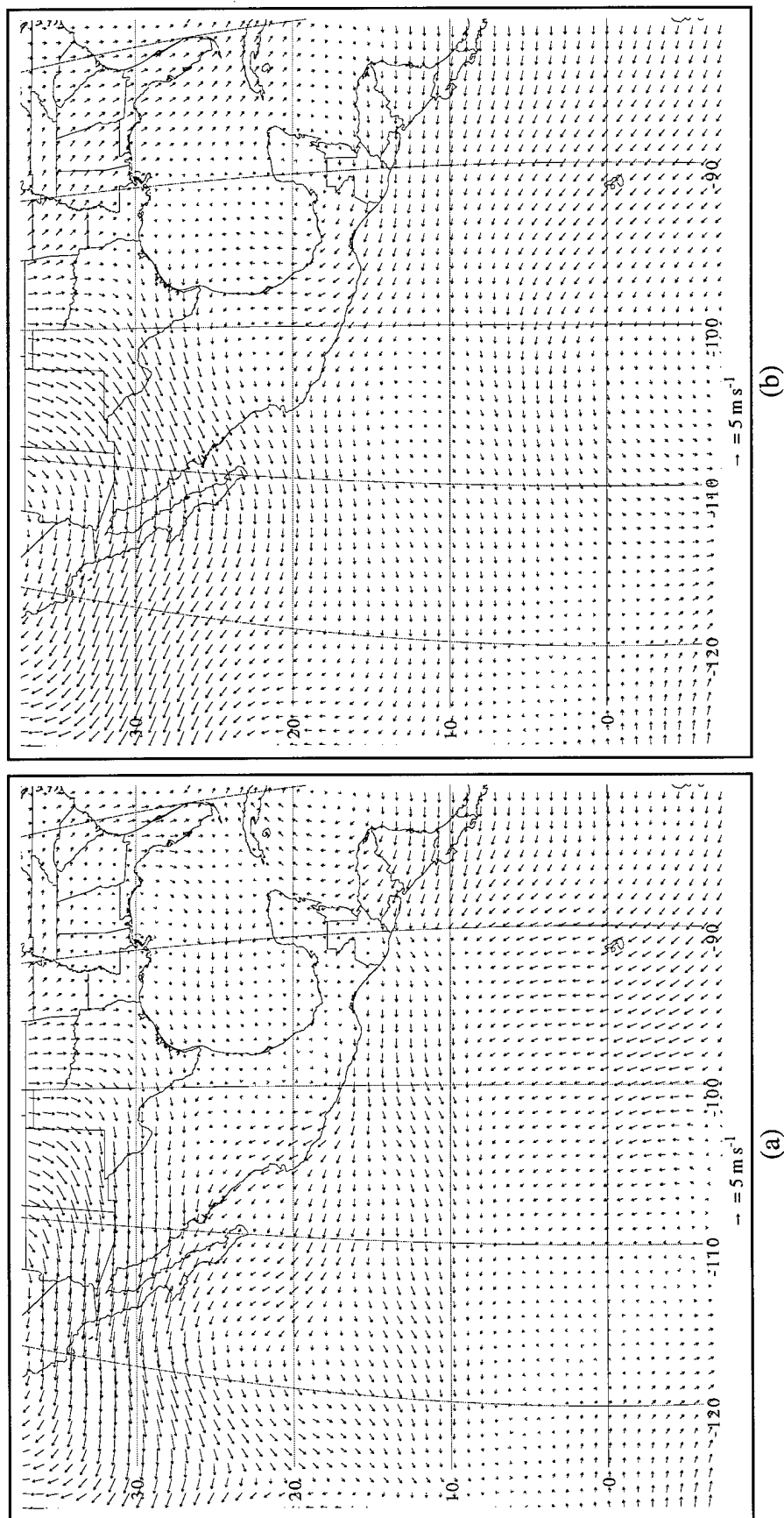Figure C.7.　200 mb wind anomalies in m s$^{-1}$ for JJA 1996 for (a) MM5 and (b) NCEP.
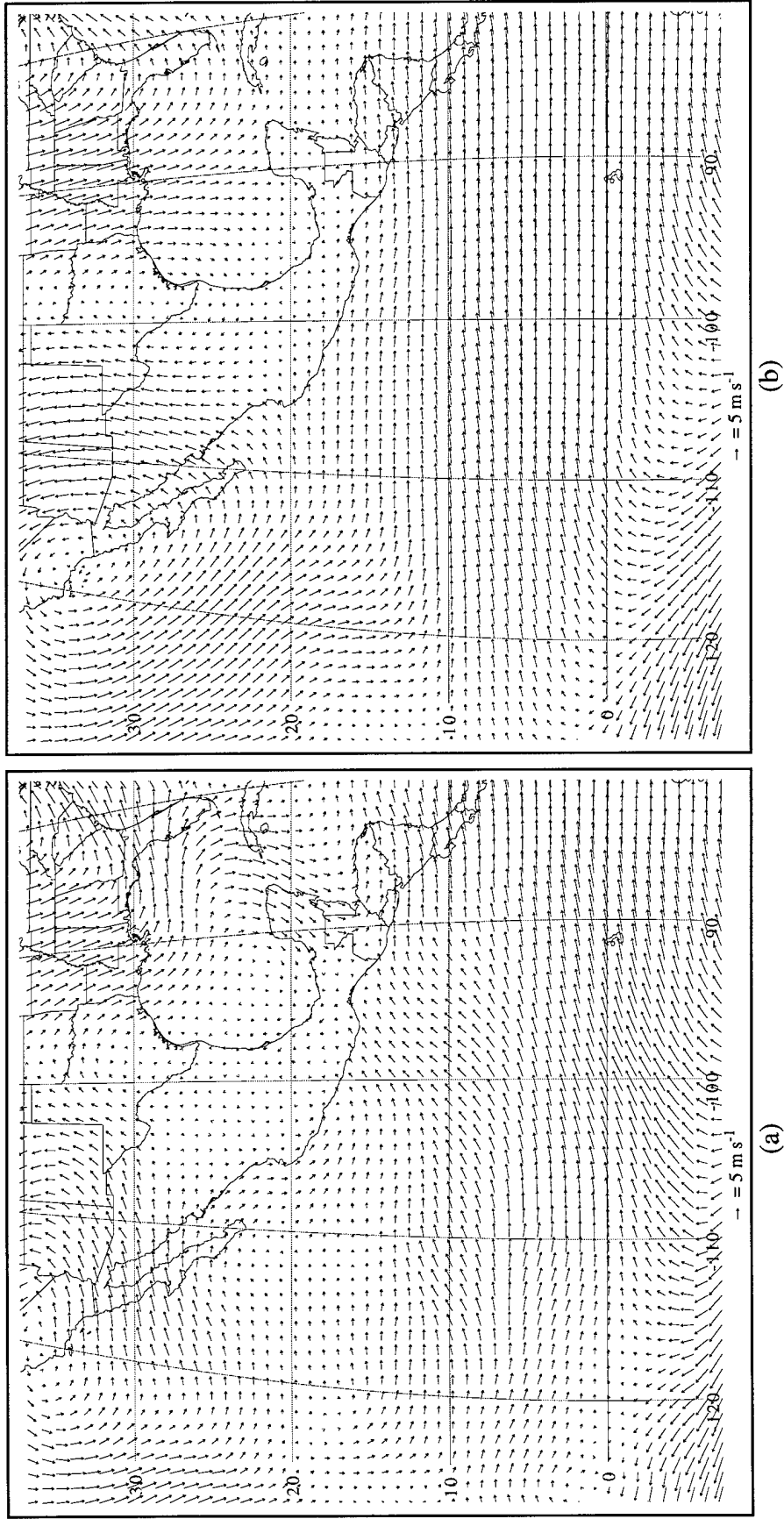
(b)

(a)

Figure C.8.    200 mb wind anomalies in m s$^{-1}$ for JJA 1997 for (a) MM5 and (b) NCEP.
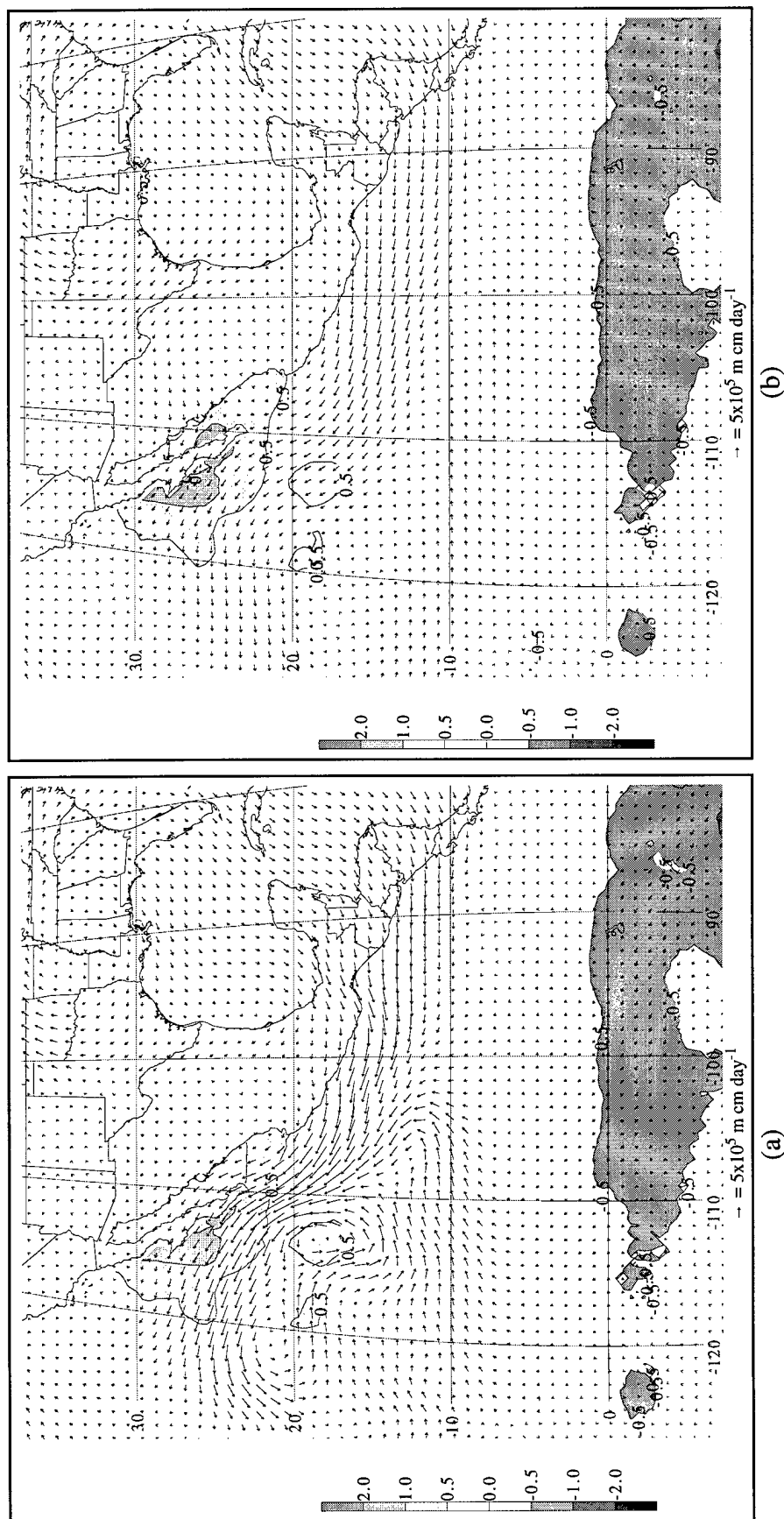
APPENDIX D

VERTICALLY INTEGRATED MOISTURE FLUX ANOMALIES

Figure D.1.  Total vertically integrated moisture flux anomalies in $10^5$ m cm day$^{-1}$ and SST anomalies in °C for JJA 1990 for (a) MM5 and (b) NCEP. Moisture flux anomalies in units of $10^5$ m cm day$^{-1}$. Contour intervals for SST anomalies are ±0.5 °C and ±1 °C thereafter. Values ≥ 0.5 °C and ≤ -0.5 °C are shaded.

(a)

(b)

Figure D.2. Total vertically integrated moisture flux anomalies in $10^5$ m cm day$^{-1}$ and SST anomalies in °C for JJA 1991 for (a) MM5 and (b) NCEP. Moisture flux anomalies in units of $10^5$ m cm day$^{-1}$. Contour intervals for SST anomalies are ±0.5 °C and ±1 °C thereafter. Values ≥ 0.5 °C and ≤ -0.5 °C are shaded.

Figure D.3. Total vertically integrated moisture flux anomalies in 10[5] m cm day^{-1} and SST anomalies in °C for JJA 1992 for (a) MM5 and (b) NCEP. Moisture flux anomalies in units of 10[5] m cm day^{-1}. Contour intervals for SST anomalies are ±0.5 °C and ±1 °C thereafter. Values ≥ 0.5 °C and ≤ -0.5 °C are shaded.
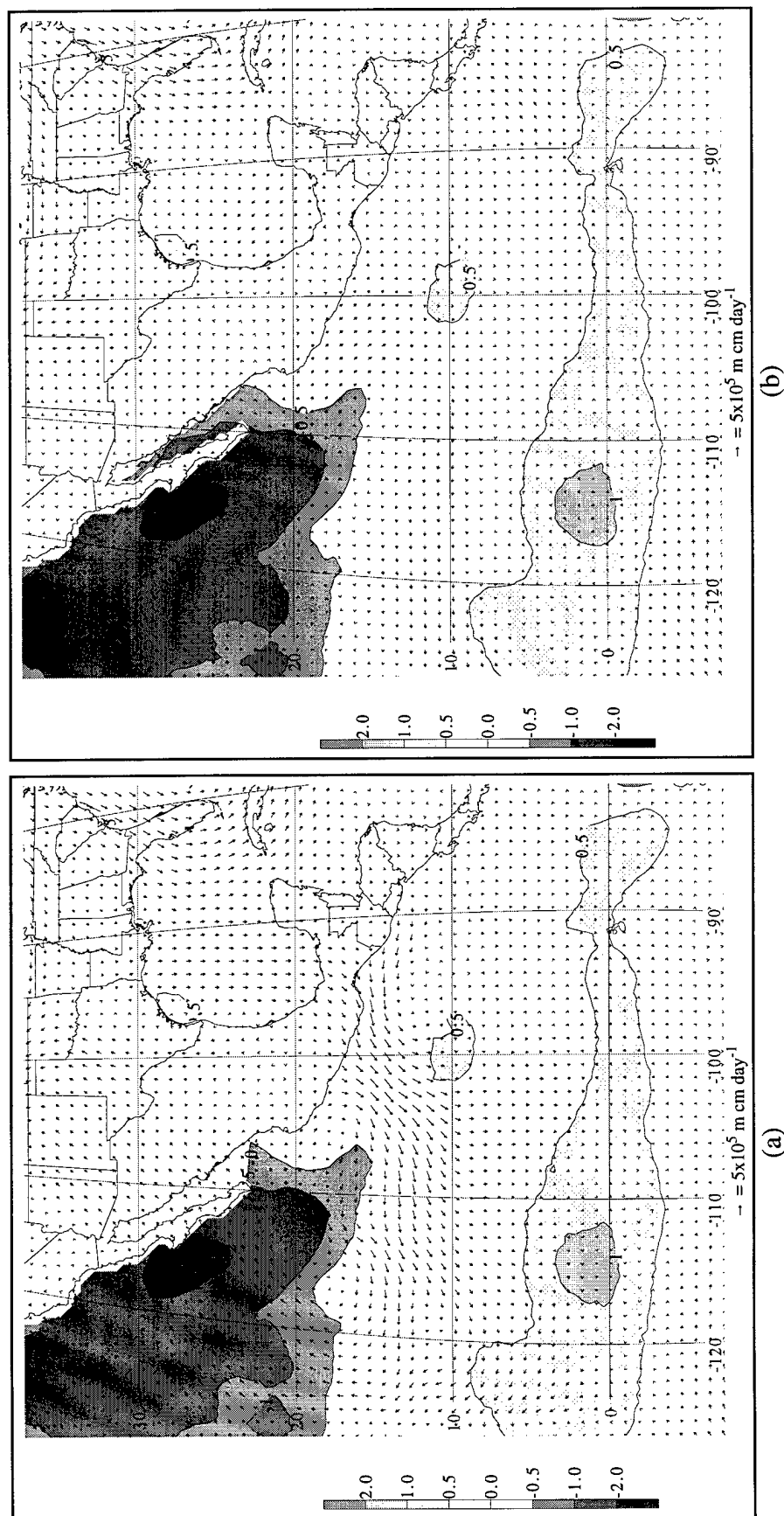
(a)　　　　　　　　　　　　　　　　　(b)

Figure D.4.　　Total vertically integrated moisture flux anomalies in $10^5$ m cm day$^{-1}$ and SST anomalies in °C for JJA 1993 for (a) MM5 and (b) NCEP. Moisture flux anomalies in units of $10^5$ m cm day$^{-1}$. Contour intervals for SST anomalies are ±0.5 °C and ±1 °C thereafter. Values ≥ 0.5 °C and ≤ -0.5 °C are shaded.
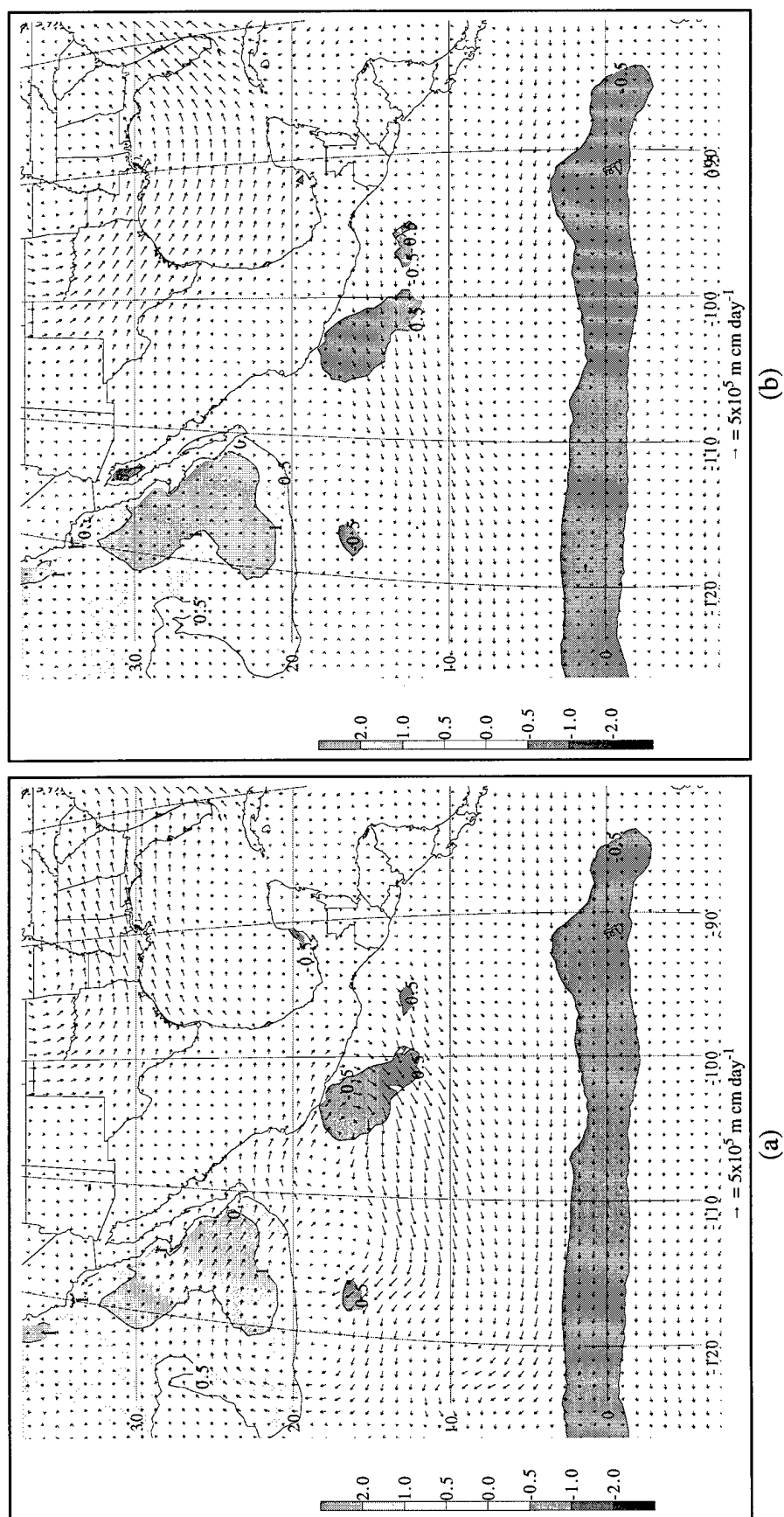
(a)

(b)

Figure D.5.    Total vertically integrated moisture flux anomalies in $10^5$ m cm day$^{-1}$ and SST anomalies in °C for JJA 1994 for (a) MM5 and (b) NCEP. Moisture flux anomalies in units of $10^5$ m cm day$^{-1}$. Contour intervals for SST anomalies are ±0.5 °C and ±1 °C thereafter. Values ≥ 0.5 °C and ≤ -0.5 °C are shaded.
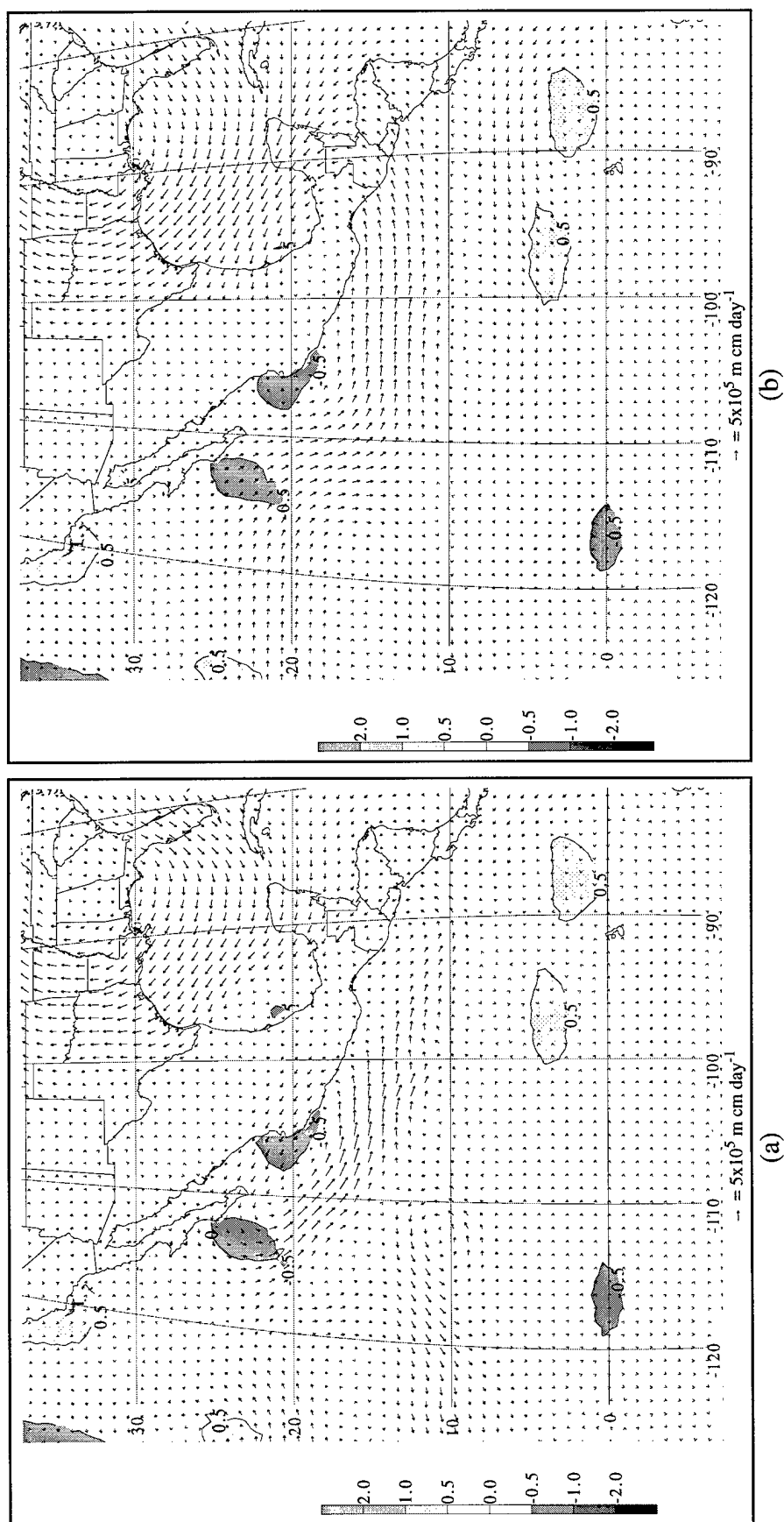
(a)

(b)
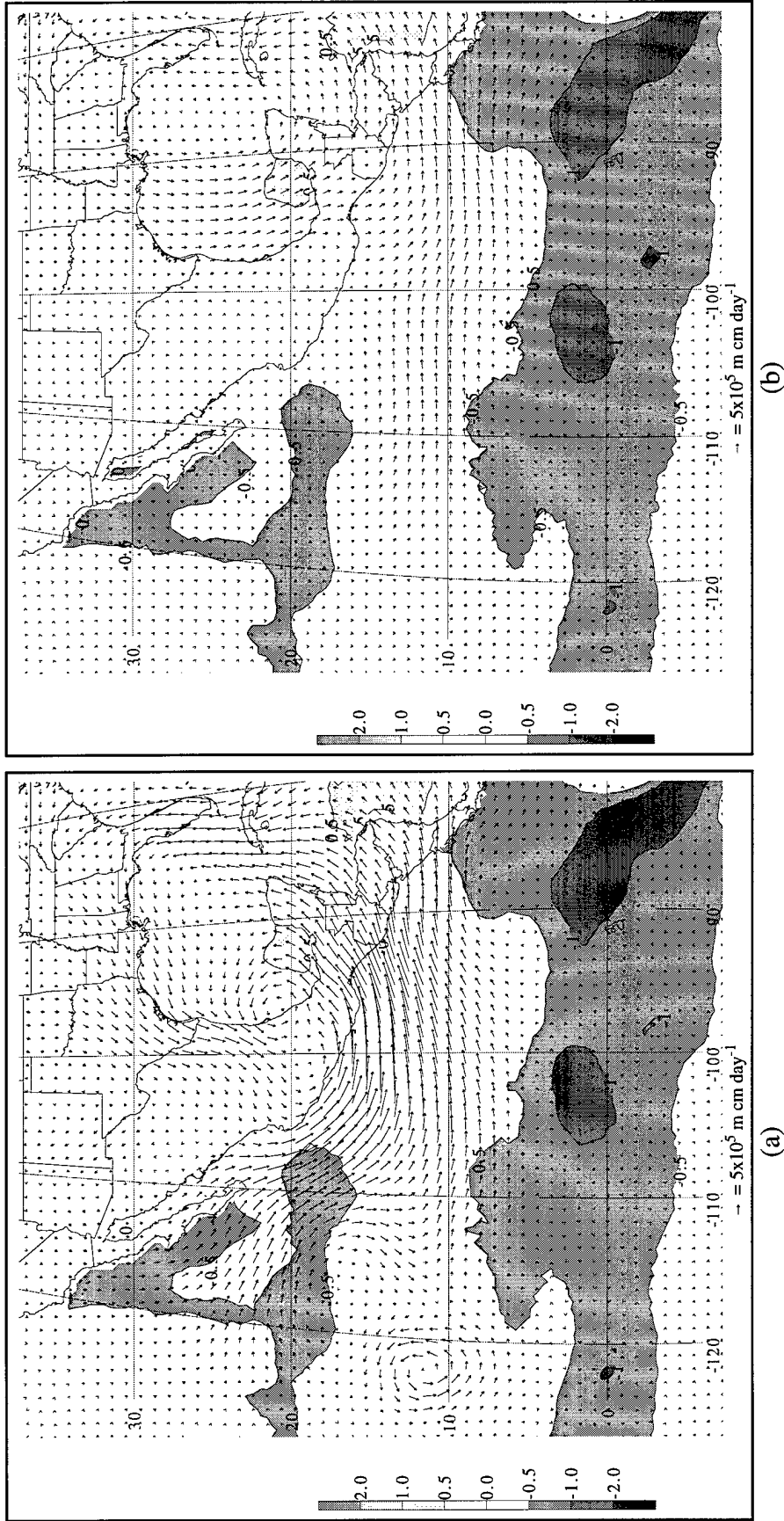
Figure D.6. Total vertically integrated moisture flux anomalies in $10^5$ m cm day$^{-1}$ and SST anomalies in °C for JJA 1995 for (a) MM5 and (b) NCEP. Moisture flux anomalies in units of $10^5$ m cm day$^{-1}$. Contour intervals for SST anomalies are ±0.5 °C and ±1 °C thereafter. Values ≥ 0.5 °C and ≤ -0.5 °C are shaded.

(a)

(b)
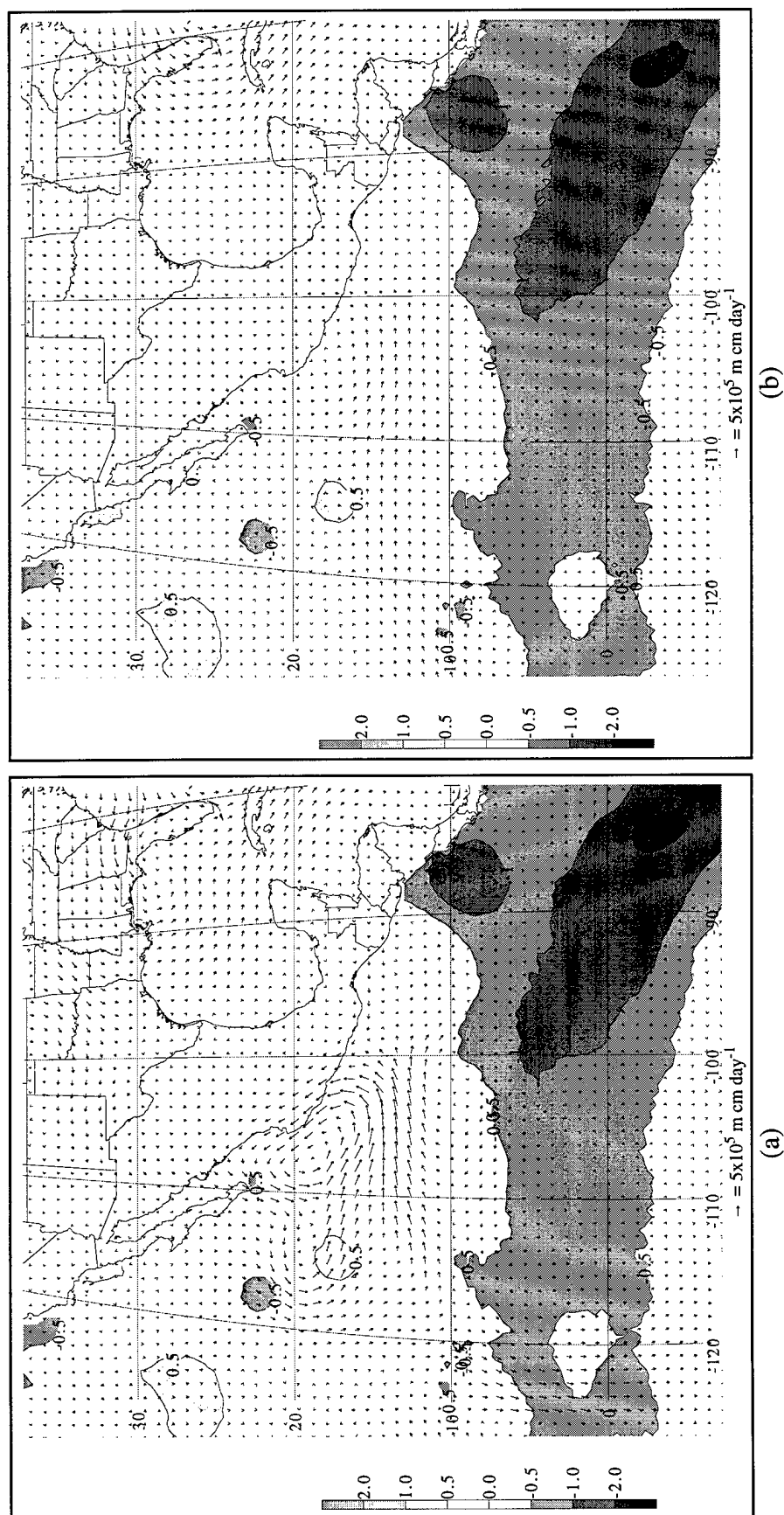
Figure D.7.  Total vertically integrated moisture flux anomalies in $10^5$ m cm day$^{-1}$ and SST anomalies in °C for JJA 1996 for (a) MM5 and (b) NCEP. Moisture flux anomalies in units of $10^5$ m cm day$^{-1}$. Contour intervals for SST anomalies are ±0.5 °C and ±1 °C thereafter. Values ≥ 0.5 °C and ≤ -0.5 °C are shaded.

(b)

(a)
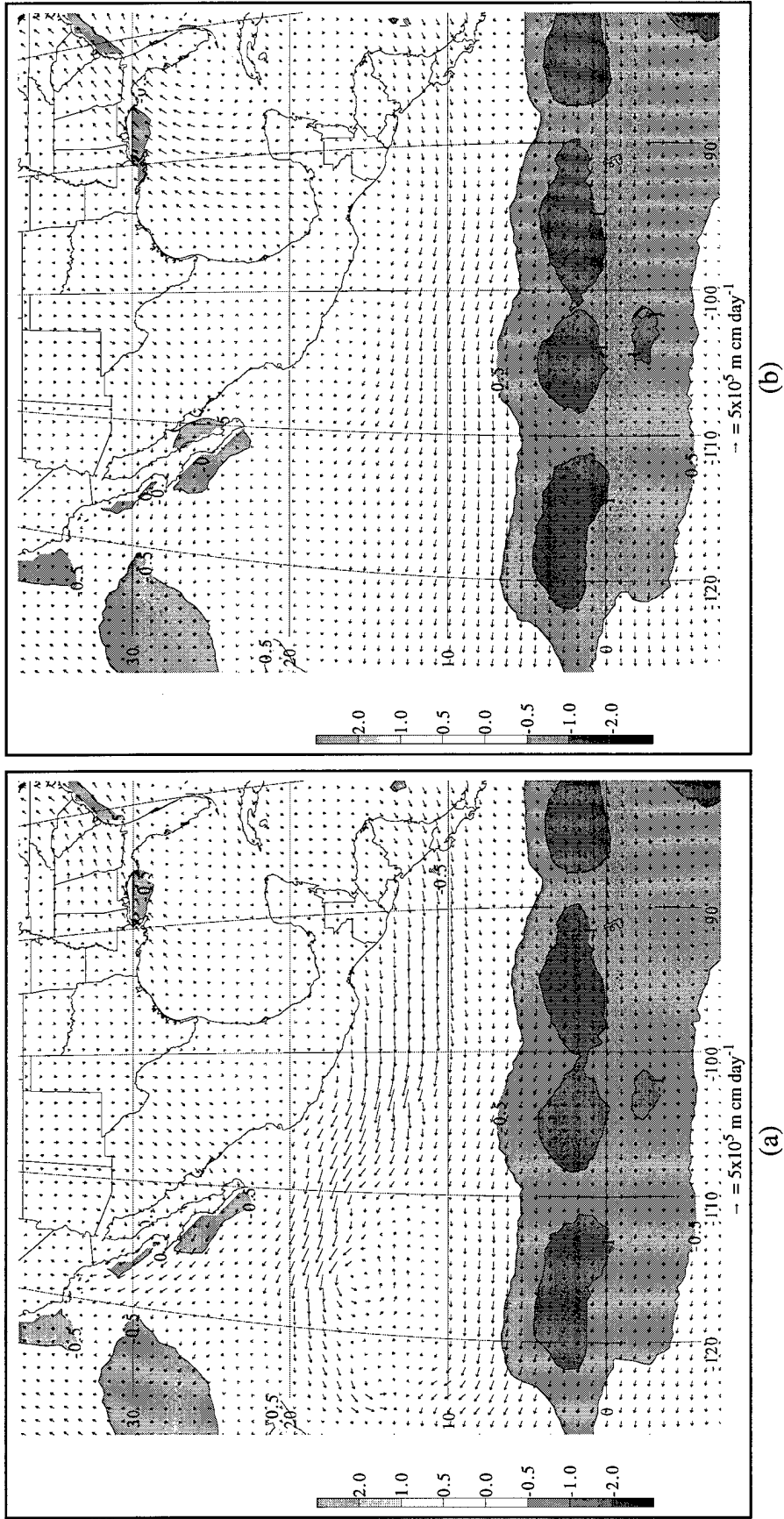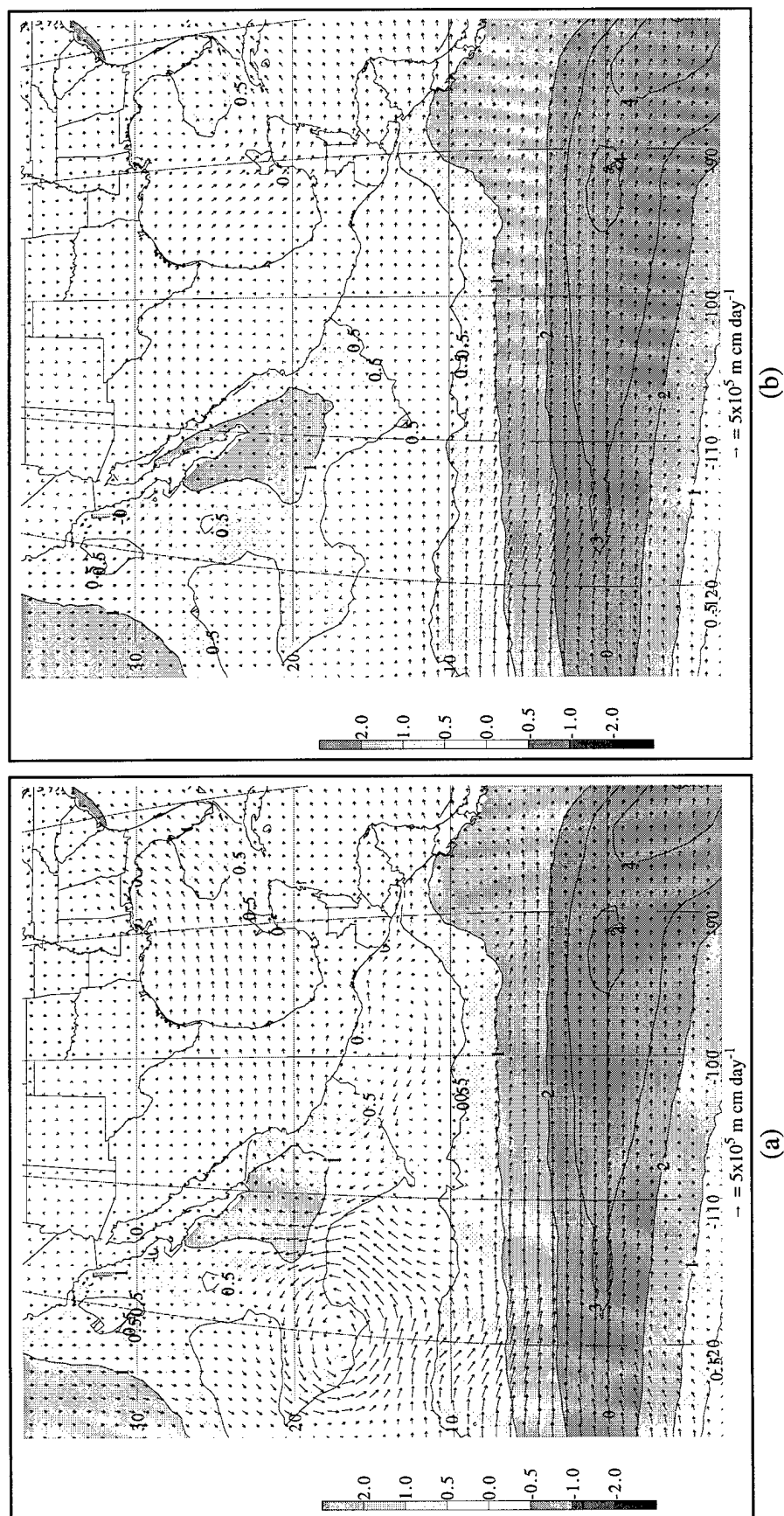
Figure D.8.    Total vertically integrated moisture flux anomalies in 10^5 m cm day^-1 and SST anomalies in °C for JJA 1997 for (a) MM5 and (b) NCEP. Moisture flux anomalies in units of 10^5 m cm day^-1. Contour intervals for SST anomalies are ±0.5 °C and ±1 °C thereafter. Values ≥ 0.5 °C and ≤ -0.5 °C are shaded.

APPENDIX E


VERTICAL CROSS SECTIONS ALONG 105° W

137



Figure E.1.　Vertical cross-section for JJA 1990 along 105° W from 5° S to 35° N. The vertical coordinate is pressure in mb. The thin dashed lines are $\theta_e$ in K. The thicker solid lines denote the meridional wind component in m s$^{-1}$. The shaded regions and associated contours are total LWC in 10$^{-2}$ g kg$^{-1}$. The lower graph contains the average precipitation rate in cm day$^{-1}$ (solid line) and the average surface temperature in °C (dashed line) along 105° W.

Figure E.2.    Vertical cross-section for JJA 1991 along 105° W from 5° S to 35° N. The vertical coordinate is pressure in mb. The thin dashed lines are $\theta_e$ in K. The thicker solid lines denote the meridional wind component in m s$^{-1}$. The shaded regions and associated contours are total LWC in 10$^{-2}$ g kg$^{-1}$. The lower graph contains the average precipitation rate in cm day$^{-1}$ (solid line) and the average surface temperature in °C (dashed line) along 105° W.

Figure E.3.  Vertical cross-section for JJA 1992 along 105° W from 5° S to 35° N. The vertical coordinate is pressure in mb. The thin dashed lines are $\theta_e$ in K. The thicker solid lines denote the meridional wind component in m s$^{-1}$. The shaded regions and associated contours are total LWC in 10$^{-2}$ g kg$^{-1}$. The lower graph contains the average precipitation rate in cm day$^{-1}$ (solid line) and the average surface temperature in °C (dashed line) along 105° W.
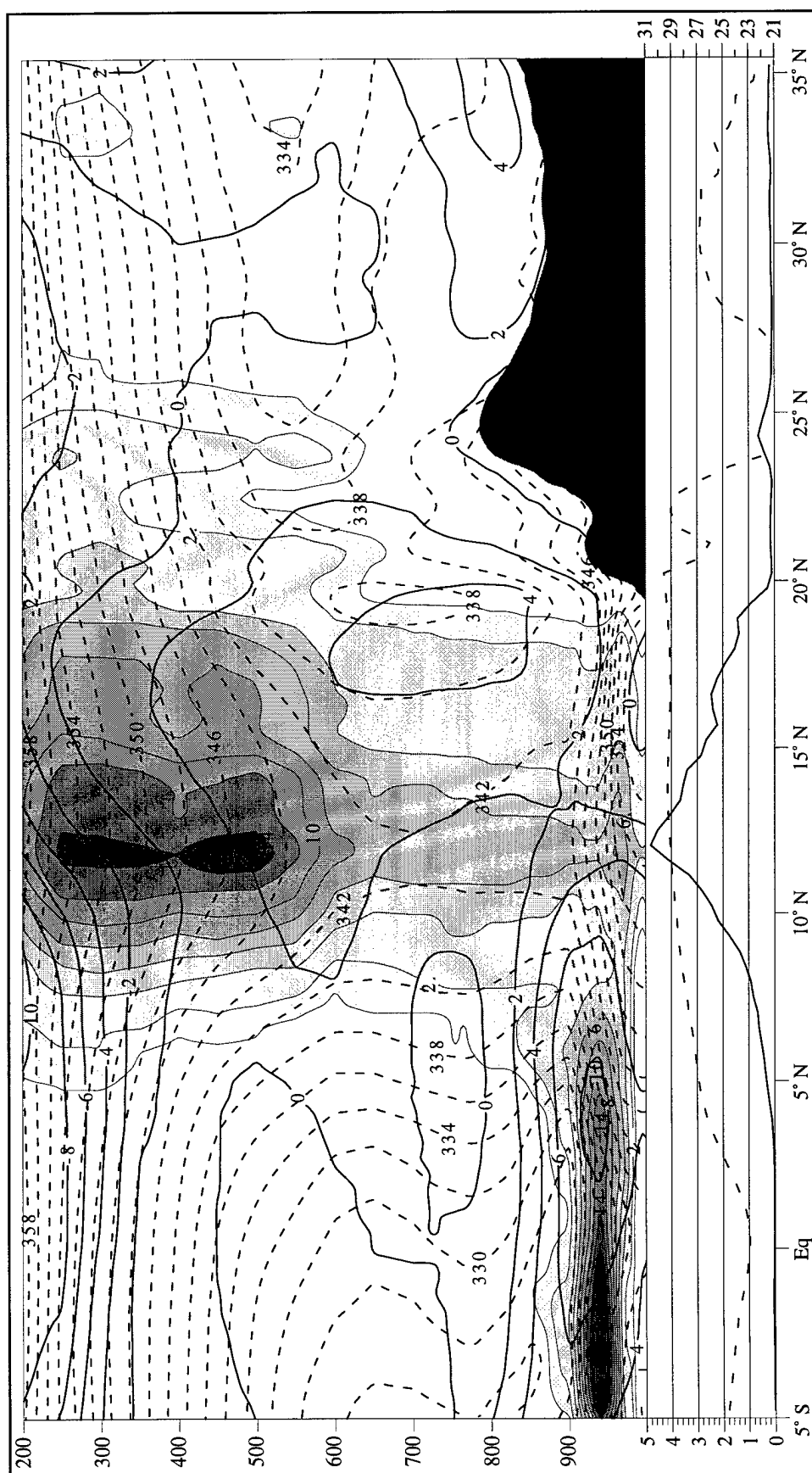
Figure E.4. Vertical cross-section for JJA 1993 along 105° W from 5° S to 35° N. The vertical coordinate is pressure in mb. The thin dashed lines are $\theta_e$ in K. The thicker solid lines denote the meridional wind component in m s$^{-1}$. The shaded regions and associated contours are total LWC in 10$^{-2}$ g kg$^{-1}$. The lower graph contains the average precipitation rate in cm day$^{-1}$ (solid line) and the average surface temperature in °C (dashed line) along 105° W.
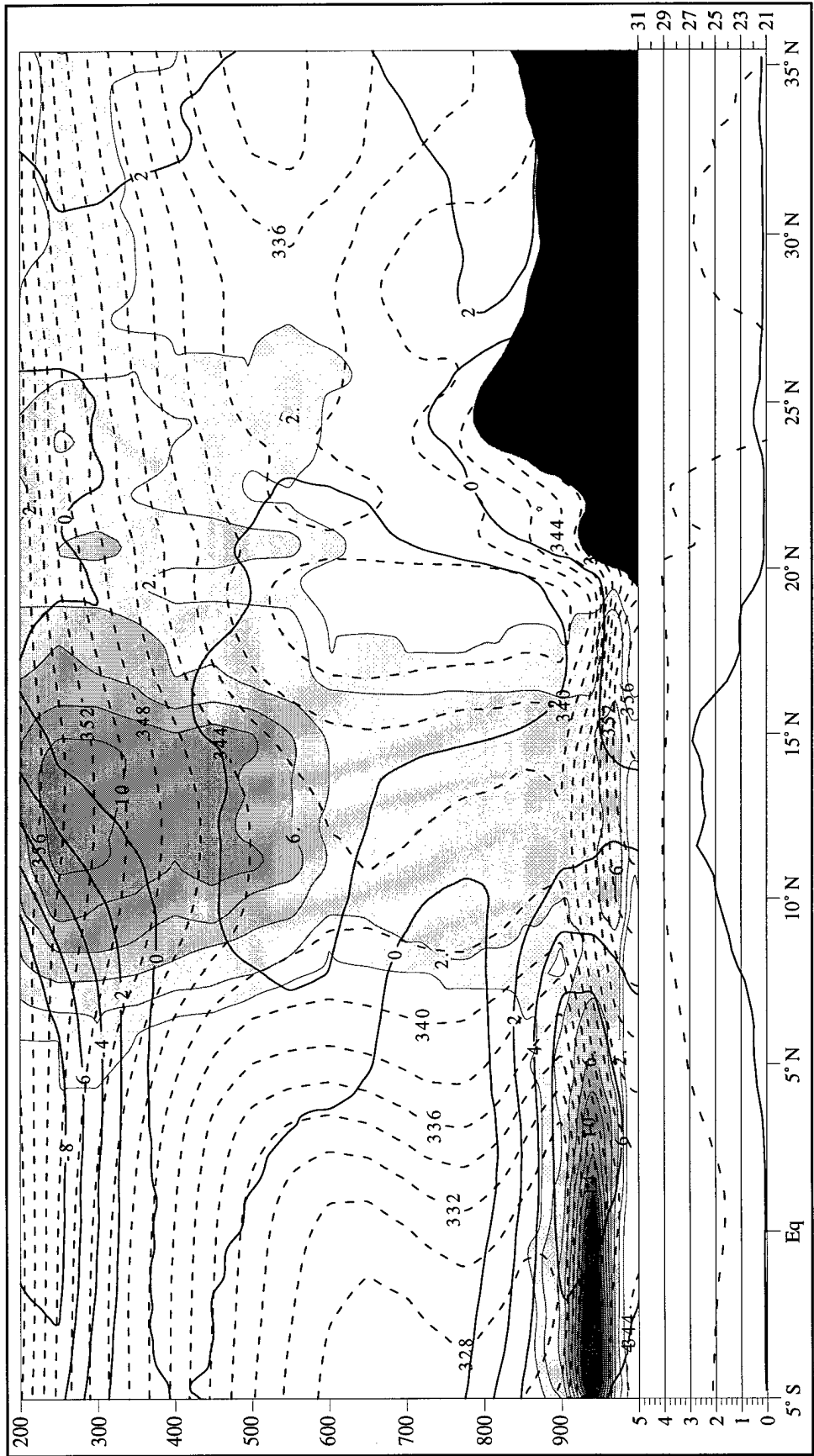
Figure E.5.    Vertical cross-section for JJA 1994 along 105° W from 5° S to 35° N. The vertical coordinate is pressure in mb. The thin dashed lines are $\theta_e$ in K. The thicker solid lines denote the meridional wind component in m s$^{-1}$. The shaded regions and associated contours are total LWC in 10$^{-2}$ g kg$^{-1}$. The lower graph contains the average precipitation rate in cm day$^{-1}$ (solid line) and the average surface temperature in °C (dashed line) along 105° W.

Figure E.6. Vertical cross-section for JJA 1995 along 105° W from 5° S to 35° N. The vertical coordinate is pressure in mb. The thin dashed lines are $\theta_e$ in K. The thicker solid lines denote the meridional wind component in m s$^{-1}$. The shaded regions and associated contours are total LWC in 10$^{-2}$ g kg$^{-1}$. The lower graph contains the average precipitation rate in cm day$^{-1}$ (solid line) and the average surface temperature in °C (dashed line) along 105° W.
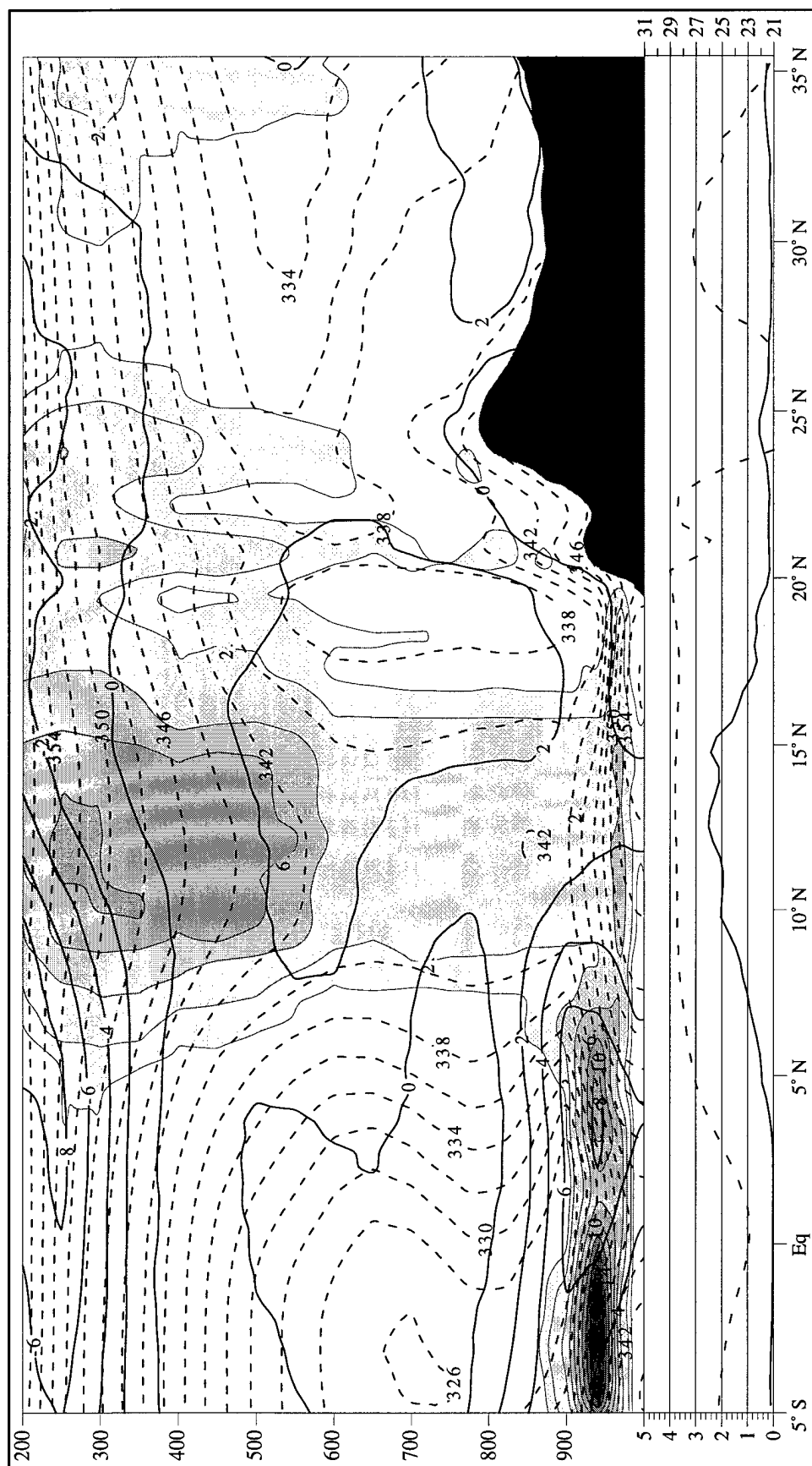
143



Figure E.7.　Vertical cross-section for JJA 1996 along 105° W from 5° S to 35° N. The vertical coordinate is pressure in mb. The thin dashed lines are $\theta_e$ in K. The thicker solid lines denote the meridional wind component in m s$^{-1}$. The shaded regions and associated contours are total LWC in 10$^{-2}$ g kg$^{-1}$. The lower graph contains the average precipitation rate in cm day$^{-1}$ (solid line) and the average surface temperature in °C (dashed line) along 105° W.
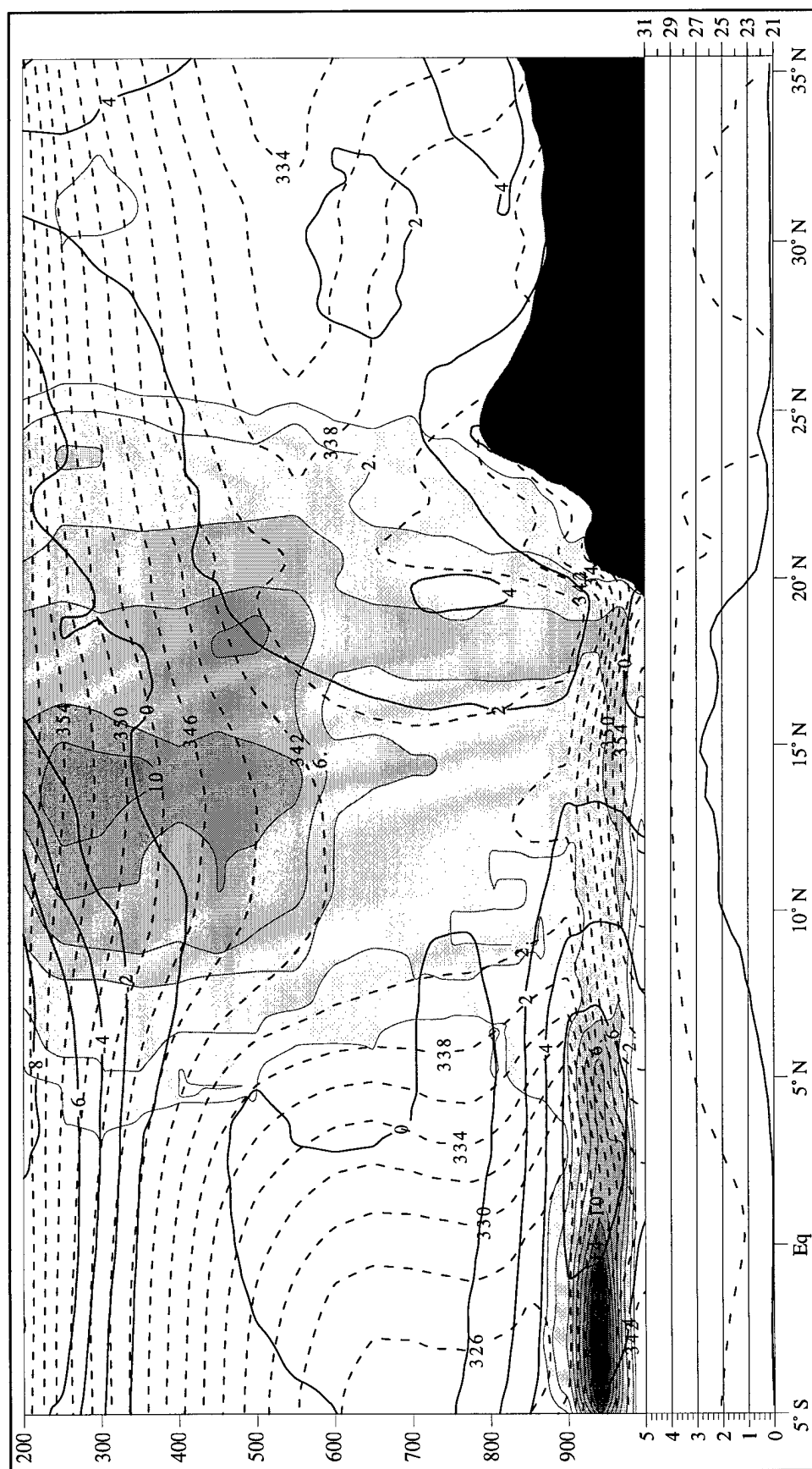
Figure E.8. Vertical cross-section for JJA 1997 along 105° W from 5° S to 35° N. The vertical coordinate is pressure in mb. The thin dashed lines are $\theta_e$ in K. The thicker solid lines denote the meridional wind component in m s$^{-1}$. The shaded regions and associated contours are total LWC in 10$^{-2}$ g kg$^{-1}$. The lower graph contains the average precipitation rate in cm day$^{-1}$ (solid line) and the average surface temperature in °C (dashed line) along 105° W.

# APPENDIX F

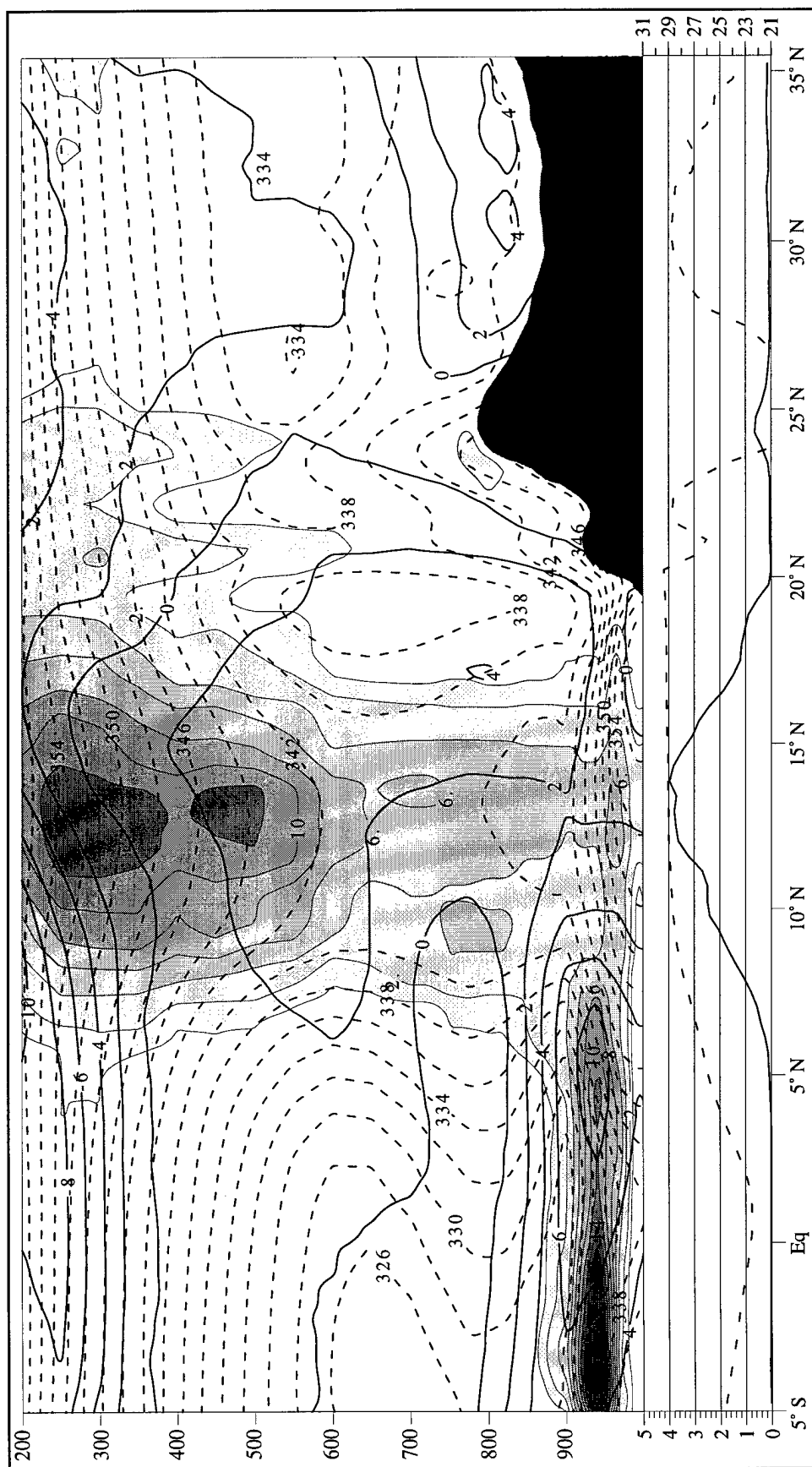# VERTICAL CROSS SECTIONS ALONG 95° W

Figure F.1.    Vertical cross-section for JJA 1990 along 95° W from 5° S to 35° N. The vertical coordinate is pressure in mb. The thin dashed lines are $\theta_e$ in K. The thicker solid lines denote the meridional wind component in m s$^{-1}$. The shaded regions and associated contours are total LWC in 10$^{-2}$ g kg$^{-1}$. The lower graph contains the average precipitation rate in cm day$^{-1}$ (solid line) and the average surface temperature in °C (dashed line) along 95° W.
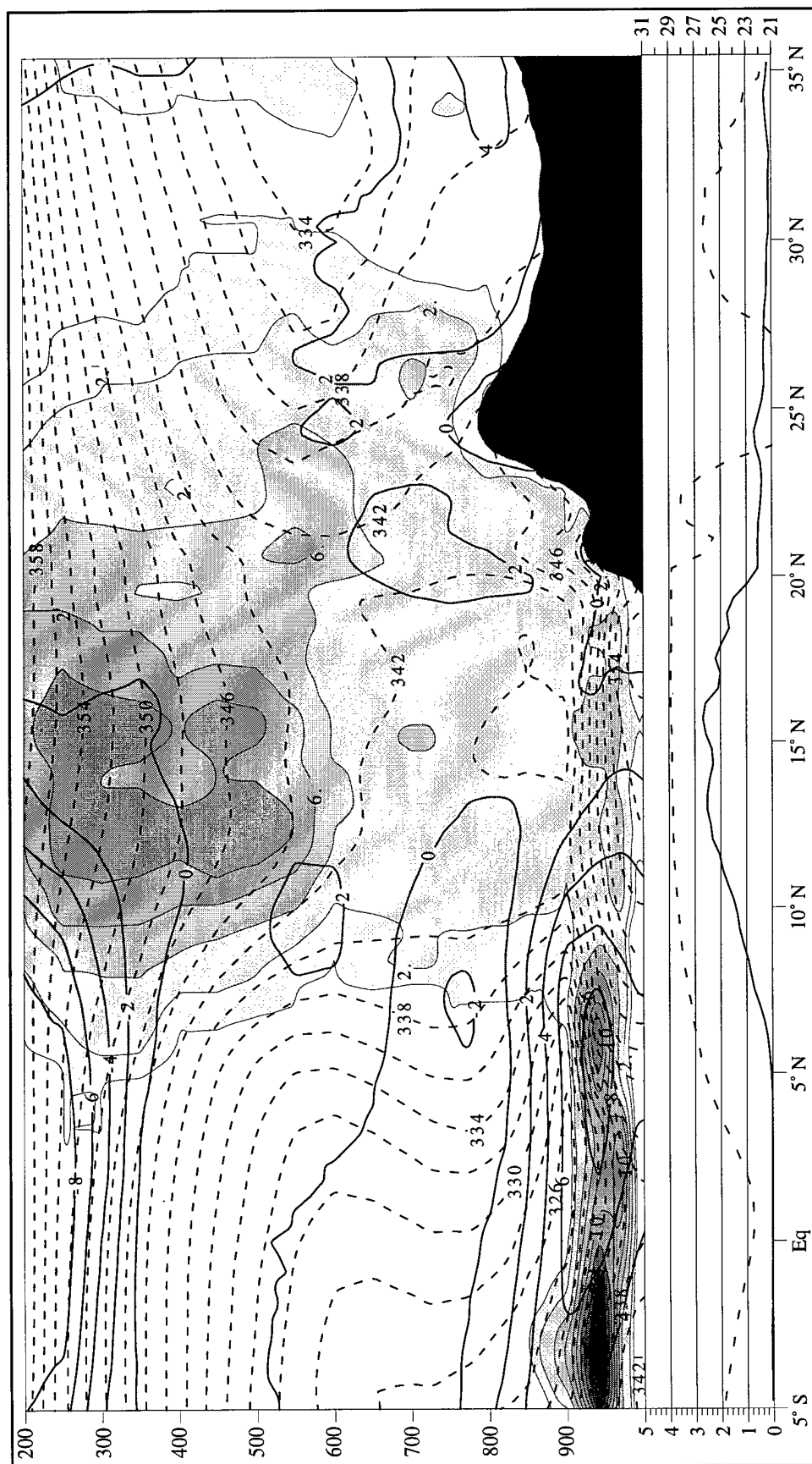
Figure F.2.  Vertical cross-section for JJA 1991 along 95° W from 5° S to 35° N. The vertical coordinate is pressure in mb. The thin dashed lines are $\theta_e$ in K. The thicker solid lines denote the meridional wind component in m s$^{-1}$. The shaded regions and associated contours are total LWC in 10$^{-2}$ g kg$^{-1}$. The lower graph contains the average precipitation rate in cm day$^{-1}$ (solid line) and the average surface temperature in °C (dashed line) along 95° W.
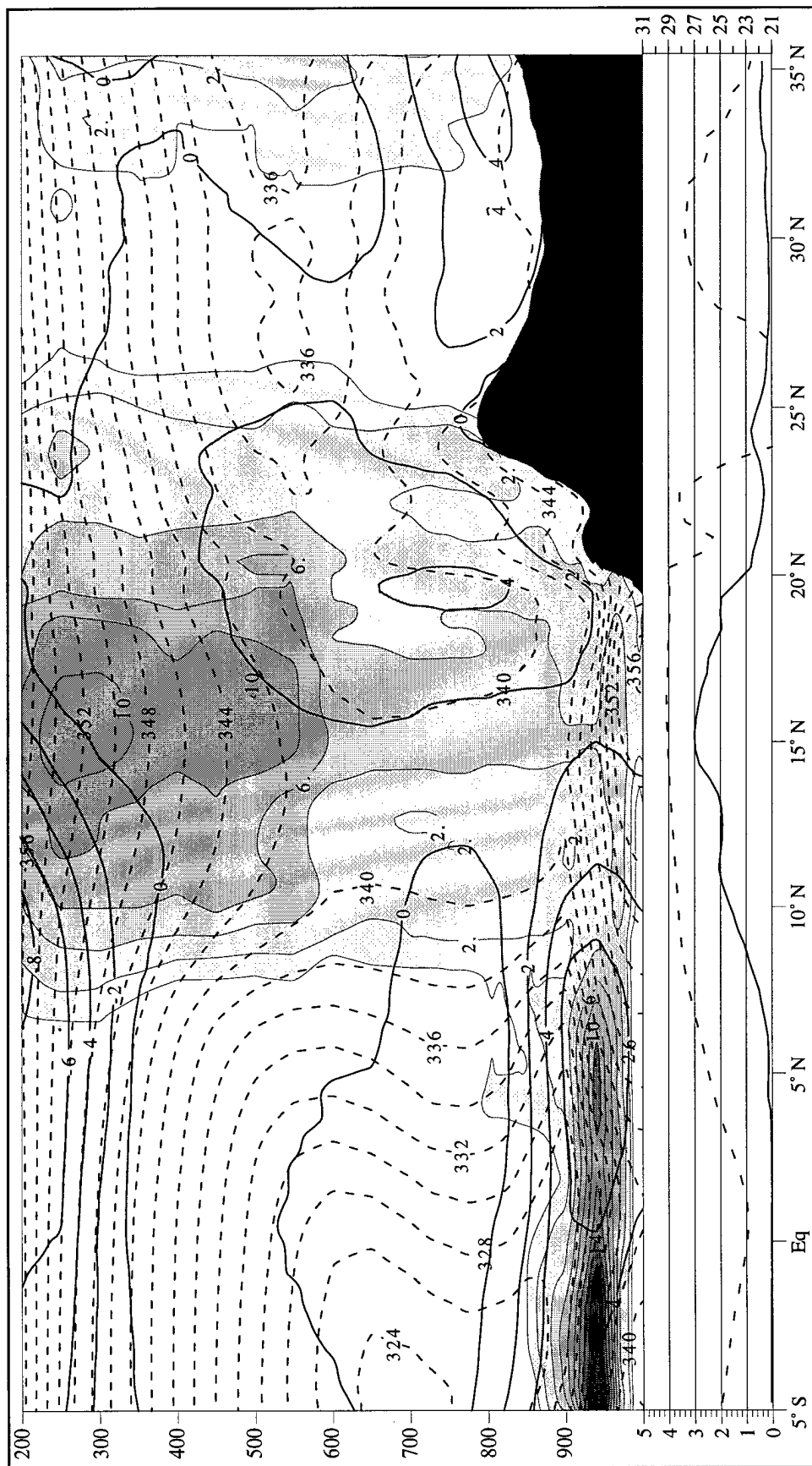
Figure F.3.    Vertical cross-section for JJA 1992 along 95° W from 5° S to 35° N. The vertical coordinate is pressure in mb. The thin dashed lines are $\theta_e$ in K. The thicker solid lines denote the meridional wind component in m s$^{-1}$. The shaded regions and associated contours are total LWC in 10$^{-2}$ g kg$^{-1}$. The lower graph contains the average precipitation rate in cm day$^{-1}$ (solid line) and the average surface temperature in °C (dashed line) along 95° W.
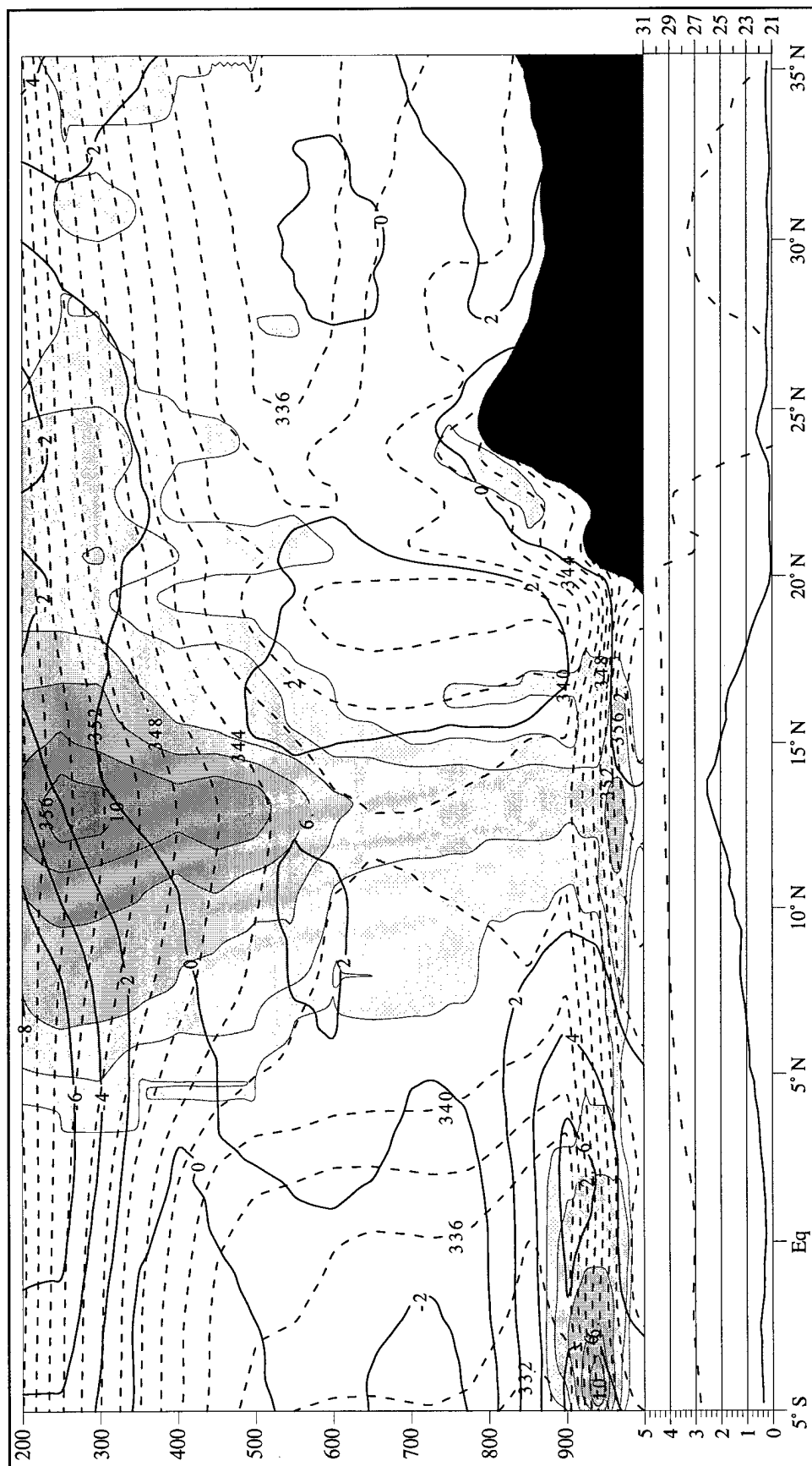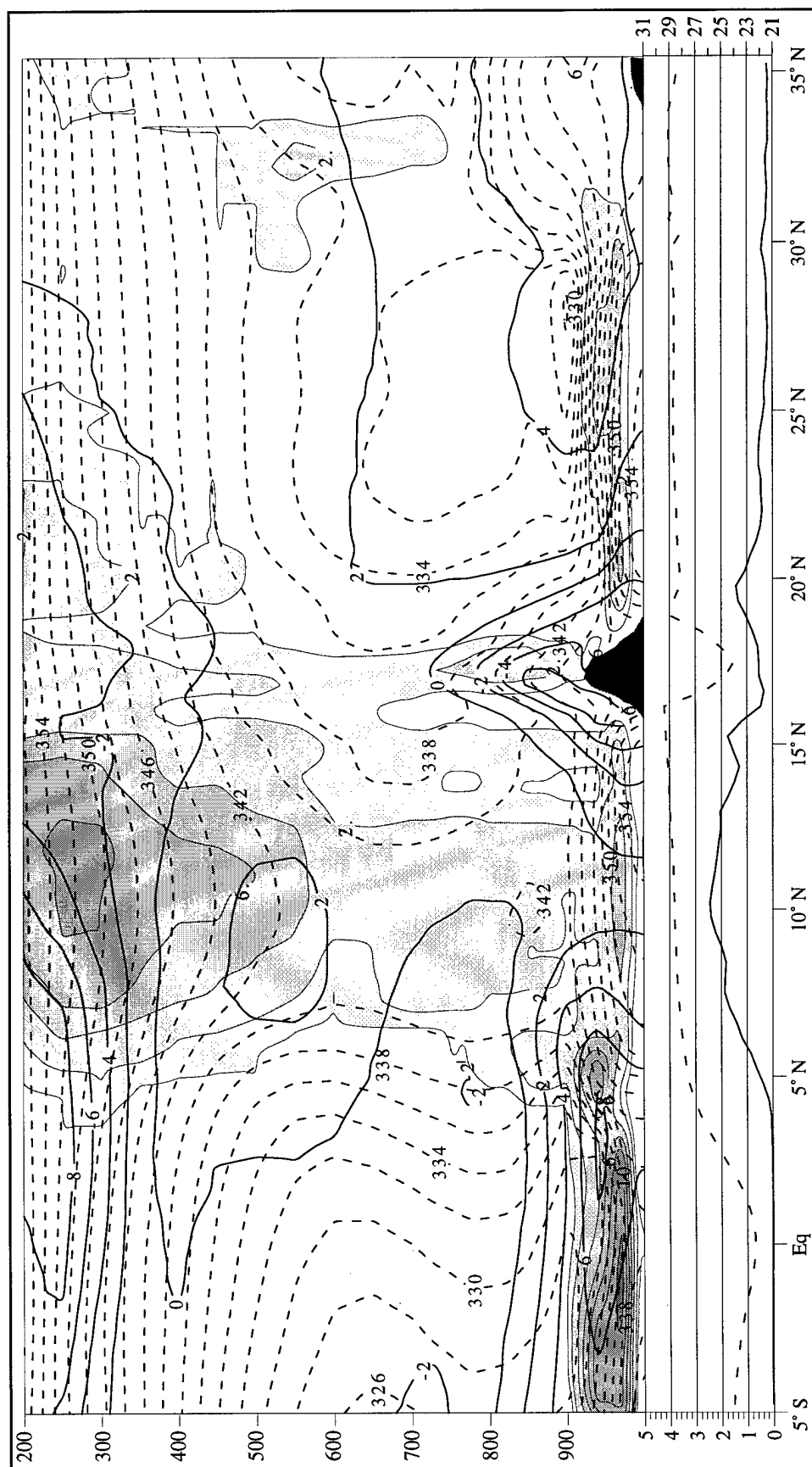
Figure F.4.    Vertical cross-section for JJA 1993 along 95° W from 5° S to 35° N. The vertical coordinate is pressure in mb. The thin dashed lines are $\theta_e$ in K. The thicker solid lines denote the meridional wind component in m s$^{-1}$. The shaded regions and associated contours are total LWC in $10^{-2}$ g kg$^{-1}$. The lower graph contains the average precipitation rate in cm day$^{-1}$ (solid line) and the average surface temperature in °C (dashed line) along 95° W.
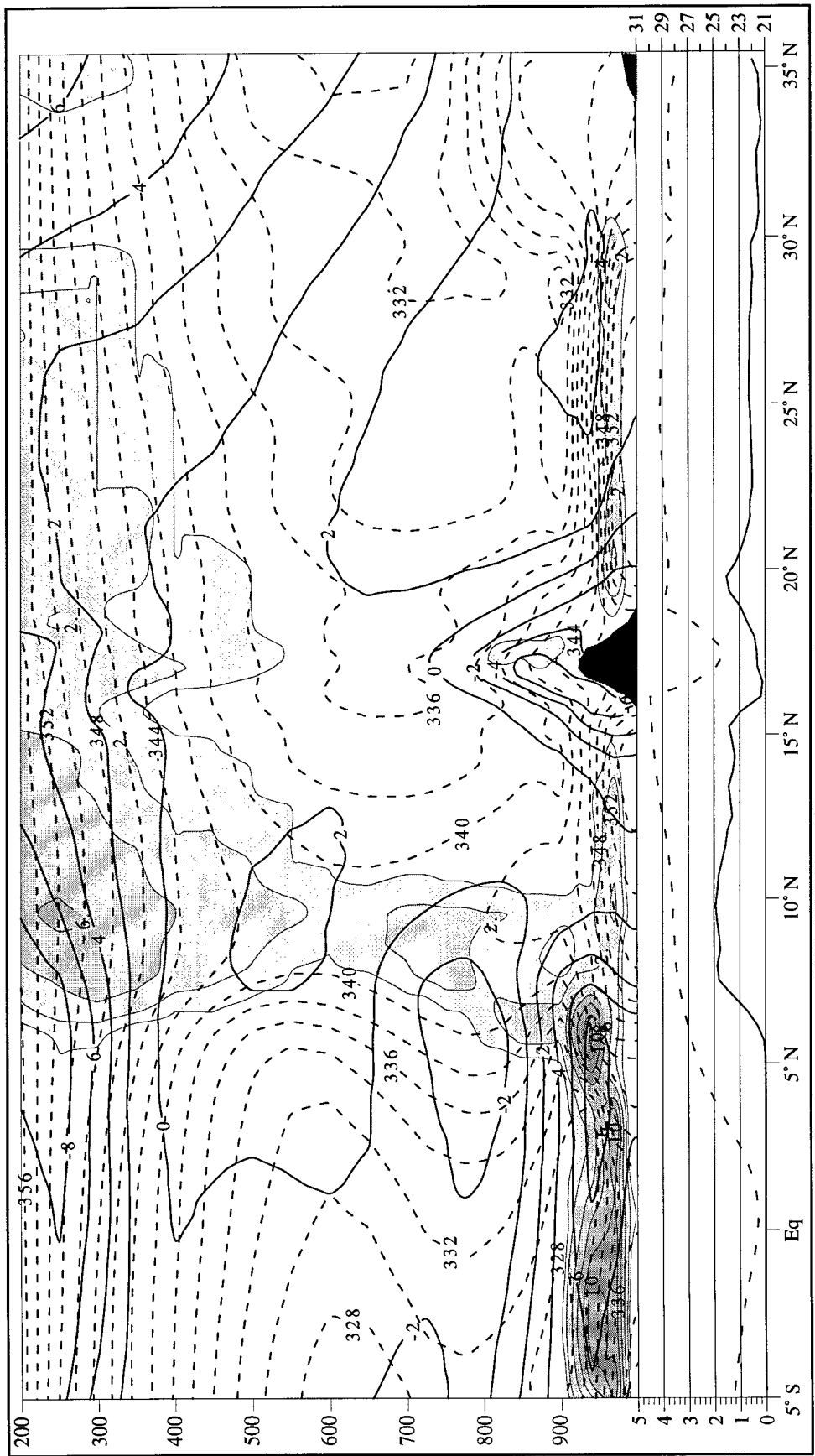
Figure F.5.    Vertical cross-section for JJA 1994 along 95° W from 5° S to 35° N. The vertical coordinate is pressure in mb. The thin dashed lines are $\theta_e$ in K. The thicker solid lines denote the meridional wind component in m s$^{-1}$. The shaded regions and associated contours are total LWC in 10$^{-2}$ g kg$^{-1}$. The lower graph contains the average precipitation rate in cm day$^{-1}$ (solid line) and the average surface temperature in °C (dashed line) along 95° W.
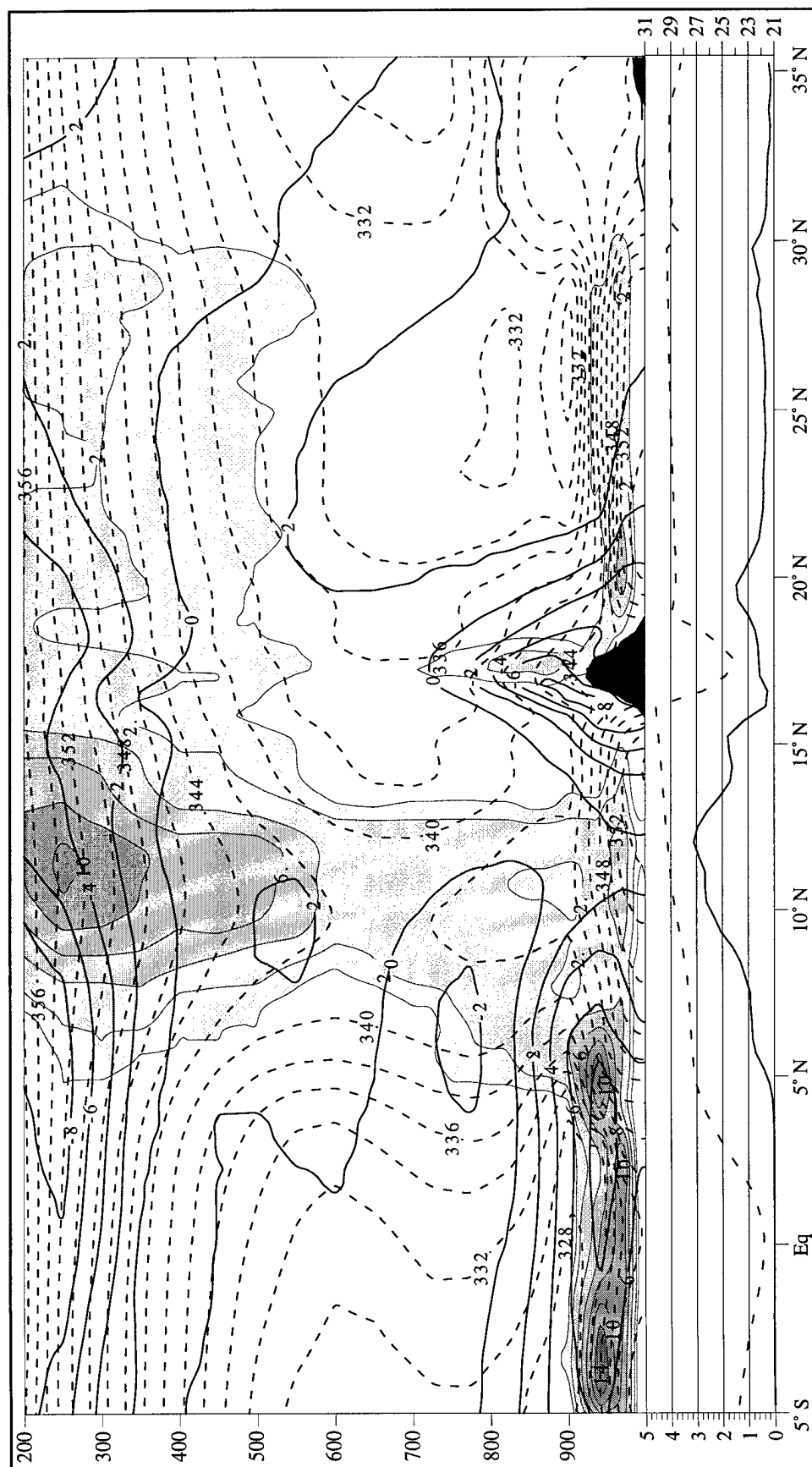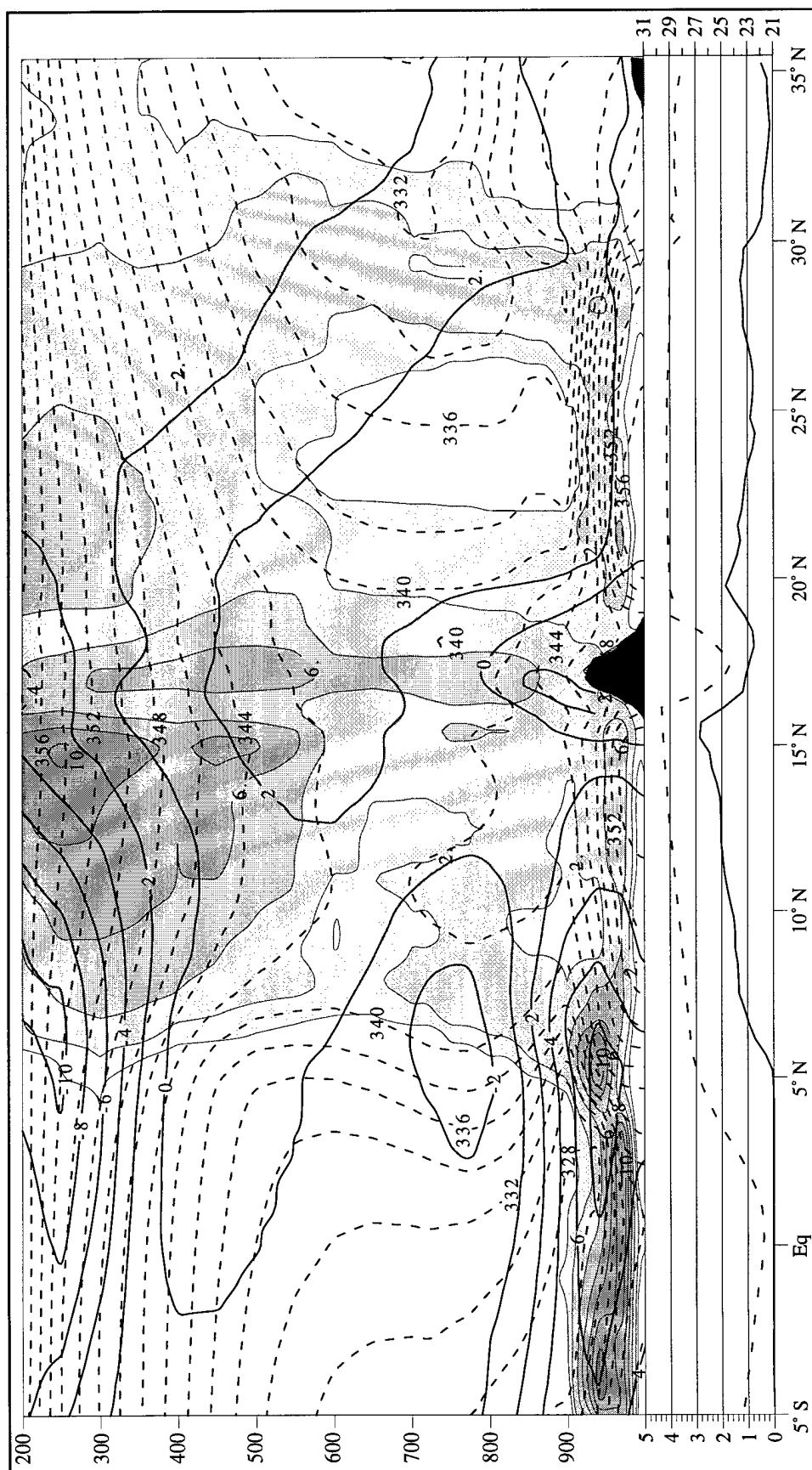
Figure F.6.    Vertical cross-section for JJA 1995 along 95° W from 5° S to 35° N. The vertical coordinate is pressure in mb. The thin dashed lines are $\theta_e$ in K. The thicker solid lines denote the meridional wind component in m s$^{-1}$. The shaded regions and associated contours are total LWC in $10^{-2}$ g kg$^{-1}$. The lower graph contains the average precipitation rate in cm day$^{-1}$ (solid line) and the average surface temperature in °C (dashed line) along 95° W.
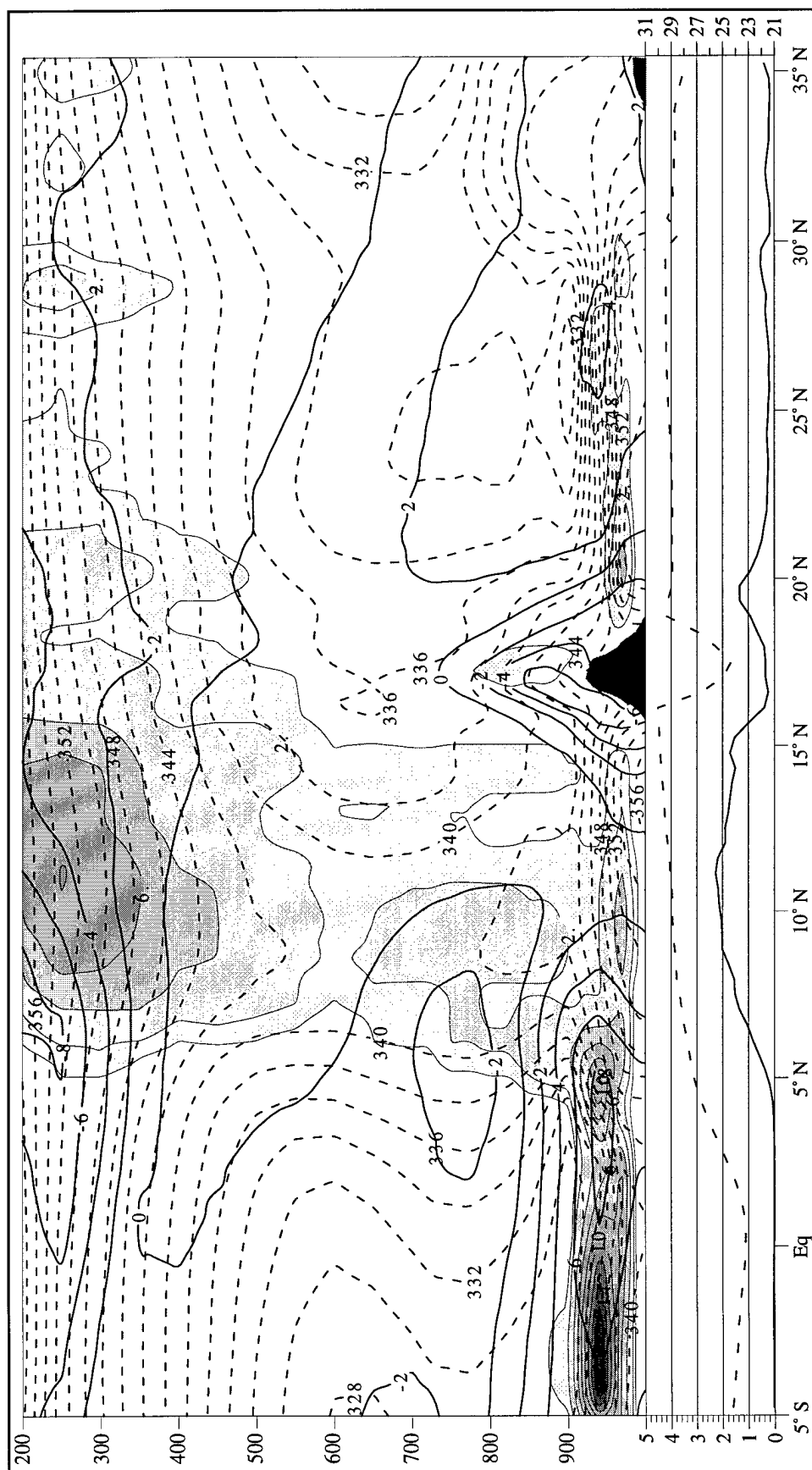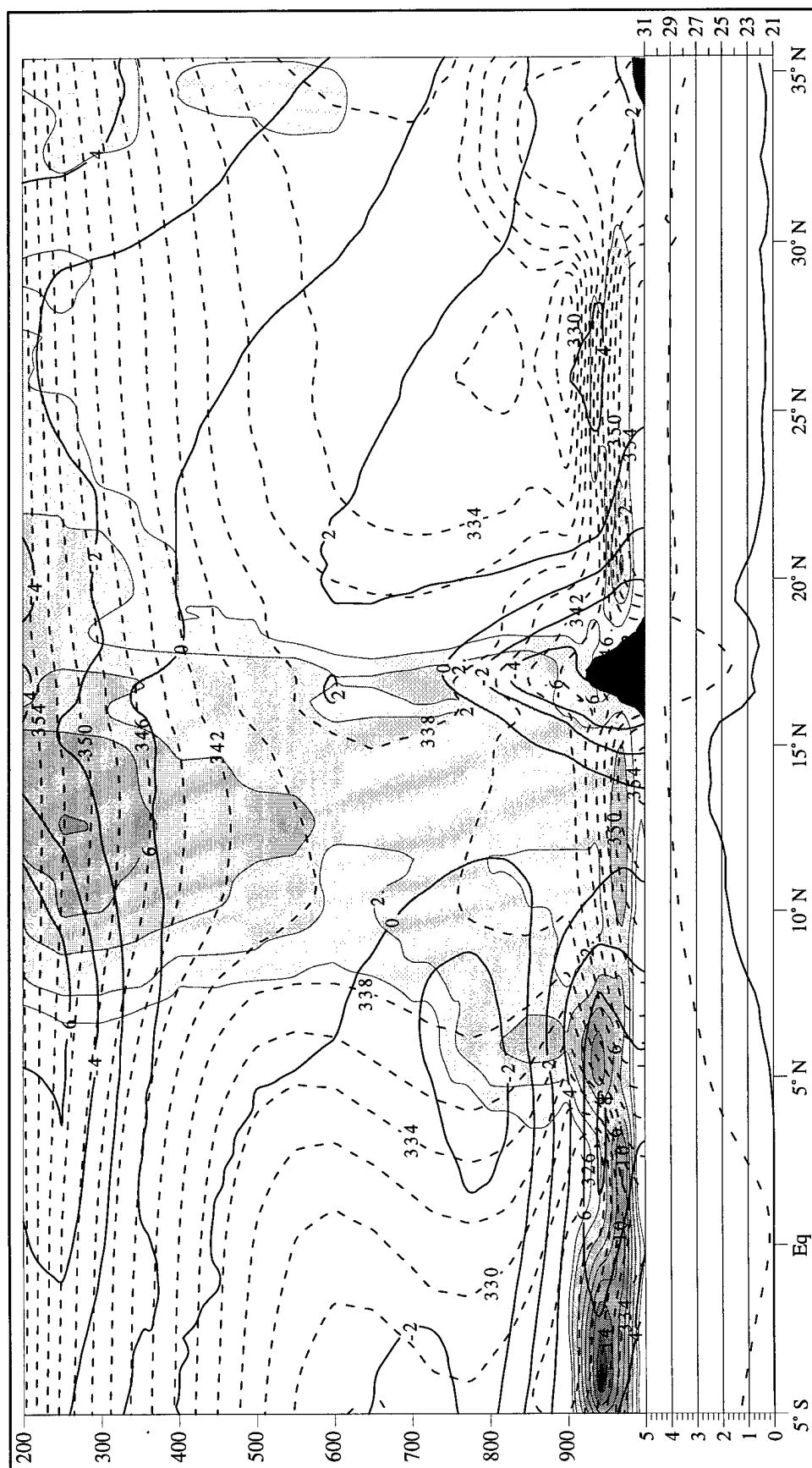
Figure F.7.    Vertical cross-section for JJA 1996 along 95° W from 5° S to 35° N. The vertical coordinate is pressure in mb. The thin dashed lines are $\theta_e$ in K. The thicker solid lines denote the meridional wind component in m s$^{-1}$. The shaded regions and associated contours are total LWC in $10^{-2}$ g kg$^{-1}$. The lower graph contains the average precipitation rate in cm day$^{-1}$ (solid line) and the average surface temperature in °C (dashed line) along 95° W.
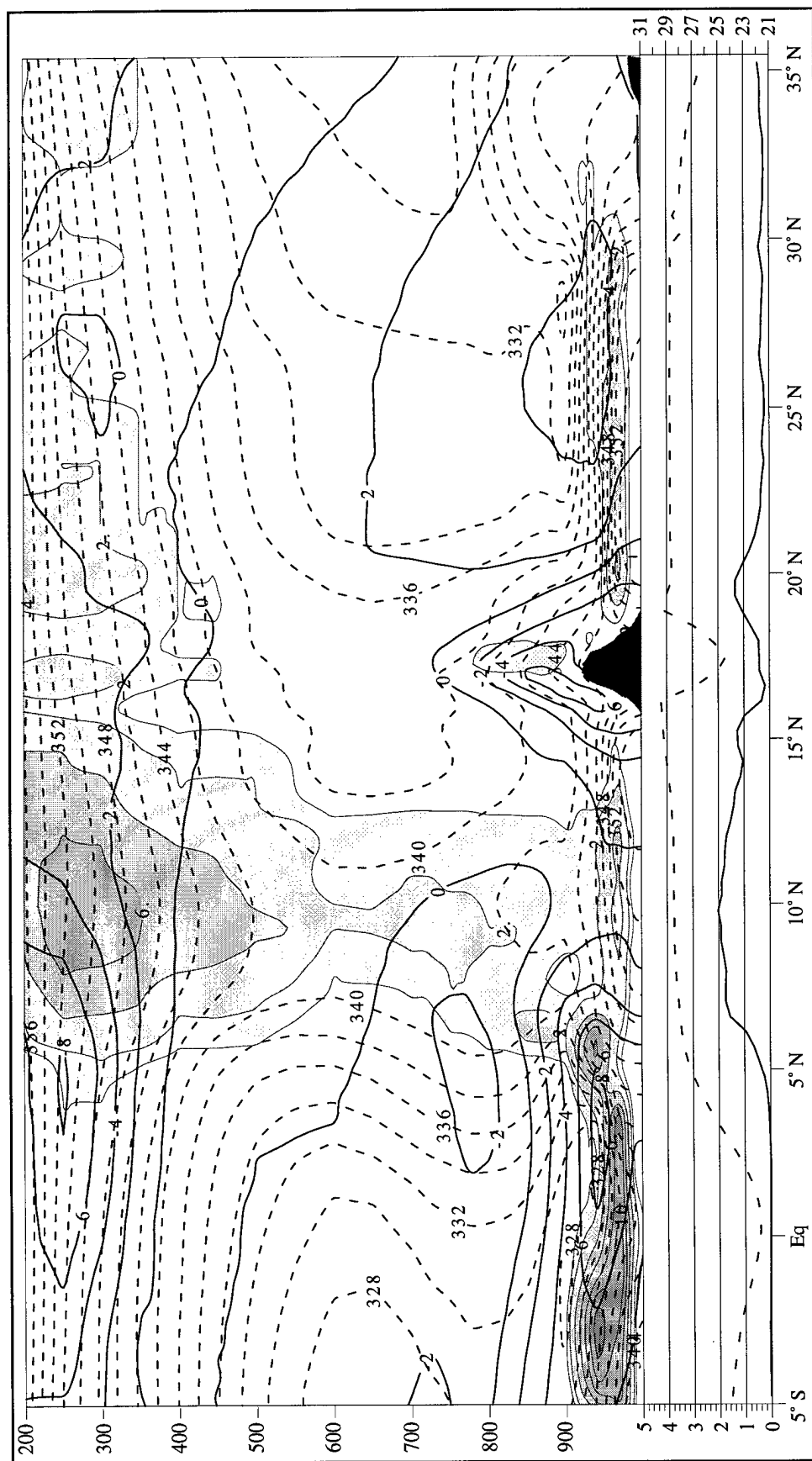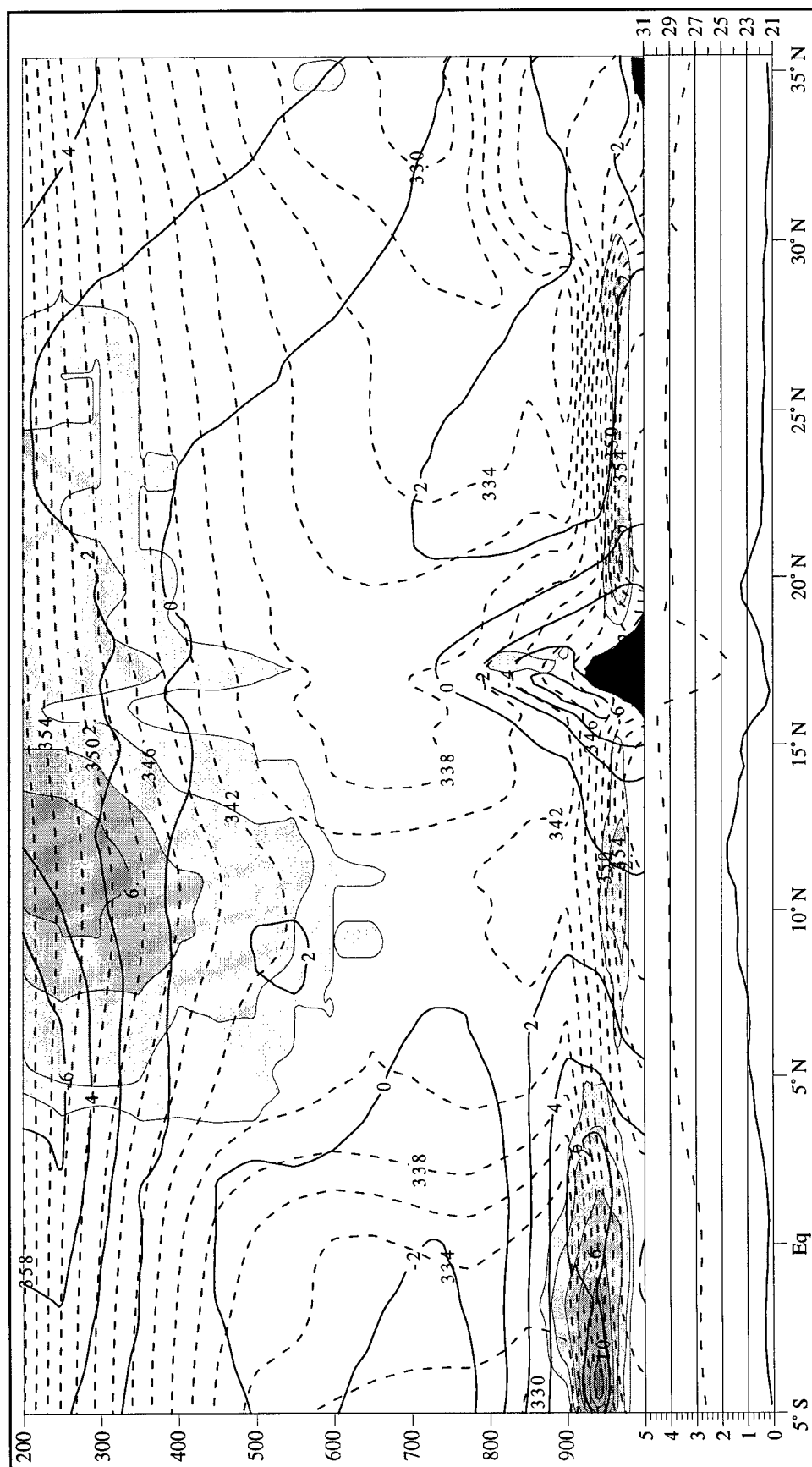
Figure F.8.    Vertical cross-section for JJA 1997 along 95° W from 5° S to 35° N. The vertical coordinate is pressure in mb. The thin dashed lines are $\theta_e$ in K. The thicker solid lines denote the meridional wind component in m s$^{-1}$. The shaded regions and associated contours are total LWC in $10^{-2}$ g kg$^{-1}$. The lower graph contains the average precipitation rate in cm day$^{-1}$ (solid line) and the average surface temperature in °C (dashed line) along 95° W.

Delecluse, P., M. K. Davey, Y. Kitamura, S. G. H. Philander, M. Suarez, and L. Bengtsson, 1998: Coupled general circulation modeling of the tropical Pacific. *J. Geophys. Res.*, **103**, 14,357-14,373.

Delworth, T., and S. Manabe, 1989: The influence of soil wetness on near surface atmospheric variability. *J. Climate*, **2**, 1447-1462.

des Jardins, M. L., K. F. Brill, and S. S. Schotz, 1991: *GEMPAK5 User's Guide*. NASA Tech. Memo. 4260.

Douglas, M. W., 1995: The summertime low-level jet over the Gulf of California. *Mon. Wea. Rev.*, **123**, 2334-2347.

___, and S. Li, 1996: Diurnal variation of the lower-tropospheric flow over the Arizona desert from the SWAMP-1993 observations. *Mon. Wea. Rev.*, **124**, 1211-1224.

___, R. A. Maddox, K. Howard, and S. Reyes, 1993: The Mexican monsoon. *J. Climate*, **6**, 1665-1677.

Dudhia, J., 1989: Numerical study of convection observed during the Winter Monsoon Experiment using a mesoscale two-dimensional model. *J. Atmos. Sci.*, **46**, 3077-3107.

Dunn, L. B., and J. Horel, 1994: Prediction of central Arizona convection. Part I: Evaluation of the NGM and Eta model precipitation forecasts. *Wea. Forecasting.*, **9**, 495-507.

Elsberry, R. L., W. M. Frank, G. J. Holland, J. D. Jarrell, and R. L. Southern, 1987: *A Global View of Tropical Cyclones*. University of Chicago Press, 185 pp.

Farfán, L. M., and J. A. Zehnder, 1997: Orographic influence on the synoptic-scale circulations associated with the genesis of Hurricane Guillermo. *Mon. Wea. Rev.*, **125**, 2683-2698.

Giorgi, F., 1990: Simulation of regional climate using a limited area model nested in a general circulation model. *J. Climate*, **3**, 941-963.

Godfrey, J. S., R. A. Houze Jr., R. H. Johnson, R. Lukas, J. -L. Redelsperger, A. Sumi, and R. Weller, 1998: Coupled ocean-atmosphere response experiment (COARE): An interim report. *J. Geophys. Res.*, **103**, 14,395-14,45.

Grell, G. A., J. Dudhia, and D. R. Stauffer, 1994: A description of the fifth-generation Penn State/NCAR mesoscale model (MM5), NCAR technical note, NCAR/TN-398+STR.

Hales, J. E. Jr., 1972: Surges of maritime tropical air northward over the Gulf of California. *Mon. Wea. Rev.*, **100**, 298-306.

___, 1974: Southwestern United States summer monsoon source - Gulf of Mexico or Pacific Ocean? *J. Appl. Meteor.*, **13**, 331-342.

Higgins, R. W., K. C. Mo, and S. D. Schubert, 1996: The moisture budget of the Central United States in the spring as evaluated in the NCEP/NCAR and the NASA/DAO reanalyses. *Mon. Wea. Rev.*, **124**, 939-963.

___, Y. Chen, and A. V. Douglas, 1998: Interannual variability of the North American warm season precipitation regime. *J. Climate*, in press.

Horel, J. D., 1982: On the annual cycle of the tropical Pacific atmosphere and ocean. *Mon. Wea. Rev.*, **110**, 1863-1878.

___, A. H. Hahmann, and J. E. Geisler, 1989: An investigation of the annual cycle of convective activity over the tropical Americas. *J. Climate*, **11**, 1388-1403.

Houze, Jr., R. A., 1993: *Cloud Dynamics.* Academic Press, 573 pp.

Hsie E. -Y., R. A. Anthes, and D. Keyser, 1984: Numerical simulation of frontogenesis in a moist atmosphere. *J. Atmos. Sci.*, **41**, 2581-2594.

Huffman, G. J., R. F. Alder, P. Arkin, A. Chang, R. Ferraro, A. Gruber, J. Janowiak, A. McNab, B. Rudolf, and U. Schneider, 1997: The global precipitation climatology project (GPCP) combined precipitation dataset. *Bull. Amer. Meteor. Soc.*, **78**, 5-20.

Janowiak, J. E., P. A. Arkin, P. Xie, M. L. Morrissey, and D. R. Legates, 1995: An examination of the East Pacific ITCZ rainfall distribution. *J. Climate*, **8**, 2810-2823.

Kalnay, E., M. Kanamitsu, R. Kistler, W. Collins, D. Deaven, L. Gandin, M. Iredell, S. Saha, G. White, J. Woollen, Y. Zhu, M. Chelliah, W. Ebisuzaki, W. Higgins, J. Janowiak, K. C. Mo, C. Ropelewski, J. Wang, A. Leetmaa, R. Reynolds, R. Jenne, and D. Joseph, 1996: The NCEP/NCAR 40-year reanalysis project. *Bull. Amer. Meteor. Soc.*, **77**, 437-471.

Kain, J. S., and J. M. Fritsch, 1990: A one-dimensional entraining/detraining plume model and its application in convective parameterization. *J. Atmos. Sci.*, **47**, 2784-2802.

Kessler, W. S., L. M. Rothstein, and D. Chen, 1998: The annual cycle of SST in the eastern tropical Pacific, diagnosed in an ocean GCM. *J. Climate*, **11**, 777-799.

Klein, S. A., and D. L. Hartmann, 1993: The seasonal cycle of low stratiform clouds. *J. Climate*, **6**, 1587-1606.

Kloesel, K. A., and B. A. Albrecht, 1989: Low-level inversions over the tropical Pacific - thermodynamic structure of the boundary layer and the above-inversion moisture source. *Mon. Wea. Rev.*, **117**, 87-101.

Krishnamurti, T. N., and L. Bounoua, 1996: *Numerical Weather Prediction Techniques*, CRC Press, 293 pp.

Latif, M., D. Anderson, T. Barnett, M. Cane, R. Kleeman, A. Leetmaa, J. O'Brien, A. Rosati, and E. Schneider, 1998: A review of the predictability and prediction of ENSO. *J. Geophys. Res.*, **103**, 14,375-14,393.

Lawrence, M. B., and E. N. Rappaport, 1994: Eastern North Pacific hurricane season of 1992. *Mon. Wea. Rev.*, **122**, 549-558.

Legates, D. R., and C. J. Wilmott, 1990: Mean seasonal and spatial variability in gauge-corrected global precipitation. *Int. J. Climate*, **9**, 1531-1545.

Liou, K. N., 1992: *Radiation and Cloud Processes in the Atmosphere*, Oxford University Press, 487 pp.

McPhaden, M. J., A. J. Busalacchi, R. Cheney, J. Donguy, K. S. Gage, D. Halpern, M. Ji, P. Julian, G. Meyers, G. T. Mitchum, P. P. Niiler, J. Picaut, R. W. Reynolds, N. Smith, and K. Takeuchi, 1998: The tropical ocean-atmosphere observing system: A decade of progress. *J. Geophys. Res.*, **103**, 14,169-14,240.

Mechoso, C. R., A. W. Robinson, N. Barth, M. K. Davey, P. Delecluse, P. R. Gent, S. Ineson, B. Kirtman, M. Latif, H. Le Treut, T. Nagai, J. D. Neelin, S. G. H. Philander, J. Polcher, P. S. Schopf, T. Stockdale, M. J. Suarez, L. Terray, O. Thual, and J. J. Tribbia, 1995: The seasonal cycle over the tropical Pacific in coupled ocean - atmosphere general circulation models. *Mon. Wea. Rev.*, **123**, 2825-2838.

Mo, K. C., and R. W. Higgins, 1996: Large-scale atmospheric moisture transport as evaluated in the NCEP/NCAR and the NASA/DAO reanalyses. *J. Climate*, **9**, 1531-1545.

Mohr, K. I., and E. J. Zipser, 1996: Mesoscale convective systems defined by their 85GHz ice scattering signature: Size and intensity comparison over tropical oceans and continents. *Mon. Wea. Rev.*, **124**, 2417-2437.

Negri, A. J., R. F. Adler, R. A. Maddox, K. W. Howard, and P. R. Keehn, 1993: A regional rainfall climatology over Mexico and the Southwest United States derived from passive microwave and geosynchronous infrared data. *J. Climate*, **6**, 2144-2161.

Nelson, N. B., 1998: Spatial and temporal extent of sea surface temperature modifications by hurricanes in the Sargasso Sea during the 1995 season. *Mon. Wea. Rev.*, **126**, 1364-1368.

NOAA, 1998: *PACS: A Scientific Prospectus and Implementation Plan.* S. K. Esbenson, Ed., NOAA, 40 pp. NOAA OGP, Washington D.C.

Paegle, J., 1989: A variable resolution global model based upon Fourier and finite element representation. *Mon. Wea. Rev.*, **117**, 583-606.

Paegle, J. N., and K. C. Mo, 1997: Alternating wet and dry conditions over South America during summer. *Mon. Wea. Rev.*, **125**, 279-291.

Pasch, R. J., and M. Mayfield, 1996: Eastern North Pacific hurricane season of 1994. *Mon. Wea. Rev.*, **124**, 1579-1590.

Rappaport, E. N., and M. Mayfield, 1992: Eastern North Pacific hurricane season of 1991. *Mon. Wea. Rev.*, **120**, 2697-2708.

___, L. A. Avila, M. B. Lawrence, M. Mayfield, and R. Pasch, 1998: Eastern North Pacific hurricane season of 1995. *Mon. Wea. Rev.*, **126**, 1152-1162.

Rasmusson, E. M., and K. C. Mo, 1996: Large-scale atmospheric moisture cycling as evaluated from the NMC global analysis and forecast products. *J. Climate*, **9**, 3276-3297.

Reynolds, R. W., and T. M. Smith, 1994: Improved global sea surface temperature analyses using optimum interpolation. *J. Climate*, **7**, 929-948.

Robinson, M. K., 1973: *Atlas of Mean Monthly Sea Surface and Subsurface Temperatures in the Gulf of California, Mexico,* San Diego Society of Natural History, Memoir 5, San Diego, 76 pp.

Schmitz, J. T., and S. L. Mullen, 1996: Water vapor transport associated with the summertime North American monsoon as depicted by ECMWF analyses. *J. Climate*, **9**, 1621-1634.

Stensrud, D. J., R. L. Gall, S. L. Mullen, and K. W. Howard, 1995: Model climatology of the Mexican monsoon. *J. Climate*, **8**, 1775-1794.

___, R. L. Gall, and M. K. Nordquist, 1997: Surges over the Gulf of California during the Mexican monsoon. *Mon. Wea. Rev.*, **125**, 417-437.

Steenburgh, W. J., D. M. Schultz, and B. A. Colle, 1997: The structure and evolution of gap outflow over the Gulf of Tehuantepec, Mexico. *Mon. Wea. Rev.*, Submitted: Aug., 1997.

Tang M., and E. R. Reiter, 1984: Plateau monsoons of the northern hemisphere: A comparison between North America and Tibet. *Mon. Wea. Rev.*, **112**, 617-637.

Velasco, I., and J. M. Fritsch, 1987: Mesoscale convective complexes in the Americas. *J. Geophys. Res.*, **92**, 9591-9613.

Vitart, F., J. L. Anderson, and W. F. Stern, 1997: Simulation of interannual variability of tropical storm frequency in an ensemble of GCM integrations. *J. Climate*, **10**, 745-760.

Wallace, J. M., T. P. Mitchell and C. Deser, 1989: The influence of sea-surface temperature on surface wind in the eastern equatorial Pacific: Seasonal and interannual variability. *J. Climate*, **2**, 1492-1499.

___, E. M. Rasmusson, T. P. Mitchell, V. E. Kousky, E. S. Sarachik, and H. von Storch, 1998: On the structure and evolution of ENSO-related climate variability in the tropical Pacific: Lessons from TOGA. *J. Geophys. Res.*, **103**, 14,241-14,259.

Wang, M., and J. Paegle, 1996: Impact of analysis uncertainty upon regional atmospheric moisture flux. *J. Geophys. Res.*, **101**, 7291-7303.

Wang, W., and N. L. Seaman, 1997: A comparison study of convective parameterization schemes in a mesoscale model. *Mon. Wea. Rev.*, **125**, 252-278.

Warner, T. T., R. A. Peterson, and R. E. Treadon, 1997: A tutorial on lateral boundary conditions as a basic and potentially serious limitation to regional numerical weather prediction. *Bull. Amer. Meteor. Soc.*, **78**, 2599-2617.

Xie, P., and P. A. Arkin, 1998: Global monthly precipitation estimates from satellite-observed outgoing longwave radiation. *J. Climate*, **11**, 137-164.

Xie, S., 1998: Ocean-atmosphere interaction in the making of the Walker circulation and equatorial cold tongue. *J. Climate*, **11**, 189-201.

Zhang, D., and R. A. Anthes, 1982: A high-resolution model of the planetary boundary layer-sensitivity test and comparisons with SESAME-79 data. *J. Appl. Meteor.*, **21**, 1594-1609.

# REFERENCES

Adams, D. K., and A. C. Comrie, 1997: The North American monsoon. *Bull. Amer. Meteor. Soc.*, **78**, 2197-2213.

Avila, L. A., 1991: Eastern North Pacific hurricane season of 1990. *Mon. Wea. Rev.*, **119**, 2034-2046.

___, and M. Mayfield, 1995: Eastern North Pacific hurricane season of 1993. *Mon. Wea. Rev.*, **123**, 897-906.

Barlow, M., S. Nigam, and E. H. Berbery, 1998: Evolution of the North American monsoon system. *J. Climate*, in press.

Bengtsson, L., M. Botzet, and M. Esch, 1995: Hurricane-type vortices in a general circulation model. *Tellus*, **47A**, 175-196.

Berbery, E. H., E. M. Rasmusson, and K. E. Mitchell, 1996: Studies of North American continental-scale hydrology using Eta model forecast products. *J. Geophys. Res.*, **101**, 7305-7319.

Betts, A. K., S. Hong, and H Pan, 1996: Comparison of the NCEP-NCAR reanalysis with 1987 FIFE data. *Mon. Wea. Rev.*, **124**, 1480-1498.

Bister, M., and K. A. Emanuel, 1997: The genesis of Hurricane Guillermo: TEXMEX analyses and a modeling study. *Mon. Wea. Rev.*, **125**, 2662-2682.

Bond, N. A., 1992: Observations of planetary boundary-layer structure in the eastern equatorial Pacific. *J. Climate*, **5**, 699-706.

Bowen, B. M., 1996: Rainfall and climate variation over a sloping New Mexico plateau during the North American monsoon. *J. Climate*, **9**, 3432-3442.

Brenner, I. S., 1974: A surge of maritime tropical air - Gulf of California to the southwestern United States. *Mon. Wea. Rev.*, **102**, 375-389.

Chen, W. Y., and H. M. Van den Dool, 1997: Atmospheric predictability of the seasonal, annual and decadal climate means and the role of the ENSO cycle: A model study. *J. Climate*, **10**, 1236-1254.

Delecluse, P., M. K. Davey, Y. Kitamura, S. G. H. Philander, M. Suarez, and L. Bengtsson, 1998: Coupled general circulation modeling of the tropical Pacific. *J. Geophys. Res.*, **103**, 14,357-14,373.

Delworth, T., and S. Manabe, 1989: The influence of soil wetness on near surface atmospheric variability. *J. Climate*, **2**, 1447-1462.

des Jardins, M. L., K. F. Brill, and S. S. Schotz, 1991: *GEMPAK5 User's Guide*. NASA Tech. Memo. 4260.

Douglas, M. W., 1995: The summertime low-level jet over the Gulf of California. *Mon. Wea. Rev.*, **123**, 2334-2347.

___, and S. Li, 1996: Diurnal variation of the lower-tropospheric flow over the Arizona desert from the SWAMP-1993 observations. *Mon. Wea. Rev.*, **124**, 1211-1224.

___, R. A. Maddox, K. Howard, and S. Reyes, 1993: The Mexican monsoon. *J. Climate*, **6**, 1665-1677.

Dudhia, J., 1989: Numerical study of convection observed during the Winter Monsoon Experiment using a mesoscale two-dimensional model. *J. Atmos. Sci.*, **46**, 3077-3107.

Dunn, L. B., and J. Horel, 1994: Prediction of central Arizona convection. Part I: Evaluation of the NGM and Eta model precipitation forecasts. *Wea. Forecasting.*, **9**, 495-507.

Elsberry, R. L., W. M. Frank, G. J. Holland, J. D. Jarrell, and R. L. Southern, 1987: *A Global View of Tropical Cyclones*. University of Chicago Press, 185 pp.

Farfán, L. M., and J. A. Zehnder, 1997: Orographic influence on the synoptic-scale circulations associated with the genesis of Hurricane Guillermo. *Mon. Wea. Rev.*, **125**, 2683-2698.

Giorgi, F., 1990: Simulation of regional climate using a limited area model nested in a general circulation model. *J. Climate*, **3**, 941-963.

Godfrey, J. S., R. A. Houze Jr., R. H. Johnson, R. Lukas, J. -L. Redelsperger, A. Sumi, and R. Weller, 1998: Coupled ocean-atmosphere response experiment (COARE): An interim report. *J. Geophys. Res.*, **103**, 14,395-14,45.

Grell, G. A., J. Dudhia, and D. R. Stauffer, 1994: A description of the fifth-generation Penn State/NCAR mesoscale model (MM5), NCAR technical note, NCAR/TN-398+STR.

Hales, J. E. Jr., 1972: Surges of maritime tropical air northward over the Gulf of California. *Mon. Wea. Rev.*, **100**, 298-306.

___, 1974: Southwestern United States summer monsoon source - Gulf of Mexico or Pacific Ocean? *J. Appl. Meteor.*, **13**, 331-342.

Higgins, R. W., K. C. Mo, and S. D. Schubert, 1996: The moisture budget of the Central United States in the spring as evaluated in the NCEP/NCAR and the NASA/DAO reanalyses. *Mon. Wea. Rev.*, **124**, 939-963.

___, Y. Chen, and A. V. Douglas, 1998: Interannual variability of the North American warm season precipitation regime. *J. Climate*, in press.

Horel, J. D., 1982: On the annual cycle of the tropical Pacific atmosphere and ocean. *Mon. Wea. Rev.*, **110**, 1863-1878.

___, A. H. Hahmann, and J. E. Geisler, 1989: An investigation of the annual cycle of convective activity over the tropical Americas. *J. Climate*, **11**, 1388-1403.

Houze, Jr., R. A., 1993: *Cloud Dynamics*. Academic Press, 573 pp.

Hsie E. -Y., R. A. Anthes, and D. Keyser, 1984: Numerical simulation of frontogenesis in a moist atmosphere. *J. Atmos. Sci.*, **41**, 2581-2594.

Huffman, G. J., R. F. Alder, P. Arkin, A. Chang, R. Ferraro, A. Gruber, J. Janowiak, A. McNab, B. Rudolf, and U. Schneider, 1997: The global precipitation climatology project (GPCP) combined precipitation dataset. *Bull. Amer. Meteor. Soc.*, **78**, 5-20.

Janowiak, J. E., P. A. Arkin, P. Xie, M. L. Morrissey, and D. R. Legates, 1995: An examination of the East Pacific ITCZ rainfall distribution. *J. Climate*, **8**, 2810-2823.

Kalnay, E., M. Kanamitsu, R. Kistler, W. Collins, D. Deaven, L. Gandin, M. Iredell, S. Saha, G. White, J. Woollen, Y. Zhu, M. Chelliah, W. Ebisuzaki, W. Higgins, J. Janowiak, K. C. Mo, C. Ropelewski, J. Wang, A. Leetmaa, R. Reynolds, R. Jenne, and D. Joseph, 1996: The NCEP/NCAR 40-year reanalysis project. *Bull. Amer. Meteor. Soc.*, **77**, 437-471.

Kain, J. S., and J. M. Fritsch, 1990: A one-dimensional entraining/detraining plume model and its application in convective parameterization. *J. Atmos. Sci.*, **47**, 2784-2802.

Kessler, W. S., L. M. Rothstein, and D. Chen, 1998: The annual cycle of SST in the eastern tropical Pacific, diagnosed in an ocean GCM. *J. Climate*, **11**, 777-799.

Klein, S. A., and D. L. Hartmann, 1993: The seasonal cycle of low stratiform clouds. *J. Climate*, **6**, 1587-1606.

Kloesel, K. A., and B. A. Albrecht, 1989: Low-level inversions over the tropical Pacific - thermodynamic structure of the boundary layer and the above-inversion moisture source. *Mon. Wea. Rev.*, **117**, 87-101.

Krishnamurti, T. N., and L. Bounoua, 1996: *Numerical Weather Prediction Techniques*, CRC Press, 293 pp.

Latif, M., D. Anderson, T. Barnett, M. Cane, R. Kleeman, A. Leetmaa, J. O'Brien, A. Rosati, and E. Schneider, 1998: A review of the predictability and prediction of ENSO. *J. Geophys. Res.*, **103**, 14,375-14,393.

Lawrence, M. B., and E. N. Rappaport, 1994: Eastern North Pacific hurricane season of 1992. *Mon. Wea. Rev.*, **122**, 549-558.

Legates, D. R., and C. J. Wilmott, 1990: Mean seasonal and spatial variability in gauge-corrected global precipitation. *Int. J. Climate*, **9**, 1531-1545.

Liou, K. N., 1992: *Radiation and Cloud Processes in the Atmosphere*, Oxford University Press, 487 pp.

McPhaden, M. J., A. J. Busalacchi, R. Cheney, J. Donguy, K. S. Gage, D. Halpern, M. Ji, P. Julian, G. Meyers, G. T. Mitchum, P. P. Niiler, J. Picaut, R. W. Reynolds, N. Smith, and K. Takeuchi, 1998: The tropical ocean-atmosphere observing system: A decade of progress. *J. Geophys. Res.*, **103**, 14,169-14,240.

Mechoso, C. R., A. W. Robinson, N. Barth, M. K. Davey, P. Delecluse, P. R. Gent, S. Ineson, B. Kirtman, M. Latif, H. Le Treut, T. Nagai, J. D. Neelin, S. G. H. Philander, J. Polcher, P. S. Schopf, T. Stockdale, M. J. Suarez, L. Terray, O. Thual, and J. J. Tribbia, 1995: The seasonal cycle over the tropical Pacific in coupled ocean - atmosphere general circulation models. *Mon. Wea. Rev.*, **123**, 2825-2838.

Mo, K. C., and R. W. Higgins, 1996: Large-scale atmospheric moisture transport as evaluated in the NCEP/NCAR and the NASA/DAO reanalyses. *J. Climate*, **9**, 1531-1545.

Mohr, K. I., and E. J. Zipser, 1996: Mesoscale convective systems defined by their 85GHz ice scattering signature: Size and intensity comparison over tropical oceans and continents. *Mon. Wea. Rev.*, **124**, 2417-2437.

Negri, A. J., R. F. Adler, R. A. Maddox, K. W. Howard, and P. R. Keehn, 1993: A regional rainfall climatology over Mexico and the Southwest United States derived from passive microwave and geosynchronous infrared data. *J. Climate*, **6**, 2144-2161.

Nelson, N. B., 1998: Spatial and temporal extent of sea surface temperature modifications by hurricanes in the Sargasso Sea during the 1995 season. *Mon. Wea. Rev.*, **126**, 1364-1368.

NOAA, 1998: *PACS: A Scientific Prospectus and Implementation Plan.* S. K. Esbenson, Ed., NOAA, 40 pp. NOAA OGP, Washington D.C.

Paegle, J., 1989: A variable resolution global model based upon Fourier and finite element representation. *Mon. Wea. Rev.*, **117**, 583-606.

Paegle, J. N., and K. C. Mo, 1997: Alternating wet and dry conditions over South America during summer. *Mon. Wea. Rev.*, **125**, 279-291.

Pasch, R. J., and M. Mayfield, 1996: Eastern North Pacific hurricane season of 1994. *Mon. Wea. Rev.*, **124**, 1579-1590.

Rappaport, E. N., and M. Mayfield, 1992: Eastern North Pacific hurricane season of 1991. *Mon. Wea. Rev.*, **120**, 2697-2708.

___, L. A. Avila, M. B. Lawrence, M. Mayfield, and R. Pasch, 1998: Eastern North Pacific hurricane season of 1995. *Mon. Wea. Rev.*, **126**, 1152-1162.

Rasmusson, E. M., and K. C. Mo, 1996: Large-scale atmospheric moisture cycling as evaluated from the NMC global analysis and forecast products. *J. Climate*, **9**, 3276-3297.

Reynolds, R. W., and T. M. Smith, 1994: Improved global sea surface temperature analyses using optimum interpolation. *J. Climate*, **7**, 929-948.

Robinson, M. K., 1973: *Atlas of Mean Monthly Sea Surface and Subsurface Temperatures in the Gulf of California, Mexico,* San Diego Society of Natural History, Memoir 5, San Diego, 76 pp.

Schmitz, J. T., and S. L. Mullen, 1996: Water vapor transport associated with the summertime North American monsoon as depicted by ECMWF analyses. *J. Climate*, **9**, 1621-1634.

Stensrud, D. J., R. L. Gall, S. L. Mullen, and K. W. Howard, 1995: Model climatology of the Mexican monsoon. *J. Climate*, **8**, 1775-1794.

___, R. L. Gall, and M. K. Nordquist, 1997: Surges over the Gulf of California during the Mexican monsoon. *Mon. Wea. Rev.*, **125**, 417-437.

Steenburgh, W. J., D. M. Schultz, and B. A. Colle, 1997: The structure and evolution of gap outflow over the Gulf of Tehuantepec, Mexico. *Mon. Wea. Rev.*, Submitted: Aug., 1997.

Tang M., and E. R. Reiter, 1984: Plateau monsoons of the northern hemisphere: A comparison between North America and Tibet. *Mon. Wea. Rev.*, **112**, 617-637.

Velasco, I., and J. M. Fritsch, 1987: Mesoscale convective complexes in the Americas. *J. Geophys. Res.*, **92**, 9591-9613.

Vitart, F., J. L. Anderson, and W. F. Stern, 1997: Simulation of interannual variability of tropical storm frequency in an ensemble of GCM integrations. *J. Climate*, **10**, 745-760.

Wallace, J. M., T. P. Mitchell and C. Deser, 1989: The influence of sea-surface temperature on surface wind in the eastern equatorial Pacific: Seasonal and interannual variability. *J. Climate*, **2**, 1492-1499.

___, E. M. Rasmusson, T. P. Mitchell, V. E. Kousky, E. S. Sarachik, and H. von Storch, 1998: On the structure and evolution of ENSO-related climate variability in the tropical Pacific: Lessons from TOGA. *J. Geophys. Res.*, **103**, 14,241-14,259.

Wang, M., and J. Paegle, 1996: Impact of analysis uncertainty upon regional atmospheric moisture flux. *J. Geophys. Res.*, **101**, 7291-7303.

Wang, W., and N. L. Seaman, 1997: A comparison study of convective parameterization schemes in a mesoscale model. *Mon. Wea. Rev.*, **125**, 252-278.

Warner, T. T., R. A. Peterson, and R. E. Treadon, 1997: A tutorial on lateral boundary conditions as a basic and potentially serious limitation to regional numerical weather prediction. *Bull. Amer. Meteor. Soc.*, **78**, 2599-2617.

Xie, P., and P. A. Arkin, 1998: Global monthly precipitation estimates from satellite-observed outgoing longwave radiation. *J. Climate*, **11**, 137-164.

Xie, S., 1998: Ocean-atmosphere interaction in the making of the Walker circulation and equatorial cold tongue. *J. Climate*, **11**, 189-201.

Zhang, D., and R. A. Anthes, 1982: A high-resolution model of the planetary boundary layer-sensitivity test and comparisons with SESAME-79 data. *J. Appl. Meteor.*, **21**, 1594-1609.